

# Statement of Originality

This thesis contains no material which has been accepted for the award of a degree or diploma in this or any other university. To the best of the candidate's knowledge and belief, this thesis contains no material previously published or written by another person except where due reference is made in the text of this thesis.

.....  
Candidate : B.T. Tan

# Vortex Shedding and Interaction in Flows around Bluff Plates

by

Tan Boon Thong

Thesis submitted to Monash University

for the degree of

Doctor of Philosophy

July 2000

Department of Mechanical Engineering

Monash University

# Abstract

This is a study of laminar flow around long plates. Two cases are considered: the flow past a plate with an aerodynamic leading edge and, a rectangular cross-sectioned plate. An aerodynamic leading-edge plate is a natural precursor to the flow past a rectangular plate because the shedding is only from the trailing edge. The flow around rectangular plates is more complex because it involves the interaction between leading- and trailing-edge shedding. Both natural and forced shedding cases are studied. The source of the forcing is a small sinusoidal cross-flow oscillation added to the free stream. The acoustic resonance generated when a rectangular plate is placed in a duct is also examined. Finally, a limited study on the transition from two- to three-dimensional flow for these geometries is presented.

In this study, the flow is predicted by solving the incompressible Navier-Stokes equations numerically. A combination of spectral-element and global spectral schemes is used for the spatial discretisation. Two different time stepping methods are evaluated. The numerical scheme is validated by simulating the backward-facing step flow and the driven cavity flow. Several simulations of the flow around the plates are performed to determine an adequate domain size and temporal and spatial resolution.

The aerodynamic leading-edge plates mainly consisted of plates with elliptical leading edges (5:1 axes ratio). The aspect ratio and Reynolds number varied between  $3.5 \leq c/t \leq 12.5$  and  $200 \leq Re \leq 700$  respectively ( $c$  being the chord and  $t$  being the thickness). The shedding frequency is determined in the natural shedding case and reasonable agreement is found with a correlation obtained from experimental data at higher Reynolds numbers. In the forced shedding case, the behaviour of the flow around these plates shows several similarities with that around short bluff bodies. There is only a small range of frequencies for which the flow is locked but this range grows with forcing amplitude. Outside the lock-in range, the mean base pressure approaches that for the unforced case but the time varying base pressure trace shows the characteristics of *beating* between the Strouhal frequency and the forcing frequency. Within the lock-in range, the mean base pressure is very sensitive to the forcing frequency. Two distinct cases are

observed in the parameter range studied; one that occurs for lower Reynolds number or longer plates, and the other for higher Reynolds number or shorter plates. These two parameters control the thickness of the boundary layer at the trailing edge which directly influences the shedding process. For most of the lock-in range, both cases show a linear increase in mean base suction with increasing frequency. For the case with shorter plates (or higher Reynolds numbers), the mean base suction is noticeably lower than that of the natural shedding case at the lower frequency end of the lock-in range. The other case shows a drastic phase shift in shedding relative to the forcing which is associated with a drop in mean base suction at the higher frequency end of the lock-in range. Overall the drag force mimics the behaviour of the base suction. Within the lock-in range, there is a decrease in the fluctuating lift force because of a narrower wake. The simulations show that the mean base suction in the lock-in range is strongly related to the rate of generation of vorticity (of one sign) and the vortex formation length.

The flows around rectangular plates with aspect ratios in the range  $3 \leq c/t \leq 16$  and Reynolds numbers between  $300 \leq Re \leq 500$  are simulated next. Three cases are considered: (a) natural shedding; (b) where the flow is forced by a small sinusoidal cross-flow oscillation; and (c) where the plate is placed in a duct and a flow induced acoustic resonance can occur. In the natural shedding case below a certain aspect ratio and Reynolds number, the flow appears to lock to an impinging leading-edge vortex (ILEV) instability mode. This results in a stepwise increase in Strouhal number (based on chord) with increasing aspect ratio. The ILEV instability described by Naudascher & Wang (1993) comprises of: (i) the leading-edge shear layer shedding discrete vortices; (ii) the convection of these vortices past the trailing edge; (iii) and an accompanying pressure pulse that travel upstream and locks the leading-edge shedding and thus completes a feedback loop. These simulations with a rectangular plate shows strong base shedding with vortices forming between the passing of leading-edge vortices. An important conclusion from the research is the proposal that it is the pressure fluctuations from the base shedding which has a dominant role in controlling the leading-edge shedding. A modification to the original ILEV mechanism to incorporate this is described. In addition, both the forced shedding and duct resonance cases are also strongly influenced by trailing-edge shedding. In the forced shedding case, the lock-in range is large and the mean base pressure is not strongly sensitive to the forcing amplitude and Reynolds number. The forcing frequency which results in a peak mean base suction also shows a stepwise response. The duct acoustic resonance case involves a plate placed in a solid walled duct. The sound generated by the flow around the plate may generate an acoustic resonance in the duct which locks the flow. The flow-sound interaction is modelled using Howe's acoustic theory (Howe, 1975, 1980). The frequency range where resonance occurs also shows a stepwise response. In all three cases, the stepping in Strouhal number based on chord

is approximately described by the relationship  $St_c = 0.55n$ , where  $n$  is the step number. This trend matches experimental observations which are performed at higher Reynolds numbers; especially for the forced and duct acoustic resonance cases. This shows that the essential physical mechanisms involved are captured in these (low  $Re$ , two-dimensional) simulations. The stepwise response in all three cases requires a synchronisation between the leading- and trailing-edge shedding. In the natural shedding case, this is a result of the flow at the trailing-edge sending a pressure pulse to lock the leading edge. In the forced shedding and duct acoustic resonance cases, the leading-edge shedding is phase-locked to the forcing/acoustic field. The peak base suction for the forced shedding case, and the resonance range in the duct resonance case, consistently occurs at approximately the same phase in the flow cycle relative to the forcing. To maintain the phase relationship between the leading- and trailing-edge flow, the shedding modes can only increase by having a complete pair of vortices along the plate. This results in the step change in the shedding mode once critical aspect ratios are exceeded. The levels of the steps show that the average convective velocity of the flow structures along the plate is approximately 55% of the free-stream velocity in all cases. Consistent with this are the calculations of convective velocity along the plate for both the natural and forced shedding cases which show that the velocity is not significantly influenced by aspect ratio and forcing/shedding frequency. The mean base suction and drag are generally stronger at the lower aspect ratio end of each step in both the natural and forced shedding cases. This is a result of more compact vortices forming at the trailing edge at higher forcing/shedding frequency. The fluctuating lift force in the natural shedding case is approximately constant which means that the force coefficient (which is scaled on chord) is inversely proportional to aspect ratio. In the forced shedding case, the peaks in the fluctuating lift coefficient also show a stepwise response. This is governed by the phase at which the leading-edge vortices pass the trailing edge relative to the generation at the leading edge.

Some three-dimensional simulations were performed to capture the main instability modes close to the onset of three-dimensional flow. For the elliptical leading-edge plates, the trailing-edge wake vortices develop three-dimensionality similar to the wake transition for a circular cylinder. Both *Mode A* and *B* shedding (Williamson, 1988) were observed. The transition occurs at a much higher Reynolds number (between  $Re = 400$  and  $500$  for  $c/t = 7.5$ ), compared with  $Re = 180$  for a circular cylinder. This is presumably due to the thicker boundary layers at the trailing edge. For the rectangular plate, the boundary layer modes were examined. Experiments indicate the existence of two distinct mode topologies (*Pattern A* and *B*, Sasaki & Kiya, 1991). The current study only found the presence of *Pattern B*. It is unclear why the initial instability mode was not found. A stability analysis is planned to resolve this discrepancy.

# Acknowledgement

The Author wishes to thank the following for assistance during the course of this study.

My supervisor, Dr. Mark C. Thompson, for providing excellent guidance and supervision.

The added input of Associate Professor Kerry Hourigan, whose ideas led to numerous investigations.

Dr Paul Morris, which assisted in the early stages with numerical aspects of the study.

The High Performance Computing facility at Monash University and its dedicated staff, which provided a large portion of the computing resources for this study.

The financial support from the Monash Graduate Scholarship (MGS) and the International Postgraduate Research Scholarships (IPRS).

# Contents

<b>1</b>	<b>Introduction</b>	<b>1</b>
1.1	Flow instabilities . . . . .	3
1.2	Natural shedding . . . . .	5
1.2.1	Leading-edge shedding . . . . .	6
1.2.2	Trailing-edge shedding . . . . .	6
1.2.3	Rectangular plate . . . . .	7
1.2.4	Summary of feedback mechanisms in the natural shedding case . . .	14
1.3	Applied forcing . . . . .	15
1.3.1	Leading edge . . . . .	16
1.3.2	Short bluff bodies . . . . .	16
1.3.3	Long bluff bodies . . . . .	19
1.3.3.1	Duct acoustic resonance . . . . .	23
1.4	Spanwise flow instabilities . . . . .	30
1.4.1	Short bluff bodies . . . . .	30
1.4.2	Long rectangular plate . . . . .	33
1.4.2.1	Forced shedding . . . . .	35
<b>2</b>	<b>Numerical Techniques</b>	<b>37</b>

2.1	Numerical scheme . . . . .	38
2.1.1	Spatial scheme . . . . .	38
2.1.1.1	Two-dimensional discretisation . . . . .	38
2.1.1.2	Spanwise discretisation . . . . .	40
2.1.2	Temporal scheme . . . . .	41
2.1.3	Boundary conditions . . . . .	42
2.1.4	Stopping criteria for temporal evolution . . . . .	42
2.2	Validation . . . . .	43
2.2.1	Backward-facing step flow . . . . .	43
2.2.2	Driven cavity . . . . .	45
2.2.2.1	Steady state . . . . .	47
2.2.2.2	Global spectral scheme . . . . .	51
2.2.2.3	Time dependence of High $Re$ cavity flow . . . . .	53
2.2.2.4	Runge-Kutta versus Adams-Bashforth . . . . .	54
2.3	Flow around long plates . . . . .	55
2.3.1	Computational domain and boundary conditions . . . . .	57
2.3.2	Domain size . . . . .	58
2.3.2.1	Elliptical leading-edge plate . . . . .	58
2.3.2.2	Rectangular plate . . . . .	60
2.3.3	Spatial and temporal resolution . . . . .	60
2.4	Post-processing . . . . .	62
2.4.1	Vortex cores . . . . .	62
2.4.2	Circulation . . . . .	64
2.4.3	Howe's acoustic model . . . . .	64

<b>3</b>	<b>Flow Past a Plate with an Elliptical Leading Edge</b>	<b>67</b>
3.1	Natural shedding . . . . .	67
3.2	The effect of applied cross-stream forcing . . . . .	70
3.2.1	Mean base pressure . . . . .	72
3.2.1.1	The effect of Reynolds number . . . . .	72
3.2.1.2	The effects of forcing amplitude . . . . .	74
3.2.1.3	The effects of aspect ratio . . . . .	74
3.2.1.4	Effect of nose geometry . . . . .	76
3.2.2	Comparison of mean base pressure with experiments . . . . .	78
3.2.3	Base pressure trace . . . . .	81
3.2.3.1	State selection . . . . .	85
3.2.4	Lift and drag forces . . . . .	88
3.3	Further analysis . . . . .	89
3.3.1	Shedding phase relative to forcing . . . . .	89
3.3.2	Vortex trajectory . . . . .	93
3.3.3	Vortex formation length . . . . .	98
3.3.4	Circulation . . . . .	104
3.3.4.1	Theory . . . . .	104
3.3.4.2	Comparison with simulations . . . . .	106
<b>4</b>	<b>Flow Past a Long Rectangular Plate</b>	<b>112</b>
4.1	Natural shedding . . . . .	112
4.1.1	Effects of Reynolds number . . . . .	113
4.1.2	Shedding modes . . . . .	117
4.1.3	Base pressure and forces . . . . .	123

4.2	Applied forcing . . . . .	126
4.2.1	Effect of Reynolds number . . . . .	126
4.2.2	Effects of the amplitude of forcing . . . . .	129
4.2.3	The response at various aspect ratios . . . . .	131
4.2.3.1	Smaller forcing amplitude . . . . .	135
4.2.4	The applied forcing without the mean flow . . . . .	135
4.2.5	Lift and drag forces . . . . .	142
4.2.6	Peaks in mean base suction . . . . .	143
4.3	Dynamics of the flows . . . . .	145
4.3.1	Phase of leading-edge shedding . . . . .	147
4.3.2	Convective velocity . . . . .	149
4.3.2.1	Natural Shedding . . . . .	149
4.3.2.2	Fixed aspect ratio, variable forcing frequency . . . . .	150
4.3.2.3	Forcing frequency constant, aspect ratio varies . . . . .	150
4.3.3	Phase of trailing-edge shedding . . . . .	150
4.3.4	On the stepping in the natural and forced shedding cases . . . . .	156
4.3.5	Relating the fluctuating lift forces to the flow field . . . . .	159
4.3.6	On the variation in magnitude of the peak mean base suction . . . . .	161
4.3.6.1	Vortex formation length . . . . .	162
4.4	Duct acoustic resonance . . . . .	166
4.4.1	Applying Howe's theory . . . . .	167
4.4.2	Results from Howe's model . . . . .	169
4.4.3	Resonant ranges . . . . .	173
4.4.4	Flow dynamics . . . . .	173

4.4.5	Discussion on the duct acoustic resonance . . . . .	177
4.4.6	On the modelling of the acoustic particle velocity . . . . .	181
<b>5</b>	<b>Three Dimensional Flow Simulations</b>	<b>186</b>
5.1	Flow around elliptical leading-edge plates . . . . .	186
5.1.1	Natural shedding case . . . . .	188
5.1.1.1	$c/t = 7.5$ . . . . .	188
5.1.1.2	$c/t = 2.5$ . . . . .	189
5.1.1.3	Wavelength of <i>Mode A</i> shedding . . . . .	191
5.1.2	Forced shedding . . . . .	196
5.2	Flow around rectangular plates . . . . .	197
5.2.1	The unforced case . . . . .	198
5.2.1.1	$c/t = 6$ . . . . .	198
5.2.1.2	$c/t = 10$ . . . . .	198
5.2.1.3	$c/t = 13$ . . . . .	199
5.2.1.4	Comparison with two-dimensional simulation . . . . .	204
5.2.2	Applied Forcing . . . . .	205
<b>6</b>	<b>Summary and Conclusions</b>	<b>206</b>
6.1	Computational aspects . . . . .	206
6.1.1	Numerical technique . . . . .	206
6.1.2	Benchmark test . . . . .	207
6.1.3	On using the Runge-Kutta scheme for the convective sub-step . . . . .	208
6.1.4	Simulation of flow around plates . . . . .	209
6.2	Flow around elliptical leading-edge plates . . . . .	210

6.2.1	Natural shedding . . . . .	210
6.2.2	Forced shedding . . . . .	211
6.3	Flow around rectangular plates . . . . .	214
6.3.1	Results from simulations . . . . .	215
6.3.1.1	Natural shedding . . . . .	215
6.3.1.2	Forced shedding . . . . .	216
6.3.1.3	Duct acoustic resonance . . . . .	217
6.3.2	On the controlling mechanism . . . . .	217
6.3.2.1	Natural shedding . . . . .	218
6.3.2.2	Forced shedding . . . . .	220
6.3.2.3	Duct acoustic resonance . . . . .	223
6.3.2.4	Similarity between cases . . . . .	224
6.3.2.5	On the feedback mechanism in the natural shedding cases	224
6.4	Three-dimensional simulations . . . . .	227
6.4.1	Elliptical leading-edge plate . . . . .	227
6.4.2	Rectangular plate . . . . .	228
<b>7</b>	<b>References</b>	<b>229</b>
7.1	Publications resulting from this work . . . . .	237

# Nomenclature

$A$	physical area.
$A_o$	amplitude of the sinusoidal perturbation.
$c$	plate chord length.
$c_d$	drag coefficient based on plate thickness and free-stream velocity.
$c_l$	lift coefficient based on plate chord and free-stream velocity.
$c_p$	pressure coefficient based on plate thickness and free-stream velocity.
$c_s$	speed of sound.
$d^*$	displacement thickness.
$E(t)$	the total kinetic energy of the driven cavity flow as a function of time.
$F$	number of Fourier planes in the spanwise direction.
$F_t$	reduced frequency based on $t'$ .
$f$	shedding/resonant frequency.
$H$	channel height.
$h$	step height.
$K$	number of elements in a two-dimensional plane.
$k$	loop counter for the Runge-Kutta algorithm.
$l_1$	distance between inflow boundary and the plate relative to the plate thickness $t$ .
$l_2$	distance between the plate and the side boundary relative to the plate thickness $t$ .
$l_3$	distance between the plate and the outflow boundary relative to the plate thickness $t$ .
$N$	number of nodes in one direction of an element.
$n$	shedding mode (step number) for the flow around a rectangular plate.
$m$	order of the Legendre polynomial.
$P$	instantaneous acoustic power.
$P_m$	Legendre polynomial of degree $m$ .
$p$	kinematic pressure.
$\bar{p}^{n+1}$	average pressure field at the end of a timestep.
$r$	reattachment length.

$St$	Strouhal number based on thickness.
$St_c$	Strouhal number based on chord.
$St_{t'}$	Strouhal number based on $t'$ .
$s$	order of the Runge-Kutta scheme.
$Re$	Reynolds number based on plate thickness or diameter and free-stream velocity.
$Re_{t'}$	Reynolds number based on $t'$ .
$\vec{s}$	tangent vector to an iso-surface of vorticity.
$S$	integral path along the solid surface.
$T$	time of one shedding period.
$t$	plate thickness.
$t$	simulated non-dimensional time using the velocity and length scale.
$t'$	plate thickness + $2 \times$ displacement thickness.
$\Delta t$	size of the timestep.
$U_\infty$	mean free-stream velocity.
$\mathbf{u}$	velocity vector of the flow field.
$\mathbf{u}^*, \mathbf{u}^{**}$	intermediate velocity vector field.
$\mathbf{u}^n, \mathbf{u}^{n+1}$	velocity vector field at the start and end of a timestep.
$u, v, w$	velocity components in the $x$ , $y$ and $z$ direction.
$v_{pert}$	forcing amplitude relative to the free-stream velocity.
$V$	volume.
$V_{conv}$	convective speed of the vortices.
$\mathbf{v}$	acoustic particle velocity vector.
$w_j$	local weighting coefficients for the Gauss-Lobatto-Legendre quadrature.
$x, y, z$	Cartesian coordinates.
$x_f$	vortex formation length.
$x_{le}$	distance downstream from the leading edge.
$x_{te}$	distance downstream from the trailing edge.
$\Gamma$	circulation generated between the leading edge to the trailing edge of the plate.
$\gamma_l$	circulation per unit length.
$\Gamma_o$	magnitude of the circulation produced in one shedding cycle non-dimensionalised with the free-stream velocity and the plate thickness.
$\nu$	kinematic viscosity.
$\xi, \eta$	Cartesian coordinates in a local element (in computational space).
$\rho_0$	mean fluid density.
$\sigma_{c_l}$	standard deviation of the lift coefficient.

$\phi$	phase shift.
$\Phi$	velocity potential of the acoustic particle velocity.
$\Phi_s$	space dependent part of the acoustic particle potential.
$\Phi_t$	time dependent part of the acoustic particle potential.
$\vec{\omega}$	vorticity vector of the flow field.

# Chapter 1

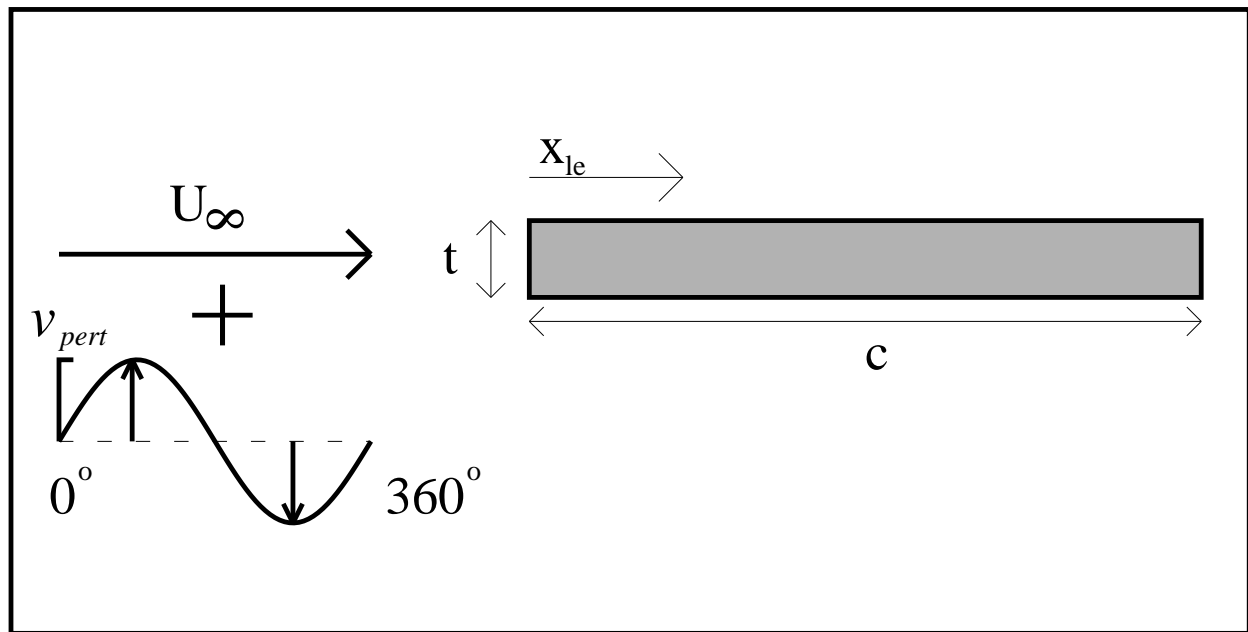
## Introduction

The study of flow around bluff bodies is one of fundamental importance in fluid mechanics. It underpins areas as diverse as wind engineering and structural loading, automotive aerodynamics, cross-flow heat exchangers, mixing, maritime transport, sub-sea structures and flow induced acoustics.

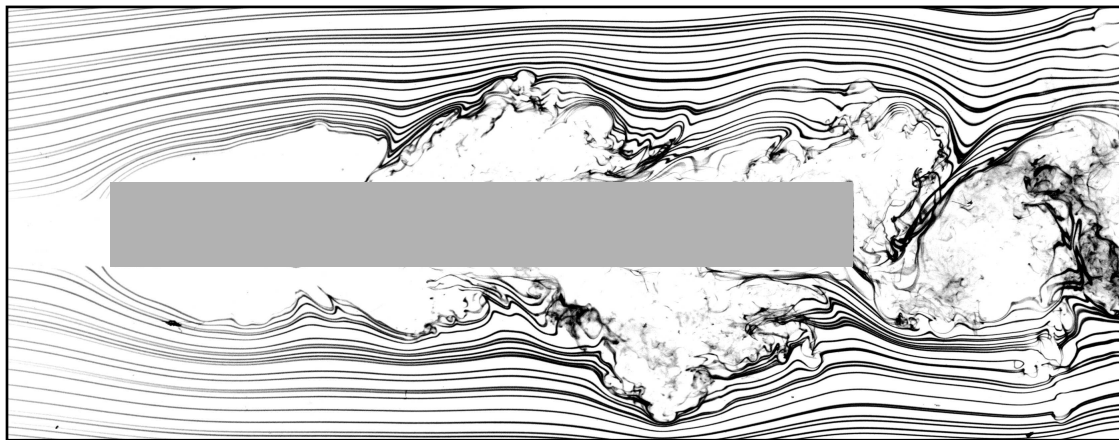
Many studies have concentrated on pseudo two-dimensional geometries with short after-bodies such as cylinders, squares or prisms (Roshko, 1961, Bearman & Obasaju, 1982, Bearman, 1984, Williamson, 1988). The two- and three-dimensional instabilities that develop in the different flow regimes have resulted in many interesting observations. Long bluff bodies are a natural extension of this work.

More recently, there have been studies on high aspect ratio geometries and, in particular, long rectangular plates. These have the complication of vortical flow structures developing at both the leading and trailing edges. Studies of this flow will need to include the interaction between them. Although this is a basic geometry and is used to further the fundamentals and understanding, several studies on this particular bluff body have been inspired by practical applications. These include wind structure interactions (Nakamura *et al.*, 1991), heat exchangers (Cooper *et al.*, 1986) and acoustic flow control (Stokes & Welsh, 1986).

This work is building on many previous experimental observations and some computational studies done in association with the Department of Mechanical Engineering, Monash University and CSIRO Division of Building, Construction and Engineering. Welsh & Gibson (1979) and Stokes & Welsh (1986) investigated the case where the plate is placed in a duct and develops a strong acoustic resonance. Parker & Welsh (1983), and Mills (1998) investigated the plate in an open jet wind tunnel with applied acoustic forcing. Cooper *et al.* (1986) used the acoustic forcing to try to improve heat transfer. While



(a)



(b)

Figure 1.1: (a) A schematic of the long rectangular plate with a sinusoidal perturbation added to the mean flow and (b) a smoke visualisation from Mills *et al.* (1995) where an acoustic perturbation is introduced by speakers in anti-phase placed above and below the plate.

these studies concentrated on flow induced acoustics and acoustic control, the long rectangular plate has also been investigated for its relevance in wind engineering (Nakamura *et al.*, 1991, Deniz & Staubli, 1997).

A schematic of the general geometry and set up for the flow is shown in Figure 1.1(a). The long side of the rectangular plate is aligned with the flow. Perturbations to the mean flow may be added by vibrating the bluff body or adding a cross stream component as in acoustic control. Figure 1.1(b) is a smoke visualisation from Mills *et al.* (1995) showing the flow around a rectangular plate subjected to cross-flow perturbations. This chapter will review studies on bluff-body flows with a focus on long rectangular plates. These include (a) the natural shedding case which has no external excitation,

(b) the forced shedding case where perturbations are introduced to the flow and (c) the duct acoustic resonance case. The development of three-dimensional instabilities on bluff bodies at low and moderate Reynolds numbers will also be discussed.

## 1.1 Flow instabilities

Several assumptions are commonly made when studying fundamental bluff body aerodynamics which include the fluid being Newtonian, incompressible and isotropic. This allows the fluid to be mathematically modelled using the time-dependent incompressible Navier-Stokes equations and is the basis of the stability analysis and the numerical modelling here.

The flow around bluff bodies will eventually reach a steady state below a critical Reynolds number. Any disturbances either from the initial conditions or imposed on the flow will decay or be convected out of the system and the system will reach an equilibrium state. As the Reynolds number is increased past a critical point, disturbances are no longer damped and the flow becomes time dependent. The transition between steady and time-dependent flow is part of the study of hydrodynamic stability.

A standard approach is to use the Navier-Stokes equations to predict the behaviour of a flow represented by the sum of a mean flow plus a perturbation. The equations are linearised with respect to the perturbation and can be used to predict the growth or decay of Fourier components. In a local analysis the flow is assumed to be parallel. The resulting equations are called the Orr-Sommerfeld equations. The analysis identifies temporal frequencies and spatial wavelengths that will grow for a given velocity profile and Reynolds number. The two possible types of instabilities predicted by this analysis are the convective and absolute instabilities.

The convective instability only convects the disturbance downstream from the source. It is not locally self sustaining and will decay if the source of the disturbance is removed. The absolute instability is locally self sustaining and the disturbances propagate upstream and downstream of the source. The convective type of instability is generally receptive to a wider range of frequencies than the absolute instability which is generally receptive only over a very narrow band of frequencies. This leads to an absolute instability being called an oscillator and a convective instability a noise amplifier.

There have been several analyses of the wake behind a rectangular plate. The leading edge is assumed to be streamlined and with no upstream disturbances, the flow is parallel at the trailing edge making it an ideal problem for this analysis. Using linear

stability analysis, Koch (1985) analysed the profiles in the wake near the critical Reynolds number. As the Reynolds number is increased towards the critical value, regions of convective instability develop. As part of the transition process, the analysis shows regions with absolute instability in the recirculating region past the critical Reynolds number. Hannemann & Oertel (1989) studied the instability by numerically simulating the wake behind the plate. Initially an artificial boundary condition is imposed along the centreline to maintain symmetry. This is removed once the flow has reached a quasi-steady state. After that time there is a linear growth of one pure frequency before reaching a transition to saturation and finally a non-linear saturated state.

Several methods have been proposed to predict the frequency selection in the linear regime including the initial resonance criterion by Monkewitz & Nguyen (1987) and the maximum growth criterion by Pierrehumbert (1984). The frequency of shedding in the saturated state near the critical Reynolds number can be predicted using Koch's resonance criteria (Koch, 1985) which is based on the linear stability analysis. The hypothesis is that the saturated state is dominated by the local resonance occurring spatially at the transition from absolute to convective instability. Most simulations and experiments are at a Reynolds number significantly larger than the critical Reynolds number. Although this analysis is strictly applicable only near the critical Reynolds number, it can be applied at supercritical Reynolds numbers with the assumption that the non-linear saturated state is still governed by this local resonance. The theoretical stability analysis has been further developed to include more physics. While the local linear stability analysis is based on the initial growth of disturbances in parallel flows, the nonlinear saturated state can be analysed with the Ginsburg-Landau equation. The spatial developing nature of the flow which is not considered in the local analysis can be analysed when considering weakly non-parallel flows and results in the predictions of global instabilities (Huerre & Monkewitz, 1990).

Wake instabilities are present in most bluff body flows above a critical Reynolds number. With long bluff bodies, it is possible for the flow to separate at the leading edge and reattach while shedding large-scale vortices. A detailed investigation into the nature of this separated and reattaching flow is found in Cherry *et al.* (1984). The instabilities involved are the Kelvin-Helmholtz instability present in the shear layer and the instability causing the large-scale shedding. The nature of the instability causes a weak flapping of the shear layer and shedding to be irregular. Experiments by Soria & Wu (1992) used long rectangular plates to isolate any trailing-edge effects. The separating and reattaching flow is shown to be predominantly convectively unstable and receptive to a broad range of frequencies. The weak flapping of the shear layer without external perturbation could be the result of regions of local absolute instabilities.

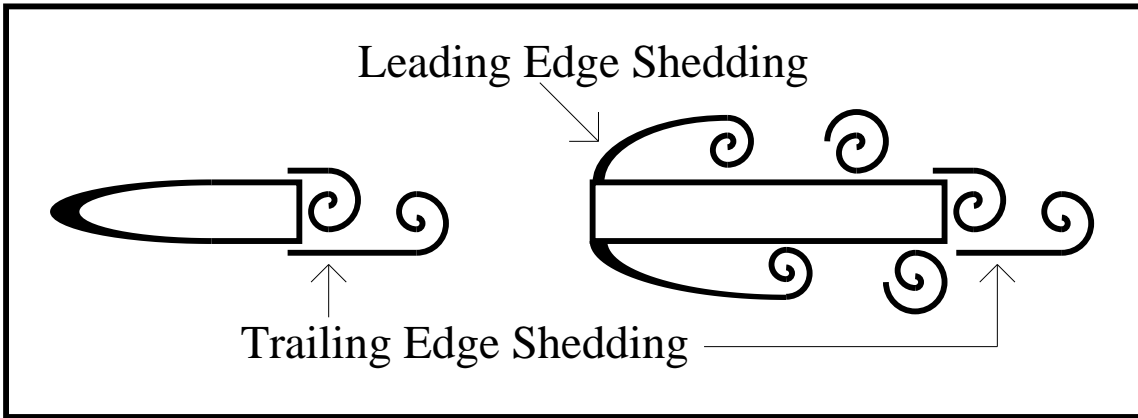


Figure 1.2: A sketch of the instabilities developing from a plate with a streamlined and a blunt leading edge, and blunt trailing edges.

Figure 1.2 shows the long plates studied and their associated instabilities. With an elliptical leading edge, the instability at the trailing edge results in the classical Karman vortex shedding. A rectangular plate is different from a circular cylinder in that the blunt leading edge forces the fluid to separate at a fixed point forming a shear layer. The instability in the shear layer results in it rolling up to form discrete vortices. For a blunt trailing edge, the interaction between the leading- and trailing-edge flow structures will be explored in this thesis.

A closely related instability occurs when a local convective instability interacts with a solid boundary downstream. Disturbances from the object downstream propagate upstream to complete a feedback loop. These types of instabilities occur when a jet or a mixing layer impinges on a solid boundary downstream such as bluff bodies, walls or edges. A classical example of this is the cavity flow where the separating shear layer from the upstream edge of the cavity interacts with the downstream edge. A comprehensive review is found in Rockwell & Naudascher (1979). The concept of global instability was associated with these sort of flows by Rockwell (1990). This instability is of importance to the cases with a rectangular plate because the shear layer from the leading edge interacts with either the trailing edge or the sides of the plate. Further discussion on this is included when the flow around rectangular plates is reviewed.

## 1.2 Natural shedding

This section focuses on flow over a fixed bluff body. The two-dimensional instabilities are reviewed in three sections: the flow structures developing at the leading edge; trailing

edge; and the interaction between these elements.

### 1.2.1 Leading-edge shedding

In this case the flow separates from the edge and forms a shear layer which reattaches further downstream. Above a critical Reynolds number, the shear layer rolls up into discrete vortices. In the absence of any controlling influence this shedding is irregular. Cherry *et al.* (1984) attempted to study the unsteady nature of this flow. The experiments were performed at approximately  $Re = 3,200$ . Near the separation point, the shear layer exhibits a low-frequency flapping possibly due to changes to the bubble in the shedding process. The growth of the shear layer is similar to a plane mixing layer up to about 60% of the bubble length before being influenced by the reattachment process. The shedding goes through phases of pseudo-periodic shedding of vortices, large scale irregular shedding and relatively quiescent phases with 'necking' of the shear layer after reattachment. In the pseudo-periodic phase, the spacing between the vortices is between 60% to 80% of the separation bubble length. Velocity correlations along the span showed that the flow became three-dimensional soon after separation and the spanwise scales grow linearly until reattachment. The shedding of large scale structures does not immediately show three dimensionality although the shear layer is three-dimensional.

Sasaki & Kiya (1991) experimented at moderate Reynolds numbers ( $80 < Re < 800$ ) and studied the nature of the reattachment and the resulting spanwise instability from the shed vortices. The reattachment length reaches a maximum of about  $6.5t$  at  $Re = 320$ . This is the onset of the roll up of the shear layer and vortices being shed. The reattachment length approaches a constant value of  $4.5t$  for  $Re > 380$ . The shed vortices also develop spanwise instability which will be discussed in Section 1.4.2.

Simulations by Tafti & Vanka (1991) studied the reattachment and the shed vortices at  $Re = 1,000$ . Although the calculations were two-dimensional (the shear layer develops a strong three-dimensionality), it reproduced some experimental trends such as shedding frequency and convective velocity.

### 1.2.2 Trailing-edge shedding

With a streamlined leading edge, flow structures from the trailing edge can be studied in isolation. The trailing-edge shedding is a simple bluff body wake with the interaction of two boundary layers. The experiment by Eisenlohr & Eckelmann (1988) showed the relationship between the trailing-edge shedding frequency and the displacement thickness

of the boundary layer at the trailing edge. The experiment used a laminar boundary layer and aspect ratios of between 50 to 800. The data for all the plates correlated well with equation 1.1 if the characteristic length was taken to be the plate thickness plus two times the displacement thickness of the boundary layer. The non-dimensional relationship was found to be

$$F_{t'} = -39.2 + 0.286 Re_{t'} \quad (1.1)$$

where

$$F_{t'} = \frac{f t'^2}{\nu}$$

$$Re_{t'} = \frac{v t'}{\nu}$$

$t'$  = plate thickness( $t$ ) + 2 x displacement thickness( $d^*$ ).

Measurements of base pressure as a function of momentum thickness were presented in Petrusma & Gai (1994). An aerofoil leading edge with  $c/t = 10$  was used with Reynolds numbers of the order of  $Re = 50,000$ . The results were limited to when the momentum thickness was less than  $0.05t$  and the base pressure did not vary significantly with smaller momentum thickness. The mean base pressure coefficient saturated to  $c_p = -0.55$  for a laminar boundary layer. When the flow is tripped such that the boundary layer was turbulent, the mean base pressure coefficient was  $c_p = -0.62$ .

### 1.2.3 Rectangular plate

While studying the effect of sound, Parker & Welsh (1983) also noted the different natural shedding regimes that occurred over a wide range of aspect ratios. Varying the Reynolds number between  $14,800 < Re < 31,000$  showed no significant change in the flow. There are four different vortex shedding regimes for the rectangular plate depending on the aspect ratio which are summarised in Table 1.1 below. A plot of the shedding frequency as a function of aspect ratio is presented in Figure 1.3. The first transition is accompanied by a discontinuous change in frequency and is sensitive to external conditions resulting in small variations between studies (i.e. Okajima *et al.* 1983 at  $c/t = 2.8$ , Parker & Welsh 1983 at  $c/t = 3.2$ , Okajima *et al.* 1992 (numerical) at  $c/t = 2.1$ ) A detailed study of the transition from leading-edge shedding directly into the wake to periodic reattachment was presented by Okajima (1982). The transition characterised by a distinct change in shedding frequency is dependent on Reynolds number and occurs between  $2 < c/t < 3$  but

asymptotes to  $c/t = 2.8$  at high Reynolds numbers. The second regime ( $3.2 < c/t < 7.6$ ) exhibited a distinct shedding frequency in the wake. This is not present in the next regime ( $7.6 > c/t > 16$ ) and plates longer than  $c/t > 16$  exhibited trailing-edge shedding independent of the leading edge. Since then Nakamura *et al.* (1991) and many others (Ozono *et al.*, 1992, Naudascher & Wang, 1993) have shown that the second and third regimes, namely aspect ratios between approximately  $3 \leq c/t \leq 15$ , are dominated by the global instability which synchronises the leading- and trailing-edge shedding at low and moderate Reynolds numbers.

This behaviour is not observed for a rounded leading edge which undergoes only one transition at  $c/t = 1.2$  (Parker & Welsh, 1983). This results in a step change in the shedding frequency shown in Figure 1.8. Below that aspect ratio, the shear layer from the leading edge interacts directly to form the vortices in the wake. Longer plates showed only trailing-edge shedding.

$c/t$	Characteristics
$c/t < 3.2$	Separation from leading edge never reattaches to the side faces Shear layer interacts directly to form vortex shedding.
$3.2 \leq c/t \leq 7.6$	Separation from leading edge reattaches periodically. Separation bubble grows and envelopes trailing edge.
$7.6 < c/t \leq 16$	Separation from leading edge always reattaches. Vortices randomly generated from leading edge move downstream and interact with trailing edge producing irregular shedding from the trailing edge.
$c/t > 16$	Separation from leading edge always reattaches. Vortices randomly generated from leading edge move downstream but diffuse before reaching the trailing edge.

Table 1.1 : Summary of flow regimes for flat plate (Parker & Welsh, 1983)

The early studies were inspired by the wind induced excitation of bridge decks at relatively low wind speeds. Nakamura & Nakashima (1986) studied rectangular, H and T cross-sections in both a wind tunnel and a water tunnel with aspect ratios,  $c/t$  between 2.0 and 5.0. In the wind tunnel, the model was free to vibrate ( $Re = 5, 500$ ) and flow visualisations were performed in a water tunnel ( $Re = 1, 200$ ). Observation in both situations for all the bluff bodies showed a feed-back instability. The H geometry resembles two cavities with a common bottom plate. The instability in the cavity flow was called the impinging shear layer instability by Rockwell & Naudascher (1978). This led to

Nakamura & Nakashima (1986) using the classification and in their case the shear layer does impinge directly on the trailing edge. The instability manifested itself by distinctive frequency selection. The shedding frequency shows that the instability is still present even with a splitter plate attached to the trailing edge or the  $\vdash$  geometry at large aspect ratios. This shows that the trailing-edge shedding is not a necessity for this one sided instability.

A detailed study of the rectangular plate with  $c/t$  from 3 to 15 at  $Re = 1,000$  was presented in Nakamura *et al.* (1991). An analysis of the shedding frequency showed that peaks in the spectrum corresponded to a stepwise increase in Strouhal number based on chord as shown in Figure 1.3. Each step corresponded to a shedding mode which has a Strouhal number base on chord approximately an integer multiple of 0.6. Phase measurements along the plate showed that an integer number of vortices,  $n$ , developed along the plate. This number,  $n$ , corresponds to the shedding mode as represented by the sketch in Figure 1.4. The steps in Strouhal numbers (i.e.,  $St_c = 0.6n, n = 1, 2, \dots$ ) corresponding to the number of vortices along the side, suggests that the average convective velocity of the flow structures along the plate is approximately 60% of the free-stream velocity (elaborated in Section 4.1.2). At aspect ratios close to where the shedding mode changes, namely  $c/t = 8$  and 11, two peaks appear in the spectrum. The shedding in those cases switch randomly between the two modes.

The theory underlying this global instability was based on the cavity flow as described above. The flapping of the leading-edge shear layer interacts directly with the trailing edge of the plate. This leads to the emission of a pressure pulse which controls the evolution of the leading-edge shear layer. This establishes a feed back loop and locks both the leading- and trailing-edge shedding after a transient period (see Figure 1.6(b)). This strictly only applies to the first mode,  $n = 1$ , of shedding which occurs for approximately  $c/t = 3-6$  (Nakamura *et al.*, 1991). The shear layer rolls up into discrete vortices on longer plates. Instead of the shear layer, the second ( $n = 2$ ), third ( $n = 3$ ) or fourth ( $n = 4$ ) vortex from the leading edge interacts with the trailing edge completing the feed-back loop (see Figure 1.6(b)). A better description of this global instability that encompasses all the modes is the impinging leading-edge vortex (ILEV) instability described by Naudascher & Wang (1993). This was summarised in Naudascher & Rockwell (1994) and discussed by Mills *et al.* (1995) who proposed that this better describes the instability. A refinement to the flow classification by Parker & Welsh (1983) was proposed by Naudascher & Wang (1993) which incorporated the ILEV instability. The categories are summarised in Figure 1.5 with shorter plates (i.e.  $c/t < 3$ ) called leading-edge vortex shedding (LEVS) and longer plates (i.e  $c/t > 16$ ) called trailing-edge vortex shedding (TEVS). The shorter plates are in the same category as short after-body geometries such as cylinders, squares and triangles. For the longer plates, the vortices shed from the leading edge are too diffuse

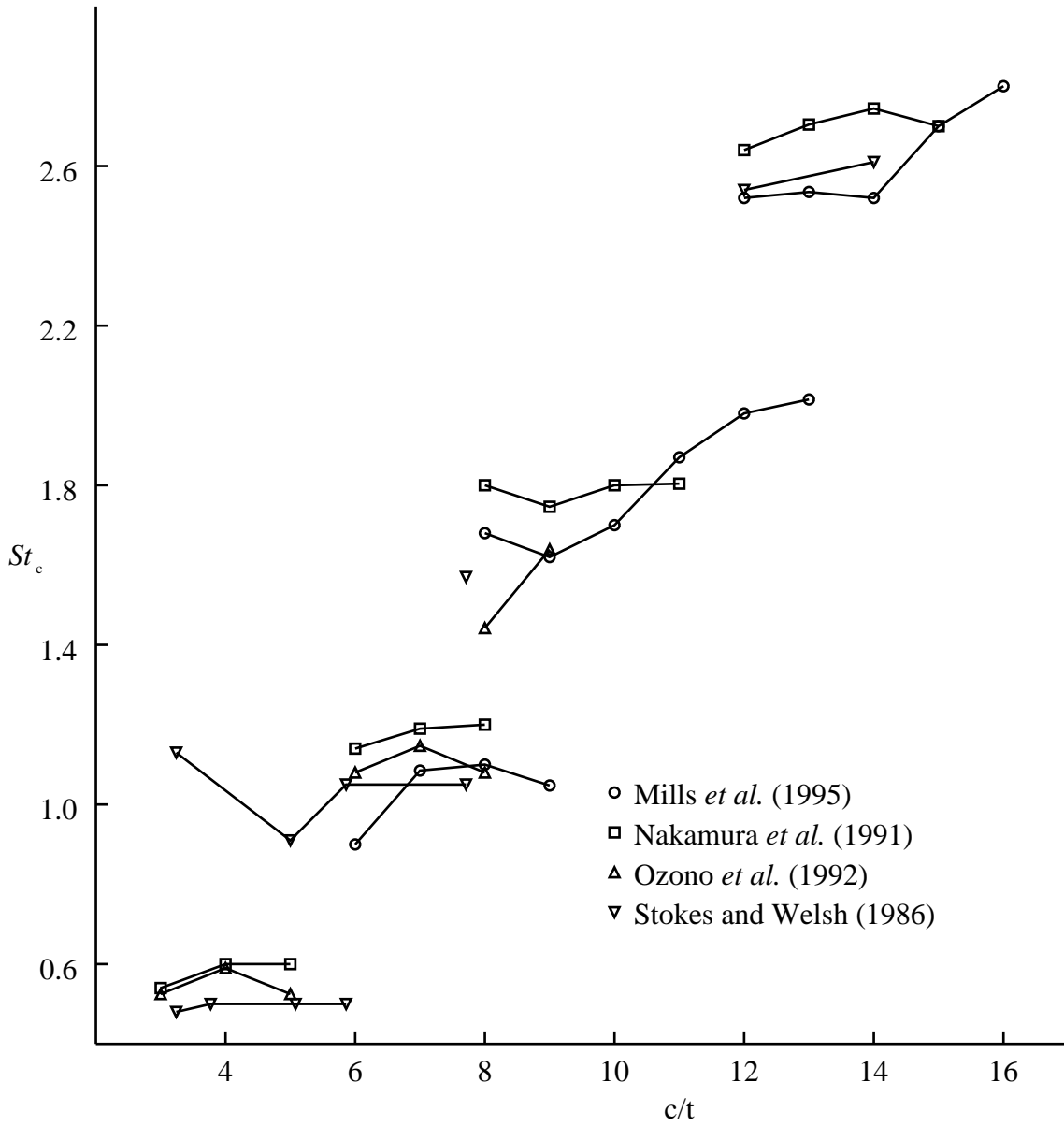


Figure 1.3: Strouhal number based on chord as a function of aspect ratio,  $c/t$ , from several studies. (See text for details.)

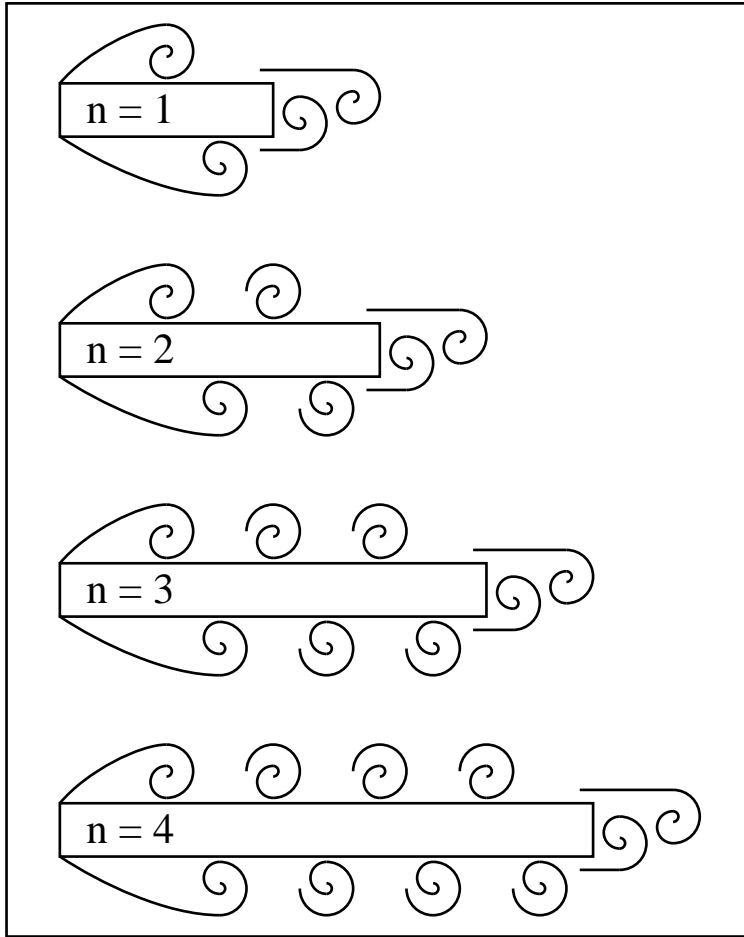


Figure 1.4: A sketch of the flow around a rectangular plate showing the different modes of shedding.

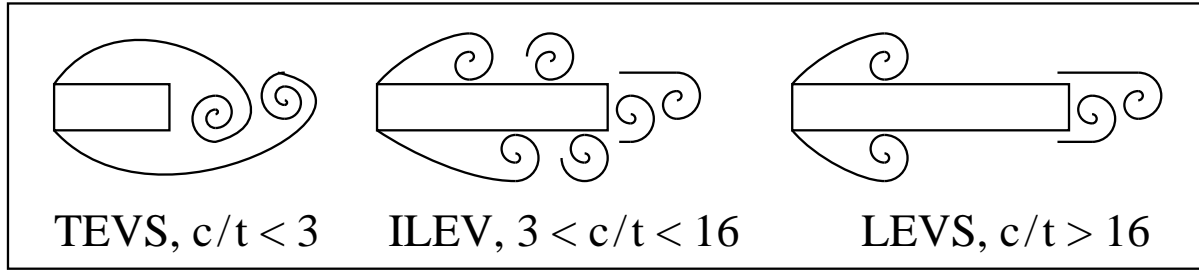


Figure 1.5: Flow classification by Naudascher and Wang (1993) for the long rectangular plate. The aspect ratios stated are only an approximate.

to have any influence at the trailing edge.

These instabilities have been successfully simulated numerically. Okajima *et al.* (1990) showed that at  $c/t$  of 2.8 and 6 there was a distinct change in shedding frequency and flow pattern between  $Re = 500$  and  $Re = 1,200$ . The shear layer from the leading edge of shorter plates ( $c/t < 2.8$ ) directly form vortices in the wake. Above  $c/t = 2.8$  the leading-edge shear layer reattaches to form what is now known as the first mode ( $n = 1$ ). Okajima (1990) then showed that this compared well with experiments. Okajima *et al.* (1992) performed more simulations at  $Re = 1,000$  and showed that the first step occurs at  $c/t = 2.1$  in the simulations but  $c/t = 2.8$  in the experiment. Ozono *et al.* (1992) and Ohya *et al.* (1992) attempted to simulate the observations of Nakamura *et al.* (1991). The simulations at  $Re = 1,000$  showed the stepwise change in Strouhal number based on chord between  $c/t = 3$  and  $c/t = 9$  as shown Figure 1.3. For longer plates, the system did not lock into a particular shedding mode even after several hundred dimensionless time units of simulation. The shedding switched modes at  $c/t = 6$  and  $c/t = 8$  with the latter randomly switching between modes. The lift coefficient showed that at the start of each step (i.e.,  $c/t = 3, 6$  and  $9$ ), the flow was more regular and periodic. As the aspect ratio is increased, the shedding loses regularity until it locks to the next mode. Nakayama *et al.* (1993) performed simulations at  $Re = 200, 400$  and  $1,000$  for  $c/t = 3$  to  $10$ . At  $Re = 200$  there was no shedding from the leading edge which resulted in only a linear increase in Strouhal number based on chord with aspect ratio. This has been observed experimentally. The simulations at  $Re = 400$  showed the same stepping at  $Re = 1,000$  but with less irregularity at certain aspect ratios.

Nakamura (1996) showed that the global instability that control the shedding from the plate also influences short after-body geometries with splitter plates. Nakamura (1994) experimented on a circular cylinder, half circular cylinder, half circular cylinder connected to a 2:1 square block, normal flat plate and H section. The splitter plates extended up to 15 diameters downstream. In general, from measurements of the shedding

frequency, the flow gradually switched from Karman shedding to the first mode ( $n = 1$ ) and then through a frequency jump corresponding to the transition to the second mode ( $n = 2$ ). For the circular cylinder, these transitions occurred at  $c/t = 2.5$  and  $c/t = 6.5$  respectively. These differ from the rectangular plate probably because of the differences in the leading-edge shear layer and the absence of trailing-edge shedding. At longer aspect ratios, there was no single dominant frequency. Within the Reynolds number range of  $1600 < Re < 5300$  used in the experiment, this instability was almost independent of Reynolds number but observed more easily at lower Reynolds numbers. The half circular cylinder with a rectangular block showed a different trend from the other geometries. The ILEV instability is concluded to result in the shedding frequency displaying distinct steps (i.e  $St_c = 0.6n, n = 1, 2, \dots$ ). In those cases where the trailing-edge shedding is suppressed by a splitter plate, the interaction of the leading-edge vortices past the trailing edge still feeds back to result in out of phase shedding from both sides of the leading edge and the system locking to a particular shedding mode.

The feedback discussed previously relies on a weak pressure pulse to complete the loop. Above a Reynolds number of several thousand, the flow does not lock into these shedding modes (e.g., Stokes and Welsh, 1986 ( $Re = 15,000 - 30,000$ ); Mills *et al.*, 1995 ( $Re = 9,000$ ); Nakamura *et al.*, 1991 ( $Re > 2000$ )). Parker & Welsh (1983) did observe a distinctive frequency in the wake for  $3.2 < c/t < 7.6$  at  $Re = 23,700$  and flow structures which are similar to the first shedding mode ( $n = 1$ ). Nakamura *et al.* (1991) proposed that the ILEV mechanism is still present but too weak to lock the flow at higher Reynolds numbers or longer aspect ratios but would manifest itself with additional control of the leading-edge shedding such as vibrating the plate or external forcing. If some external excitation is present such as the acoustic resonance examined by Stokes and Welsh (1986), or the acoustic forcing demonstrated by Mills *et al.* (1995), a similar stepwise response in  $St_c$  with aspect ratio is observed. This will be discussed in more detail in the next section.

At high Reynolds number, where the ILEV instability does not lock the flow, the mean base pressure and drag are also not influenced by the ILEV instability. At a fixed Reynolds number ( $Re = 8,667$ ), the general trend is a increasing mean base suction and drag with increasing chord for  $6 \leq c/t \leq 15$  (Mills, 1998). With increasing aspect ratio, there is less interference of the leading-edge structures and more regular vortex shedding from the trailing edge. If the Reynolds number is low enough so that the shedding is locked to the ILEV instability, the mean base suction and drag is stronger at shorter aspect ratios within each mode (Okajima *et al.* 1992). This is where the shedding frequency is higher and the shedding, especially at the trailing edge, is more vigorous.

## 1.2.4 Summary of feedback mechanisms in the natural shedding case

A schematic summarising the proposed controlling mechanisms involved in each of the cases discussed above is given in figure 1.6. The governing mechanisms for long plates depend on aspect ratio and can be broadly classified as follows.

1. **Bodies with an aerodynamic leading-edge and blunt trailing edge (figure 1.6a).** In this case only trailing-edge shedding occurs. During the formation of trailing-edge vortices, there is an associated lowering of the pressure field in the vicinity of the trailing edge. This causes a time variation in the pressure field at the leading edge which can affect the formation of the boundary layer there. However, in this case, there is no leading-edge shedding to close the feedback loop. This situation is depicted in figure 1.6(a).
2. **Bodies of rectangular cross-section of moderate aspect ratio (figure 1.6b).** With a bluff leading edge, the shear layer separates from the leading edge. For plates of aspect ratio less than  $c/t \approx 6$ , the shear layer does not have time to form discrete vortex structures before reaching the end of the plate. Instead the flapping shear layer periodically reattaches in the vicinity of the trailing edge resulting in a modification of the pressure field which, in turn, is propagated back upstream to the leading edge of the plate. This can affect the formation of the leading-edge shear layer, controlling further flapping. Hence a feedback loop can be established. This has been referred to as an impinging shear layer instability by Nakamura *et al.* (1991), and also occurs for a shear layer separating and reattaching to the corners of a cavity.
3. **Bodies of rectangular cross-section of larger aspect ratio (figure 1.6c).** For longer plates, the leading-edge shear layer sheds discrete vortices. In this case, it has been proposed that the impinging shear layer instability becomes an impinging leading edge vortex instability (Naudascher & Wang, 1993). Here, the pressure pulse produced when the leading-edge vortices pass the trailing edge perturbs the further development of the leading-edge shear layer, completing a feedback loop that locks the leading-edge shedding. This mechanism occurs for other long bluff bodies such as  $\vdash$  sections and shorter bluff bodies fitted with splitter plates (Nakamura, 1996).

An important focus of this research, (especially chapter 4) concerns the situation described in item (3) above. Evidence is provided that the feedback loop as described needs modification, and that the controlling mechanism for flow past a long plate is

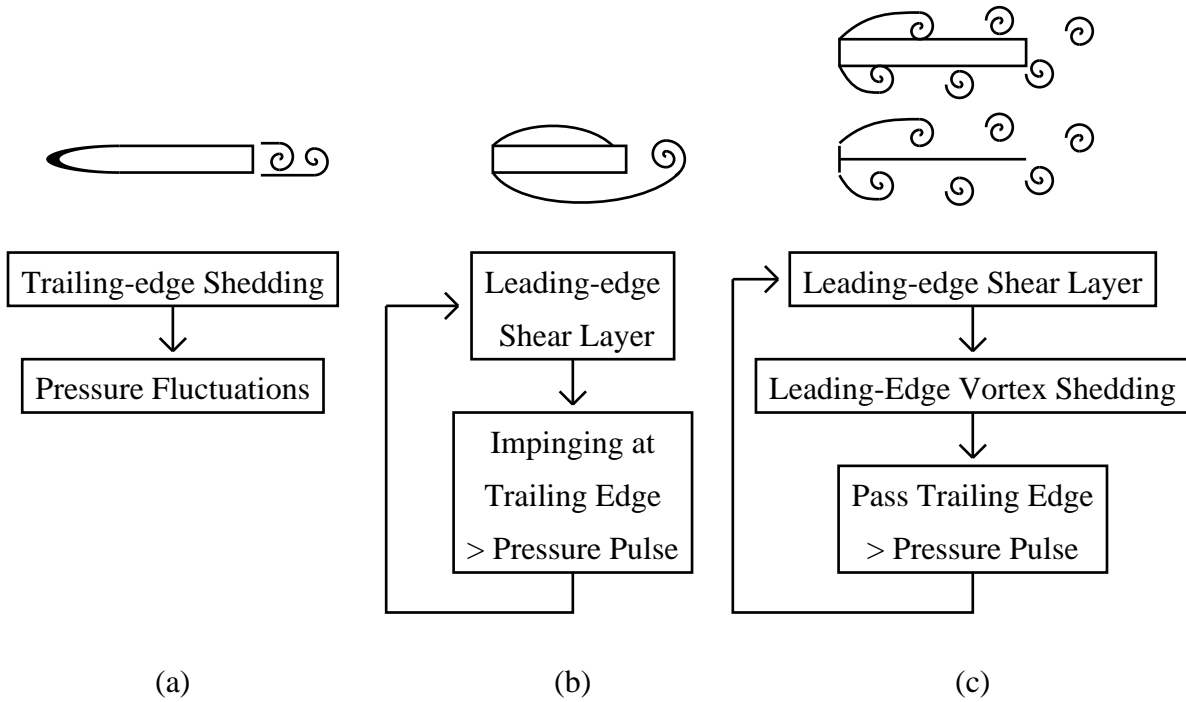


Figure 1.6: A schematic showing the mechanism involved for (a) trailing-edge vortex shedding (TEVS), (b) impinging shear layer instability and (c) impinging leading-edge vortex instability (ILEV).

different from that for shorter bodies with splitter plates, or flow past wide cavities where the ILEV instability description is adequate.

### 1.3 Applied forcing

In many situations, the bluff body is not rigid but may exhibit vibrations due to the fluctuating forces caused by interactions with the fluid. This introduces added complexity including structural stiffness and damping. A simplification when concentrating on the fluid mechanics is to apply forcing at small amplitudes relative to length scales, pressures or velocities of the system. This forcing can be achieved by vibrating the bluff body or adding a small perturbation to the free-stream velocity such as due to acoustic forcing. A small perturbation either by external forcing or flow-induced excitation can result in significant changes in the flow characteristics.

These excitations have been broadly classified into three separate categories by Naudascher & Rockwell (1994): namely extraneously induced excitation (EIE), instability induced excitation (IIE) and movement induced excitation (MIE). EIE occurs when the fluctuations to the flow field and pressure are from an independent external source such

as forced oscillations, acoustic forcing (e.g., Parker & Welsh, 1983, Mills *et al.*, 1995) and the velocity perturbation used in this study. Instability induced excitations (IIE) are caused by instabilities inherent to the flow such as LEVS, ILEV and TEVS described in the previous section. Structures which vibrate due to fluid forces can amplify the forcing and experience MIE including phenomena such as flutter and lock-on.

### 1.3.1 Leading edge

Sigurdson (1995) studied the behaviour of the leading-edge shear layer to applied forcing. The experimental apparatus consisted of a cylinder mounted coaxially to the flow (i.e. Axis of the cylinder parallel to the free stream). An acoustic speaker mounted within the cylinder, which had a small gap at the edge, provided a small local perturbation. The experiments confirmed many characteristics associated with forcing applied to the shear layer, such as shorter reattachment lengths and stronger surface pressure fluctuations. The presence of the Kelvin-Helmholtz instability of the shear layer and large-scale shedding instability influenced the response to the perturbation. The maximum effect is observed when the forcing frequency is close to the frequency of the large scale shedding instability. The shear layer amplifies a broad band of frequencies from approximately the shedding frequency to the frequency of the Kelvin-Helmholtz instability.

Soria & Wu (1992) studied the shear layer at the leading edge of a rectangular plate at  $Re = 900$ . A small perturbation is introduced by sinusoidally vibrating the side walls of the water tunnel. The experiments showed that the shear layer is convectively unstable and receptive to a broad range of frequencies. Soria *et al.* (1993) extended this to include more flow visualisation. The shear layer remained nominally two-dimensional with applied forcing unlike the unforced case. Stronger vortices are shed at the forcing frequency (which was between  $St = 0.22$  and  $0.36$ ) with possible pairing downstream from the leading edge.

### 1.3.2 Short bluff bodies

The absolute instability in the flow near the trailing edge of the plate is similar to that for shorter bluff bodies. The response of the flow around short bluff bodies such as cylinders and square sections to small perturbations, typically forced oscillations applied to the geometry, has been well studied. Vorticity is normally shed from a point close to the leading edge (LEVS). In line with the theoretical predictions of absolute instability, the shedding only locks to the applied forcing in a small frequency range around the natural shedding frequency which is also known as the resonant point. The lock-in effect

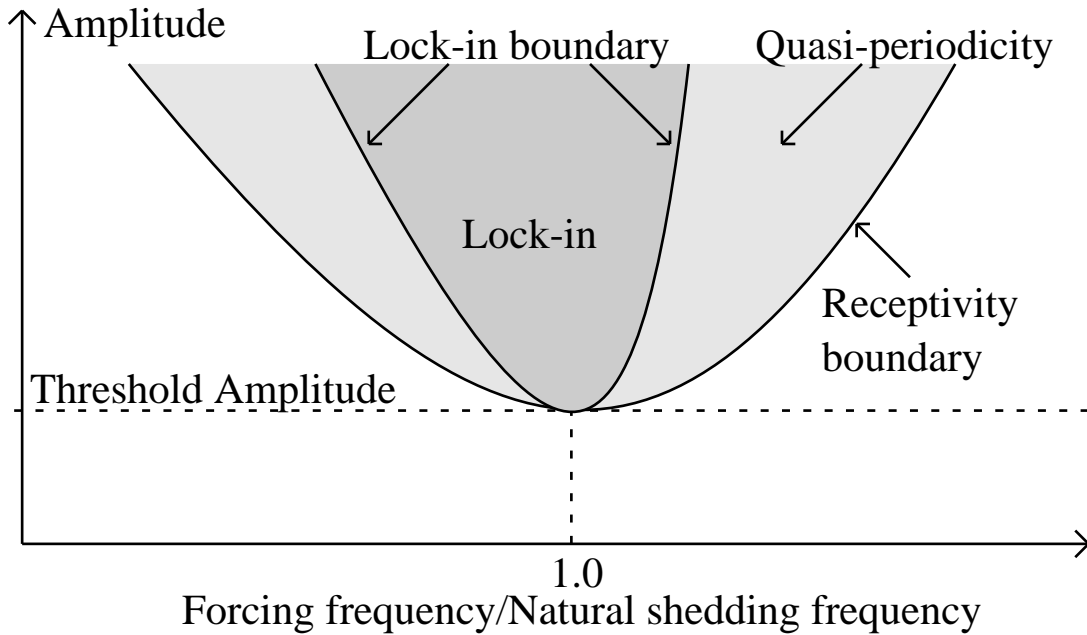


Figure 1.7: A qualitative state selection diagram for laminar wakes. (Karniadakis & Triantafyllou, 1989)

is characterised by a drop in base pressure and a drastic change in the phase between shedding and forcing at the resonant point. A review of this process is presented in Bearman (1984).

The lock-in process is governed by the amplitude and frequency of the applied perturbation or in the case of freely vibrating structures, the structures' natural frequency and damping. A description of the system with applied perturbation by Karniadakis & Triantafyllou (1989) for laminar wakes is illustrated in Figure 1.7 based on computations of flow past an oscillating circular cylinder. The amplitude of the applied perturbation has to be above a threshold to influence the flow. The frequency range where lock-in occurs, also described as the 'range of capture', increases with amplitude. Outside this range but within the receptivity range the flow exhibits a quasi-periodic behaviour with both the forcing frequency and the natural shedding frequency present in the wake. Near the boundary between the two states, chaotic like behaviour has been observed in their study. This behaviour was also observed by Blackburn & Henderson (1996) in a freely oscillating case and was possibly due to intermittent lock-in. The flow recovers its natural shedding mode outside the receptivity range. Wind tunnel experiments by Stansby (1976) also show a similar response for the flow around a circular cylinder.

Measurements of lift and drag forces or base pressure with applied forcing are of particular interest due to obvious practical applications. In the lock-in regime, a wide

variety of bodies have been shown to experience an increase in the magnitude of base pressure including circular cylinders (Stansby, 1976, Blackburn & Henderson, 1996), flat plates placed tangential to the flow, D-shapes, and triangular sections (Bearman & Davies, 1977). The fluctuating lift component also increases in the lock-in regime as shown by Staubli (1981) for circular cylinders and Bearman & Obasaju (1982) for square sections. This is due to the vortex structures increasing in spanwise correlation (i.e. suppressing three-dimensionality) and being more compact. Applied forcing at higher frequencies has shown to decrease base suction to below the natural shedding case. This includes square and triangular sections (Bearman & Obasaju, 1982), and circular cylinders and square sections (Ongoren & Rockwell, 1988).

A comparison of several geometries has show no general relationship between the 'range of capture' and the resonant point (Bearman, 1984). The resonant point is at the lower end of the lock-in range of capture for a circular cylinder but located quite centrally for a square section. Ongoren & Rockwell (1988) showed clear visualisations of a phase shift of  $\pi$  between the forcing and the shedding as the forcing frequency crosses the resonant point for a circular cylinder and a triangular section. There have been contradicting results for a square section as the phase shift has been observed in some experiments (Bearman & Obasaju, 1982, Nakamura & Mizota, 1975) and not in others (Ongoren & Rockwell, 1988). The shift in phase occurs over a small frequency range but has been shown by Bearman & Currie (1979) to be a continuous change. The phase shift is closely related to the fluctuating lift forces and changes the direction of energy transfer between the fluid and the bluff-body which can result in an unstable condition where excitation of the body is possible.

Experimental observations of flow around a blunt trailing edge by Lofty & Rockwell (1993) showed a behaviour similar to flow around shorter bodies. The rectangular edge was oscillated in a pitching motion with an amplitude of 4% of the plate thickness. The vortex shedding locked to the oscillations when the forcing frequency was within 5% of the natural shedding frequency. Outside this range, a quasi-periodic state was observed in both velocity and pressure fluctuations in all cases, with a repeatable pattern after several shedding cycles. The number of cycles for repetition to occur increases for frequencies further away from the natural shedding frequency. Within the lock-in regime, detailed flow visualisation showed the phase shift in shedding and the increasing formation length with increasing frequency past the phase shift.

### 1.3.3 Long bluff bodies

This section reviews the response of longer plates to small perturbations. Several of these studies have used external acoustic forcing to control the flow which is analogous to vibrating the body. This is a simplification of the studies involving the bluff body placed in a rigid walled duct. In that case, the sound power generated by the flow sustains a resonance in the duct which can exert feedback control on flow. When there is a blunt leading edge, the ILEV instability changes the response of the system significantly compared with aerofoil or rounded leading-edge plates which exhibit behaviour similar to shorter bluff bodies.

Nakamura & Mizota (1975) experimented on vibrating rectangular plates with aspect ratios of  $c/t = 1, 2$  and 4. The study was concerned with the galloping instability exhibited by the shorter plates ( $c/t = 1, 2$ ) which is not present with longer plate ( $c/t = 4$ ). The longer plate showed a drastic phase change between the lift force and the applied forcing close to the natural shedding frequency. Associated with this phase change, the amplitude of the lift force varies from a minimum below the natural shedding frequency to a maximum above that frequency. This results in a small frequency range just below the natural shedding frequency where energy is transferred from the fluid to the structure (a necessary condition for self excitation).

As previously discussed, Parker & Welsh (1983) initially documented several flow regimes with varying aspect ratios in the natural shedding cases. Also included in that study was the effect of sound which was introduced using two speakers in anti-phase located above and below the plate in an open jet wind tunnel. Figure 1.8 shows the range of applied frequencies where the flow is receptive to the acoustic field. The effect of the sound was to reduce the reattachment length at the leading edge resulting in a greater curvature of the shear layer and more suction on the surface. The reattachment length also shortened with increasing frequency. The shear layer and the reattachment point oscillated at the applied frequency and there were patches of vorticity shed once per cycle from the leading edge which were  $\pi$  out of phase between the top and bottom surfaces. This was maintained until the vortices passed the trailing edge resulting in the wake also having the same frequency as the applied forcing.

Parker & Welsh (1983) found that applying sound did not have a significant effect for the shorter plates ( $c/t < 3.2$ ). The second regime ( $3.2 < c/t < 7.6$ ) only generated discrete patches of vorticity at frequencies which were significantly higher than the natural shedding frequency (above line AB in Figure 1.8). Below that, the frequency in the wake was close to that without sound applied. This threshold is independent of the strength of the acoustic field within the range studied. A possible competition between the natural

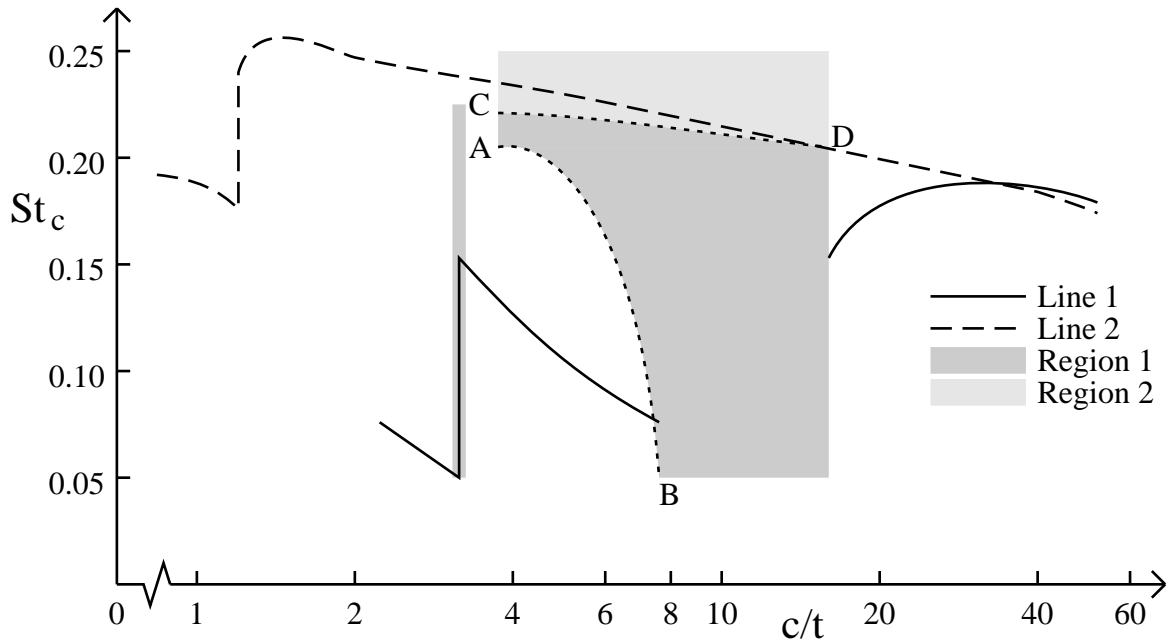


Figure 1.8: Vortex shedding and acoustic Strouhal number for flat plates with and without sound applied from Parker & Welsh (1983); sound level at mid-chord =  $16Pa$  (*rms*) for  $c/t < 3$  up to  $46Pa$  (*rms*) for  $c/t = 16$ ; Line 1: square leading edge, no applied sound,  $Re = 14,800$  to  $31,100$ ; Line 2: semi-circular leading edges, no applied sound,  $Re = 23,800$ ; Region 1: square leading edges, stable vortex streets shed near the plate at applied sound Strouhal number,  $Re = 23,800$  to  $26,500$ ; Region 2: square leading edges, unstable vortex streets shed near the plate initially at applied sound Strouhal number,  $Re = 23,800$  to  $26,500$ .

shedding frequency and the applied frequency is present in this case. Only one pair of vortices was observed to be shed along the plate in a cycle which is similar to the first natural shedding mode ( $n = 1$ ). In the third regime ( $7.6 < c/t < 16$ ), where the flow always reattaches without sound, the flow generated discrete vortices for frequencies larger than  $St > 0.05$  (lower limit of experiment) with several pairs present along the plate at a given instant. In both the second and third regimes ( $3.2 < c/t < 16$ ), although the shedding matched the applied frequency near the plate at higher frequencies, (above line CD in Figure 1.8), the wake breaks down to a lower frequency away from the trailing edge. This was close to the frequency without sound for plates in the second regime ( $3.2 < c/t < 7.6$ ). At higher frequencies but maintaining the same pressure amplitude, more energy is put into the system. This may cause the flow to be receptive at higher frequencies but break down away from the plate where the acoustic field is weaker. No results were presented on the influence of sound for plates longer than  $c/t > 16$  and frequencies higher than  $St > 0.25$  due to experimental limitations.

A similar arrangement was used by Cooper *et al.* (1986) to investigate the effects of the sound pressure level and frequency of acoustic forcing on the forced convection of heat from long rectangular plates. A heated plate with an aspect ratio of  $c/t = 9.3$  was used. The local heat transfer coefficient is relatively low in the separated region and rises to a maximum near the reattachment. When the acoustic field is imposed, the time average reattachment length decreased with frequency as in Parker & Welsh (1983) but more significantly at lower velocities and higher sound pressure levels. The discrete shedding of vortices and the reduced reattachment length results in a higher maximum local heat transfer coefficient at reattachment and also the overall heat transfer coefficient. The increase in drag is typically 10% with applied sound and is greater at lower frequencies and wind speeds. If the reattachment length is used as the characteristic length, a simple correlation exists between the local Nusselt number (non-dimensional heat transfer coefficient) at reattachment and the Reynolds number for both cases with and without sound for all experimental data. A similar correlation was found by Ota & Kon (1979) who varied the leading edge shape and McCormick *et al.* (1984) who varied the angle of attack to control the reattachment length. This suggests that the control of the reattachment length is crucial to efficient forced convection.

An extension to the study by Parker & Welsh (1983) to investigate the influence of acoustic forcing on base pressure was presented in Hourigan *et al.* (1993). The wind tunnel arrangement was similar to Parker & Welsh (1983). The study involved plates with aspect ratios of  $c/t = 10, 13$  and  $15$  at a Reynolds number around  $Re = 9,000$ . Care was taken to show that the pressure coefficient was not significantly influenced by flow velocity to show generalisation of results with respect to Reynolds number. To maintain a consistent acoustic field, the ratio of the acoustic particle velocity amplitude to the flow

velocity (Euler number) was kept constant. At  $c/t = 10$ , the base pressure coefficient showed a significant reduction close to the critical reduced frequency reaching a minimum (maximum suction) at that frequency ( $St = 0.17$ ). At  $c/t = 13$ , there is a recovery of base pressure at this critical frequency but two weaker local peaks in base suction at a lower and higher frequency. An increase in base suction, although not as strong as for  $c/t = 10$ , is observed close to the critical frequency for  $c/t = 15$ . In this study it is assumed that the convective velocity is approximately 75% of the free-stream velocity, so for an acoustic Strouhal number of  $St = 0.17$ , the vortex spacing along the plate is approximately 4.5 plate thickness. This is approximately the difference in aspect ratio between  $c/t = 10$  and 15 which in both cases are excited at this forcing frequency. It therefore suggested that the aspect ratio influences the phase in the acoustic cycle at which the leading-edge vortices arrive at the trailing edge. The interference of the leading-edge vortices and the trailing-edge shedding is reflected in the mean base pressure coefficient. Also supporting this proposition are measurements of fluctuating velocities in the wake with sound applied at the critical frequency which show a larger spectral peak when  $c/t = 10$  and 15 than at  $c/t = 13$ , due presumably to more vigorous shedding.

Some preliminary results in a water tunnel at a reduced Reynolds number of  $Re = 1300$  to ease visualisation were also included. The acoustic field is simulated by vibrating side walls of the working section. A sample of the flow visualisation is included in Figure 1.14. This showed more coherent shedding when the applied forcing is close to the critical frequency. Also observed were large-scale vortices shed from the leading edge when forcing is applied. The trailing-edge shedding is not as clear because of the position at which the hydrogen bubbles were introduced. A similar arrangement was also used by Wu *et al.* (1993) to investigate the spanwise correlation from a long plate with a rounded leading edge. The aspect ratio was  $c/t = 5$  and the experiment carried out at  $Re = 600$ . The predominant flow structures in this case are from the trailing edge only. Measurements were taken using two hot-film sensors located approximately  $3t$  from the trailing edge which were  $6t$  and  $9t$  apart. When forcing is applied at the natural shedding frequency, the spanwise correlation increased significantly from 20% without forcing until saturating at 90% above a certain level of forcing. The low correlation in the unforced case is due to phase jitter and the formation of streamwise vortices. The phase jitter is due to small fluctuations in shedding frequencies along the span resulting in a different phase of shedding along the span. The spanwise instabilities are reviewed in the next section. The forcing causes the phase of shedding along the span to match the forcing and suppresses the spanwise instabilities.

The base pressure measurements presented in Hourigan *et al.* (1993) were extended to a wide range of plates,  $6 < c/t < 16$ , and for a wide range of forcing frequencies,  $0.13 < St < 0.26$ , in Mills *et al.* (1995). A similar open jet wind tunnel arrange-

ment to Parker & Welsh (1983) was used and the results were obtained at approximately  $Re = 11,000$ . The amplitude of the sound pressure level near the speaker was kept constant for all plates and frequencies. The acoustic particle velocity is zero near the centre of the plate and accelerates around the corners. The velocity amplitude approximately  $0.1t$  horizontally from the leading edge without mean flow is 4.5% of the mean velocity for  $c/t = 10$ . There are small variations for different plates as the speed up depends on the aspect ratio of the plate. A plot of the absolute mean base pressure as a function of forcing frequency and aspect ratio is presented in Figure 1.9. There are clear discrete bands in the parameters where the absolute mean base suction reaches a local maximum. For each aspect ratio there is at least one well-defined peak. Plate lengths close to the transition between modes, such as for  $c/t = 8$ , have two less distinct peaks. When the Strouhal number based on chord length at which the mean base suction peaks is plotted as a function of chord-to-thickness ratio, as in Figure 1.3, a stepwise increase is also observed. Mills *et al.* (1995) compared this with the natural shedding case of Nakamura *et al.* (1991) and the acoustic resonance case of Stokes & Welsh (1986) and suggested that the same instability is present. At higher Reynolds numbers the weak ILEV instability is not observed naturally possibly due to turbulence and interactions with smaller scale structures. The response of the mean base pressure measurements suggest that this instability is excited by the external forcing. Smoke visualisation also confirmed earlier observations that, over a wide range of frequencies, the flow locked to the forcing and results in the out of phase shedding from opposite sides of the leading edge.

Okajima & Kitajima (1993) numerically simulated oscillating rectangular plates with  $c/t = 1, 2$  and  $3$  to study the galloping instability. The plates were oscillated at an amplitude of 14% of the plate thickness and the flow locked-in over a wide range of frequencies (i.e. from  $St = 0.076$  to  $St = 0.7$ , which was the maximum frequency used in the simulation for  $c/t = 1$ ). From the phase of the predicted lift coefficient relative to the oscillations, a narrow range of frequencies around  $St = 0.1$  was shown to be unstable. In that range there is transfer of energy from the fluid to the plate. This low frequency instability is typical of galloping.

### 1.3.3.1 Duct acoustic resonance

The behaviour of flow around long rectangular plates subjected to acoustic forcing is related to the case where the control is from an acoustic resonance generated by a plate in a duct. A vertical array of plates in cross flow are commonly used in heat exchangers and the interaction may excite an acoustic resonance (Welsh & Gibson, 1979). The neighbouring plates are replaced by intermediate duct walls to isolate the sources of sound for one plate. In these experiments a fixed plate is placed in a rigid walled duct. A

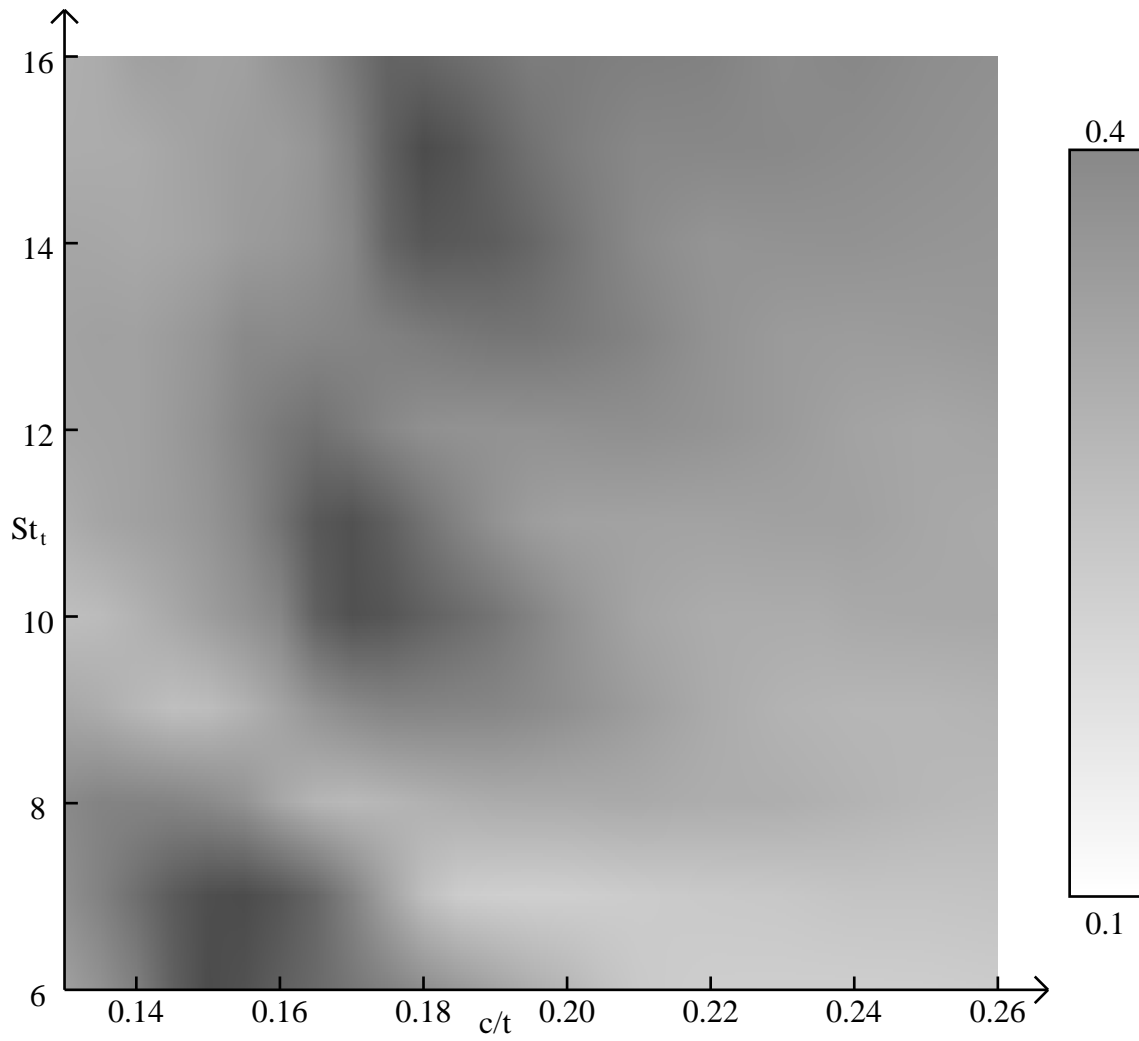


Figure 1.9: Plot of absolute mean base pressure coefficient ( $\overline{|C_p|}$ ) as a function of forcing frequency ( $St$ ) and aspect ratio ( $c/t$ ) from Mills *et al.* 1995.

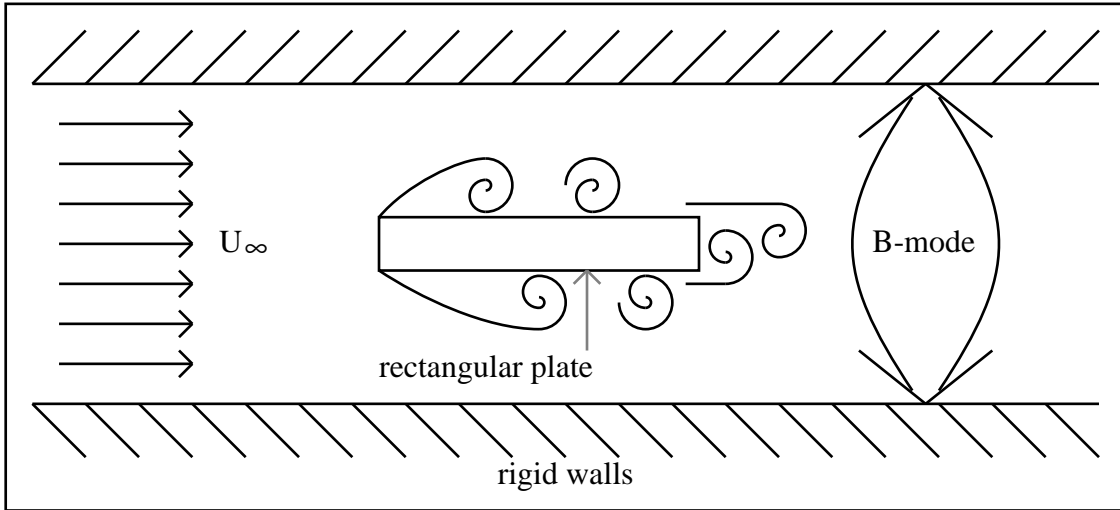


Figure 1.10: A schematic diagram of a plate in a duct influenced by the acoustic resonance.

schematic of this layout is shown in Figure 1.10. The sound generated by the flow field excites the  $\beta$ -mode which is the fundamental acoustic mode in the cross-flow direction as defined by Parker (1966). For plates with an aerodynamic leading edge, a natural acoustic resonance develops when the frequency of the natural shedding of the body matches the frequency of the  $\beta$ -mode of the duct (Welsh *et al.*, 1984). The strong acoustic resonance may reach up to 145dB and will lock the flow. Complicated duct modes can be generated in a duct which may comprise of higher harmonics which vary in phase along the span or in the longitudinal direction. Only the first  $\beta$ -mode will be considered which consists of a standing wave in the cross-flow direction with the acoustic particle velocity having an anti-node in the centre and nodes at the duct walls. This results in a predominantly cross-flow perturbation to the flow field. Measurements have shown that the acoustic particle velocity increases near the plate and decays quickly away from the plate in the streamwise direction (Welsh *et al.*, 1984).

An early investigation involving a long rectangular plate in a duct was presented in Welsh & Gibson (1979). A plate with  $c/t = 5$  was placed in the centre of a square cross-sectioned duct resulting in 2.6% blockage. The experiments ranged in Reynolds number between  $10,000 < Re < 40,000$ . At low Mach numbers, the frequency of the first  $\beta$ -mode is approximately constant. The vortex shedding frequency which was measured in the wake increased with velocity (constant  $St$ ). A natural acoustic resonance occurred when this shedding frequency was close to the frequency of the  $\beta$ -mode. This occurred in the range of  $0.10 < St < 0.12$ . An excited resonance occurred at a lower velocity where the natural shedding frequency would be about half that of the  $\beta$ -mode. This resulted in the shedding frequency nearly doubling to  $0.18 < St < 0.21$ . Flow visualisation showed that the spacing between vortices along the plate also halved. In both the fundamental

and high-order resonance, a high sound pressure level developed in the duct. The acoustic resonance is initially excited when the shedding frequency is close to a harmonic of the  $\beta$ -mode. These resonance states can also be achieved by fixing the velocity but starting the plate off centred axially and moving it towards the middle of the working section of the duct. In their experimental rig, the sound pressure level reached a maximum 3 seconds after the plate came to rest and a jump in shedding frequency occurred  $1\frac{1}{2}$  seconds before the maximum sound pressure level was observed. This suggests that the shedding feeds into the  $\beta$ -mode of the duct which then develops an acoustic resonance. The acoustic resonance then locks the flow to that frequency thus sustaining the resonance. In the resonance state the flow is in a state similar to the cases where a forced perturbation is applied.

Plates ranging from  $0.5 \leq c/t \leq 16$  in length with a rounded leading edge and either rounded or blunt trailing edges were examined by Welsh *et al.* (1984). As with the Welsh & Gibson (1979) study, the velocity in the duct was varied. The Reynolds number was in the range of  $22,500 < Re < 32,000$ . The rounded leading edge resulted in no large scale vortices from the leading edge. Unlike the blunt leading edge, no excited resonance was observed and the natural resonance occurred when the shedding frequency was close to the  $\beta$ -mode of the duct. At  $c/t = 16$ , with a rounded trailing edge, the shedding locked to the duct acoustic resonance when the natural shedding frequency was between 10% below the resonance frequency (lock-up) to 20% above (lock-down). In this range the shedding frequency is constant and matched the  $\beta$ -mode of the duct. The acoustic resonance is weaker when a blunt trailing-edge plate was used. At the same aspect ratio of  $c/t = 16$ , the lock-in range was when the natural shedding frequency was between 7% below the resonance frequency until approximately the natural shedding frequency. Flow visualisations showed stronger vortices shed from the trailing edge with more spanwise correlation in the lock-in range. The maximum sound pressure level did not vary with aspect ratio for  $c/t > 5$  but reduced for shorter plates. A switch in shedding modes corresponding to a jump in shedding frequency was observed for the shorter plates. Leading-edge shear layers shed directly into the wake when  $c/t < 1$  and no acoustic resonances were observed in the range  $1 < c/t < 1.33$  near transition.

The second part of this study presented in Stokes & Welsh (1986) used blunt leading-edge plates. Various plates with either rounded or blunt trailing edges up to  $c/t < 16$  were experimented with in the range of  $8,000 < Re < 44,300$ . The resonance range for the various plates are presented in Figure 1.11. Although there were no obvious changes in the flow, the rounded trailing-edge plates generated higher sound pressure levels resulting in a clearer visualisation of the flow field and a larger resonance range. In the second regime ( $3.2 < c/t < 7.6$ ) classified by Parker & Welsh (1983), acoustic resonance occurred at integer multiples of the natural shedding frequency. The mechanism involved

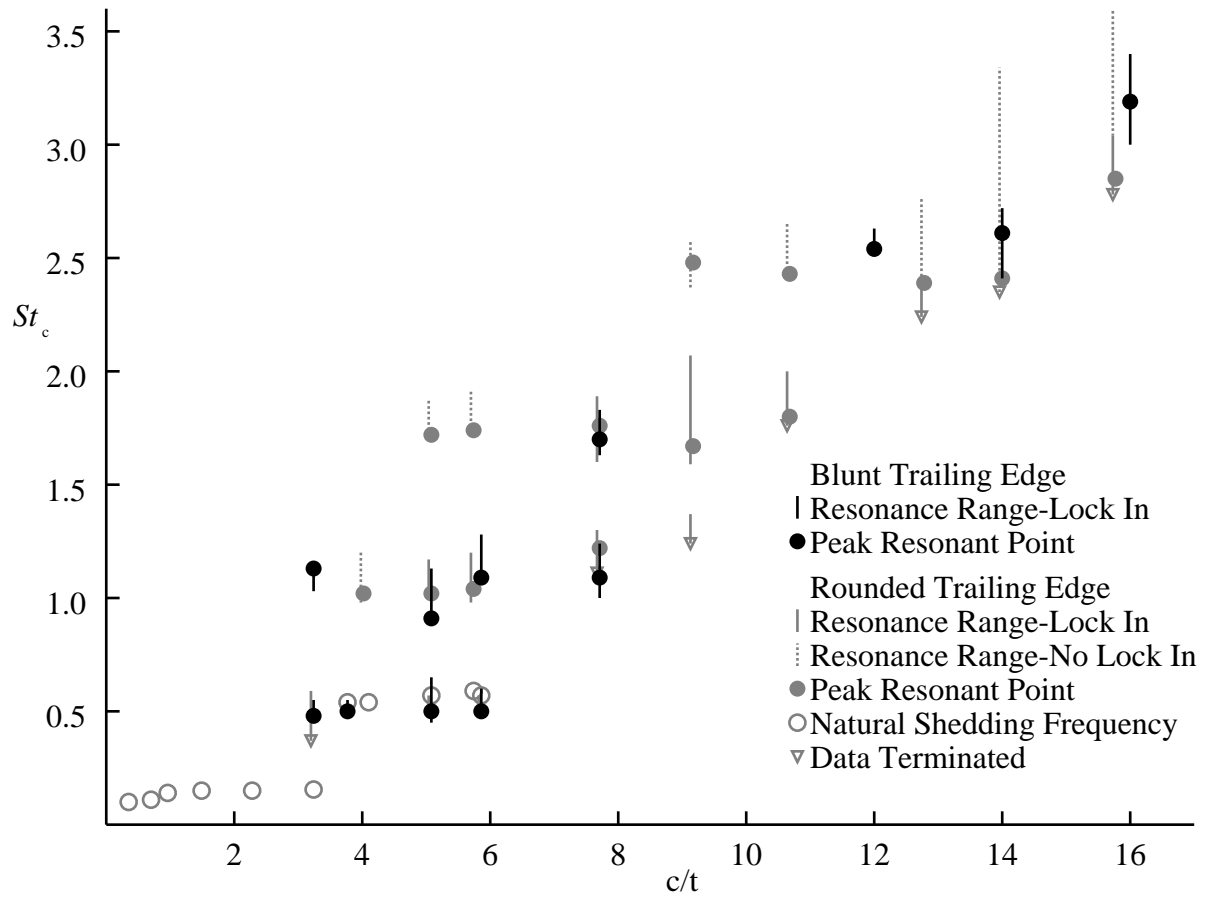


Figure 1.11: Resonant range for a blunt leading-edge plate with rounded trailing or blunt trailing-edge plates from Stokes & Welsh (1986). The data terminated due to, either the velocity limit, or the onset of higher duct modes. The dotted lines represent ranges of frequency where resonant sound was present but was not sufficient to lock the flow.

here is equivalent to that of Welsh & Gibson (1979) which has been discussed earlier. The longer plates ( $7.6 < c/t < 16$ ) which do not have a dominant natural shedding frequency, also show a continuation of this trend where resonant ranges were approximately multiples of 0.6 in Strouhal number based on chord. For these plates, the resonance could be started from the random vortices shed from the plate. Once excited, the instability in the flow field sustains the resonance completing the feedback loop. In the resonance state the flow visualisation show similar features to acoustically-forced flow. These include a shorter reattachment length, a higher base suction and out of phase shedding of discrete vortices from the leading edges which are phase locked to the forcing. As a plate locks to higher Strouhal numbers, more pairs of vortices are observed along the plate which is similar to the situation for different modes as the plates are lengthened in the natural shedding case examined in Nakamura *et al.* (1991). For example, at  $c/t = 9.17$ , the resonance ranges of  $1.3 < St_c < 1.38$ ,  $1.62 < St_c < 2.09$  and  $2.42 < St_c < 2.63$  corresponded to modes  $n = 2, 3$  and  $4$ . The resonant ranges shown in Figure 1.11 also indicate a distinct staging at multiples of approximately  $St_c = 0.6$ . In the natural shedding case, Nakamura *et al.* (1991) also observed the steps in Strouhal number base on chord to have this value. When the Strouhal number based on chord at which the duct acoustic resonance reaches a maximum sound pressure level for the rectangular plate is plotted as a function of  $c/t$  as in Figure 1.3, a stepwise increase is also observed. As discussed by Mills *et al.* (1995), the ILEV instability could be excited by the acoustic resonance of the duct.

An attempt to develop a simple mathematical model for the duct resonance was presented in Welsh *et al.* (1984), and Stokes & Welsh (1986). The flow was modelled as an inviscid flow containing discrete point vortices to model the shed vortices. The high acoustic velocities (anti-node) and low acoustic pressure (node) observed near the trailing-edge of the plate suggest that the flow is influenced by the acoustic velocity rather than acoustic pressure. The acoustic particle velocity of the resonant mode is assumed to be approximately a potential flow in the cross-flow direction varying sinusoidally. This is valid when the source region is compact relative to the duct and the flow is approximately incompressible. Using Howe's theory (Howe, 1975, 1980), which incorporates the flow field, the vorticity field and the acoustic particle velocities, the transfer of energy between the fluid and the sound field can be deduced. A positive transfer of energy from the flow field to the sound field is a necessary but not sufficient condition for acoustic resonance as the damping to the acoustic field must be considered. Acoustic resonance is sustainable when the acoustic power generated matches that leaving the system. This simple model can give a qualitative description of the system. Welsh *et al.* (1984) used this model to analyse the trailing-edge shedding from long plates which had no shedding from the leading edge. The model predicts more losses through the ends of the duct for shorter plates resulting in a lower sound pressure level and a smaller resonance range. The

analysis for a blunt leading edge was presented in Stokes & Welsh (1986). Only leading-edge vortices were considered. The generation of sound along the plate is negligible because the vortex trajectory is nearly normal to the acoustic particle velocity. The main sources or sinks of acoustic energy were from vortices passing the trailing edge because the vortex path is nearly orthogonal with the acoustic particle velocity. The phase in the acoustic cycle when the vortices pass the trailing edge was found to be the main criteria for resonance. In a half cycle, acoustic power is generated or absorbed depending on the phase of the acoustic field when the vortex passes the trailing edge. This is repeated in the next half cycle for the vortex on the other side. Contributions from pairs of vortices further downstream in the wake approximately annihilate each other. For a fixed chord, and assuming that the convective velocity of these vortices are not a function of shedding (duct) frequency, the phase at which these vortices enter the wake is controlled by the shedding frequency. Resonance occurs when the timing of these vortices (relative to the acoustic particle velocity) entering the wake results in a net transfer of energy between the flow to the acoustic field. The several distinct resonance ranges are possible because different numbers of pairs of vortices can exist along the plate while still maintaining this condition.

As a method of suppressing the acoustic resonance, Stoneman *et al.* (1988) experimented with using a second plate placed downstream. All edges of both plates were rounded with aspect ratios of  $c/t = 8\frac{1}{3}$  and  $c/t = 8$  for the upstream and downstream plate respectively. The thickness of the trailing plate was  $0.625t$  of the leading plate and experiments ranged from  $10,000 < Re < 20,000$  based on the upstream plate. As usual, the trailing-edge shedding from the front plate causes an acoustic resonance for a range of Strouhal numbers when the shedding frequency is near the  $\beta$ -mode of the duct. Experiments concentrated in suppressing resonance in this range. In this rig, the leading edge alone produces a sound pressure level of  $150dB$ . When varying the distance between the plates, the downstream plate can be a source or sink of acoustic energy and the sound pressure level rises and drops with a period of approximately 3.75 plate thickness of the upstream plate. The acoustic resonance can be lowered to  $94dB$  or amplified to  $153dB$ . When the acoustic resonance is significantly damped, there is a narrower lock-in range. An improved numerical model was developed to simulate and analyse the system. A discrete vortex model is used to model the flow and the sound field is found by solving the wave equation which gives a more realistic acoustic particle velocity field than the potential flow model as it simulates the nodes at the duct walls and the anti-nodes along the centreline of the plate. The acoustic power and energy is calculated using Howe's theory (Howe, 1975, 1980). The model predicts that the suppression or augmentation of acoustic energy depends on the phase of the acoustic cycle when the vortices from the upstream plate reach the leading edge of the downstream plate. This in turn depends on

the convective velocity of the vortices and the plate spacing. Similar to the single plate case, near the leading edge of the downstream plate, the vortex path is nearly orthogonal to the acoustic particle velocity creating either a net source or sink of acoustic energy depending on the direction of the acoustic field in relation to the sign of the vorticity in the vortex.

A review of experiments involving the interaction of the sound field and the fluid flow was presented in Welsh *et al.* (1990). This included experiments on long plates subjected to external sources of sound and plates placed in ducts which generated acoustic resonance. Although high sound pressure levels (i.e. up to 150dB) generated by acoustic resonance have an obvious influence on the flow and can be easily detected by experimenters, however, low levels (about 70dB) can also influence the flow field but the presence of the acoustic modification of the flow field is not as obvious. The influence of low levels of acoustic resonance on the flow field was shown with rounded leading-edge plates in solid duct wall at flow velocities well below the critical velocity where loud acoustic resonance occurs. The authors warn that low levels of acoustic resonance can influence the results of wind tunnel experiments.

## 1.4 Spanwise flow instabilities

The flow over two-dimensional bodies develops three-dimensional or spanwise instabilities above a critical Reynolds number. There have been many bluff body studies, especially on circular cylinders, at low Reynolds number near the initial transition to three dimensionality with the aim of understanding phenomena observed at much higher Reynolds numbers. Apart from being observed experimentally, these have also been successfully modelled theoretically and numerically in recent times (e.g., Thompson *et al.*, 1996, Henderson & Barkley, 1996).

### 1.4.1 Short bluff bodies

Many studies have concentrated on circular cylinders because it is a simple geometry with the only free parameter being the Reynolds number. Although this geometry has been studied for a long time, recent attention has been focused in the range of  $190 < Re < 260$  which spans the onset of three dimensionality. The first transition is at  $Re \approx 45$  where the flow changes from being steady in time to large scale von Karman shedding. The onset of three dimensionality results in distinct changes in the relationship between shedding frequency and base pressure with Reynolds number. The Strouhal number in

the wake undergoes discontinuities in the Reynolds number ranges  $180 < Re < 194$  and  $230 < Re < 260$  (Williamson, 1988). These ranges cannot be narrowed because the first discontinuity is hysteretic and the second involves a gradual change with both frequencies present within the range. Measurements of mean base pressure show a drop in base suction at the first transition and a local peak in base suction at the second transition (Williamson & Roshko, 1990). The drop in mean base suction at the first transition is due to the reduced spanwise correlation. At the second transition, the primary vortex shedding recovers spanwise correlation resulting in the peak in base suction before being influenced by smaller three-dimensional structures at higher Reynolds numbers. Early measurements by Roshko (1955) and visualisation by Hama (1957) showed the transition to three dimensionality.

A detailed study and classification of these instabilities was presented in Williamson (1988). The first spanwise instability to develop in the range of  $180 < Re < 194$  is called *Mode A*. There is a transfer of energy between the first and second mode, called *Mode B* in the range of  $230 < Re < 260$  with apparently only *Mode B* present above this range. *Mode B* persists well into the turbulent regime although the regularity decreases as the flow becomes more turbulent making it more difficult to visualise. Spanwise correlations of the flow for  $Re > 1,000$  by Wu *et al.* (1994) clearly indicate the presence of *Mode B* streamwise vortical structures. Since the initial classifications, many researchers have confirmed the presence of these two transitions. Experiments by Norberg (1994) have also confirmed the presence of these instabilities. Thompson *et al.* (1994, 1996), and Henderson & Barkley (1996) were the first to accurately predict these instabilities numerically and theoretically. A combination of flow visualisation from experimental and numerical simulations by Williamson (1988) and Thompson *et al.* (1996) shown here in Figure 1.12 highlights the vortical structures of the two different instabilities. The spanwise wavelength of *Mode A* is approximately 3 to 4 diameters and that of *Mode B* is about 0.8 to 1 diameters (Williamson, 1988).

The theoretical prediction by Barkley & Henderson (1996) using the Floquet stability analysis has identified the most unstable wavelengths and critical Reynolds number for each shedding mode. The calculations show the critical Reynolds numbers for *Mode A* and *Mode B* are  $Re = 188.5 \pm 1.0$  and 259 respectively. At the onset of these instabilities, the spanwise wavelengths are  $3.96 \pm 0.02$  and 0.822 diameters for these two modes. An analysis by Williamson (1996) linked these wavelengths to different physical structures. *Mode A* appears to be an elliptical instability of the two-dimensional vortex cores, while *Mode B* appears to be an instability of the braid regions between the rollers. Importantly, the different instabilities lead to two different topologies for the modes. For *Mode A*, the streamwise vortical structures connecting the largely two-dimensional vortex rollers are aligned in the downstream direction so that they are of opposite sign on opposite sides

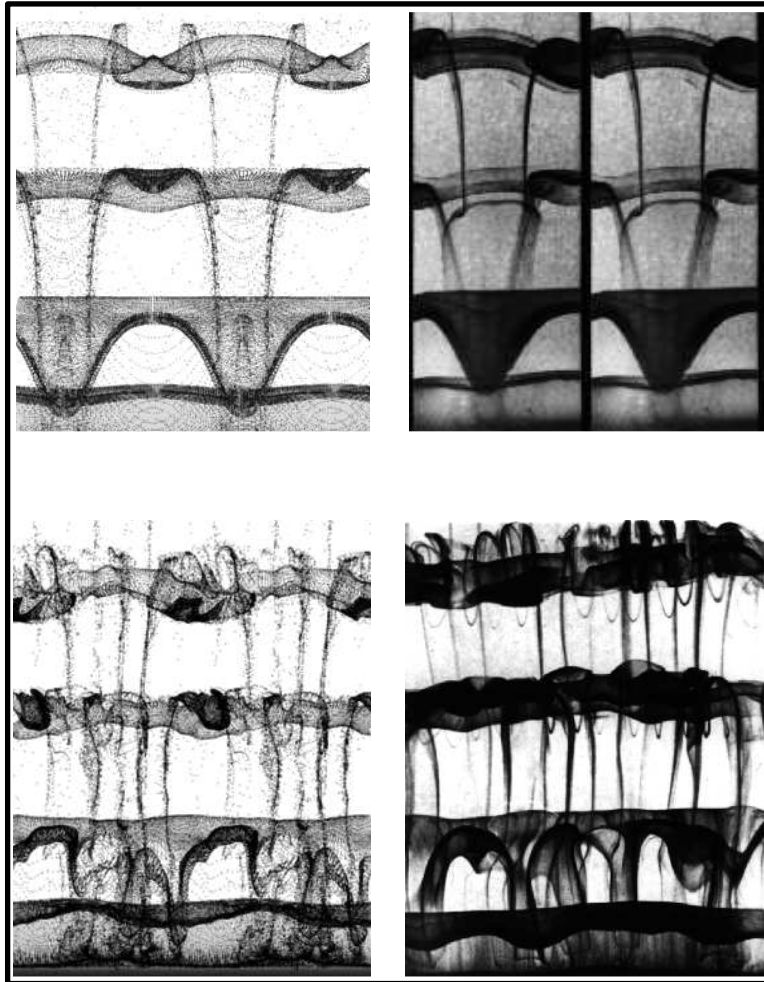


Figure 1.12: Visualisation of *Mode A* (top) and *Mode B* (bottom) taken from above the cylinder. The pictures on the left is from Thompson *et al.* (1996) in which tracer particles are placed in the simulated flow. The pictures on the right is from experiments by Williamson (1988).

of the wake. For *Mode B*, the reverse is true; here the structures are of the same sign on each side of the wake.

These spanwise instabilities have been observed on other short bluff bodies. Numerical simulations have been performed on elliptical cylinders, normal flat plates and squares. Although Mittal & Balchandar (1996) mainly concentrated on the numerical scheme and the lift and drag forces on an elliptical cylinder, spanwise *Mode B* patterns were observed. A flat plate normal to the flow was studied by Najjar & Balchandar (1998). A direct numerical simulation at  $Re = 250$  showed the system oscillated between a high and low drag state with a period of 10 times the vortex shedding period. The high drag state had coherent Karman vortices with the presence of well organised *Mode B* structures with a spanwise wavelength of  $1.2t$ . Robichaux *et al.* (1999) performed a Floquet stability analysis for a square-sectioned cylinder. This analysis predicted the growth of the first spanwise instability at  $Re = 161$  and the second at  $Re = 190$ . The spanwise wavelengths of the first and second modes were  $5.2t$  and  $1.2t$  and their vortical structures were similar to *Mode A* and *Mode B* respectively. A third instability called *Mode S* was also predicted which was present above  $Re > 200$  and has a spanwise wavelength of  $2.8t$ . Unlike the other two modes, this instability is subharmonic and has twice the period of the two-dimensional shedding. The numerical simulations by Sohankar *et al.* (1999) on a square section showed the presence of a both *Mode A* and *Mode B* in the three-dimensional wake transition process.

Only the most basic spanwise phenomena are considered here. Experiments on bluff bodies, especially circular cylinders at low to moderate Reynolds numbers, have demonstrated many other features including oblique/parallel shedding, vortex dislocations and cellular shedding. It may be possible to study these numerically or theoretically in future with improvements in computing speed and numerical techniques.

### 1.4.2 Long rectangular plate

Unlike short bluff bodies such as the circular cylinder, there has been less interest in three-dimensional transition for flow around long rectangular plates. Only vortical structures from the leading edge have been considered in detail as their interaction with the trailing-edge structures significantly increases the complexity. Spanwise instabilities develop in the large-scale vortices shed from the leading edge at low to moderate Reynolds numbers and the separating shear layer at higher Reynolds numbers.

Sasaki & Kiya (1991) observed the flow near the leading edge of long rectangular plates in a water tunnel. The plates used had an aspect ratio of  $c/t = 10, 20$  and  $40$  and the

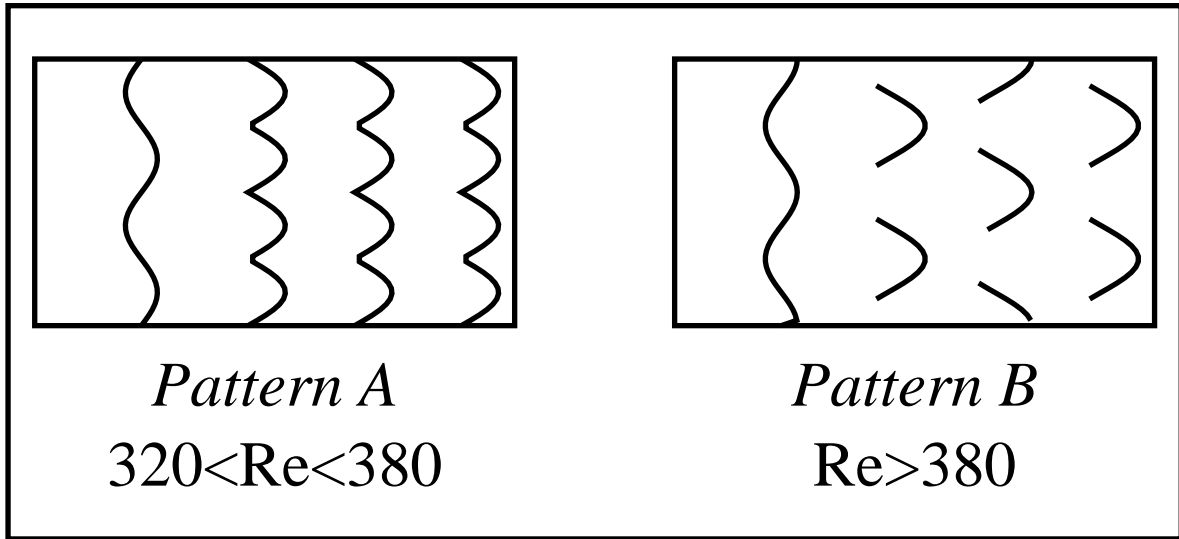


Figure 1.13: A top view of the long rectangular plate showing a sketch of the spanwise structures of the shed vortices observed by Sasaki & Kiya (1991).

Reynolds number range in the experiment was  $80 < Re < 800$ . Clear flow visualisations were obtained using dye tracers and hydrogen bubbles. No large-scale vortices were shed from the leading edge below  $Re < 320$ . Once shedding was observed, the reattachment length was approximately  $4.5t$  in this Reynolds number range. Measurements were taken between 0.6 to 2 times the re-attachment length. Spanwise instabilities were observed at the onset of shedding. A sketch of the two instabilities observed in this Reynolds number range is shown in Figure 1.13. The first mode named *Pattern A* by Sasaki and Kiya (1991) is observed in the range of  $320 < Re < 380$ . Slight disturbances could cause the deformation of the vortex cores. This is amplified by high velocity gradients in the vortices, near the plate and in the shear layer resulting in  $\wedge$ -shape structures. The streamwise vortex structures which occur between the two-dimensional spanwise vortices are in phase with subsequent streamwise vortices. The streamwise and spanwise wavelengths are both approximately between  $2t$  and  $2.5t$ . For Reynolds numbers in excess of  $Re > 380$ , a different mode becomes dominant which has been called *Pattern B*. This mode has a wavelength of  $3t$  to  $4t$  in both the spanwise and streamwise directions. The streamwise vortices form hairpin-like structures which are significantly stretched in the streamwise direction. These structures still form in rows but each row is staggered with respect to the next one. The vortices downstream induce the formation of the initially two-dimensional upstream vortex to develop waviness shifted by half a wavelength. The pattern is less regular with increasing Reynolds number.

Similar spanwise instabilities have been observed in wall bounded shear flows. These are studied in the context of transition to turbulence and unlike the plate, there

is no separation of the shear layer. At sufficiently high Reynolds numbers, slight perturbations to the boundary layer readily generate Tollmien-Schlichting waves which are discrete patches of vorticity but these waves may also occur without perturbation. Three-dimensional structures can be observed when the perturbation is not uniform along the span. Using a vibrating trip wire, Perry *et al.* (1981) observed  $\Lambda$ -shape structures similar to *Pattern A*. An alternative structure, called a subharmonic, has been observed by Kachanov & Levchenko (1984) and Saric & Thomas (1984). The vortex pattern had twice the wavelength of the Tollmien Schlichting waves because the hairpin structures were staggered between rows in the streamwise direction. Both patterns were observed before turbulent transition further downstream. At higher Reynolds numbers when the boundary layer is turbulent, Head & Banyopadhyay (1981) have observed hairpin vortices.

The separating shear layer prior to reattachment and the shedding of large scale vortices exhibit three-dimensional instabilities at higher Reynolds numbers. As observed by Cherry *et al.* (1984), at  $Re = 3,200$  the shear layer develops three-dimensionality soon after separation and the spanwise correlation decreases with the development of the shear layer. The effect of higher Reynolds number and smaller scales is to blur the visualisation of coherent structures; the same applies to the large scale shedding at higher Reynolds numbers. Without any perturbation, clear flow structures were not observed for flow over a rectangular plate at  $Re = 900$  by Soria *et al.* (1993) and at  $Re = 1,300$  by Hourigan *et al.* (1993). The random development of three-dimensional structures in the shed vortices leads to smaller scale structures downstream. Although some horseshoe-like structures could be observed further downstream, the pattern is not clear and regular. A flow visualisation by Hourigan *et al.* (1993) in Figure 1.14(a) show the randomness of spanwise structures without forcing. Regular large-scale vortex structures would not be expected at higher Reynolds numbers.

#### 1.4.2.1 Forced shedding

Experiments by Soria *et al.* (1993) and Hourigan *et al.* (1993) included spanwise flow visualisation of flow around long rectangular plates in a water tunnel. Perturbations are applied by oscillations of the side walls of a water tunnel. The velocity amplitude near the walls was  $v_{pert} = 5\%$  of free-stream velocity in Soria *et al.* (1993). Two-dimensional vortex cores develop from the shear layer and spanwise vortex structures develop in a repeatable manner across the span. Staggered horseshoe structures were observed over a wide range of frequencies ( $0.22 < St < 0.36$ ) used in the experiment. Clear visualisation was obtained by Hourigan *et al.* (1993) at the same level of perturbation. Figure 1.14(b) shows the flow pattern at an applied perturbation frequency of  $St = 0.20$ . Together with a shorter reattachment and stronger shed vortices, the applied perturbation also causes

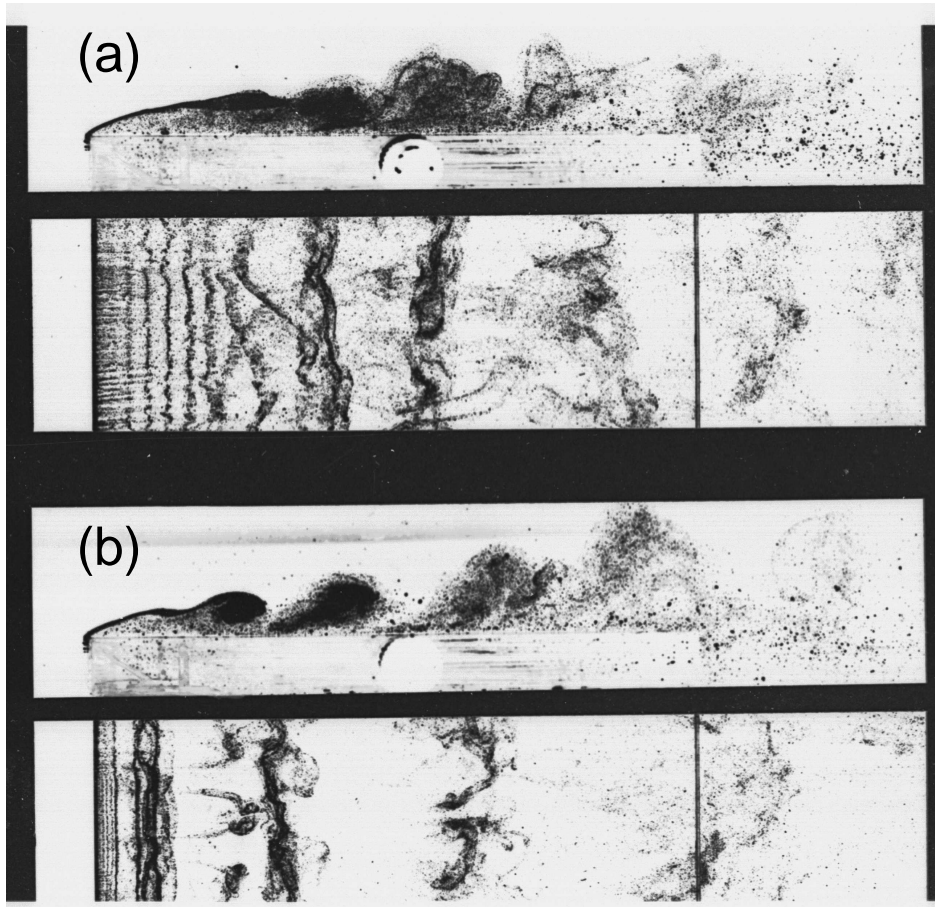


Figure 1.14: Flow visualisation from Hourigan *et al.* (1993) showing the side and top view (not at the same instant) of a rectangular plate (a) without applied perturbation and (b) with applied perturbation at  $St = 0.2$

the formation of staggered horseshoe-like structures.

# Contents

<b>1</b>	<b>Introduction</b>	<b>1</b>
1.1	Flow instabilities . . . . .	3
1.2	Natural shedding . . . . .	5
1.2.1	Leading-edge shedding . . . . .	6
1.2.2	Trailing-edge shedding . . . . .	6
1.2.3	Rectangular plate . . . . .	7
1.2.4	Summary of feedback mechanisms in the natural shedding case . . .	14
1.3	Applied forcing . . . . .	15
1.3.1	Leading edge . . . . .	16
1.3.2	Short bluff bodies . . . . .	16
1.3.3	Long bluff bodies . . . . .	19
1.4	Spanwise flow instabilities . . . . .	30
1.4.1	Short bluff bodies . . . . .	30
1.4.2	Long rectangular plate . . . . .	33

# Chapter 2

## Numerical Techniques

Many previous studies on the flow around rectangular plates, especially those with applied forcing have been done experimentally. This study aims to simulate some of the experimental observations and test some hypotheses previously proposed or suggested by others. Although the maximum Reynolds number is more limited in the numerical simulations, it is hypothesised that the important flow physics can still be captured. Comparison with experimental results will be used to test this claim. Numerical simulations also hope to give more insight into the physics of the problem by providing detailed time-dependent data.

Direct numerical simulations with no sub-grid scale or turbulence models are used to accurately model the flow. As the geometry being studied is a moderately simple one, a high-order spatial scheme can be used without significant complications. A high-order scheme uses less nodes to achieve the same resolution, and if well implemented, can result in a reduction in memory and computational requirements. A unstructured spectral-element technique is used for spatial discretisation in two dimensions because it allows for mesh flexibility and can achieve a high order of accuracy. As the geometry is only two dimensional, a Fourier expansion is used to extend the model to three dimensions because it is easy to implement and is computationally efficient. A classical three-step time-splitting scheme is used to advance the simulation in time.

This chapter will describe both the temporal and spatial discretisation used in this study. A description of the boundary conditions used in the numerical model is included. To test the accuracy of the model, two benchmark problems were used to validate the scheme, namely the backward-facing step flow and the driven cavity flow. To accurately simulate the flow over a rectangular plate, the size of the domain and the required spatial and temporal resolution are determined. A description of the application

of Howe’s acoustic model is given. Finally, other post-processing steps are also elucidated.

## 2.1 Numerical scheme

The main software used in this study implements a numerical solver for the time-dependent incompressible Navier-Stokes equations. These consist of the momentum equation

$$\frac{\partial \mathbf{u}}{\partial t} = -(\mathbf{u} \cdot \nabla) \mathbf{u} - \nabla p + \frac{1}{Re} \nabla^2 \mathbf{u}, \quad (2.1)$$

and the incompressibility constraint

$$\nabla \cdot \mathbf{u} = 0. \quad (2.2)$$

As will be discussed in the following sections, the spatial derivatives are evaluated using a mixture of spectral-element and global spectral discretisations while the equations are integrated forward in time using a classical three step splitting scheme. This program is a modification of finite-element software to incorporate high-order interpolation within each element. It was mainly developed by Mark C. Thompson and Kerry Hourigan from the Department of Mechanical Engineering, Monash University. This software was initially developed to study flow past a circular cylinder and has accurately modelled the spanwise instabilities at low Reynolds numbers (Thompson *et al.*, 1994, 1996).

### 2.1.1 Spatial scheme

The spatial discretisation is based on a two-dimensional spectral-element scheme. This is extended into the spanwise direction using a global Fourier spectral scheme. The spectral-element technique was first applied to the study of fluid dynamics by Patera (1984). Since then, further refinements have been introduced by Karniadakis (1989, 1990). The technique employed in this study is similar to that used by Karniadakis & Triantafyllou (1992) to simulate three-dimensional bluff body flows. Initially, this section will review the spectral-element scheme used for the two-dimensional simulations and then describe the extension to three dimensions through a Fourier expansion.

#### 2.1.1.1 Two-dimensional discretisation

Traditionally, the finite-element method has found favour because of its ability to handle complex geometries. Typically first- or second-order elements are used because this scheme is more computationally efficient using these elements. A global spectral method

(Canuto *et al*, 1988) can achieve “spectral convergence” when implemented correctly but handles only the simplest of geometries without significant complications. The spectral-element technique is a hybrid of these two techniques. The spectral-element method is essentially a modification of the Galerkin finite-element method to incorporate a spectral expansion within each element. When a problem results in a continuous and smooth solution, the spectral-element technique can achieve exponential convergence, with significant savings in computations over high-order finite element techniques especially when high accuracy is required. The end result is a high-order spatial scheme that incorporates much of the ability of the finite element technique to handle geometries.

The main difference between the traditional Galerkin finite-element method and spectral-element method is in the choice of basis functions. After mapping the elements to a computational square, the spectral-element technique uses the tensor product of high-order Lagrangian polynomials to interpolate the solution variables in each direction within each element. Importantly, within each local element, the nodes are chosen to be at the Gauss-Lobatto-Legendre quadrature points which are the roots of the equation,

$$(1 - \xi^2)P'_m(\xi) = 0 \quad \text{with} \quad -1 \leq \xi \leq 1 \quad (2.3)$$

where the Legendre polynomials are

$$P_m = \frac{1}{2^m m!} \frac{d^m}{d\xi^m} (x^2 - 1)^m \quad \text{where} \quad m = 0, 1, 2, \dots \quad (2.4)$$

The nodes are stretched towards the boundaries of each element as shown in Figure 2.1 and Figure 2.3(b). Typically between 6th ( $m = 6$ ) and 12th ( $m = 12$ ) order polynomials are used, resulting in an equivalent order of accuracy, and hence between  $N = 7$  to 13 nodes in each direction. The Galerkin weighted residual method is used to form equations for the solution variables at the nodal points. The momentum equations are multiplied by the nodal weighting functions, in this case the associated Lagrange polynomials, and integrated over all space. Because the weighting functions are only non-zero within the element, the resulting integrals only depend on the local and neighbouring elements. These integrals are evaluated numerically by Gauss-Lobatto-Legendre quadrature. It turns out that this is much more efficient computationally than the normal finite-element approach of using Gauss-Legendre quadrature. For Gauss-Lobatto-Legendre quadrature the weighting coefficients are given by

$$w_j = \frac{2}{m(m+1)} \frac{1}{[P'_m(x_j)]^2} \quad \text{with} \quad j = 0, 1, \dots, m. \quad (2.5)$$

This allows an integral to be evaluated by the following approximation :

$$\int_{-1}^1 f(x) dx \cong \sum_{j=1}^N w_j f(x_j) \quad (2.6)$$

and is exact if  $f(x)$  is a polynomial of degree  $2N - 3$  or less. (This is slightly less accurate than for Gauss-Legendre quadrature where the approximation is exact for polynomials of degree  $2N - 1$  or less.)

Earlier implementations of these schemes positioned the nodes at the Gauss-Lobatto-Chebyshev points (Patera, 1984, Karniadakis, 1989) but later used Gauss-Lobatto-Legendre points (Karniadakis, 1990, Karniadakis & Triantafyllou, 1992). This is mainly because the compression of the nodes towards element boundaries is not as severe.

Using Lagrange polynomial basis functions and locating the nodes at the Gauss-Lobatto-Legendre points leads to significant computational benefits. Only a limited number of nodes in an element contribute to the equations formed at a particular node. For example, the “Mass” matrix is diagonal which markedly improves the efficiency of time-stepping problems. This is not the case for traditional finite-element implementations where Gauss-Legendre quadrature is used. Static condensation techniques further reduce the computational requirements. This technique takes advantage of the fact that the equations for the internal nodes in each element are only a function of the element boundary nodes. This allows the matrix equations to be decoupled into two sets; one involving the element boundary nodes, and  $K$  small matrix equations for the internal nodes of each element. After solving the larger matrix equation governing the boundary nodes, the  $K$  smaller matrix equations are inverted to provide the solution at the internal nodes. Bandwidth minimisation schemes can reduce the bandwidth of the matrices and sparse matrix solvers are used to solve the large system of equations involved. If the grid, physical constants and timestep are fixed, the matrices are decomposed using LU decomposition at the start of the simulation and stored in memory. Implicit steps (i.e. for pressure and diffusion) are done by backsubstitution from the stored LU decomposition.

### 2.1.1.2 Spanwise discretisation

An efficient way to extend the method to three dimensions for two-dimensional geometries is to use a global Fourier spectral discretisation in the third direction. This approach was used in conjunction with a spectral-element method by Karniadakis (1990) and specifically on two-dimensional circular cylinders by Karniadakis & Triantafyllou (1992) and Thompson *et al.* (1996). This global spectral approach has the advantage of exponential or spectral convergence but restricts the boundary conditions in the spanwise direction to be periodic.

The spatial discretisation consists of a series of  $F$  equi-spaced planes in the spanwise direction with an identical spectral-element mesh on each plane. The flow variables are transformed into Fourier space in the spanwise direction for each node on the spectral-

element grid. A fast Fourier transform is used to reduce the operation count. This decouples the problem into a set of  $F$  Fourier modes which can be solved independently for the linear operators. This results in the generation of  $F/2$  smaller matrix equations rather than one large matrix equation with a large bandwidth which would considerably increase the storage requirements. The decoupling of the problem into effectively  $F/2$  two-dimensional planes and the use of static condensation for the spectral-elements discussed in the previous section facilitates the implementation on parallel architecture machines. This has not been implemented yet but is work in progress. In the future with advances in computational performance, it will soon be possible to perform accurate simulations with spectral-element discretisation in all three dimensions. Although this is significantly more computationally expensive, it will allow three-dimensional geometries to be simulated.

### 2.1.2 Temporal scheme

There are many techniques for integrating the Navier-Stokes equations forward in time. The three step time-splitting technique described in Karniadakis *et al.* (1991) is well suited to the spatial technique used here. It splits the Navier-Stokes equations into three sub-steps and allows a mixture of implicit and explicit high-order temporal schemes to be used for each sub-step. The momentum equations are split into three semi-discrete equations, namely the non-linear convective step,

$$\frac{\mathbf{u}^* - \mathbf{u}^n}{\Delta t} = -\mathbf{u} \cdot \nabla \mathbf{u}, \quad (2.7)$$

the pressure correction step,

$$\frac{\mathbf{u}^{**} - \mathbf{u}^*}{\Delta t} = -\nabla \bar{p}^{n+1}, \quad (2.8)$$

and the diffusive step

$$\frac{\mathbf{u}^{n+1} - \mathbf{u}^{**}}{\Delta t} = \frac{1}{Re} \nabla^2 \mathbf{u}, \quad (2.9)$$

where the superscripts  $n$  and  $n + 1$  refers to the time level at the start and end of the timestep respectively. This technique introduces two intermediate flow fields (i.e.  $\mathbf{u}^*$  and  $\mathbf{u}^{**}$ ). The pressure ( $\bar{p}^{n+1}$ ) is obtained by enforcing incompressibility at the end of step two (Equation 2.8).

The convective equations are non-linear and are normally solved explicitly using the Adam-Bashforth family of schemes to avoid iterations but this restricts the maximum size of the timestep. The diffusive step can be solved implicitly using the Adam-Moulton family of schemes resulting in a Helmholtz equation which is solved by inverting the equation matrix. The spectral-element spectral scheme used for the simulations described here uses the third-order Adam-Bashforth scheme for the non-linear step and the second-order Adam-Moulton (Crank-Nicholson) scheme for the diffusive step. For the pressure

step, the second intermediate flow field ( $\mathbf{u}^{**}$ ) is forced to satisfy the incompressibility constraint. As a result the pressure can then be found by solving a Poisson equation,

$$\nabla^2 \bar{p}^{n+1} = \frac{1}{\Delta t} \nabla \cdot \mathbf{u}^*, \quad (2.10)$$

and subsequently the pressure sub-step is used to find ( $\mathbf{u}^{**}$ ). When  $\mathbf{u}^{**}$  satisfies the continuity equation then  $\mathbf{u}^{n+1}$  also satisfies that condition (provided the initial field is divergence free).

### 2.1.3 Boundary conditions

Typically, the equation for the convective sub-step is applied to the entire domain including the boundary nodes and no boundary conditions are prescribed in this operation (i.e  $\mathbf{u}^*$  is not fixed at the boundaries). The pressure boundary condition is chosen so that the the second intermediate velocity field,  $\mathbf{u}^{**}$ , is divergence free everywhere in the domain and also at the boundaries. Boundary conditions are imposed on the final velocity field,  $\mathbf{u}^{n+1}$  when solving the Helmholtz equation for the diffusion step. This ensures that the velocity boundary condition is satisfied at the end of this timestep and the start of the next.

As shown by Karniadakis *et al.* (1991), an appropriate choice of boundary condition for the pressure gradient normal to the boundary is required to eliminate the splitting errors and ensure continuity is satisfied at the boundaries. A stable formulation is proposed in Karniadakis *et al.* (1991) which uses the flow field from previous timesteps to form a condition for the normal pressure gradient at the boundary. As shown by Karniadakis *et al.* (1991), the order of the time-marching scheme can only be one order above the order of extrapolation used to find the pressure boundary condition. The numerical scheme used in this study uses a first-order pressure boundary condition resulting in overall second-order time-accurate scheme (consistent with the order of the diffusion sub-step).

### 2.1.4 Stopping criteria for temporal evolution

In the present study, generally only the asymptotic state is of interest. Simulations are started with either a stationary fluid or a flow field which has reached an asymptotic state at a lower Reynolds number. Care is taken to ascertain if the flow has reached an asymptotic state. This sometimes required between several hundred and several thousand time units to be simulated before this is achieved (Typically there are 100 or more timesteps per time unit). The flow is judged to have reached a steady state if the maximum change

in the velocity field ( $\Delta u$ ) per timestep is four orders of magnitude below the mean flow velocity. When the asymptotic flow is not steady, a key indicator such as the total kinetic energy or the base pressure is monitored. The possible unsteady states observed in these flows include a periodic state where the flow is repeatable every period, a quasi-periodic state in that there are a few frequencies present and a chaotic or random state where there are many frequencies present. The flow is assumed to have reached a periodic state when the indicator shows a repeatable pattern over several periods. When the flow reaches a quasi-periodic state, the signal is usually repeated after a much longer time interval than in the previous case. In this case, the simulation is evolved until several periods of the longest wavelength is captured and show a repeatable pattern. In the last case, the statistical properties of the signal such as the mean and the standard deviation are calculated and the simulation is stopped after these properties are approximately constant (taken over several data sets).

## 2.2 Validation

To validate the code and investigate typical grid resolutions required, two classical test problems are studied: namely, flow over a backward-facing step and the driven cavity flow. These are two distinct problems in that the flow over a backward-facing step involves an inflow and an outflow boundary, while the driven cavity flow is a closed system. The driven cavity flow problem is also used to investigate the possibility of using a different implicit scheme for the non-linear substep namely the Runge-Kutta scheme. This is studied because the convective step is done explicitly and an improved scheme could reduce the timestep restriction.

### 2.2.1 Backward-facing step flow

There are numerous studies involving this particular problem as this is used as a benchmark problem to verify numerical methods for computing flows. Results from Kim & Moin (1985), and Gresho *et al.* (1993) will be used as validation. Simulations from Kim & Moin (1985) are chosen because results are presented for a wide range of Reynolds numbers using a time-dependent solver. A detailed study of this problem at  $Re = 800$  was presented by Gresho *et al.* (1993). Using various spatial schemes including the spectral-element method, Gresho *et al.* (1993) showed that at  $Re = 800$ , the flow is steady and stable to perturbations. Gresho *et al.* (1993) showed that if the flow is not well resolved, the spectral-element method (as well as other schemes) can predict an artificial unsteady behaviour even after a long simulation time. The resolution used in this study matches a

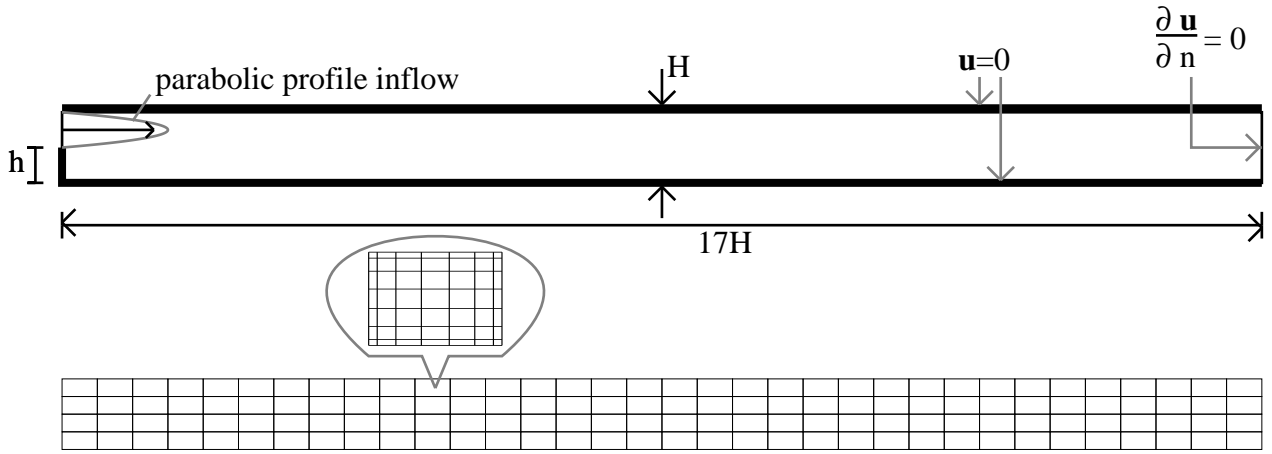


Figure 2.1: A layout for the 'flow over a backward-facing step' problem (above) and the spectral-element mesh used for the simulation (below). Note that within each spectral-element there are  $8 \times 8$  nodes ( $N = 8$ ).

resolution used in Gresho *et al.* (1993) to produce a consistent result at  $Re = 800$ . It is assumed that this will also be able to resolve the flow at lower Reynolds numbers. As is common practice, the reattachment length of the separation bubble formed in the wake of the step will be used for comparison.

The parameters for this problem is chosen so as to match Kim & Moin (1985) and Gresho *et al.* (1993). A layout of the flow over a backward-facing step problem is shown in Figure 2.1. It involves a two-dimensional channel of height  $H$  and an inflow on the left boundary above a step of height  $h$  and outflow some distance downstream. No slip boundaries are applied to the top and bottom of the channel and the step. In this particular study, the step height is chosen to be half the channel height and the outflow boundary to be  $17H$  downstream of the inflow boundary although Kim & Moin (1985) used a shorter domain ( $15H$ ). The inflow velocity profile has a parabolic profile which approximates a fully developed laminar channel flow at the entry to the expanded region. The parabolic profile is,

$$\mathbf{u}(y) = (24y(\frac{1}{2} - y), 0), \quad y \in (0, 0.5), \quad (2.11)$$

where  $y$  is the vertical distance above the step. The parabolic profile chosen has an average velocity of one unit. The Reynolds number is based on the average inflow velocity and the channel height  $H$ . The normal gradients for all flow variables are set to zero at the outflow boundary.

Simulations were performed at Reynolds numbers of  $Re = 10, 100, 200, 400$  and  $800$ . The spectral-element mesh used for this problem consisted of a  $32 \times 4$  ( $K = 128$ ) regularly spaced element with  $8 \times 8$  ( $N = 8$ ) nodes in each element as shown in Figure 2.1. The simulations were started with the flow field from a lower Reynolds number and stopped when the flow reached a steady state. Figure 2.2 shows the streamlines of the

flow at each Reynolds number after the flow has reached a steady state. The reattachment length,  $r$ , is measured by searching for the point where the flow switches direction along the first layer of nodes from the bottom boundary. Table 2.1 show a comparison of reattachment lengths,  $r$ , between the present simulations and previous studies . The two sets of results show only a small difference. A possible source of error other than from the numerical scheme is the method used for measuring the reattachment length. The spacing between the first layer of nodes and the boundary and the horizontal spacing of the nodes are different for the different schemes. This may have a small influence on the results.

$Re$	$r/h$ (Present Study)	$r/h$ (Comparison)
10	0.81	
100	3.19	3.2 (Kim & Moin, 1985)
200	5.39	5.3 (Kim & Moin, 1985)
400	8.61	8.6 (Kim & Moin, 1985)
800	12.05	12.2 (Gresho <i>et al.</i> , 1993)

Table 2.1: Comparison of reattachment length and between the present study and Kim & Moin (1985) and Gresho *et al.* (1993).

## 2.2.2 Driven cavity

The classical driven cavity flow problem consists of a square domain with three stationary walls and a 'sliding lid'. The 'sliding lid' is normally the top boundary having a uniform tangential velocity. A sketch of this is show in Figure 2.3(a). The Reynolds number is based on the length of the domain and the velocity of the lid. The velocity singularity at the top corners where the lid meets the stationary walls causes problems with high-order schemes. Some *regularisation* is required to avoid local artificial oscillations in the velocity field but only a small amount of regularisation is needed. A velocity profile for the lid is chosen so that it is uniform for a large proportion of the lid but decays to zero close the edges where it meets the stationary walls and is also continuous in the first and second spatial derivatives. The velocity profile is:

$$\mathbf{u}(x) = ((1 - \exp(-20(1 - x^2)))^3, 0), \quad x \in (-1.0, 1.0), \quad (2.12)$$

where  $x$  is the horizontal distance along the lid. This velocity profile is used for both the spectral-element and global spectral schemes.

The driven cavity flow problem is also a commonly considered benchmark problem and been used by many authors to validate numerical schemes. In the steady state regime,

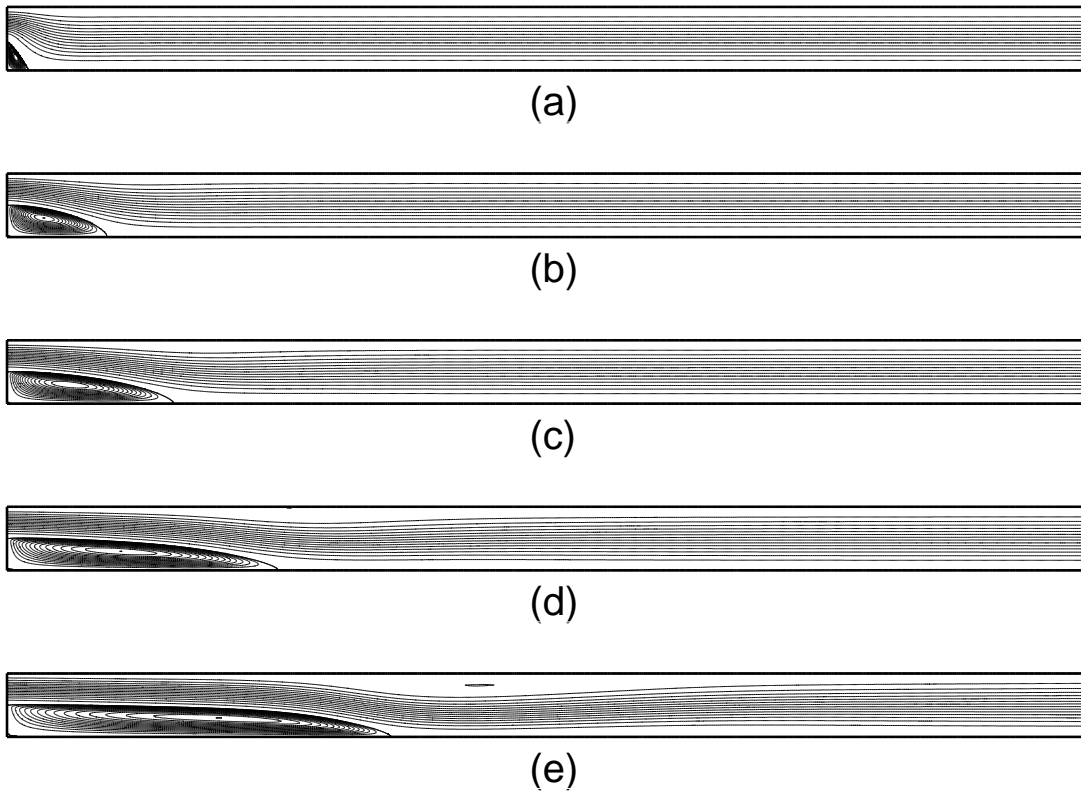


Figure 2.2: Streamline plots for flow over a backward-facing step at Reynolds numbers (a)  $Re = 10$ , (b)  $Re = 100$ , (c)  $Re = 200$ , (d)  $Re = 400$  and (e)  $Re = 800$ .

the results will be compared to Ghia *et al.* (1982) because results were presented for a wide range of Reynolds numbers. It is one of the earlier studies which presented detailed results for the driven cavity flow using a steady solver and many others have since used it for comparison. Above a critical Reynolds number, the driven cavity flow will not asymptote to a steady solution. The time-dependent solution can be periodic, quasi-periodic or chaotic. In this flow regime the spectral-element simulations will be compared with results from a global spectral scheme. The global spectral code was also used to develop and test a modified time-splitting scheme that uses the Runge-Kutta scheme instead of the Adams-Bashforth scheme for the convective term.

The mesh used for the spectral-element simulation consisted of an  $11 \times 11$  ( $K = 121$ ) elements with  $10 \times 10$  ( $N = 10$ ) nodes within each element as shown in Figure 2.3(b). The elements are stretched towards the boundaries in both directions by locating the edges of the elements at the Chebyshev collocation points. Figure 2.4 shows the streamlines of the driven cavity flow at various Reynolds numbers. For  $Re = 1,000, 5,000$  and  $7,500$ , the flow reached a steady state. At the higher Reynolds numbers of  $Re = 10,000, 14,000$  and  $17,000$  the streamlines are a snapshot in time as the flow does not reach a steady state.

### 2.2.2.1 Steady state

Simulations were performed using the spectral-element scheme at a Reynolds number of  $Re = 100, 400, 1,000, 3,200, 5,000$  and  $7,500$  which corresponded to results presented in Ghia *et al.* (1982). The simulations were started using the results from the next lower Reynolds number except for  $Re = 100$  which was started using a stationary velocity field. The flow field was integrated until a steady state solution was achieved (i.e.  $\Delta u/\Delta t < 10^{-6}$  for the entire domain) which required several thousand non-dimensional time units of integration. The simulations were performed using a timestep of  $\Delta t = 0.0012$ . Such a small timestep is a result of Courant restriction from the explicit step in the time-marching algorithm due to the fine spatial resolution. Although Ghia *et al.* (1982) presented results at  $Re = 10,000$ , those results were obtained using a steady state solver. When using this time-dependent solver, the highest Reynolds number at which the solution asymptotes to a steady state is  $Re = 8,000$ . At the next increment in Reynolds number,  $Re = 8,125$ , the solution asymptotes to a periodic state. This was the case even after several thousand more time units were simulated with the flow in a periodic state. This is in close agreement with the analytical work of Poliashenko & Aidun (1995) which predicted the flow becoming unsteady above  $Re = 7763$  with the small difference in the transition Reynolds number possibly due to the regularisation used in the lid profile for the simulations.

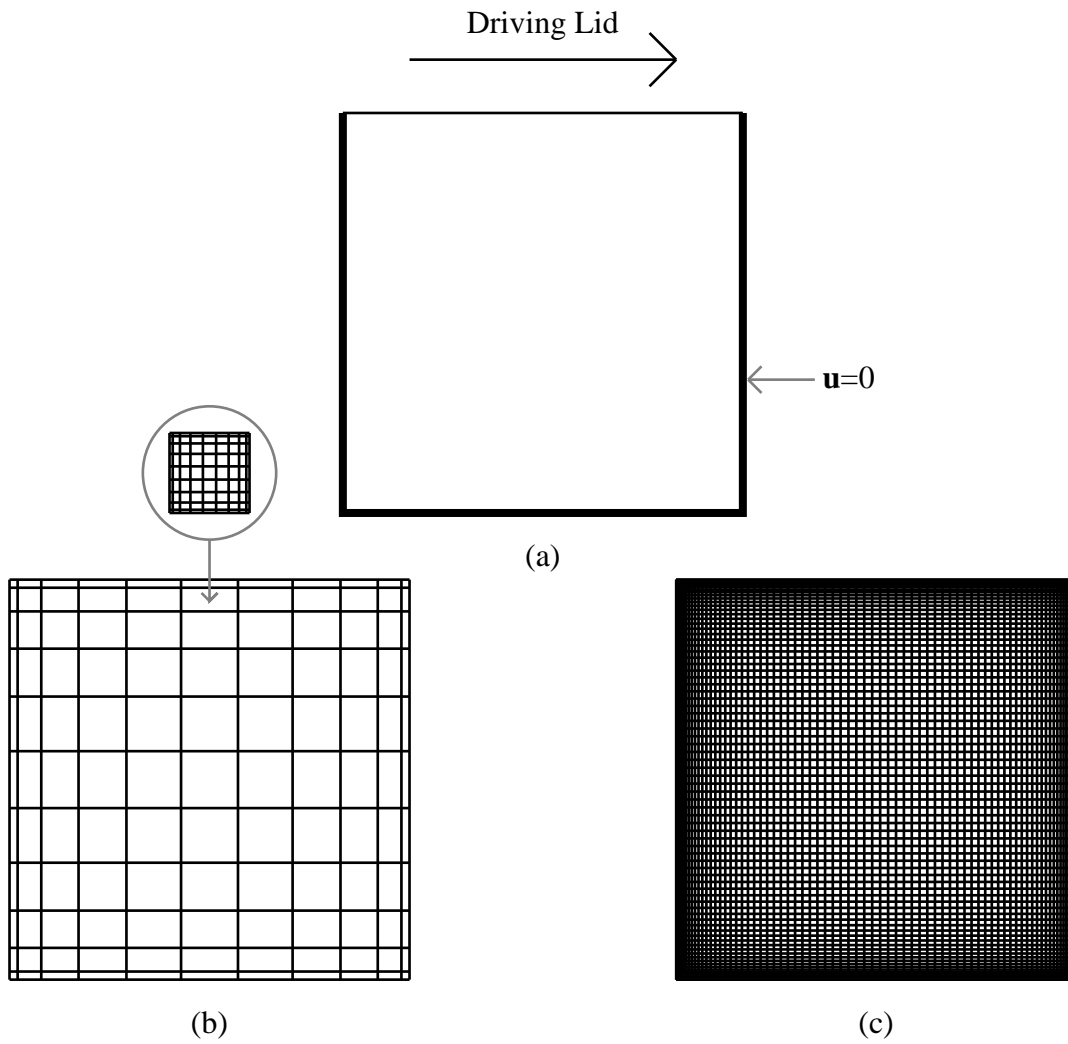


Figure 2.3: (a) A schematic of the driven cavity flow, (b) the spectral element mesh and (c) the global spectral mesh.

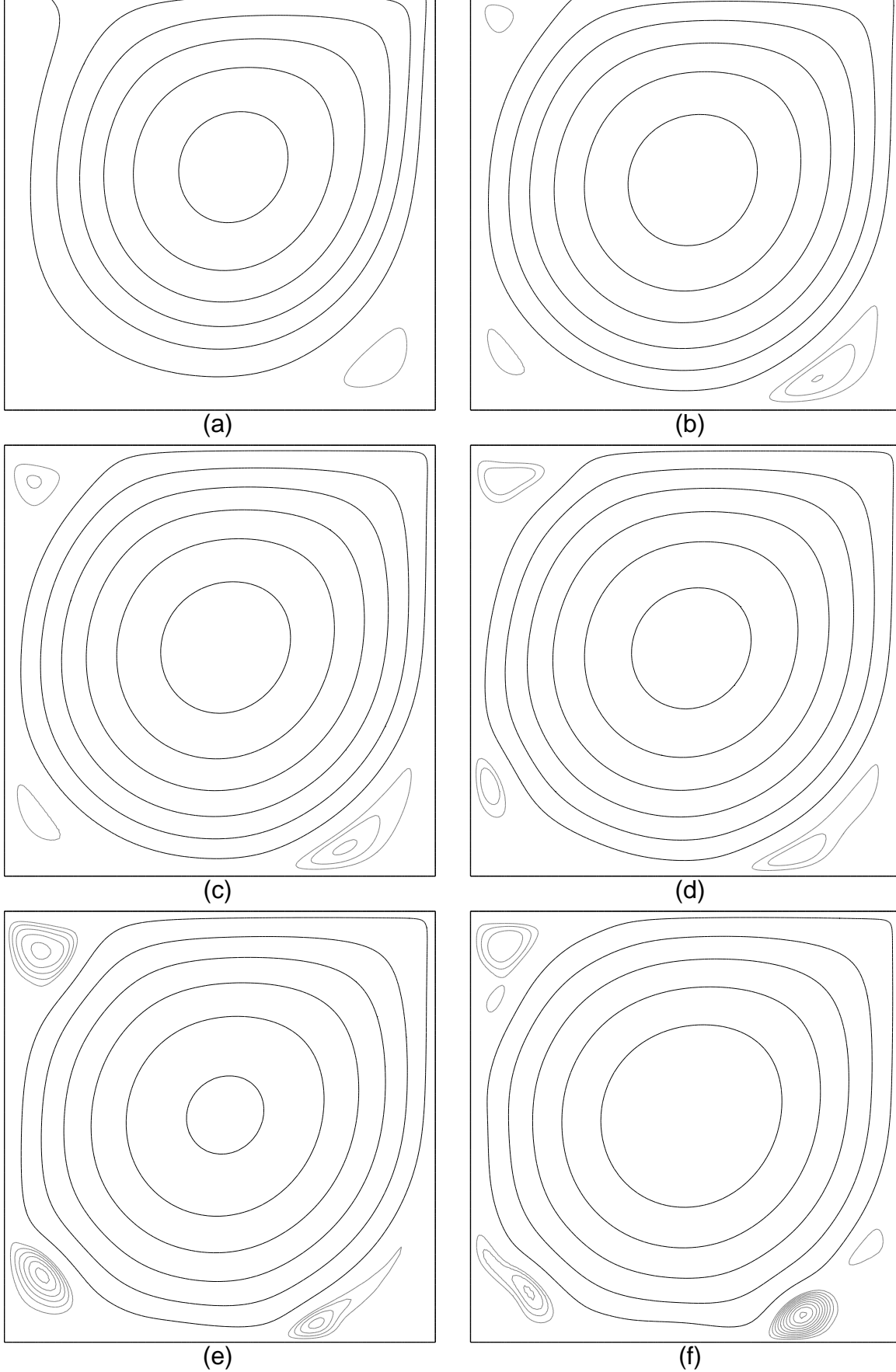


Figure 2.4: Streamlines plots of the driven cavity flow at (a)  $Re = 1,000$ , (b)  $5,000$ , (c)  $7,500$ , (d)  $10,000$ , (e)  $14,000$  and (f)  $17,000$ . Note: Black lines are positive streamlines which start at  $0.01$  with increments of  $0.02$ . Grey lines are negative streamlines which start at  $-0.001$  with decrements of  $-0.001$ . These values are non-dimensionalised with the cavity length and the lid velocity.

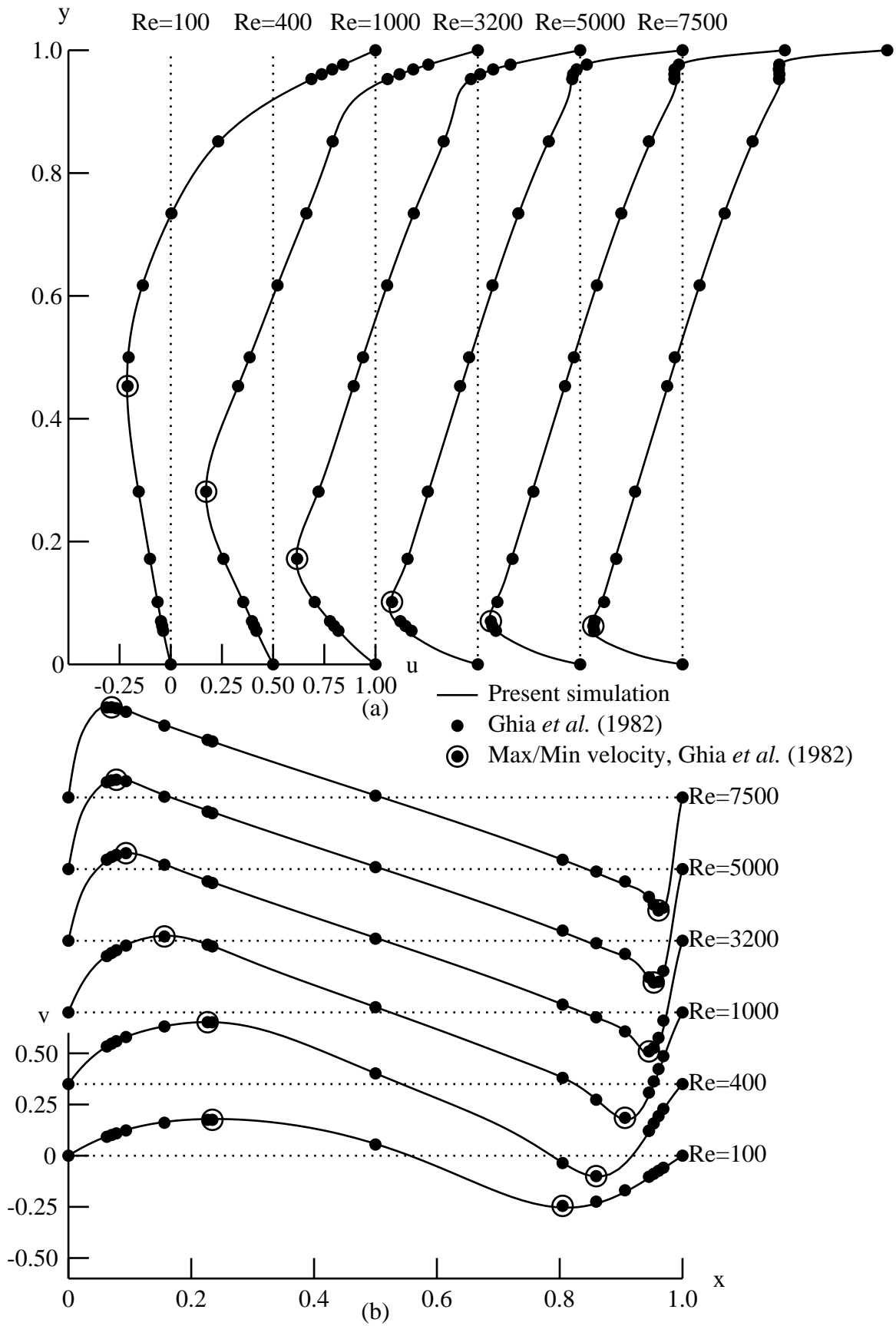


Figure 2.5: (a)  $u$  velocity profile taken vertically at the centre of the cavity and (b)  $v$  velocity profile taken horizontally at the centre of the cavity. Also plotted for comparison are results from Ghia *et al.* (1982) which include the maximum or minimum velocities in the velocity profile. (Note: The velocity profiles are offset for clarity.)

Figure 2.5 shows a comparison of velocity profiles at various Reynolds numbers with those from Ghia *et al.* (1982). Figure 2.5(a) shows the profile of the horizontal component of velocity taken vertically across the centre of the cavity while Figure 2.5(b) shows the profile of the vertical component of velocity taken horizontally across the centre of the cavity. Also shown are the minimum and maximum velocities within each profile found by Ghia *et al.* (1982). In this comparison, the two separate simulations produce graphically identical velocity profiles. The magnitude and location of the maximum and minimum velocities found by Ghia *et al.* (1982) are also consistent with the present simulations. Although there is a small amount of regularisation of the velocity profile of the 'driving lid', the effect on the overall flow field appears to be small.

### 2.2.2.2 Global spectral scheme

A global spectral scheme was developed to study the practical implementation of a Runge-Kutta scheme for the non-linear term. A global spectral scheme is used because it is a simpler scheme to implement and the spectral convergence allows spatial error to be much smaller than the temporal errors. The global spectral scheme was developed under the guidance of Dr. Paul Morris who was formerly with the Department of Mechanical Engineering at Monash University and is currently at Kodak (Aust.). The implementation and results acquired have been published in Tan *et al.* (1998).

An outline of the spatial technique is presented in Canuto *et al.* (1988). As the flow is wall bounded, a Global-Galerkin technique is employed with Chebyshev polynomials used to interpolate the flow variables in both directions within the domain. This node positioning is ideal for studying this problem as the natural compression towards the boundaries improves the resolution of boundary layers. Other polynomials could be used but the Chebyshev polynomials have traditionally been favoured because a Fast Fourier transform exists to convert between real and polynomial space and, of course, they exhibit spectral convergence. Although a Fast Fourier transform exists, for the large grids used in the computations, an optimised matrix multiplication routine is found to be faster for derivatives calculation. Although the operation count is higher, the transform method is slower because of the numerous logical operations and reordering of the matrices required by this method. Shen (1991) also found the matrix multiplication to be faster when studying the regularised driven cavity using a similar spectral method. A direct matrix method also allows any arbitrary resolution to be used rather than powers of two. The implicit steps are performed using a matrix diagonalisation technique given by Canuto *et al.* (1988).

The classical time-splitting scheme (Equations 2.7, 2.8 and 2.9) uses the Adam-

Bashforth family of schemes to advance the convective step as shown in Karniadakis *et al.* (1991). As this is an explicit step, the Courant stability limit restricts the maximum allowable timestep especially for finer grids. For finite difference discretisation of the convection or diffusion operators on an equi-spaced grid, the maximum timestep when using fourth-order Runge-Kutta scheme is approximately seven times larger than for the third-order Adams-Bashforth scheme (Canuto *et al.*, 1988). Although the fourth-order Runge-Kutta scheme requires approximately four times more computation than the third-order Adams-Bashforth scheme, an overall saving is gained from the less restrictive timestep. This led to the investigation into the use of the Runge-Kutta scheme instead of the Adams-Bashforth scheme.

The initial attempt was for each timestep to advance only Equation 2.7 (the convective term) with the fourth-order Runge-Kutta scheme and then solve Equation 2.8 and 2.9 using the same method described earlier. This led to results which were more dissipative than expected. For example this particular problem was found to asymptote to a steady solution at  $Re = 10,000$  while the spectral-element scheme using the traditional time-marching algorithm and a prediction by Liffman (1996) both showed the flow to asymptote to an unsteady state. The error resulted from the Runge-Kutta step which is meant to advance the equation a full timestep rather than to an intermediate velocity field( $\mathbf{u}^*$ ). In other words, it leads to a splitting error. When the Runge-Kutta scheme is applied to Equation 2.7 and summed with Equation 2.8 and 2.9, the result is not the original Navier-Stokes equation but instead a similar equation containing some spurious terms. This was realised after tests showed that the convergence was less than first-order in time.

To overcome this problem, a modified time-splitting scheme is developed to correctly implement the Runge-Kutta scheme to advance the non-linear term. The temporal schemes for the pressure correction step and the diffusion step remains the same. This scheme basically advances all three terms within each Runge-Kutta sub-step. As all the equations do not explicitly depend on time, a memory efficient Runge-Kutta scheme described in Canuto *et al.* (1988) is used. The resulting algorithm is shown below.

```

Set  $\mathbf{u} = \mathbf{u}^n$ 
For  $k = s, 1, -1$ 
 $\frac{\mathbf{u}^* - \mathbf{u}^n}{\Delta t/k} = -\mathbf{u} \cdot \nabla \mathbf{u}$ 
 $\frac{\mathbf{u}^{**} - \mathbf{u}^*}{\Delta t/k} = -\nabla p \quad \nabla \cdot \mathbf{u}^{**} = 0$ 
 $\frac{\mathbf{u} - \mathbf{u}^{**}}{\Delta t/k} = \frac{1}{2 Re} (\nabla^2 \mathbf{u} + \nabla^2 \mathbf{u}^n)$ 
End For
Set  $\mathbf{u}^{n+1} = \mathbf{u}$ .

```

The order of the Runge-Kutta scheme is set to four ( $s = 4$ ) for all the simulations. The

global spectral scheme produces results which were consistent with the spectral-element scheme and Liffman (1996) when the above algorithm was used. Simple convergence tests showed that this scheme is second-order accurate when using a first-order pressure boundary condition. A comparison between the global spectral technique and the spectral-element technique for the driven cavity flow in the unsteady regime will be presented in the next section.

### 2.2.2.3 Time dependence of High $Re$ cavity flow

This section presents a comparison between the time-dependent characteristics of the driven cavity flow predicted by the spectral-element technique and the global spectral technique. For this particular problem, both schemes predicted the system evolved to a steady state for Reynolds number up to  $Re = 8,000$ . Additional simulations were performed at  $Re = 9,000, 10,000, 12,000, 14,000, 15,000, 16,000$  and  $17,000$  with the different schemes for comparison. The total kinetic energy is used to compare the separate simulations because it is a global measurement which provides an indication of the state of the flow. This method has been used previously for studying driven cavity flow, e.g., Shen (1991), Liffman (1996), and Tan *et al.* (1998). The total kinetic energy of the flow is defined as,

$$E(t) = \int \frac{1}{2} |u|^2 dA, \quad (2.13)$$

with the integration over the entire domain. For the spectral-element simulation, this integral is performed using the Gauss-Legendre-Lobatto quadrature within each element and then by summing over all elements. In the global spectral case, the integral is obtained by transforming the field into Chebyshev space where finding the integral is only a simple arithmetic operation.

The global spectral simulations were performed on a  $80 \times 80$  grid as shown in Figure 2.3(c) with a timestep of  $\Delta t = 0.0025$ . To ascertain that this resolution is sufficient, a  $100 \times 100$  simulation was performed at the highest Reynolds number. The difference in the statistical properties in the kinetic energy trace was less than 2%. The spectral-element simulations were performed on the same grid used for the steady state case but the timestep reduced at  $Re = 12,000, 14,000, 15,000, 16,000$  and  $17,000$  to  $\Delta t = 0.008, 0.008, 0.006, 0.006$  and  $0.005$  respectively. The simulations were performed until an asymptotic state was reached and then the evolution of the kinetic energy is recorded over approximately 300 time units. For those cases where a periodic state is attained, the period was also recorded. Additional results of the global spectral simulation can be found in Tan *et al.* (1998).

$Re$	Spectral-Element			Global Spectral		
	Mean	Period	Std. Dev.	Mean	Period	Std. Dev.
9,000	$4.551 \times 10^{-2}$	2.28	$7.380 \times 10^{-6}$	$4.536 \times 10^{-2}$	2.28	$7.357 \times 10^{-6}$
10,000	$4.523 \times 10^{-2}$		$9.349 \times 10^{-6}$	$4.472 \times 10^{-2}$		$9.338 \times 10^{-6}$
12,000	$4.347 \times 10^{-2}$	1.48	$1.381 \times 10^{-5}$	$4.388 \times 10^{-2}$	1.47	$1.351 \times 10^{-5}$
14,000	$4.172 \times 10^{-2}$		$1.652 \times 10^{-5}$	$4.188 \times 10^{-2}$		$1.637 \times 10^{-5}$
15,000	$4.070 \times 10^{-2}$	1.60	$1.938 \times 10^{-5}$	$4.078 \times 10^{-2}$	1.58	$1.833 \times 10^{-5}$
16,000	$3.986 \times 10^{-2}$		$2.128 \times 10^{-5}$	$3.940 \times 10^{-2}$		$1.831 \times 10^{-5}$
17,000	$3.861 \times 10^{-2}$		$7.407 \times 10^{-5}$	$3.850 \times 10^{-2}$		$8.421 \times 10^{-5}$

Table 2.2: Mean, Standard Deviation and Period of the kinetic energy trace at various Reynolds number from the spectral element simulation and the global spectral simulation.

The mean, standard deviation and period of the kinetic energy trace is summarised in Table 2.2. The results compare well with deviations not exceeding 3% in most cases. This is likely due to the different spatial and temporal errors from the different schemes and numerical round off. The larger difference in the standard deviations at  $Re = 16,000$  and  $17,000$  is because at those high Reynolds numbers the kinetic energy trace contains many wavelengths. A much longer time series has to be analysed to reduce this uncertainty.

#### 2.2.2.4 Runge-Kutta versus Adams-Bashforth

After implementing the different schemes for advancing the non-linear term and showing that the results for both schemes are consistent, a comparison was made of the performance of both schemes. Both time-marching schemes were implemented with the global spectral discretisation and several simulations were performed to assess the computational cost and timestep restriction.

In terms of operation count, to perform one timestep using the fourth-order Runge-Kutta scheme is approximately equivalent to performing four complete timesteps using the Adam-Bashforth scheme. Simulations of the driven cavity flow with various timesteps showed that the stability limit of the fourth-order Runge-Kutta scheme is approximately 6 times larger than using the third-order Adam-Bashforth scheme. This is approximately consistent with theoretical predictions for a finite difference scheme on a convective equation discussed earlier. The storage requirements of the two schemes are equivalent when using the memory efficient Runge-Kutta scheme. This result shows that the Runge-Kutta scheme can be more efficient if simulations are performed with much larger timesteps.

However, when taking larger timesteps, the overall accuracy of the scheme must also be considered. Both schemes use a first-order pressure boundary condition and a Crank-Nicholson scheme for the diffusion term which restricts them to be second-order accurate in time. This means that the larger timesteps with the Runge-Kutta scheme incur a larger temporal error. Attempts to increase the order of the scheme by using a second-order pressure boundary condition and a third-order Adam-Moulton scheme instead of the Crank-Nicholson technique significantly reduces the stability of the overall scheme. The treatment of the pressure boundary condition requires extrapolating velocity fields from previous timesteps; however increasing the order of the pressure boundary condition this way reduces the overall stability. This is also the observation of Karniadakis *et al.* (1991). Using the third-order Adam-Moulton scheme is expected to reduce the stability although it is an implicit scheme as theoretical predictions show that it is not unconditionally stable like the Crank-Nicholson scheme.

Weighting the cost between a lower operation count and the larger errors, the spectral-element code used for the simulations in the following chapters has not been modified to incorporate the Runge-Kutta scheme. The Runge-Kutta scheme would be used if the order of accuracy of the overall scheme was improved without suffering from a reduced maximum timestep. The main cause of this reduced timestep is from the implementation of the pressure boundary condition. With further development, it could be possible to formulate a stable pressure boundary condition that better suits the Runge-Kutta scheme. Even recently, second-order time-accurate schemes are still used by many authors (Sohankar *et al.*, 1999, Najjar & Balachandar, 1998, Barkley & Henderson, 1996).

## 2.3 Flow around long plates

This section will present the preliminary work performed for the simulation of flow past long plates. The two geometries studied are an elliptical leading-edge plate with a blunt trailing edge, and a rectangular plate. This section will include a description of the domain and boundary conditions used. Several simulations were performed to verify that the computational domain is large enough. A domain which is too small significantly influences surface pressures due to blockage and therefore hydrodynamic forces on the plate. Simulations with different resolution and timesteps are performed to verify that the resolution is sufficient.

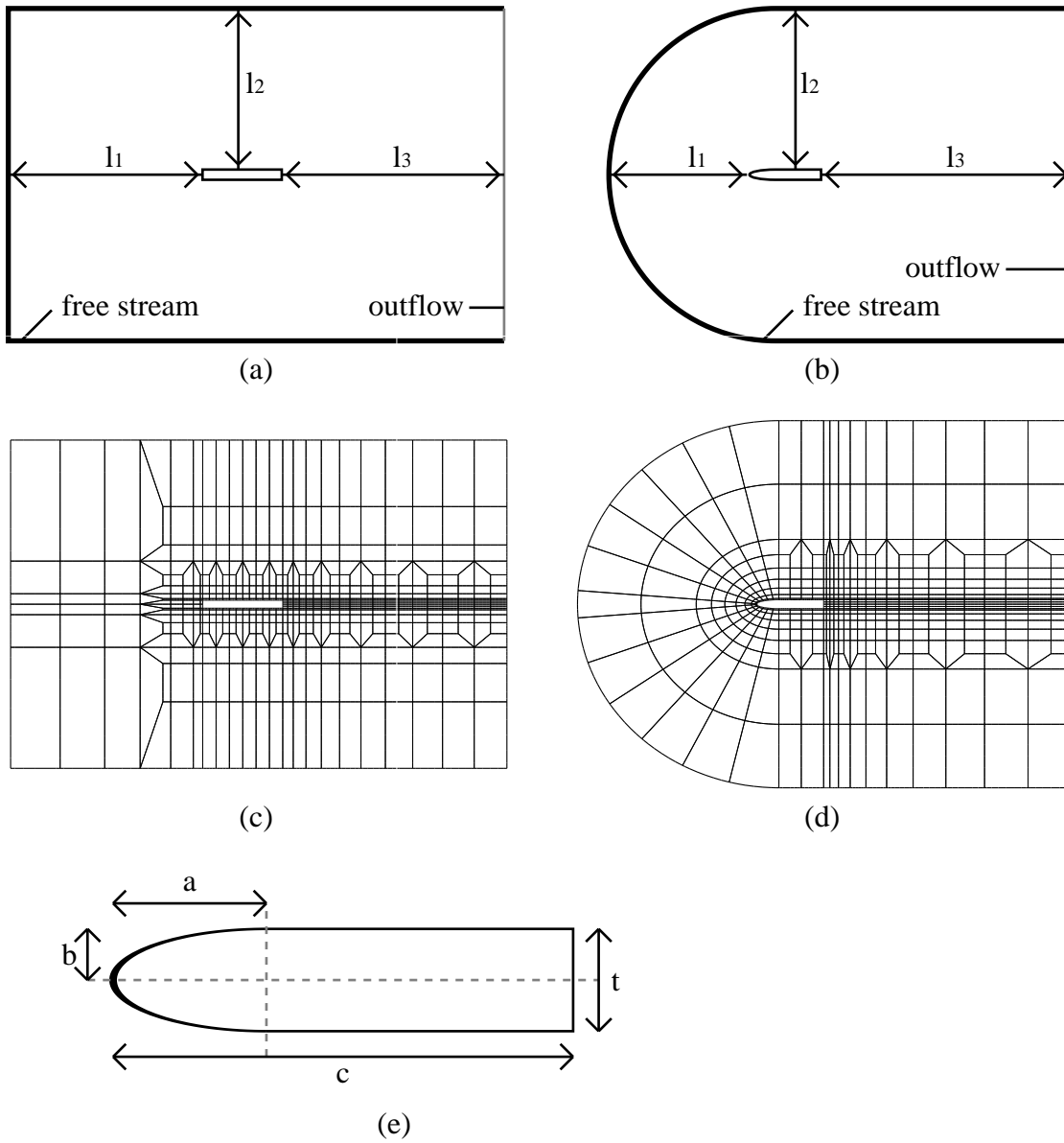


Figure 2.6: The computational domain for (a) the rectangular plate and (b) the elliptical leading-edge plate. The computational mesh for (c) a plate with  $c/t = 10$ , ( $K = 562$ ) and (d) an elliptical leading-edge plate with  $c/t = 7.5$ , ( $K = 557$ ). (e) A sketch showing an elliptical leading-edge plate with an axes ratio of  $a:b$  and an aspect ratio of  $c/t$ .

### 2.3.1 Computational domain and boundary conditions

A sketch of the computational domain is shown in Figure 2.6(a) and Figure 2.6(b) for a rectangular plate and a elliptical leading-edge plate respectively. With the flow direction from left to right, the inlet, top and bottom boundaries are set to a free-stream condition which has a unit velocity in the horizontal direction. The normal gradients for all velocity components are set to zero at the outflow boundary on the right. The velocity on the plate is set to zero. In those simulations where forcing is applied to the flow, a sinusoidal cross-flow component is added to all the free-stream boundaries. The resultant boundary condition is,

$$\mathbf{u}(t) = (U_\infty, A_o \sin(2\pi Stt)), \quad (2.14)$$

where  $St$  is the non-dimensional forcing frequency. In later chapters, the phase in the forcing cycle used to describe the different times in a period is based on the sine wave.

Figure 2.6(c) and Figure 2.6(d) shows typical spectral-element grids used for these simulations. The elements are concentrated towards the plate. The elements are stretched towards the plate from the top, left and bottom boundary using a cosine stretching function. The first few elements from the boundary are merged to reduce the overall number of elements. Between the plate and the outflow boundary, this stretching was found to be too severe and to better resolve the wake, a hyperbolic sine stretching function as described in Thompson *et al.* (1985) was used. To reduce the overall number of elements, they are adapted to a coarser mesh away from the wake in the cross-flow direction. The elements are gradually adjusted from an elliptical leading-edge geometry to a circular boundary for the elliptical leading-edge plate.

The square edges on the plates are discontinuities that restrict the spatial convergence rate of spectral-element scheme. However this effect is local and does not degrade the accuracy of the flow field away from these points. A higher concentration of elements are placed near these points to reduce this effect.

The simulations are normally started from a stationary state. The solution from a lower Reynolds number is used if one is available. The flow starts shedding between approximately 80 – 150 time units depending on the Reynolds number. Typically the flow is evolved for another 100 time units to allow it to settle to an asymptotic state. In those cases where forcing is applied, the solution of the unperturbed flow is used as an initial condition.

Extending the model into the spanwise dimension is currently restricted only to periodic boundaries (effectively an infinite cylinder) by using a Fourier series. The free parameters in this case are the number of Fourier planes and the size of the spanwise

domain.

### 2.3.2 Domain size

When simulating viscous flows over bluff bodies, the size of the domain significantly influences the surface pressure on the body (Barkley & Henderson, 1996). As the two-dimensional simulations aim to generate quantitative results of the pressure and forces on the plate, it is important to determine the required size of the domain in order to reduce this effect below a certain tolerance. Several simulations were performed on the flow over an elliptical leading-edge plate to ascertain the required domain size. This size was then tested on the rectangular plate. These tests were performed without external forcing and at a low Reynolds number of  $Re = 300$  where the flow structures are larger and the overall system is more affected by close boundaries. The resolution near the plate is approximately the same for all the domain sizes tested. The next section will show that this resolution is adequate.

For the two geometries in this study, there are three parameters that govern the size of the domain. From Figure 2.6 these are:  $l_1$  is the distance from the inflow to the leading-edge of the plate,  $l_2$  is the distance between the top or bottom boundary to the plate and  $l_3$  is the distance from the trailing edge to the outflow boundary. All distances are normalised by plate thickness.

In the three-dimensional simulations, the computational domain on each spectral-element plane is much smaller than for the two-dimensional simulations. This reduces the size of the problem to a manageable one. These computations are aimed at simulating the qualitative flow structures. A restrictive domain may affect pressure measurements but should not significantly influence the large scale flow structures. The majority of the three-dimensional simulations were with the spanwise domain of  $2\pi t$  wide.

#### 2.3.2.1 Elliptical leading-edge plate

Simulations were performed on the elliptical leading-edge plate with a 5:1 axes ratio and an overall aspect ratio of  $c/t = 7.5$ . The domain has a rounded inflow boundary hence  $l_1$  is equivalent to  $l_2$ . This results in only two free parameters. At this Reynolds number, the flow asymptotes to a periodic state. The mean base pressure (measured at the centre of the trailing edge) and the peak-to-trough is recorded in Table 2.3 for comparison. On increasing the size of the domain, the results converged to a mean base pressure of  $c_p = -0.274$  and a peak-to-trough value of 0.050.

$l_2$	$l_3$	Mean $c_p$	Peak-to-trough
10	4	-0.450	0.085
14	6	-0.353	0.081
20	10	-0.311	0.072
22	12	-0.283	0.055
24	15	-0.279	0.057
28	20	-0.273	0.054
40	27	-0.274	0.051
40	40	-0.273	0.051
60	60	-0.274	0.050

Table 2.3: The mean base pressure and peak-to-trough base pressure difference for various domain sizes.

It is important to model the essential physics in the two-dimensional simulations. A small error due to boundary proximity is acceptable so that less elements are required; especially far away from the plate thereby speeding up computations and allowing a larger parameter space to be studied. It was decided that an error of less than 2% would be tolerated as this is comparable with other uncertainties which include modelling assumptions and numerical error.

$l_2$	Mean $c_p$	Peak-to-trough
12	-0.292	0.042
20	-0.277	0.054
27	-0.275	0.053
40	-0.273	0.051

Table 2.4: The mean base pressure and peak-to-trough base pressure difference with  $l_3$  fixed at 40.

$l_3$	Mean $c_p$	Peak-to-trough
28	-0.277	0.054
34	-0.275	0.054
40	-0.273	0.051

Table 2.5: The mean base pressure and peak-to-trough base pressure difference with  $l_2$  fixed at 20.

To determine the required distance for  $l_2$  and  $l_3$ , initially  $l_3$  is fixed at 40. From Table 2.4, a distance of  $l_2 = 20$  would be sufficient to reduce the errors due to the

boundaries below the acceptable limit. Next  $l_2$  is fixed at 20 and various values of  $l_3$  are experimented on. From Table 2.4, a distance of  $l_3 = 28$  appears to be adequate. Subsequent simulations with elliptical leading-edge plates were performed using  $l_2 = 20$  and  $l_3 = 28$ .

### 2.3.2.2 Rectangular plate

The rectangular plate geometry with  $c/t = 10$  is tested with this domain size to determine if it is adequate. This domain size is compared with another which is 5 units larger in each direction. Simulations at a higher Reynolds number of  $Re = 400$  is also used as numerous simulations will be performed at that Reynolds number. At the lower Reynolds number of  $Re = 300$ , the base pressure shows a regular periodic signal but at  $Re = 400$ , the signal is not perfectly periodic because the system is not as strongly locked into a particular shedding mode. Therefore the peak-to-trough base pressure difference is not presented at  $Re = 400$ . From the base pressure predictions show in Table 2.5, the smaller domain appears to be adequate and was used in further computations.

$Re$	$l_1$	$l_2$	$l_3$	Mean $c_p$	Peak-to-trough
300	24	20	28	-0.334	0.074
300	29	25	33	-0.341	0.071
400	24	20	28	-0.482	
400	29	25	33	-0.487	

Table 2.5: The mean base pressure and peak-to-trough base pressure difference for flow around a rectangular plate simulated with two different domain sizes at  $Re = 300$  and 400.

### 2.3.3 Spatial and temporal resolution

Simulations were performed on the same grid as in the previous section but the number of nodes in each element was increased to determine the resolution required to adequately resolve the flow. The domain size determined previously was used in these simulations. The grids for the rectangular plate and the elliptical leading-edge plate is shown in Figure 2.6(c) and Figure 2.6(d) respectively. The investigation will involve both the natural and forced shedding cases. Base pressure measurements are used for comparison. When the spatial resolution is increased, the size of the timestep needs to be decreased because of the stability restrictions imposed by the Courant stability restriction.

For the elliptical leading-edge plate, the simulations were performed on a plate with an elliptical (5:1 axes ratio) leading edge and a overall aspect ratio of  $c/t = 7.5$ . The simulations were performed at a Reynolds number of  $Re = 500$  for two different resolutions. At this Reynolds number, the system reaches a periodic shedding state. Identical meshes were used, one with a lower resolution of  $7 \times 7$  ( $N = 7$ ) nodes per elements and the other higher resolution simulation had  $9 \times 9$  ( $N = 9$ ) nodes per elements. A timestep of  $\Delta t = 0.007$  was used for the lower resolution and  $\Delta t = 0.004$  for the higher resolution. The results of base pressure predictions as shown in Table 2.6 below confirms that the lower resolution is sufficient to resolve the flow at this Reynolds number.

$N$	$\Delta t$	Mean $c_p$	Peak-to-trough
7	0.007	-0.439	0.135
9	0.004	-0.438	0.134

Table 2.6: The mean base pressure and peak-to-trough base pressure difference at two different resolutions for a elliptical leading-edge plate at  $Re = 500$ .

To ensure that this resolution was sufficient when applied forcing is introduced, the same geometry was simulated at a Reynolds number of  $Re = 500$  with a sinusoidal forcing in the cross-flow direction added to the free stream with an amplitude of  $v_{pert} = 2.5\%$ . A forcing frequency of  $St = 0.2025$  was used because it locks the flow and produce the strongest mean base suction within the range tested. Again the simulations were performed on an identical domain but at two resolutions. The lower resolution used  $7 \times 7$  ( $N = 7$ ) noded elements and the higher,  $9 \times 9$  ( $N = 9$ ) noded elements. The timestep for each simulation were  $\Delta t = 0.007$  and  $\Delta t = 0.004$  respectively. Table 2.7 show the predicted base pressure. Again, this indicates the lower resolution is sufficient to resolve the forced shedding case.

$N$	$\Delta t$	Mean $c_p$	Peak-to-trough
7	0.007	-0.592	0.305
10	0.004	-0.585	0.309

Table 2.7: The mean base pressure and peak-to-trough base pressure difference at two different resolutions for a elliptical leading-edge plate at  $Re = 500$  with a sinusoidal cross-flow.

A limited number of simulations were performed at a Reynolds number of  $Re = 700$ . At this particular Reynolds number, the same mesh was used but the resolution within each element was increased to  $8 \times 8$  ( $N = 8$ ) nodes and the timestep reduced

to  $\Delta t = 0.005$ . To verify that this resolution was adequate, a simulation with  $10 \times 10$  ( $N = 10$ ) nodes with a timestep of  $\Delta t = 0.003$  was performed. The results from Table 2.8 indicate that the lower resolution is adequate.

$N$	$\Delta t$	Mean $c_p$	Peak-to-trough
8	0.005	-0.582	0.288
10	0.003	-0.583	0.286

Table 2.8: The mean base pressure and peak-to-trough base pressure difference at two different resolutions for a elliptical leading-edge plate at  $Re = 700$ .

A similar experiment was performed on the rectangular leading-edge plate at  $Re = 400$ . The difference in this case was that a sinusoidal oscillation with an amplitude of  $v_{pert} = 2.5\%$  was applied to all free-stream boundaries. The simulations were carried out using  $7 \times 7$  ( $N = 7$ ) and  $9 \times 9$  ( $N = 9$ ) noded elements with a timestep of  $\Delta t = 0.007$  and  $\Delta t = 0.004$  respectively. The flow generates stronger vortices when forcing is applied therefore a resolution that sufficiently resolves this flow can resolve one without applied forcing. Figure 2.7 shows a plot of the mean base pressure coefficient for various forcing frequencies. The lower resolution appear to be able to resolve the flow.

Subsequent simulations with various geometries are performed using grids with a similar resolution near the plates and  $7 \times 7$  ( $N = 7$ ) noded elements. A timestep of  $\Delta t = 0.007$  is maintained for those simulations. This corresponds to between approximately 700 to 1200 timesteps in a typical shedding period. Tests have shown that increasing the resolution only changed the properties of the base pressure by less than 2%.

## 2.4 Post-processing

Once the simulations are performed in subsequent chapters, results are presented which analyse the results of the simulations. From the vorticity field, the movement of the vortex cores can be tracked and the circulation evaluated. The application of Howe’s acoustic model is also done as a post-processing step. The techniques used to implement these procedures are outlined in this section.

### 2.4.1 Vortex cores

The shed vortices can be tracked over some time interval to gain more insight into the flow. The convective velocity of these vortices can also be evaluated. The location of

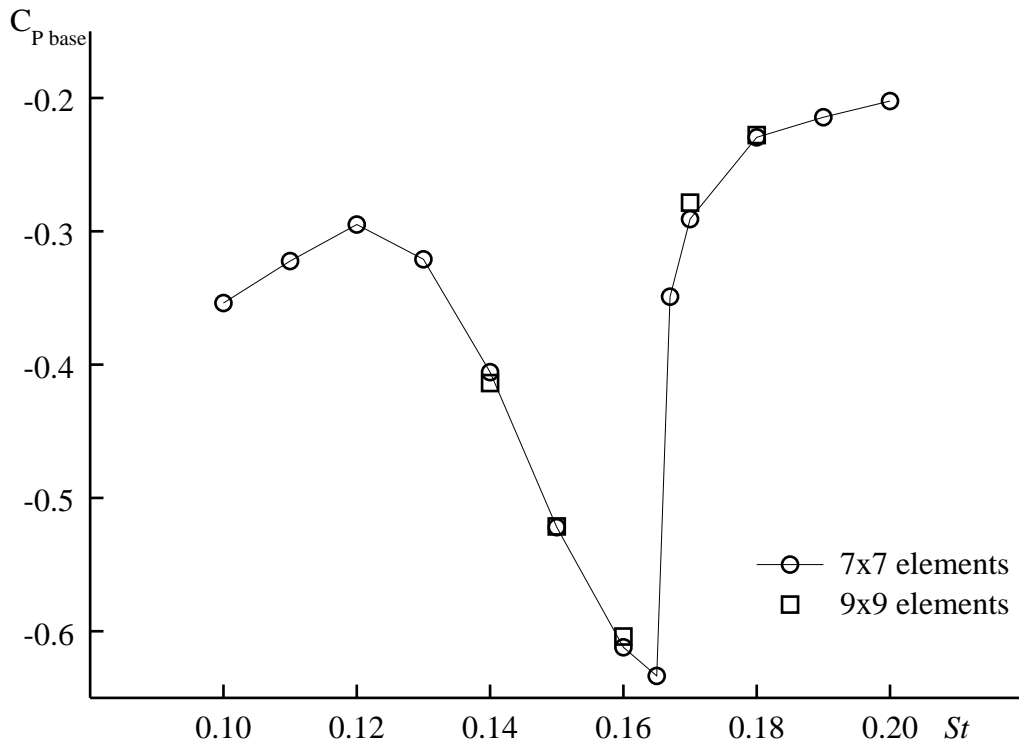


Figure 2.7: Mean base pressure measurements as a function of forcing frequency for flow around a plate with  $c/t = 10$  at  $Re = 400$  and  $v_{pert} = 2.5\%$ . These predictions are from two different spatial and temporal resolutions.

the local maximum or minimum in the vorticity field is used to define the location of the vortex core. This task is more difficult as this scheme is an Eulerian technique which solves the flow on a fixed grid. To locate the peak value of vorticity within a patch of vorticity, initially the local maximum value on a node is located. A two-dimensional Newton-Raphson method is used to refine that location. The same interpolants used within each spectral-element to solve the flow variables are used when interpolating. The stopping criteria for the Newton-Raphson iterations are when the change in location is less than 0.001% of the plate thickness. This process is may be repeated at regular time intervals to obtain the trajectories of the vortex cores.

### 2.4.2 Circulation

The point of this exercise is to evaluate the amount of circulation contained in a shed vortex. To calculate the amount of circulation within a two-dimensional region, either an area integral or a line integral around the region can be used. In this instance, the circulation is calculated using the line integral given by,

$$\Gamma = \oint \mathbf{u} \cdot d\vec{s}. \quad (2.15)$$

To perform this line integral, the closed path of integration around a region containing vorticity has to be located. A small value of vorticity is chosen as the cut off value with the aim of capturing as much of the circulation of a particular vortex while avoiding other flow structures. The flow field velocity is then found at regular intervals of  $0.04t$  along this iso-contour. The interpolation is done using the same polynomials as the spectral element scheme. The tangent vector to the iso-contour is found using a cubic spline between the neighbouring nodes. The integral is evaluated using a first-order method. Again all interpolation is done using the spectral-element interpolants.

### 2.4.3 Howe's acoustic model

Howe's theory (1975, 1980) has been developed to calculate the sound power generated by the flow in the presence of an external sound field. This can be used to predict the acoustic resonance when a plate is placed in a duct. The length and time scales of the flow and sound field are several orders of magnitude apart when the Mach number is low. This model is used instead of simulating the fully compressible flow because of the high computational cost involved due to the small timestep required to capture the compressible behaviour.

In this case the sound is generated by the vortical flow around the plate. This

feeds into the sound field in the duct and may generate an acoustic resonance. The resonance will then lock the flow to that frequency. This model is used to determine the amount of power transferred between the flow field and the acoustic field. A positive transfer is a necessary condition for duct resonance to occur. This is not a sufficient condition because it neglects damping in the duct and receptivity of the flow. An applied forcing is used to lock the flow in the simulations.

The remainder of this section describes how the model is implemented. This model has been formulated assuming the flow is rotational, inviscid and isentropic. From the acoustic model, the acoustic power in a region of the flow is given by the volume integral,

$$P = -\rho_0 \int \vec{\omega} \cdot (\mathbf{u} \times \mathbf{v}) dV. \quad (2.16)$$

The volume integral reduces to an area integral in two dimensions. The vorticity,  $\vec{\omega}$ , and velocity,  $\mathbf{u}$ , are properties of the flow field,  $\rho_0$  is the mean fluid density and  $\mathbf{v}$  is the acoustic particle velocity.

The acoustic velocity field for the first  $\beta$ -mode (described in the previous chapter) in a duct is approximately a standing wave with nodes at the top and bottom walls of the duct, anti-nodes along the centreline and decaying away from the plate in the streamwise directions. This leads to the velocity potential of the acoustic particle velocity,  $\Phi$ , satisfying the wave equation. This is expressed as,

$$\frac{D^2\Phi}{Dt^2} = c_s^2 \nabla^2 \Phi, \quad (2.17)$$

where  $c_s$  is the speed of sound. This has also been used previously by Stoneman *et al.* (1988) to model the acoustic particle velocity.

The wave equation is solved by assuming the solution can be separated into a function only dependent on time and another on space such that

$$\Phi(x, y, z, t) = \Phi_t(t) \Phi_s(x, y, z). \quad (2.18)$$

Neglecting the convective terms, using this assumption the wave equation reduces to the following equation for the temporal variation,

$$\frac{d^2\Phi_t}{dt^2} + (2\pi f)^2 \Phi_t = 0, \quad (2.19)$$

together with the equation for the spatial variation,

$$\nabla^2 \Phi_s + \left( \frac{2\pi f}{c_s} \right)^2 \Phi_s = 0. \quad (2.20)$$

Solving for the time dependence gives

$$\Phi_t = A_o \sin(2\pi f t + \phi), \quad (2.21)$$

with the resonant frequency,  $f$ , and phase of oscillations,  $\phi$  matching that of the applied forcing (i.e.  $\phi = 0$ ) used to lock the flow. The amplitude of the oscillations,  $A_o$ , is set to unity leaving the only arbitrary scaling factor to be in the spatial part. Solving the spatial part basically results in the amplitude (as a function of space) of the acoustic particle velocity in the duct. The spatial part results in an eigenvalue problem which is solved on the same grid as the flow by modifying the spectral-element scheme. The boundary condition for the spatial part of the wave equation are zero normal gradients for all boundaries including the duct centreline except for the plate surface where  $\Phi_t = 0$ . This will result in a solution that is mirrored across the centre line and decays away from the plate. Note that this solution can be arbitrarily scaled. For uniformity between aspect ratios, the amplitude of the acoustic particle velocity is set to one unit at the centre of the leading or trailing edge of the plate (the value at these two points are equal because of symmetry).

As some of the earlier studies (Welsh *et al.*, 1984, Stokes *et al.*, 1988) used a sinusoidally varying potential flow to model the acoustic particle velocity, this has also been done for comparison. Firstly, the potential flow around a circular cylinder is found. Then the space around the cylinder is transformed to the space around a rectangular plate using the Schwarz-Christoffel transformation (Churchill *et al.*, 1974). Finally the velocity field around the circular cylinder is also transformed to that around a rectangular plate.

A positive time-average acoustic power transfer from the flow to the acoustic field is necessary to sustain the resonance. Selecting the size of the integration domain is complicated by the vortices convecting downstream and the finite domain size. The method used for time averaging and overcoming the finite domain size is addressed when the model is applied in the Chapter 4.

# Contents

<b>2</b>	<b>Numerical Techniques</b>	<b>37</b>
2.1	Numerical scheme . . . . .	38
2.1.1	Spatial scheme . . . . .	38
2.1.2	Temporal scheme . . . . .	41
2.1.3	Boundary conditions . . . . .	42
2.1.4	Stopping criteria for temporal evolution . . . . .	42
2.2	Validation . . . . .	43
2.2.1	Backward-facing step flow . . . . .	43
2.2.2	Driven cavity . . . . .	45
2.3	Flow around long plates . . . . .	55
2.3.1	Computational domain and boundary conditions . . . . .	57
2.3.2	Domain size . . . . .	58
2.3.3	Spatial and temporal resolution . . . . .	60
2.4	Post-processing . . . . .	62
2.4.1	Vortex cores . . . . .	62
2.4.2	Circulation . . . . .	64
2.4.3	Howe’s acoustic model . . . . .	64

# Chapter 3

## Flow Past a Plate with an Elliptical Leading Edge

The elliptical leading-edge plate is studied as a precursor to the rectangular plate. The majority of the simulations in this chapter are performed with the leading edge in the form of an ellipse with a 5:1 axes ratio. As the nose shape is aerodynamic, the flow does not separate from the leading edge. This is unlike the rectangular plate and the overall complexity of the flow is reduced. A boundary layer develops on the plate as the fluid convects and separates at the sharp trailing edge to form vortex structures in the wake. This leads to a periodic shedding from alternate edges, typical of bluff bodies above a critical Reynolds number.

In this chapter, the flow over an elliptical leading-edge plate is analysed; in particular two-dimensional natural and forced shedding. Initially, the flow without external forcing is simulated at different Reynolds numbers and the variation in shedding frequency analysed. The predicted base pressure is one measure used to gauge the response of the system to low amplitude forcing. Further analysis of the flow field to find the phase of the shedding relative to the forcing, vortex formation length, and trajectory of the vortices and circulation contained within them, enables the forces on the plate to be correlated with the properties of the wake.

### 3.1 Natural shedding

Simulations are performed for the elliptical leading-edge plate with an aspect ratio of  $c/t = 7.5$  at Reynolds numbers between  $Re = 200$  and  $700$ . A snap shot of the flow at a Reynolds number of  $Re = 500$  is presented in the vorticity plot in Figure 3.1. In this

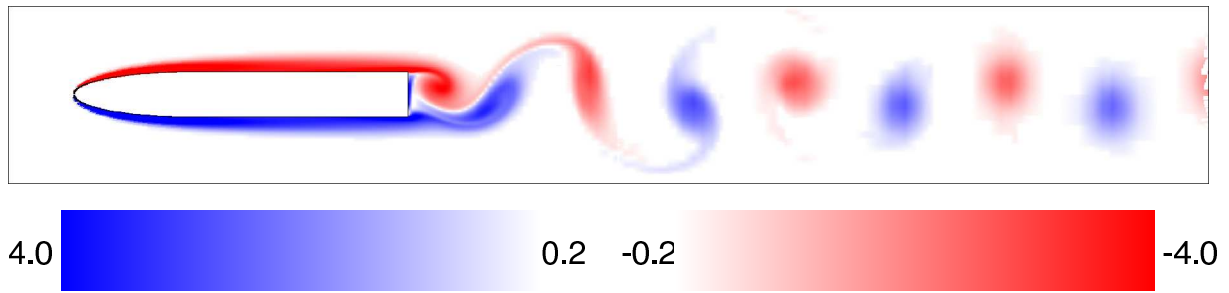


Figure 3.1: A vorticity plot of the flow over an elliptical leading-edge plate at  $Re = 500$ . Note: The vorticity key is also applicable to subsequent vorticity plots. Levels between the blue and red range are not coloured and levels outside the range (i.e. larger magnitude) are coloured with the maximum intensity.

section, the shedding frequency at various Reynolds numbers will be compared to those predicted by the correlation of Eisenlohr & Eckelmann (1988).

The base pressure coefficient measurements shown in Figure 3.2(a) were taken at the centre of the trailing face. They show the flow reaches a periodic state in the Reynolds number range simulated. This signal is used to determine the shedding frequency. As expected, these signals show the mean, amplitude and frequency increasing with Reynolds number. The signals show a frequency twice that of the shedding frequency because they are taken at the centre of the trailing face. The correlation between the (modified) Reynolds number and shedding frequency determined by Eisenlohr & Eckelmann (1988), as described in Section 1.2.2, uses a modified length scale to incorporate the momentum thickness at the trailing edge. Figure 3.2(b) shows the displacement thickness as a function of Reynolds number. The displacement thickness is determined from the boundary layer profile at the trailing edge. Also plotted is the inverse of the displacement thickness as a function of Reynolds number. Consistent with boundary layer theory, the displacement thickness is (approximately) inversely proportional to Reynolds number. The small deviation from this relationship is likely caused by the leading-edge geometry which is not considered by the theory (i.e. the development of the boundary layer as the flow goes around the nose may cause some deviation).

The next step is to compare the shedding frequency variation with Reynolds number with the experimental observations. The experiments of Eisenlohr & Eckelmann (1988) found a correlation between the shedding frequency and the Reynolds number if a modified length scale is used in determining the Reynolds number. This length scale,  $t'$ , is the thickness of the plate plus twice the momentum thickness at the trailing edge. Figure 3.3 is a plot of the shedding frequency,  $F_{\nu}$ , as a function of Reynolds number,  $Re_{\nu}$ , with both parameters scaled with the modified length scale. The correlation from

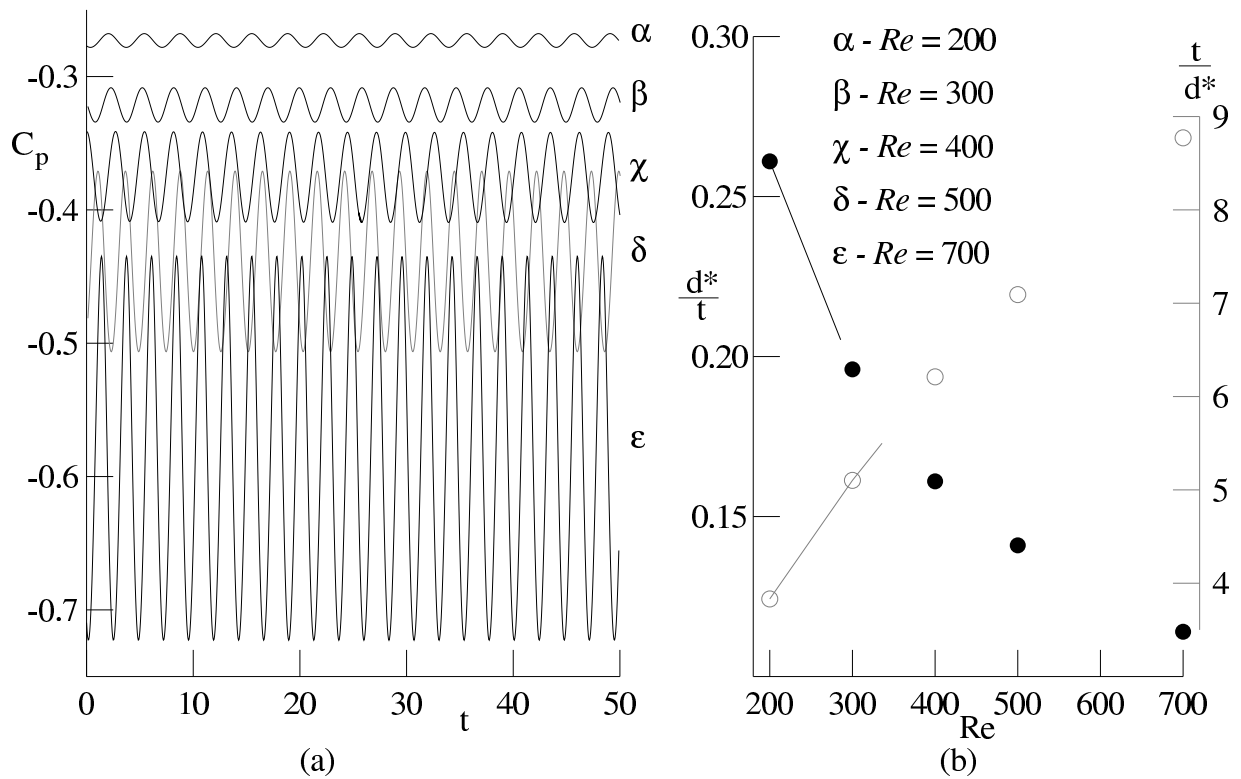


Figure 3.2: (a) A sample trace of 50 time units of the base pressure coefficient taken after a periodic state has been reached and, (b) the displacement thickness and reciprocal (in gray) at various Reynolds numbers for a 5:1 elliptical leading-edge plate with  $c/t = 7.5$ . The base pressure coefficient at  $Re = 500$  is in gray for clarity because of the overlap.

experimental data found by Eisenlohr & Eckelmann (1988) is also plotted for comparison. There is a spread of about  $St_{\nu} = 0.04$  in the experimental data which is represented by the gray region.

The experimental data collapses to a linear relationship between the modified frequency,  $F_{\nu}$ , and Reynolds number,  $Re_{\nu}$ . The predictions also show approximately a linear relationship between these two parameters. The gradient of the predicted variation is also close to that of the experimental correlation. Although most of the predicted data falls within the range of experimental error associated with the experiments, there appears to be a shift which is approximately 20 units of  $F_{\nu}$ . There are some notable differences between the experiments and the numerical predictions that cause this difference. In particular, the experimental correlation was determined for much longer plates ( $50 \leq c/t \leq 800$ ). This probably means that the boundary layer profile at the trailing edge has become self similar. For the short plate used in the simulation ( $c/t = 7.5$ ), the effect of the elliptical leading edge is probably still influencing the boundary layer at the trailing edge. In addition, the lower limit of the Reynolds number range for the experiments was  $Re = 300$  (and the upper limit at  $Re = 15,000$ ). Thus the experimental correlation is likely to be less reliable at the Reynolds numbers used for the simulations. It is also possible that boundary layer three-dimensionality is influencing the experimental results at the higher Reynolds number end of the range studied.

## 3.2 The effect of applied cross-stream forcing

This section will present the results of simulations of flow past elliptical leading-edge plates under the influence of external oscillatory cross-flow forcing. In particular, the mean base pressure coefficient is recorded as a function of forcing frequency, Reynolds number, forcing amplitude and plate geometry. These results are compared with data from wind tunnel experiments by Mills (1998). The time trace of base pressure coefficient is used to ascertain the range of forcing frequencies over which lock-in occurs. In addition, outside this range, the trace of base pressure coefficient is used to determine if the flow behaves in a quasi-periodic manner or sheds at approximately its natural shedding frequency. Comparisons of the flow characteristics between the natural shedding cases and the lock-in range of the forced shedding cases are presented in the next section and these are related to the base pressure and forces experienced by the plates.

A snapshot of the vorticity distribution when the flow is in the lock-in state is shown in Figure 3.4. This simulation is performed at  $Re = 500$ , and the forcing is at  $St = 0.2025$  and  $v_{pert} = 2.5\%$ . This particular snapshot is taken at  $270^\circ$  in the sinusoidal

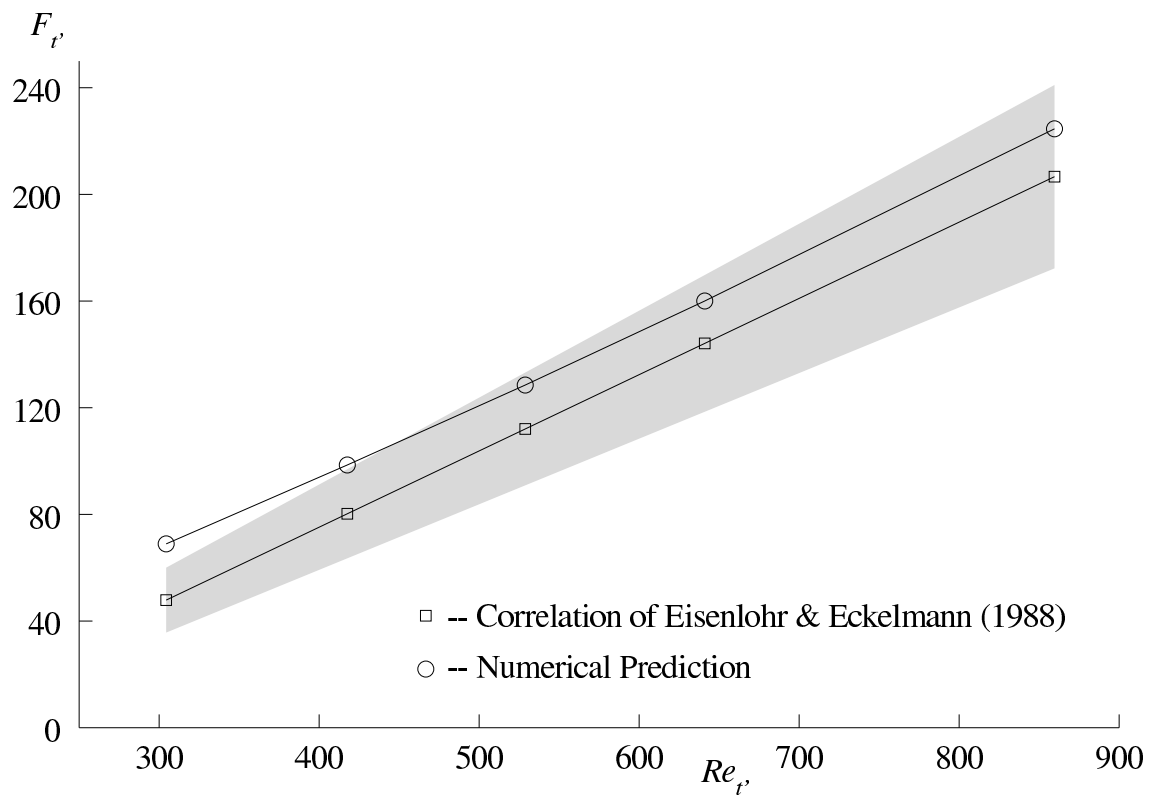


Figure 3.3: A plot of the non-dimensional shedding frequency,  $F_{\nu'}$ , as a function of the Reynolds number  $Re_{\nu'}$  for the flow around an elliptical leading-edge plate with  $c/t = 7.5$ . The correlation obtained from experiments by Eisenlohr & Eckelmann (1988) is plotted for comparison. The gray region is indicative of the spread in the experimental data.

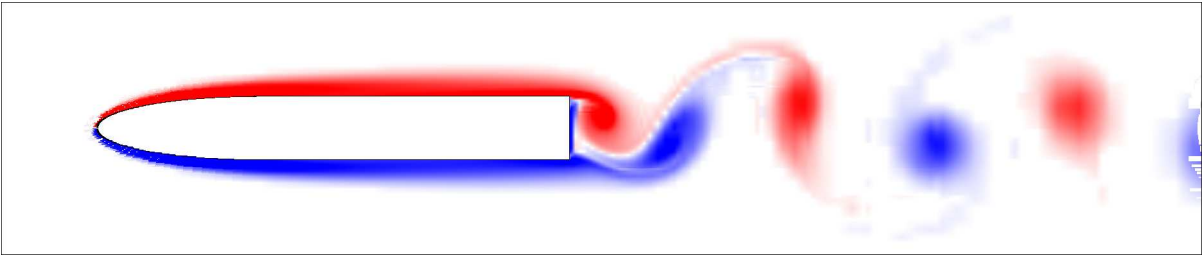


Figure 3.4: A vorticity plot of the flow around an elliptical leading-edge plate at  $Re = 500$  with forcing at  $St = 0.2025$  and  $v_{pert} = 2.5\%$ , taken  $270^\circ$  in the forcing cycle.

forcing cycle. Compared with the natural shedding case shown in Figure 3.1, the shed vortices are more compact and the formation length reduced.

### 3.2.1 Mean base pressure

Simulations are performed over a range of forcing frequencies. The effects of various parameters namely Reynolds numbers, forcing amplitudes, plate aspect ratio and leading-edge geometries are investigated. The range of forcing frequency is chosen to span the vicinity surrounding the natural shedding frequency. The base pressure coefficient is used to monitor the flow as it is strongly related to the overall drag and provides a good indication of the flow state because it is taken at a location where the trailing-edge flow structures develop. The length of the pressure trace required to determine the mean depends on the system parameters. When the flow is periodic, averaging over several periods is sufficient to accurately determine the mean (although one simple period is adequate). If the signal is quasi-periodic or displays some randomness, a much longer trace is required. In the quasi-periodic state, the signal typically has a repeatable cycle which can be up to 20 shedding cycles. In this case the sampling is taken over a few of these longer or near repeatable cycles.

#### 3.2.1.1 The effect of Reynolds number

The flow over the elliptical leading-edge plate with a 5:1 axes ratio and  $c/t = 7.5$  is subjected to a sinusoidal cross-flow forcing with  $v_{pert} = 2.5\%$ . The simulations were performed at Reynolds numbers of  $Re = 300, 500$  and  $700$ . Plots of the mean base pressure coefficient for these flows at various forcing frequencies are shown in Figure 3.5. When the forcing frequency is significantly below or above the natural shedding frequency, the mean base pressure coefficient approaches that of the natural shedding. When the

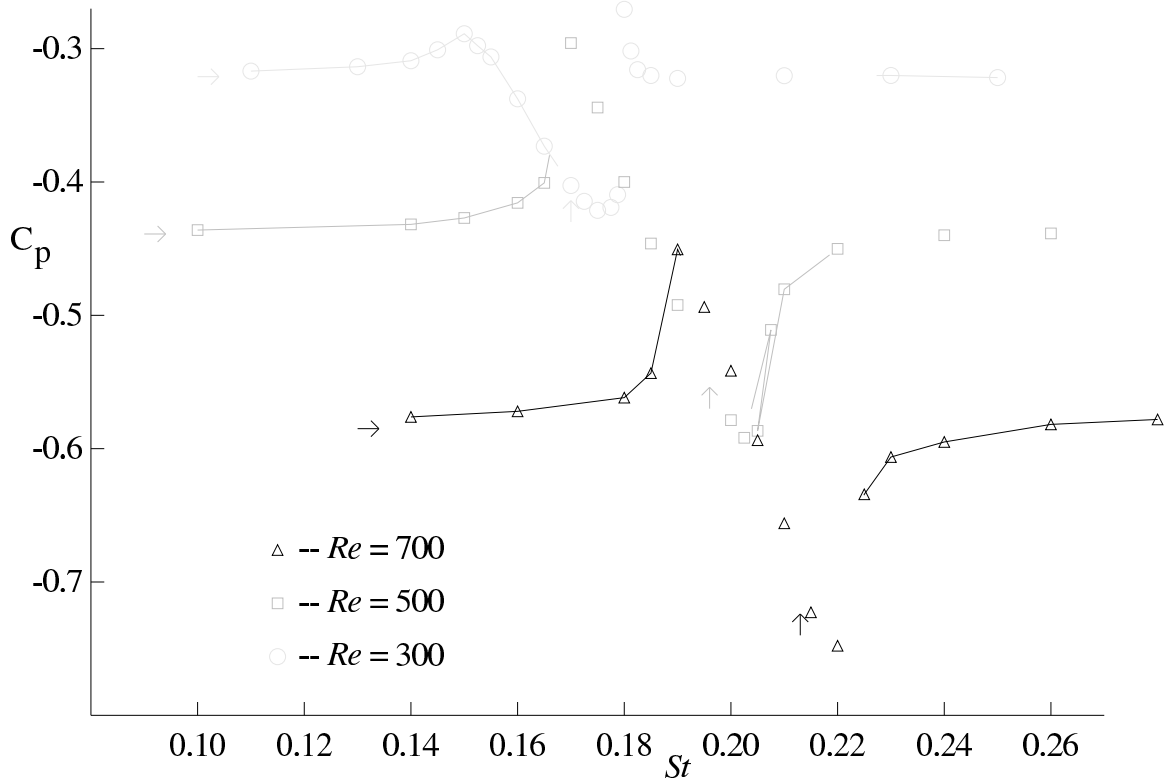


Figure 3.5: The mean base pressure coefficient for the flow over a 5:1 elliptical leading-edge plate as a function of forcing frequency at various Reynolds numbers. The amplitude of the applied perturbation is  $v_{pert} = 2.5\%$ . The vertical arrows represent the natural shedding frequency and the horizontal arrows show the mean base pressure coefficient in the absence of forcing.

forcing frequency approaches the natural shedding frequency from below, there is an initial rise in the mean base pressure coefficient (reduction in base suction). This is more significant at the higher Reynolds numbers of  $Re = 500$  and  $700$  than at  $Re = 300$ . As the forcing frequency is increased still further, there is an increase in base suction which peaks at a forcing frequency slightly above the natural shedding frequency. After it peaks, the mean base pressure coefficient approaches that of the unforced case. This is not so for the low Reynolds number case of  $Re = 300$  which rises in a small interval after the mean base suction peaks. As will be shown in the next section, the steep rise in mean base pressure at this Reynolds number of  $Re = 300$  is associated with a drastic change in the relative phase between the forcing and the shedding. Also different at the lower Reynolds number is that the system is responsive to a smaller range of forcing frequencies, i.e., the mean base pressure coefficient is altered by the forcing in a smaller frequency band.

### 3.2.1.2 The effects of forcing amplitude

The same plate is then subjected to different amplitudes of forcing. The simulations were performed at a Reynolds number of  $Re = 500$  with two additional forcing amplitudes, namely  $v_{pert} = 1.0\%$  and  $5.0\%$ . The mean base pressure coefficients for these simulations are presented in Figure 3.6. The system appears to be very sensitive to the amplitude of the applied forcing even when the level of forcing is small relative to the free-stream velocity. As before, at forcing frequencies significantly away from the natural shedding frequency, the mean base pressure approaches that of the natural shedding case. As the forcing frequency is increased, there is a rise in the mean base pressure coefficient (drop in base suction). This occurs at lower forcing frequencies for larger perturbation amplitudes. The level of increase in base pressure appears to have saturated when the forcing amplitude is  $v_{pert} = 2.5\%$ , as the case with  $v_{pert} = 5.0\%$  shows a similar pressure rise. The forcing frequency at which the mean base suction peaks occurs above the natural shedding frequency for all the cases studied. The forcing frequency at which it peaks approaches the natural shedding frequency as the amplitude of perturbation is reduced. This is expected because when the forcing amplitude approaches zero, the flow would shed at its natural shedding frequency. Both the level of the peak in mean base suction and the frequency range where the flow is receptive to the forcing increases with amplitude. The increase in receptivity is shown by the larger frequency range where applied forcing has an influence on the mean base pressure coefficient and the larger lock-in range which will be shown in a later section (Section 3.2.3.1). The level of the peak in mean base suction increases with forcing amplitude and the overall forcing frequency range where the system is receptive to the applied forcing increases with the amplitude of the perturbation. This is consistent with results for typical short bluff bodies. As with all cases, when the forcing frequency is further increased, the mean base pressure approaches that of the natural shedding frequency.

### 3.2.1.3 The effects of aspect ratio

Next, the plates with identical leading-edge geometries but with different aspect ratios are studied. The Reynolds number of the flow is  $Re = 300$  and the forcing amplitude is  $v_{pert} = 2.5\%$ . In addition to the plate used previously (aspect ratio  $c/t = 7.5$ ), one shorter and one longer plate with aspect ratios of  $c/t = 3.5$  and  $c/t = 12.5$  respectively are examined. Figure 3.7 shows the mean base pressure coefficient as a function of forcing frequency. As in previous cases, the mean base pressure coefficient approaches that of the unforced case far away from the natural shedding frequency and the mean base suction peaks at a forcing frequency higher than the natural shedding frequency. For the longer plate, as the forcing

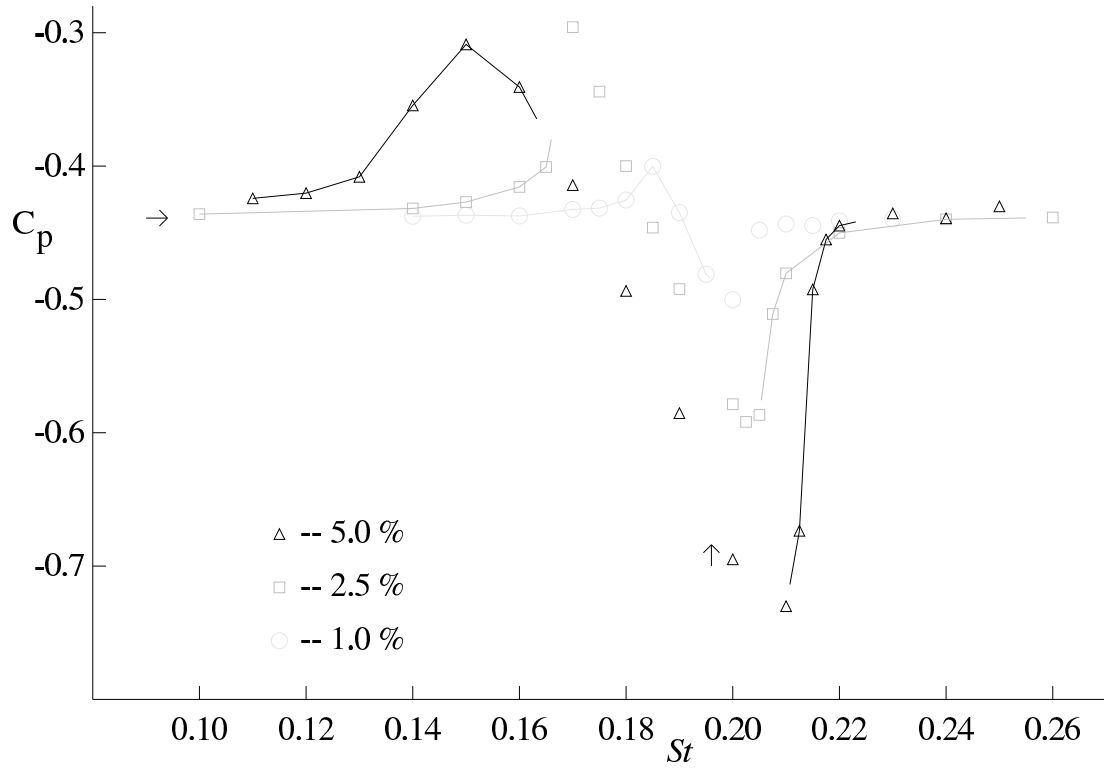


Figure 3.6: The mean base pressure coefficient for the flow over an elliptical leading-edge plate as a function of forcing frequency at  $Re = 500$  and at various perturbation amplitudes. The amplitude of the applied perturbation is relative to the free-stream velocity. The vertical arrow represent the natural shedding frequency and the horizontal arrow shows the mean base pressure coefficient in the absence of forcing.

frequency is increased toward the natural shedding frequency, there is a less significant rise in the mean base pressure coefficient (drop in mean base suction). As the forcing frequency is increased past the value at which the mean base suction peaks, there is a sharp rise in mean base pressure coefficient for plates with aspect ratios of  $c/t = 7.5$  and  $12.5$ . This will be shown in a later section (Section 3.3.1) to be associated with a dramatic phase shift. The longer plate with  $c/t = 12.5$  shows a larger frequency range where the mean base pressure coefficient is above the natural shedding value. However the magnitude of this rise for plates with aspect ratios  $c/t = 7.5$  and  $c/t = 12.5$  is approximately the same. The behaviour of the shorter plate is contrary to that for longer plates. There is a significant rise in mean base pressure coefficient (drop in mean base suction) as the forcing frequency is increased towards the natural shedding frequency (before the base suction increase). As the forcing frequency is increased past the forcing frequency which results in the peak of mean base suction, the mean base pressure coefficient gradually approaches that of the natural shedding case. The magnitude of the peak in mean base suction relative to the mean base suction in the natural shedding case is approximately the same for all three plate lengths. Comparing these results with the those in Figure 3.4 (where the Reynolds number is varied), reducing the aspect ratio of the plate or increasing the Reynolds number (or vice-versa) produces a similar behaviour. This can be expected because as the boundary layer grows along the plate, a longer plate will have a thicker boundary layer and a shorter plate a thinner boundary layer. For a plate with a fixed aspect ratio, increasing (or decreasing) the Reynolds number will result in a thinner (or thicker) boundary layer. As this boundary layer has a significant influence on the trailing-edge shedding, increasing the plate length or lowering the Reynolds number should have the same effect.

#### 3.2.1.4 Effect of nose geometry

Simulations are performed with a rounded leading edge to investigate the effects of the leading-edge geometry. This geometry does not lead to vortex shedding from the leading edge at the Reynolds numbers simulated. Plates with two different lengths were investigated, namely with aspect ratios of  $c/t = 3.5$  and  $c/t = 7.5$ . The perturbation amplitude was fixed at  $v_{pert} = 2.5\%$ . Figure 3.8 shows the mean base pressure coefficient over a range of forcing frequencies at Reynolds numbers of  $Re = 300$  and  $500$ . Simulations for the shorter plate were not performed at the higher Reynolds number of  $Re = 500$ . Comparing these results with Figure 3.5 and Figure 3.7, the response to the applied forcing is similar to the elliptical leading-edge plate at the corresponding Reynolds number and aspect ratio. The rounded leading edge being less aerodynamic than the elliptical leading edge results in the development of a thicker boundary layer. This results in a lower mean

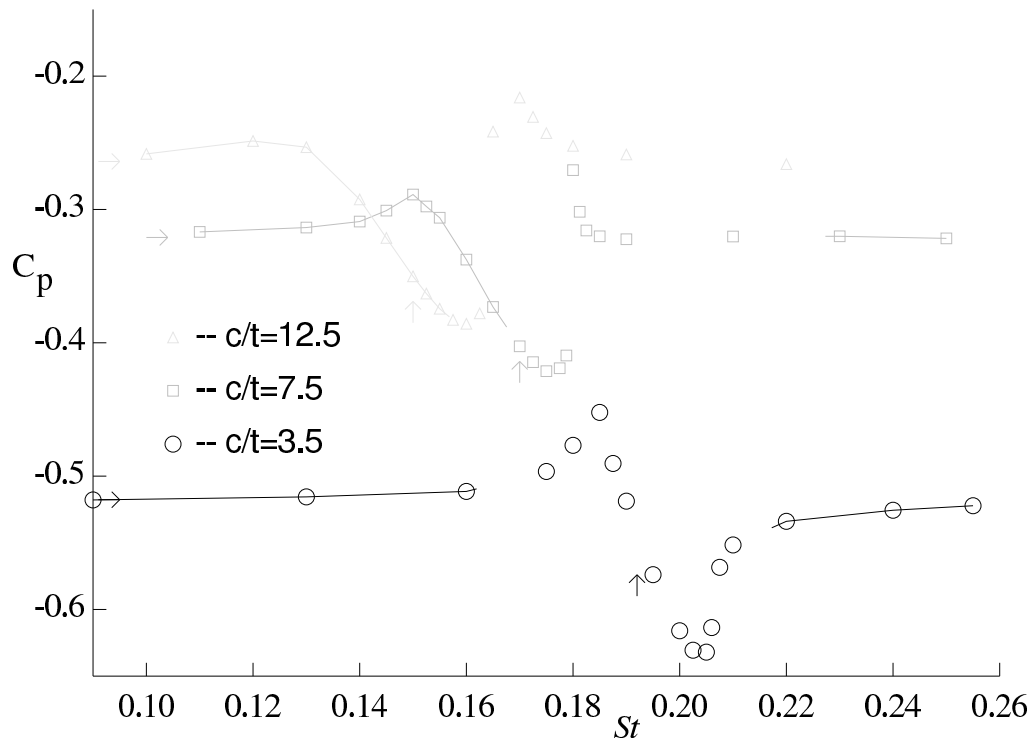


Figure 3.7: The mean base pressure coefficient for the flow over an elliptical leading-edge plate for various aspect ratios as a function of forcing frequency. The flow is at  $Re = 300$  and the amplitude of the forcing is  $v_{pert} = 2.5\%$ . The vertical arrows represent the natural shedding frequency and the horizontal arrows show the mean base pressure coefficient in the absence of forcing.

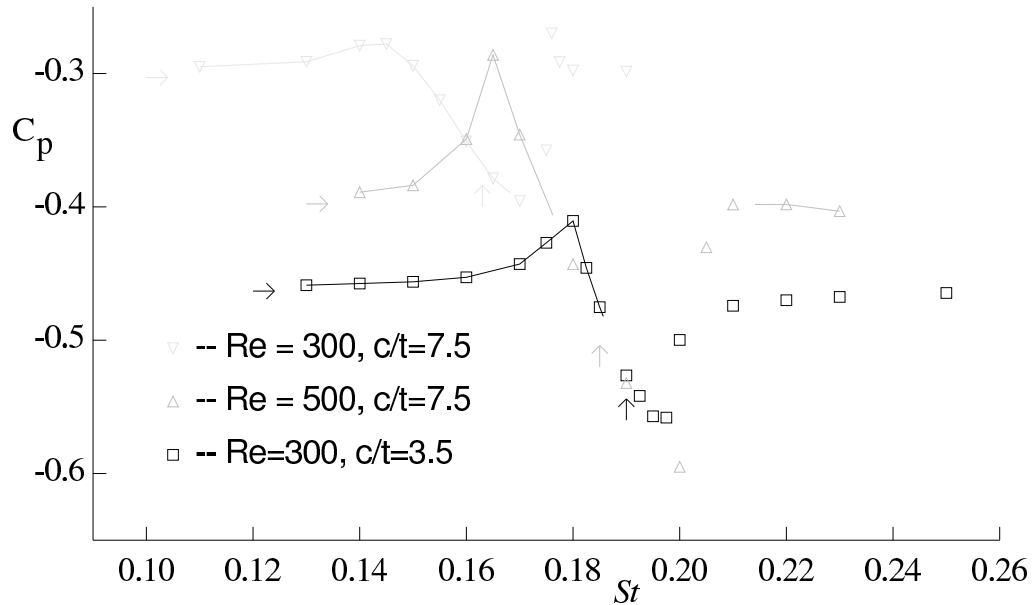


Figure 3.8: The mean base pressure coefficient for rounded leading-edge plates as a function of forcing frequency. The cases simulated are with  $c/t = 7.5$  at  $Re = 300$  and  $Re = 500$ , and  $c/t = 3.5$  at  $Re = 300$ . The amplitude of the applied perturbation is  $v_{pert} = 2.5\%$ . The vertical arrows represents the natural shedding frequency and the horizontal arrows show the mean base pressure coefficient in the absence of forcing.

base pressure and shedding frequency in the unforced case. When forcing is applied, the behaviour of the mean base pressure coefficient reflects this change. The leading-edge geometry has only a small overall influence on the system when no leading-edge vortices are shed. The effects of varying the aspect ratio and Reynolds number are similar to those for the previous leading-edge geometry.

### 3.2.2 Comparison of mean base pressure with experiments

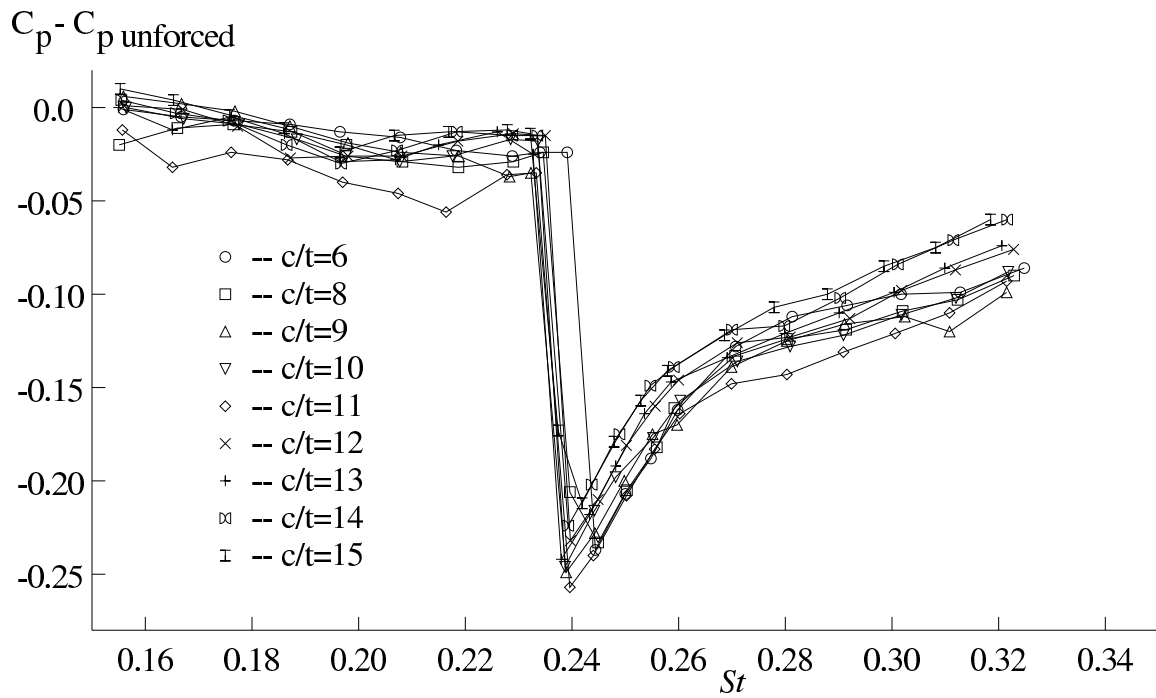
Many previous studies as discussed in Chapter 1 (Stansby, 1976, Bearman & Davies, 1977, Blackburn & Henderson, 1996) have shown that short bluff bodies experience a drop in the mean base pressure when the forcing frequency is near the natural shedding frequency. The simulations of flow over long plates with aerodynamic nose shapes also show this phenomenon. A comparison with experimental data obtained from flow over more closely related geometries is discussed in this section.

Experimental measurements of mean base pressure coefficient for the flow over a similar geometry are presented in Mills (1998). These experiments were performed at a Reynolds number of approximately  $Re \approx 9,000$  using a plate with a C4 aerofoil

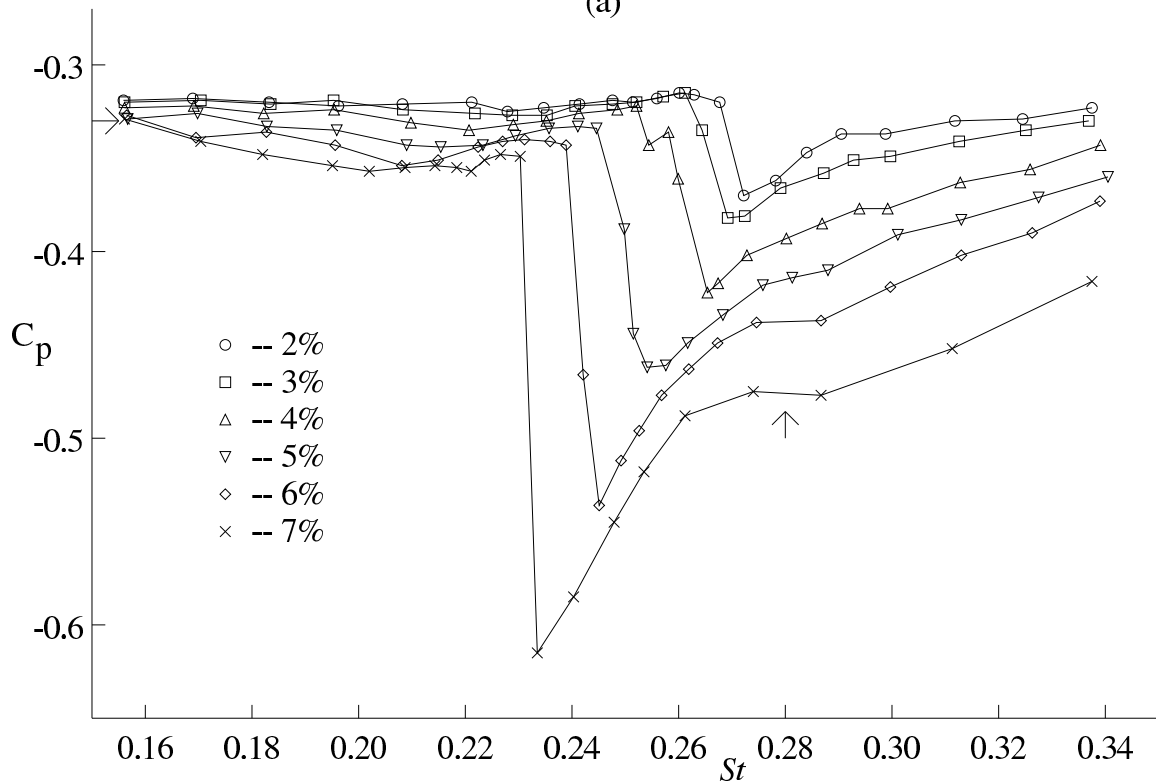
leading-edge profile. The forcing was applied using speakers connected in anti-phase mounted above and below the plate. The forcing amplitude was measured at a point  $0.077t$  vertically away from the corner of the trailing edge in the absence of any free-stream flow. As the perturbation velocity field accelerates around the plate, the perturbation level in the simulations is equivalent to a much higher value if measured at the same location as for the experiments. The next chapter will compare the level of the amplitude used in the simulations and that measured in the experiments and show that they are both small and at approximately the same level.

The mean base pressure for plates with aspect ratios ranging from  $c/t = 6$  to  $c/t = 15$  are presented in Figure 3.9(a). The amplitude of the perturbation was  $v_{pert} = 5.0\%$ . The mean base pressure of the natural shedding case has been subtracted although the variation between the shortest to the longest plate is small (approximately 0.08). These results show that the response to forcing is similar for all plates. At forcing frequencies much lower than the natural shedding frequency, the mean base pressure coefficient approaches that of the natural shedding case. As the forcing frequency is increased towards the natural shedding frequency, there is a small rise in the mean base pressure (drop in base suction) coefficient before a sudden drop. The peak in mean base suction occurs at a forcing frequency below the natural shedding frequency. As the forcing frequency is increased further, there is a gradual recovery in the mean base pressure coefficient. Figure 3.9(b) shows the effect of varying the amplitude of the perturbation for a plate with an aspect ratio of  $c/t = 10$ . The same trends as described earlier for the various aspect ratios also apply for these cases. The forcing frequency where the drastic drop in mean base suction occurs reduces and the magnitude of the mean base suction increases with increasing perturbation amplitude. The flow is receptive over a larger frequency range when a larger perturbation amplitude is applied. As with the simulations, by extrapolating the forcing frequency at which the peak mean base suction occurs to a very small forcing amplitude, it is found that this forcing frequency approaches the natural shedding frequency.

Comparing the simulations and the experimental results, there are several similar but some contradicting trends. The experiments are performed at a much higher Reynolds number where the natural shedding frequency is significantly higher and the effects of varying the aspect ratio on the mean base pressure relative to the respective unforced case is small. As with the simulations, when the forcing frequency is much lower than the natural shedding frequency, the forcing only has a small influence on the mean base pressure. As the forcing frequency increases towards the natural shedding frequency, there is a small rise of the mean base pressure coefficient in the experimental case which is similar to simulations at a lower Reynolds number or with longer plates (but much less). At higher Reynolds numbers and shorter plates, the rise in mean base pressure (drop in base suction)



(a)



(b)

Figure 3.9: Results of mean base pressure measurements of aerofoil leading-edge plates from Mills (1998). (a) Mean base pressure coefficient relative to the unforced case as a function of forcing frequency for various aspect ratios and  $v_{pert} = 5.0\%$ . (b) Mean base pressure coefficient as a function of the forcing frequency for a plate with  $c/t = 10$  at various forcing amplitudes relative to the free-stream velocity. The vertical and horizontal arrows represent the natural shedding frequency and the unforced mean base pressure respectively.

is significantly higher. As the forcing frequency is increased, the experimental data shows a sharp increase in mean base suction and the peak base suction occurs at a lower forcing frequency than the natural shedding frequency. In the discussion, Mills (1988) is unsure whether this is caused by the drastic phase change in the shedding relative to the forcing or the onset of the flow locking to the forcing. While in the simulations, there is a gradual increase in mean base suction with the peak mean base suction occurring at a higher frequency than the natural shedding frequency. As the forcing frequency is increased further, there is a gradual recovery in the mean base pressure coefficient. The simulations show the recovery in mean base pressure occurring over a smaller frequency range. Also the simulations at lower Reynolds number (or for longer plates) show a sudden rise in mean base pressure coefficient (drop in base suction) and a frequency range where the mean base pressure coefficient is above that of the natural shedding case. As the forcing amplitude is increased, both the simulations and the experiments show a larger response to the forcing. In the experiments, the forcing frequency at which the peak mean base suction occurs decreases with perturbation amplitude while the opposite occurs in the simulations.

### 3.2.3 Base pressure trace

The time trace of the base pressure coefficient has been used as an indicator of the temporal behaviour of the flow. The two cases studied are flow around plates with  $c/t = 7.5$  and  $12.5$  at  $Re = 500$  and  $300$  respectively. In both cases, the nose geometry is an ellipse with a 5:1 axes ratio and the forcing amplitude is  $v_{pert} = 2.5\%$ . From the behaviour of the mean base pressure, the first case is typical of simulations at higher Reynolds number (or for shorter plates) while the second is more characteristic of simulations at lower Reynolds number (or for longer plates). These traces were taken at the centre of the trailing face and so the frequency is double that of the shedding frequency.

The first case considered is the flow at a Reynolds number of  $Re = 500$  around a plate with an aspect ratio of  $c/t = 7.5$ . Samples of the base pressure coefficient trace at various forcing frequencies are shown in Figure 3.10. The corresponding mean base pressure is presented in Figure 3.5. At the low forcing frequencies of  $St = 0.14$  and  $St = 0.16$ , the mean base pressure coefficient is not significantly different from the natural shedding case. The time traces show that the flow is not locked to the forcing and there are two dominant frequencies.

To study this phenomenon more closely, consider the case for a forcing frequency of  $St = 0.16$ . A spectral plot of the base pressure coefficient trace is shown in Figure 3.11. The spectrum is obtained by sampling every 0.175 non-dimensional time units with a

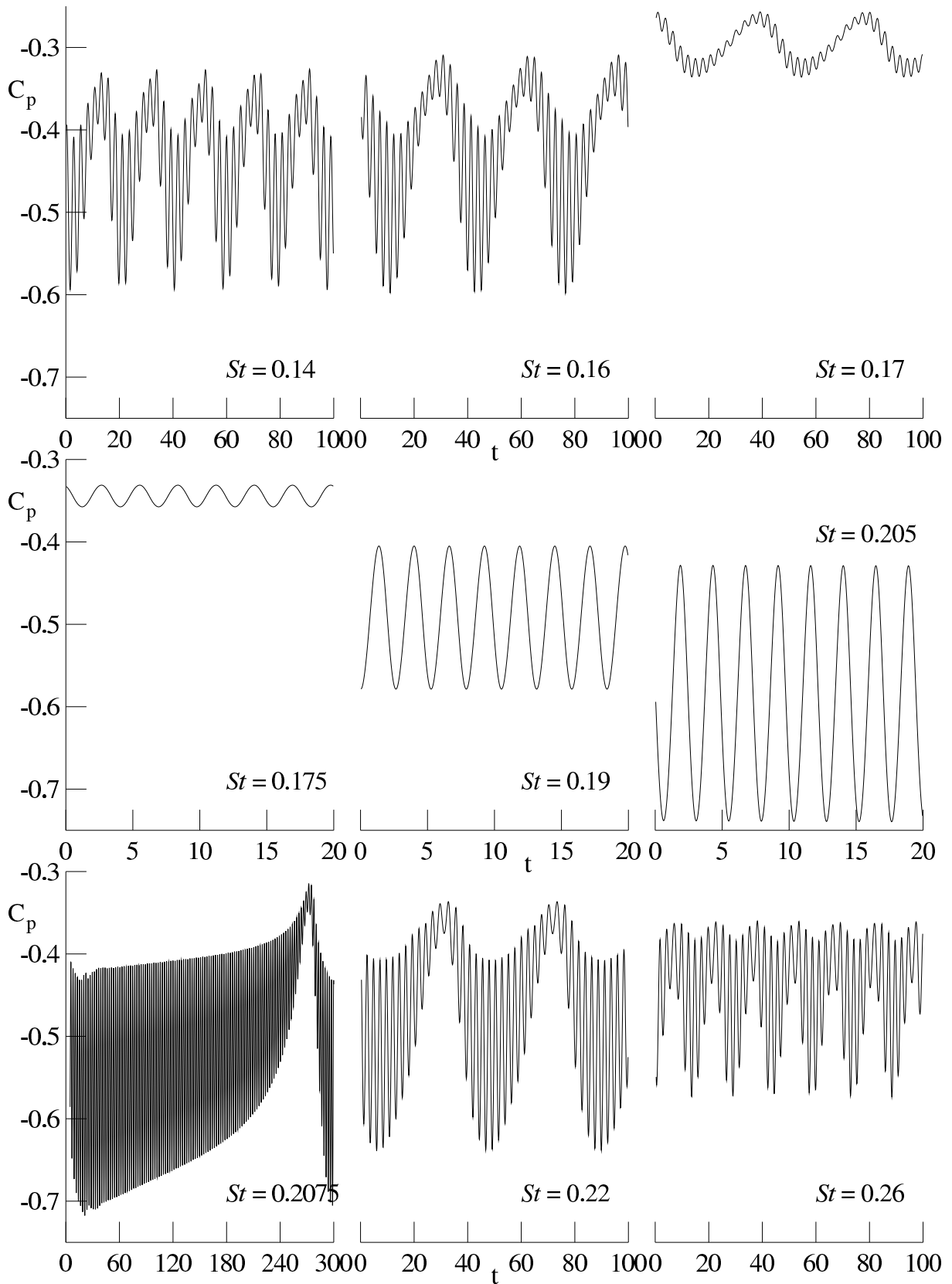


Figure 3.10: Traces of base pressure coefficient in the asymptotic state for various forcing frequencies. These were taken from flow over a 5:1 elliptical leading-edge plate with  $c/t = 7.5$  at  $Re = 500$  and  $v_{pert} = 2.5\%$

sample length of 1000 non-dimensional time units. The peak at a frequency of  $St = 0.381$  is twice the natural shedding frequency ( $St = 0.19$ ). This is associated with the natural shedding and the factor of two is caused by the monitoring point being at the centre of the trailing face. The other peak at  $St = 0.030$  is the difference between the natural shedding frequency and the applied forcing ( $St = 0.19$  and  $St = 0.16$ ). The other two minor peaks at  $St = 0.350$  and  $St = 0.411$  can be obtained by subtracting or adding the lower frequency peak with the peak associated with the natural shedding.

From the spectral plot, the response at these forcing frequencies is characteristic of *beating*. The flow is not locked to the forcing and therefore is shedding at approximately its natural shedding frequency. This explains the peak in the spectrum associated with the shedding frequency. The forcing frequency is close to but not matching the shedding frequency. Therefore, the phase between the forcing and the shedding is continually varying. This variation has a longer wavelength and this frequency is the difference between the shedding and the forcing frequency. This is reflected by the peak at the lower frequency in the spectral plot. Referring back to the base pressure trace, the high frequency fluctuations associated with the shedding show variations in the mean and amplitude between periods within one of the long periods. This is caused by the variation in the phase of the shedding relative to the forcing. This results in some shedding cycles being suppressed and others being encouraged by the forcing.

When the forcing frequency is increased further to  $St = 0.17$ , the mean base suction decreases to a minimum. From the base pressure trace, the same process as described above is occurring except in this case the high frequency fluctuations appear to be small; this suggests that the shedding is damped by the forcing. Indeed, the forcing has almost locked the shedding. As the forcing frequency is increased further to  $St = 0.175$ , the shedding is locked to the forcing. The flow remains locked to the forcing until the frequency reaches  $St = 0.205$ . Within the lock-in range, there is an increase in the amplitude and the mean of the base suction as the forcing frequency is increased. The time-mean base pressure coefficient plotted in Figure 3.5 shows approximately a linear increase with forcing frequency within this range. These observations indicate the shedding is more vigorous at a higher frequency. Later sections will show that vortices with more circulation form closer to the trailing edge at the higher forcing frequency. As the forcing frequency is increased past  $St = 0.2075$ , the flow no longer locks to the forcing. At these high frequencies, the system mirrors the behaviour occurring at the lower forcing frequencies. Again, the mean base pressure approaches that of the natural shedding. As before, two wavelengths are present : the higher frequency corresponds to the shedding and the lower frequency is the difference between the forcing and the natural shedding frequency. The fluctuations between shedding cycles over the longer period are also a result of the variation in the relative phase between the forcing and the shedding. Note

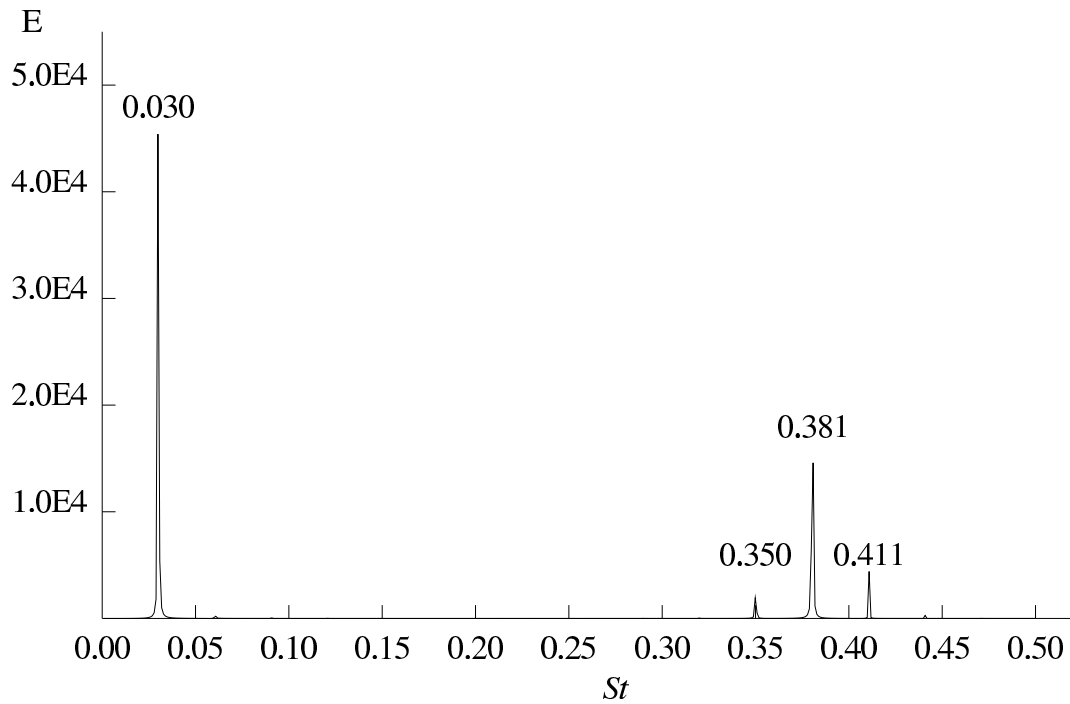


Figure 3.11: A spectral plot of the base pressure coefficient for flow around a 5:1 elliptical leading-edge plate with  $c/t = 7.5$  and  $Re = 500$ . The forcing is at  $St = 0.16$  and  $v_{pert} = 2.5\%$ .

that at a forcing frequency of  $St = 0.2075$  (just outside the lock-in range), the longer wavelength is nearly 300 non-dimensional time units. This simulation required in excess of 1,200 non-dimensional time units to allow the transients to decay.

Figure 3.12 shows the pressure traces at various forcing frequencies for the flow around a plate with  $c/t = 12.5$  at  $Re = 300$ . Comparing with the higher Reynolds number case, there are some similarities and differences. When the flow is not locked to the forcing, there are two dominant wavelengths with the shorter corresponding to the shedding and the longer the difference between the forcing frequency and the shedding. The amplitude of the higher frequency signal is generally weaker in this case reflecting the weaker shedding caused by thicker boundary layers near the trailing edge. As the forcing frequency is increased towards the natural shedding frequency, although the fluctuations in the longer wavelength increase, the mean remains approximately unchanged unlike the higher Reynolds number case. Within most of the lock-in range,  $0.13 \leq St \leq 0.16$ , the mean and fluctuating component of the base suction increases almost linearly with the forcing frequency. As the forcing frequency is increased to  $St = 0.165$ , the flow is still locked to the forcing but there is a drastic drop in the amplitude and mean of the base suction associated with the drastic phase shift between the shedding and the applied forcing (shown later in Section 3.3.1). In the higher Reynolds number case the flow no longer locks to the forcing and the mean base pressure coefficient again approaches that of the natural shedding case. As the forcing frequency is increased past  $St = 0.17$ , the response is typical of the lower frequency unlocked state.

These predictions are in agreement with the observations of Lofty & Rockwell (1993). In those experiments, the shedding from the trailing edge is excited by a pitching motion of the plate. The flow was phase-locked to the forcing within the lock-in range. Outside this range, the experiments observed a quasi-periodic state with a repeatable pattern after several shedding cycles. The experiments also showed that the length (in time) of this repeatable pattern increases when the forcing frequency is further away from the natural shedding frequency.

### 3.2.3.1 State selection

The time trace of the base pressure coefficient can be used to ascertain if the shedding from the plate is locked to the flow. Figure 3.13 shows the state of the flow as a function of forcing amplitude and frequency for the flow around a plate with  $c/t = 7.5$  and  $Re = 500$ . The lock-in behaviour for the flow for this geometry is similar to that presented in the state selection diagram of Karniadakis & Triantafyllou (1989) for a circular cylinder. As shown by the shaded region in Figure 3.13, the range of capture increases with forcing

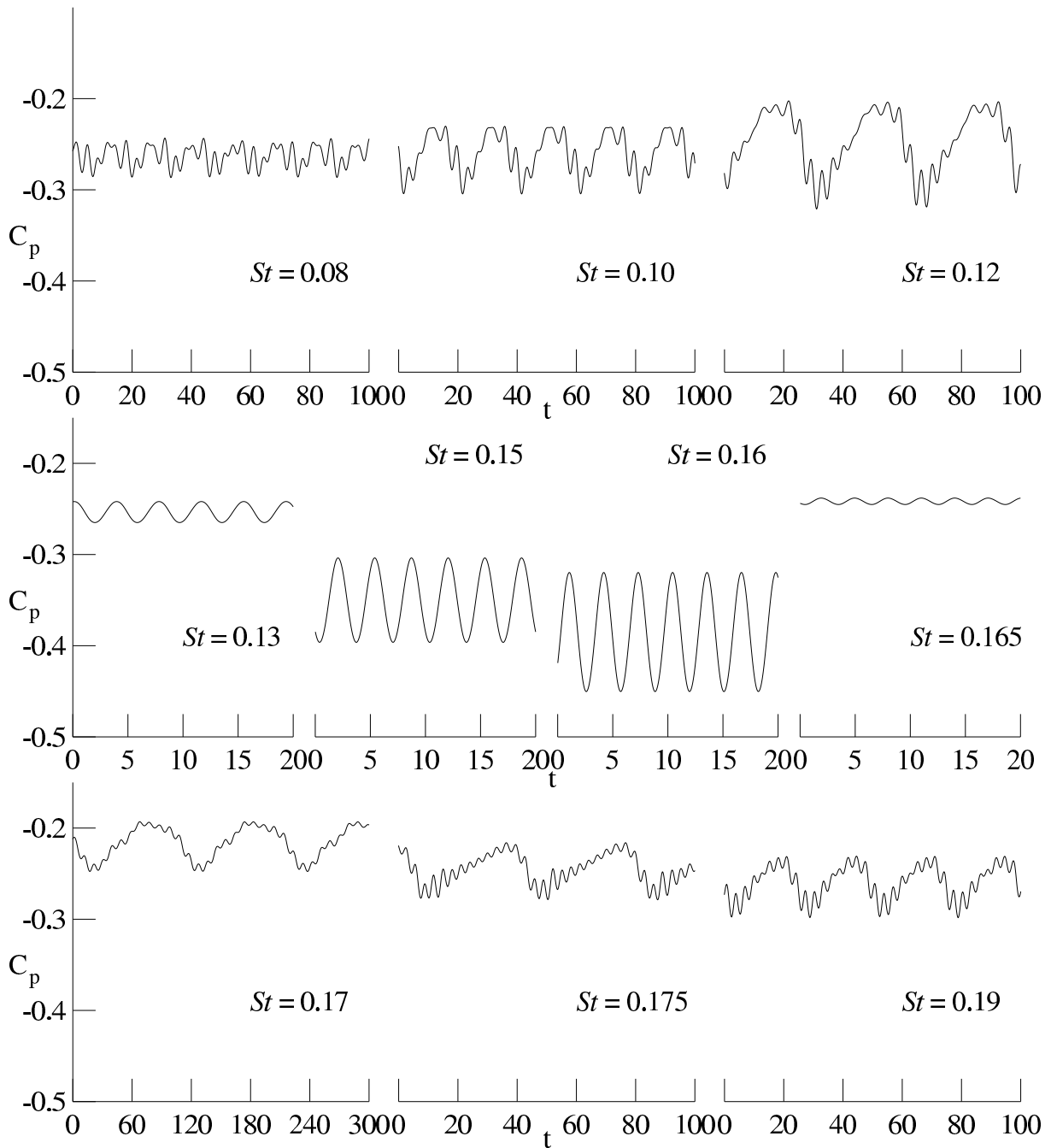


Figure 3.12: Traces of base pressure coefficient in the asymptotic state for various forcing frequencies. These were taken from flow over a 5:1 elliptical leading-edge plate with  $c/t = 12.5$ ,  $Re = 300$  and  $v_{pert} = 2.5\%$ .

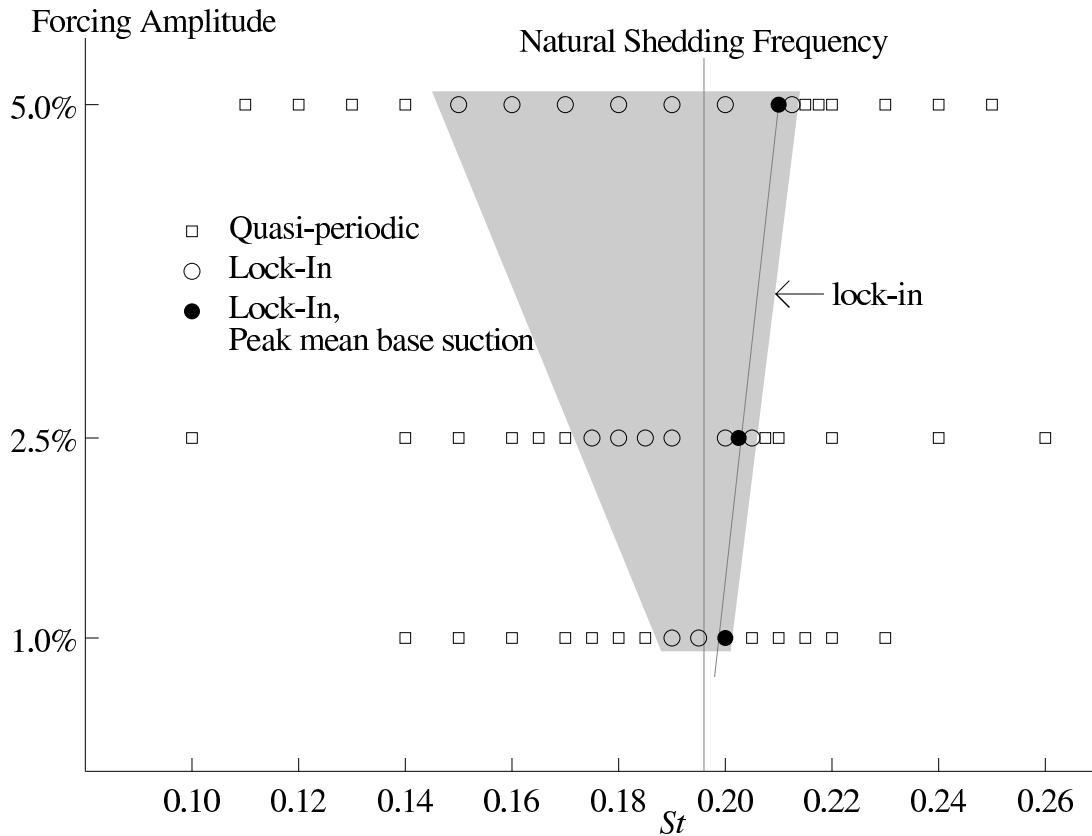


Figure 3.13: The flow state plotted as a function of forcing frequency and amplitude in a format similar to the state selection diagram in Karniadakis & Triantafyllou (1989). The forcing amplitude is relative to the free-stream velocity. The darkened circles represent the peak mean base suction as a function of the forcing frequency for a particular forcing amplitude.

amplitude. The solid gray line shows the natural shedding frequency (or the resonant point) is located towards the higher frequency end of the lock-in regime. This means there is a larger frequency range where *lock-down* occurs (shedding below the natural shedding frequency) rather than *lock-up*. Near the boundary between the two states, no chaotic behaviour has been observed although long periods in the signals have been observed. This differs from the chaotic behaviour observed by Blackburn & Henderson (1996) who simulated flow past a circular cylinder. It is possible that the thicker boundary layer at the trailing edge inhibits the chaotic behaviour or the larger steps in forcing frequency may miss capturing the chaotic range. The range of forcing frequency used was not large enough to study the flow far outside the receptivity boundary where the flow is no longer quasi-periodic. The gray broken line shows that the frequency at which the mean base suction reaches a maximum increases away from the natural shedding frequency with increasing forcing amplitude.

Comparing the range of capture in Figure 3.13 with the plots of mean base pressure coefficient at different forcing levels in Figure 3.6, the range where the flow locks to the forcing also corresponds approximately to where the forcing results in the mean base pressure coefficient deviating away from the natural shedding case. The control from the forcing in this range results in the excitation of different modes (frequencies) of shedding and the magnitude of the mean base pressure is a measure of the strength of these modes. Within this range, an increase in forcing amplitude also results in larger deviations in the mean base pressure coefficient. The shedding process is therefore effectively amplifying the response of the mean base pressure to the forcing. Therefore the overall response of the mean base pressure in the lock-in range is a result of the controlled shedding frequency and the shedding process amplifying the forcing.

### 3.2.4 Lift and drag forces

The previous sections concentrated on monitoring pressure at one point, specifically at the centre of the trailing edge. Although it is indicative of the overall flow, this section presents the results of truly global quantities. The time traces of lift and drag coefficients are found by integrating the pressure coefficient along the plate surface using the same discretisation as used to calculate the flow variables. Only the pressure forces are included as viscous forces are negligible at these moderate Reynolds numbers. As this is a symmetric geometry normal to the flow direction, there is no mean lift. Instead the standard deviation of the lift coefficient is analysed. Figure 3.14 shows the standard deviation of the lift coefficient and the mean drag coefficient as a function of the forcing frequency. Results are presented for the two cases in the previous section which involve flow around elliptical leading-edge plates with  $c/t = 7.5$  and  $12.5$  at  $Re = 500$  and  $300$  respectively. The forcing amplitude is fixed at  $v_{pert} = 2.5\%$ .

The fluctuating lift component shows a general linear increase as the forcing frequency is increased except near to where the flow is locked to the forcing. If this linear trend is extrapolated to where the forcing frequency is zero, the standard deviation of the lift coefficient will approach that of the natural shedding case. The linear increase in the fluctuating lift force with frequency is therefore a result of the forcing. At higher frequencies, there is less time for the forcing field to go from one extreme to another. This increase in acceleration causes larger surface pressure to be recorded on the plate and therefore a larger fluctuating lift force. This fluctuating lift force resists this trend in the lock-in range and decreases more where the mean base suction or drag force is greater. Plots of trajectories of the vortices in a later section (Section 3.3.2) will show that the vortices form closer to the axis of the plate in the lock-in range. The narrower wake results in less sideways force and therefore a reduction in the fluctuating lift force.

The decrease in fluctuating lift force is larger at higher Reynolds numbers because the stronger and more compact vortices contribute a larger portion of the fluctuating lift force relative to the forcing. The longer plate causes more blockage in the cross-flow direction. As will be shown in the next chapter (Section 4.2.4), this causes a larger increase in the forcing amplitude near the plate. The larger velocity fluctuations also cause larger pressure fluctuations. The longer plate generally has a larger fluctuating lift force because of the larger pressure fluctuations near the plate due to the forcing.

The fluctuating component of lift has also been shown to decrease near the natural shedding frequency for an oscillating circular cylinder in simulations by Blackburn and Henderson (1996). In experiments where the flow is at a much higher Reynolds number and three dimensional, the lock-in range shows an increase in the fluctuating component of the lift force for short bodies (Staubuli, 1981, Bearman & Obasaju, 1982). This is due to the increase in spanwise correlation in the wake when the flow locks to the forcing. This is not captured in the two-dimensional simulations.

The mean drag coefficient shows a similar trend to the mean base pressure. This is expected as the pressure at the leading edge is expected to be almost independent of the frequency of the applied forcing. The applied forcing influences the flow at the trailing edge which has a strong influence on the mean base pressure and the drag coefficient. The narrower wake in the lock-in range also results in an increase in mean drag.

### 3.3 Further analysis

In this section, a more detailed analysis of the flow in the lock-in state will be performed. The focus is in this range because the forces on the plate are significantly modified by the forcing when the flow is locked to the forcing. As in the previous section, the two cases studied are flow around plates with  $c/t = 7.5$  and  $12.5$  at  $Re = 500$  and  $300$  respectively, as these are representative of the higher and lower Reynolds number or smaller or larger aspect ratio cases. Again, the amplitude of the forcing is kept at  $v_{pert} = 2.5\%$ .

#### 3.3.1 Shedding phase relative to forcing

The phase of the shedding at the trailing edge is revealed by vorticity plots near the trailing edge taken at four times in the sinusoidal forcing cycle. Figure 3.15 shows these plots for  $c/t = 7.5$  and  $Re = 500$ . The forcing frequencies shown are  $St = 0.17$ ,  $0.185$  and  $0.2025$  which are close to the lower, middle and upper limits of the lock-in frequency

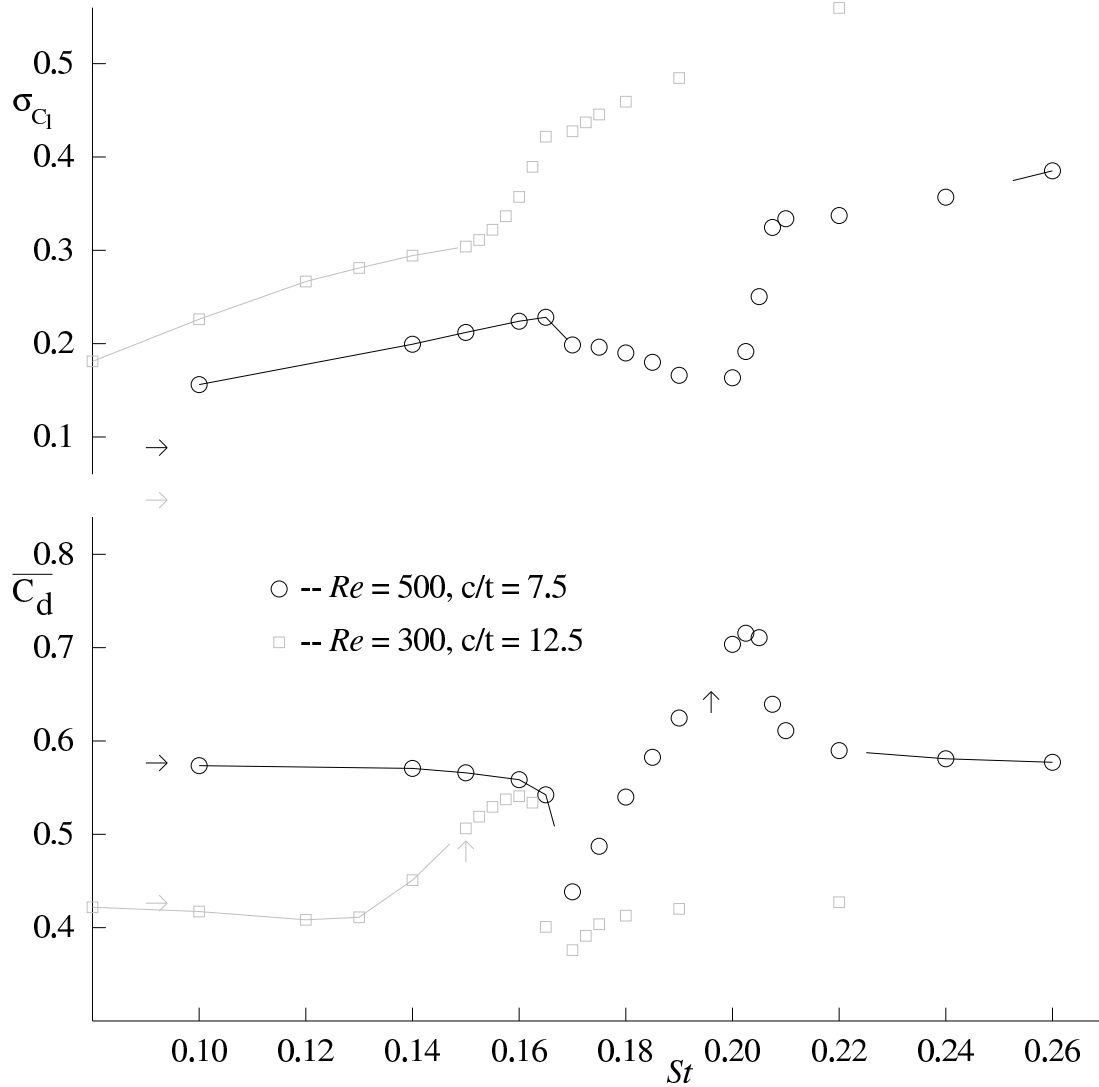


Figure 3.14: Plots of the standard deviation of lift coefficient ( $\sigma_{c_l}$ ) (top) and mean drag coefficient ( $\overline{C_d}$ ) (bottom) as a function of forcing frequency. The two cases presented are flow around an elliptical leading-edge plate with  $c/t = 7.5$  at  $Re = 500$ , and  $c/t = 12.5$  at  $Re = 300$ . The forcing amplitude is kept at  $v_{pert} = 2.5\%$ . The horizontal arrows represent the quantity without applied perturbations and the vertical arrows the natural shedding frequency.

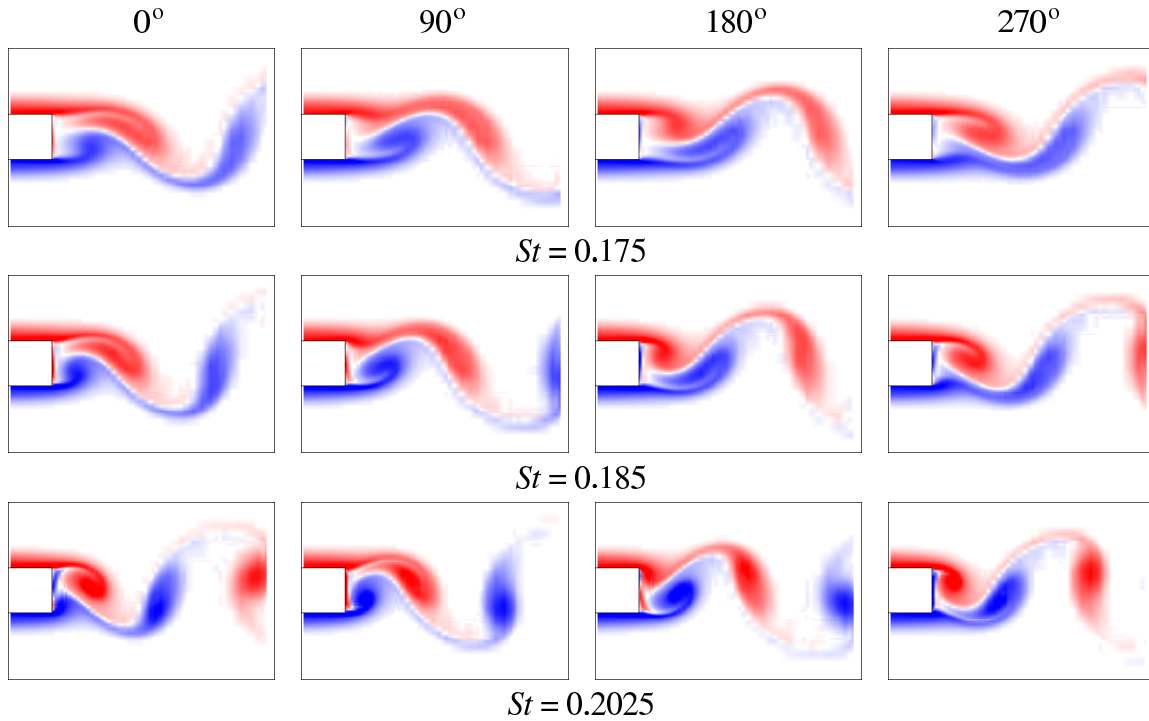


Figure 3.15: Vorticity plots taken near the trailing edge at  $0^\circ$ ,  $90^\circ$ ,  $180^\circ$  and  $270^\circ$  in the forcing cycle for flow over a  $c/t = 7.5$  elliptical leading-edge plate at  $Re = 500$ .

range. These plots show no significant change in phase between the shedding and the forcing in this frequency range. Therefore, as expected, there is no step change in the mean base suction within this frequency range which is usually associated with a large phase shift. When the flow is locked to the shedding, the forcing is seen to enhance strong shedding. The bottom vortex is formed between approximately  $90^\circ$  to  $270^\circ$  in the forcing cycle which corresponds to the perturbation velocity accelerating in the upward direction. The top vortex is formed in the other half of the cycle. This causes the vortices to form close to the centreline of the plate.

As the forcing frequency is increased, the vortices form closer to the trailing edge. The increase in the vorticity nearer the plate and the corresponding decrease in the formation length leads to the increase in mean base suction. This aspect of the flow will be pursued in the following sections.

Figure 3.16 shows the vorticity plots for flow around an elliptical leading-edge plate with  $c/t = 12.5$  and  $Re = 300$ . The first three chosen forcing frequencies of  $St = 0.13$ ,  $0.145$  and  $0.16$  represent the lock-in range and show an increase in mean base suction with forcing frequency. Within this part of the lock-in range, vortex structures in the wake are similar to the higher Reynolds number case. The phase between the shedding and the forcing is approximately constant and is similar to the higher Reynolds

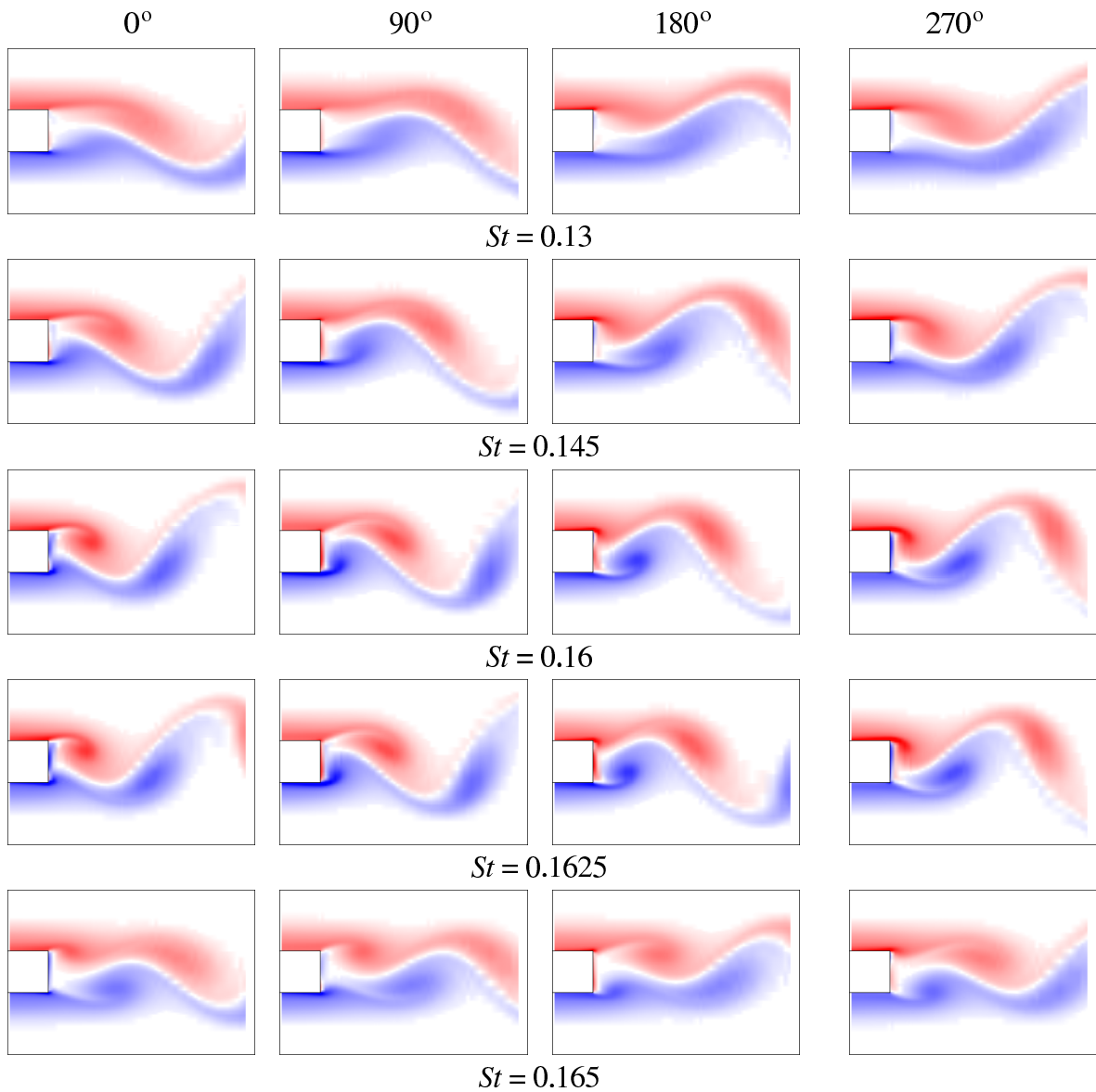


Figure 3.16: Vorticity plots taken near the trailing edge at  $0^\circ$ ,  $90^\circ$ ,  $180^\circ$  and  $270^\circ$  in the forcing cycle for flow over a  $c/t = 12.5$  elliptical leading-edge plate at  $Re = 300$ .

number case. Within this range, the increase in frequency also correlates with a shorter formation length, more concentrated vorticity nearer the plate and a stronger mean base suction. However, compared with the higher Reynolds number case, the vortices are more diffused and the formation length longer. This is because of the longer plate, lower Reynolds number and lower forcing frequencies in the lock-in range. Increasing the forcing frequency to  $St = 0.1625$  results in a small drop in mean base suction but there are only minor differences in the wake flow structures compared to  $St = 0.16$ . A small increase in forcing frequency to  $St = 0.165$  results in a large change in mean base pressure as shown in Figure 3.7. The vorticity plots shows there is approximately a  $90^\circ$  phase change from the previous cases. The drop in mean base suction corresponds to the vortices being more diffuse and forming further away from the plate surface. At this forcing amplitude, this case resides approximately on the lock-in boundary and the flow does not lock to the forcing above this frequency. A phase shift of  $180^\circ$  is observed in some short bluff bodies (Bearman & Obasaju, 1982, Nakamura & Mizota, 1975, Ongoren & Rockwell, 1988). The small frequency range where the phase shift occurs together with its proximity to the lock-in boundary may inhibit the simulations from capturing the complete ( $180^\circ$ ) phase shift. At higher Reynolds numbers, if there is a phase shift, it may occur over a much smaller frequency range thereby making it very difficult to capture. Such a phase shift is not likely as there is a gradual recovery in the mean base pressure as the forcing frequency is increased past the lock-in range shown by Figure 3.5. A phase shift would normally result in a sharp drop in mean base suction.

### 3.3.2 Vortex trajectory

The location of the local extrema of vorticity within each wake vortex structure formed at (and shed from) the trailing edge is determined at regular time intervals over a shedding (or forcing) cycle for the two cases being studied in detail. This information provides quantitative information about the wake including the vortex formation length, the phase of shedding relative to forcing and the convective velocity.

Figure 3.17 shows the location of the local peaks in the vorticity for flow around the elliptical leading-edge plate with  $c/t = 7.5$  and  $Re = 500$  taken at regular time intervals of 0.21 dimensionless time units over approximately one shedding/forcing cycle. In the natural shedding case, when the trailing-edge vortex forms, the peak moves towards the centreline of the plate as vorticity is fed from the boundary layer into the wake vortex structure. The closely spaced points near the formation region shows that the convective velocity of the vortex is low initially and it begins to accelerate when it detaches from the bluff body to approximately a constant velocity. The low convective speed near the plate is due to the low flow velocities in the immediate wake. As the vortex is shed, it

initially moves away from the centreline before returning back part of the way, finally reaching a trajectory tangential to the free stream. As the vortex is formed, the local peak in vorticity does not develop near the geometric centre of the patch of vorticity but at a corner which is away from the centreline and towards the plate. As it convects downstream, the local peak in vorticity also rotates in the direction of the vorticity about approximately the geometric centre. This rotational movement together with diffusion and the cross-annihilation of vorticity causes a redistribution of vorticity within the vortex patch and results in the local peak in vorticity initially moving away from the centreline and then back towards the centreline before convecting downstream. A more detailed examination of this behaviour will be discussed in the cases with applied forcing which also show a similar behaviour.

Also shown in Figure 3.17 are the cases with applied forcing frequencies of  $St = 0.175$ ,  $0.185$  and  $0.2025$  which represent the lower, mid and upper limits of the lock-in range. The trajectory of the vortex structures show a similar behaviour in the formation and the convection away from the plate. At  $St = 0.175$  and  $0.185$ , an added feature in the form of a secondary local peak in vorticity over some part of the forcing cycle is present. This is shown by the gray circles.

This phenomenon is investigated by a closer examination of the vorticity contours. These are shown over half a forcing cycle for the case with a forcing frequency of  $St = 0.175$  as shown in Figure 3.18. Starting at  $315^\circ$  in the forcing cycle, the vortex from the lower side of the plate with a positive sense starts to form. This vortex develops and at  $90^\circ$  in the forcing cycle, the vortex core has moved downstream and towards the centreline. As the flow is periodic and symmetric about the centreline, this development can be followed by observing the vortex forming at the top of the plate with a negative sense at  $315^\circ$  in the forcing cycle. This vortex still remains attached to the plate while the vortex on the other side of the plate is forming. This results in the vortex being stretched especially in the streamwise direction. With the separated boundary layer still connected to the plate, besides the initial local peak in vorticity translating downstream, another local peak in vorticity develops a small distance downstream which is more evident in the plots taken at  $45^\circ$  and  $90^\circ$ . This suggests that the vorticity generated by the plate is still being fed into that vortex. This development is then tracked by again reverting to the vortex patch further downstream with a positive sense at  $315^\circ$  in the forcing cycle which still shows the two local peaks in vorticity. As this vortex moves downstream, there is a redistribution in the vorticity and the two peaks approach each other until at  $90^\circ$  in the forcing cycle, there is only one local peak in vorticity present. From here on the vortex patch is mainly influenced by diffusion as it is convected downstream. These plots also show the path of the primary peak in vorticity developing nearer the corner of the vorticity patch. Similar to the natural shedding case, this peak rotates about approximately the geometric centre

of the vorticity patch in the same sense as the vorticity before coalescing with the other local peak. This explains the movement of the local peak in the cross-flow direction which initially moves away from the centreline and then back toward the centreline as it convects downstream. The secondary local peak develops near the geometric centre and undergoes mainly translational movement in the streamwise direction.

Returning to figure 3.17, for the cases in which periodic forcing is applied, the location of the peaks at approximately  $0^\circ$  and  $90^\circ$  in the forcing cycle are shown. The other half of the cycle (i.e  $180^\circ$  and  $270^\circ$ ) can be obtained by mirroring about the centreline and is omitted to reduce the complexity of the diagrams. For this plate, these diagrams also show the the phase of shedding relative to the forcing is approximately constant over the lock-in range. At  $0^\circ$  in the forcing cycle, the vortex on the top side is in the process of forming. It convects downstream and at  $90^\circ$  in the forcing cycle, it is moving away from the centreline while in the process of detaching from the plate. At  $180^\circ$  in the forcing cycle, it is moving back towards the centreline and for the rest of the cycle, it continues to convect downstream tangential to the streamwise direction.

The formation length is a measure of the distance over which the vortex develops before shedding into the wake. The distance between the trailing edge of the plate until where the vortex trajectory is tangential to the free stream is a good indicator of the formation length. As the forcing frequency is increased, the formation length of the vortices decreases and the distance of these peaks from the centreline also reduces. The former effect contributes to the higher mean base suction and drag experienced by the plate while the latter is reflected in the lower fluctuating component of lift force on the plate.

Figure 3.19 shows the location of the local peaks in vorticity for the flow around the plate with  $c/t = 12.5$  at  $Re = 300$  in the unperturbed case, and with forcing frequencies of  $St = 0.13$ ,  $0.16$  and  $0.165$ . These were taken at a regular time interval of  $0.2$  time units over a shedding/forcing cycle. The unforced case shows a much broader wake and a longer formation region compared to the higher Reynolds number flow. This is a result of the higher viscosity and the thicker boundary layer near the trailing edge. The flow in this case also experiences a significant amount of stretching of the vortices prior to detaching from the plate and the presence of another local peak in vorticity over part of the shedding cycle through a similar process to that outlined for the higher Reynolds number case with applied forcing.

The trajectories taken for applied frequencies of  $St = 0.13$ ,  $0.16$  and  $0.165$  are also included in Figure 3.19. A forcing frequency of  $St = 0.13$  is approximately the lower limit of the lock-in range. The flow shows a large formation length, and through a similar process described earlier, it develops a secondary local vorticity peak in the shed vorticity.

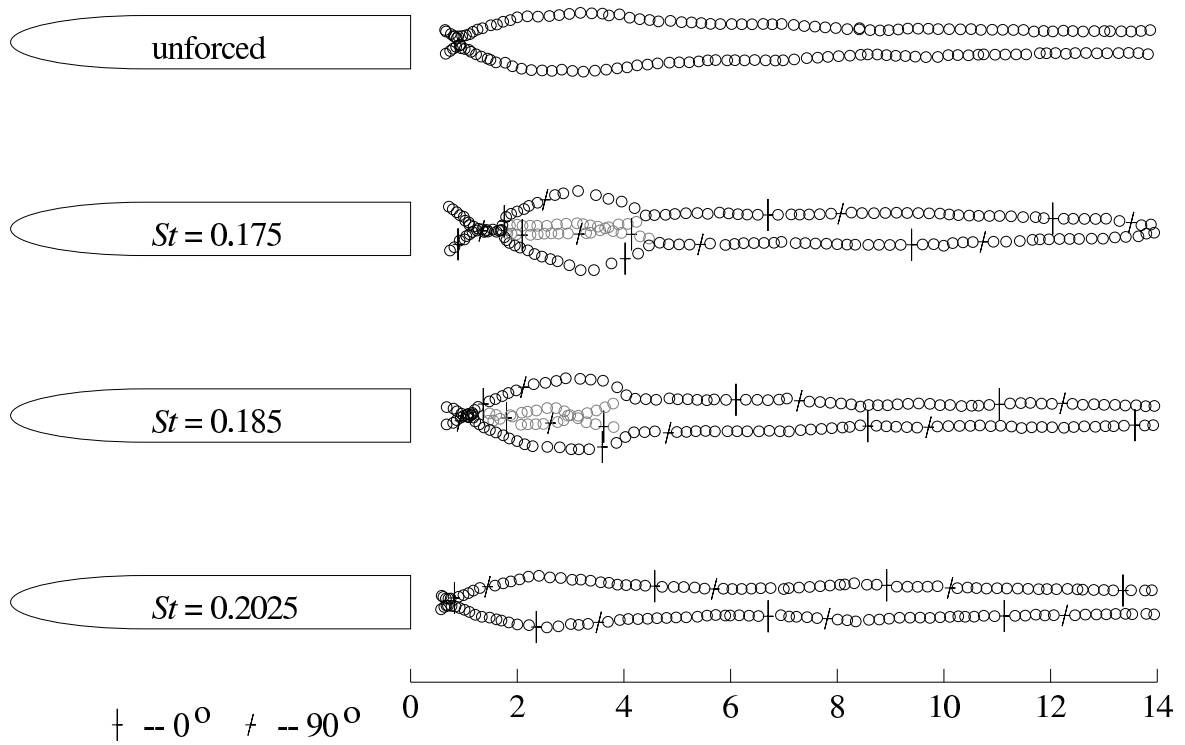


Figure 3.17: Plots of the location of the local peaks in vorticity taken at regular intervals of 0.21 dimensionless time units over a shedding/forcing cycle for the plate with  $c/t = 7.5$  and  $Re = 500$  (drawn to scale). The cases shown are without external perturbation (top) and with applied perturbation (three lower plots) with  $St = 0.175$ ,  $0.185$  and  $0.2025$ , and  $v_{pert} = 2.5\%$ .

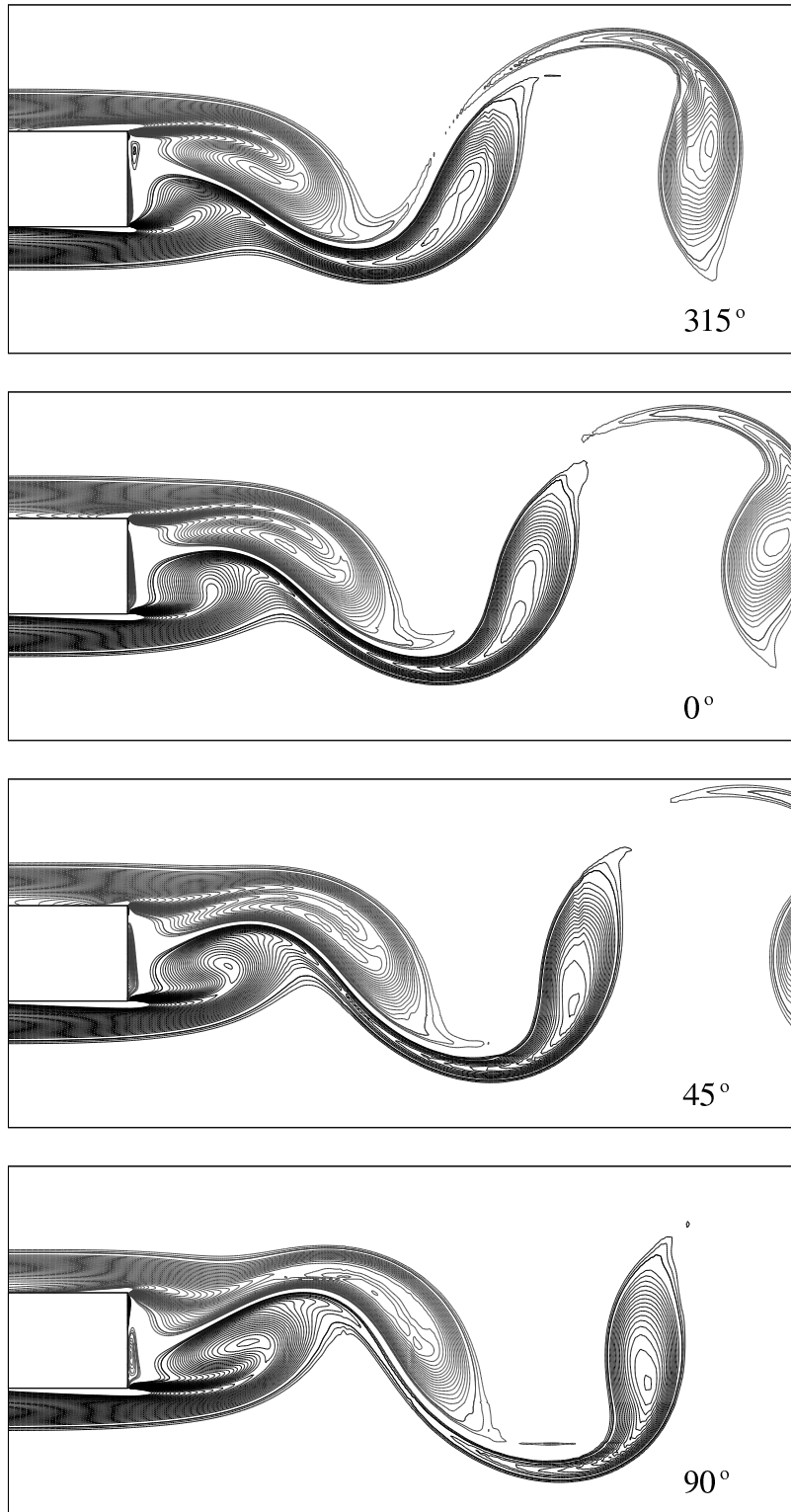


Figure 3.18: Contours of vorticity at the trailing edge taken over half a shedding cycle at four regular intervals of  $45^\circ$ . The flow is around a elliptical leading-edge plate with  $c/t = 7.5$  and  $Re = 500$  with forcing at  $St = 0.175$  and  $v_{pert} = 2.5\%$ . Contour levels start from  $+/- 0.5$  and increment/decrement in steps of  $0.1$  up to  $+/- 4.4$  with the positive levels darker and negative levels lighter.

As this is a lower Reynolds number, the length scales are larger. The larger wake and increased diffusion causes more cross-flow movement in the local vorticity peaks. As the frequency is increased to  $St = 0.16$  where the mean base suction approaches the maximum, the wake is narrower and the formation length reduced. At this forcing frequency, the phase of vortex development relative to the forcing is similar to the forcing at lower frequencies in the lock-in range and the forced cases for the higher Reynolds number flow. As shown in the previous section, an increment in forcing frequency from  $St = 0.1625$  to  $St = 0.165$  (which is close to the upper limit of the lock-in range for this case) shows a phase change of approximately  $90^\circ$ . This is also evident from the plots of the trajectory of the local peaks in vorticity. The stage in the development of the vortices at  $0^\circ$  in the forcing cycle at a forcing frequency of  $St = 0.165$  is approximately equivalent to  $90^\circ$  in the forcing cycle for the cases at a lower forcing frequency. Also associated with this phase shift is the drop in base suction which could be attributed partly to the larger formation length. As in previous cases, the large formation length and the stretched vortices are associated with the development of another local peak in vorticity within the shed vortex. In the experiments of Lofty & Rockwell (1993) which excited the plate in a pitching motion, plots in a similar format also showed the formation length increased as the plate experienced a phase shift but in their experiments, the formation length also increased as the forcing frequency was increased before the phase shift occurred.

An overall comparison between the two different plates and Reynolds numbers shows that the formation length and the width of the wake are larger in the lower Reynolds number case. This contributes to the lower drag and larger fluctuating lift forces experienced by the plates. For both cases, the lower limit of the lock-in range where the base pressure and drag are lower than the natural case also show a formation length larger than the natural shedding case.

### 3.3.3 Vortex formation length

The previous sections suggest a relationship between the vortex formation length and the mean base pressure and therefore mean drag experienced by the plate. This section attempts to show quantitatively this relationship. Although there are various definitions of the vortex formation length, a common approach, which is used in this study, is to measure the fluctuating component of the flow velocity in the cross-flow direction along the centreline of the plate downstream of the trailing edge. The vortex formation length can be defined as the distance from the trailing edge where this fluctuating component reaches a maximum (Bearman, 1965, Tombazis & Bearman, 1997). This section will focus on the natural shedding case and the cases with applied forcing in the lock-in range for the two plates and Reynolds numbers being considered in detail. Firstly, the variation of

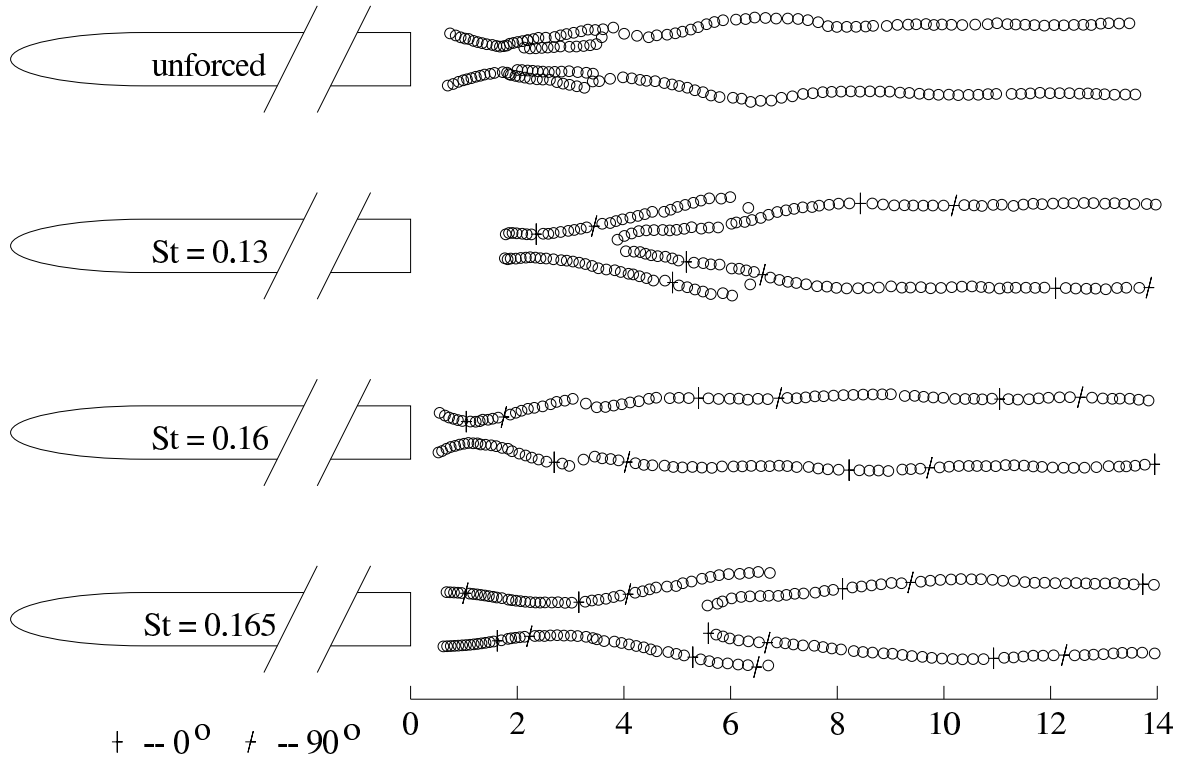


Figure 3.19: Plots of the location of the local peaks in vorticity taken at regular intervals of 0.2 dimensionless time units over a shedding/forcing cycle for the flow around the plate with  $c/t = 12.5$  at  $Re = 300$  (drawn to scale). The cases shown are without external perturbation (top) and for applied perturbation at  $St = 0.13$ ,  $0.16$  and  $0.165$  (bottom three plots), and  $v_{pert} = 2.5\%$ .

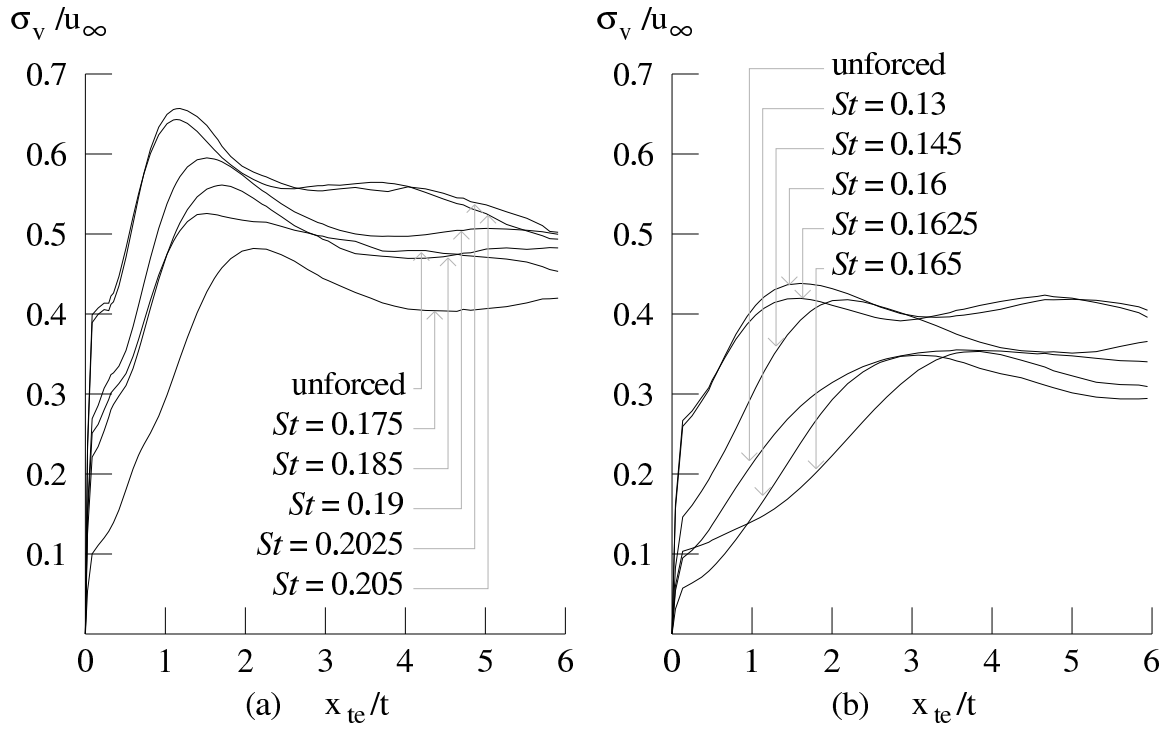


Figure 3.20: The standard deviation of the vertical component of the flow velocity measured along the centreline of the plate as a function of the downstream distance from the trailing edge for the unforced case and at several forcing frequencies. The two cases shown are at (a)  $Re = 500$  with  $c/t = 7.5$  and (b)  $Re = 300$  with  $c/t = 12.5$ . The forcing amplitude is at  $v_{pert} = 2.5\%$ .

the standard deviation of the vertical component of velocity with distance downstream of the trailing edge is determined. This is then used to find the vortex formation length which is then compared to the mean base pressure coefficient.

Figure 3.20 shows the standard deviation of the horizontal component of the flow velocity as a function of distance downstream from the trailing edge for the natural shedding cases, and selected forcing frequencies in the cases with applied forcing. For both plates and Reynolds numbers, while traversing downstream, the natural shedding case shows a steep rise before a gradual drop while all the forced shedding cases presented show a more severe drop. This region upstream of the peak is the near wake region where the velocities are small. The steeper drop in the forced shedding cases may be a combination of an amplification of the shedding near the formation region and a higher decay rate in the wake.

For the case with the higher Reynolds number of  $Re = 500$  and smaller aspect ratio of  $c/t = 7.5$ , from the lower limit of the lock-in range up to  $St = 0.2025$ , which is

near the peak in mean base suction, the magnitude of the peak increases, and the distance downstream from the trailing edge where the peak occurs decreases, as the forcing frequency is increased. The increase in magnitude of the peak suggests a more intense shedding and together with the shorter formation length contributes to the increase in mean base suction. At the lower end of the lock-in range, represented by a forcing frequency of  $St = 0.175$  in Figure 3.19(a), the magnitude of the peak is lower and the formation length is larger than the natural shedding case contributing to a lower mean base suction than the unforced case. At the other end of the lock-in range, as the forcing frequency is incremented from  $St = 0.2025$  to  $St = 0.205$ , while the formation length continues to increase, there is a drop in the magnitude of the peak. The smaller fluctuations in time indicates that the spatial gradients have also decreased (assuming velocity scales are similar). Therefore this reduction suggests that there is a decrease in the levels of vorticity within the trailing-edge structures.

There are several differences for the longer plate,  $c/t = 12.5$ , at a lower Reynolds number of  $Re = 300$ . Near the lower limit of the lock-in range, shown by the forcing frequency of  $St = 0.13$  in Figure 3.20(b) the magnitude of the peak is approximately that of the natural shedding and the formation length is less than the natural shedding case. As the forcing frequency is increased up to a forcing frequency of  $St = 0.16$ , there is a decrease in the vortex formation length and an increase in the magnitude of the peak which is similar in behaviour to the higher Reynolds number case. As the forcing frequency is incremented to  $St = 0.1625$  (similar to the upper limit of the higher Reynolds number case), there is a drop in the magnitude of the peak while the formation length continues to decrease. At the next increment to  $St = 0.165$ , associated with the phase shift, there is a significant drop in the magnitude of the peak and an increase in the vortex formation length.

Figure 3.21 shows the formation length and mean base pressure in the lock-in range for the two plates. In the higher Reynolds number case, the formation length and the mean base pressure decrease (increasing mean base suction) with the forcing frequency until  $St = 0.2025$ . At  $St = 0.205$ , there is a small recovery in the mean base suction because of the lower vorticity levels discussed earlier. This behaviour is mimicked in the lower Reynolds number case before the phase shift. At a forcing frequency of  $St = 0.165$ , associated with the phase shift, there is a significant increase in the vortex formation length which is matched by a decrease in mean base suction. The mean base pressure and the formation length of the unforced flow corresponds to the properties of some intermediate forcing frequency in the lock-in range for the higher Reynolds number case. Although they do not correspond to the same frequency, this still implies that in the higher Reynolds number case, the vortex formation length and the mean base pressure are strongly related to each other for the cases with and without applied forcing. In the

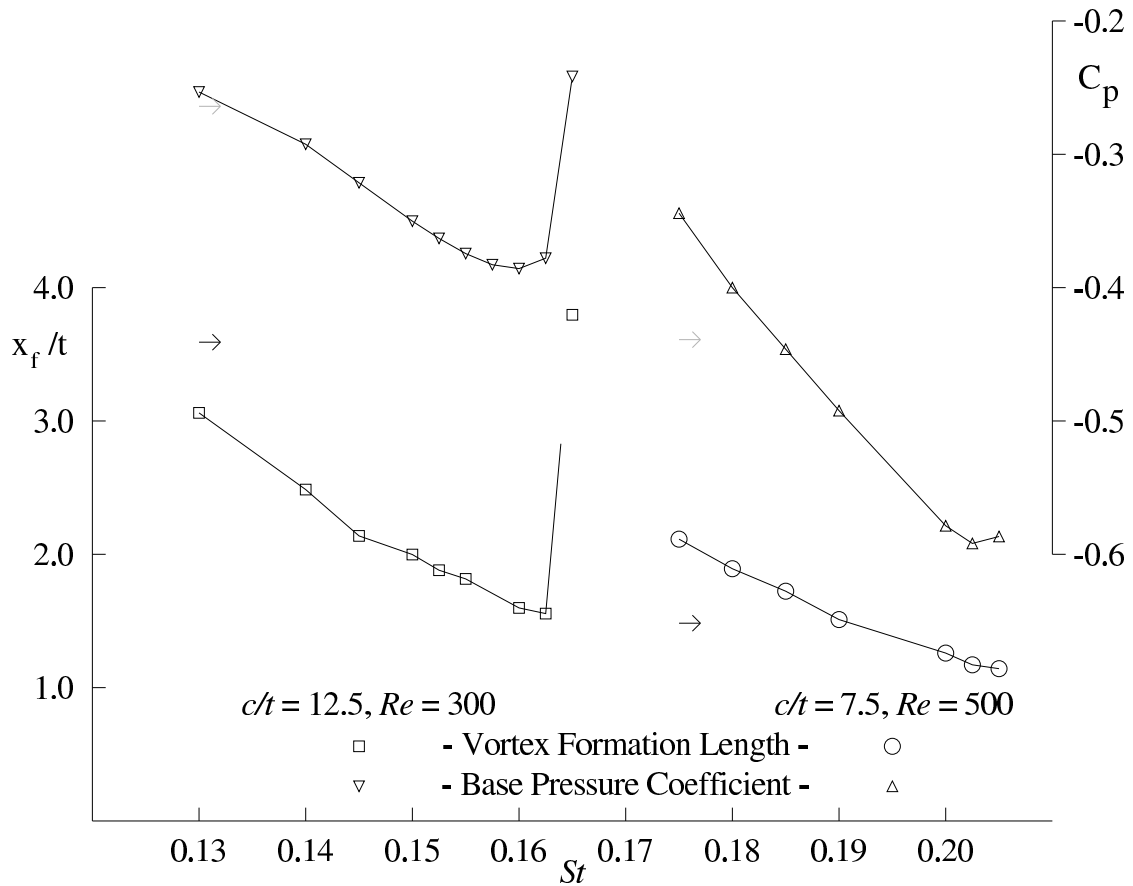


Figure 3.21: The vortex formation length and the mean base pressure coefficient as a function of the forcing frequency in the lock-in range for plates at  $Re = 500$  and  $Re = 300$  with  $c/t = 7.5$  and  $c/t = 12.5$  respectively. Dark arrows show the formation length and the gray arrows show the mean base pressure coefficient in the unforced case. Forcing amplitude is at  $v_{pert} = 2.5\%$ .

lower Reynolds number case, near the lower limit of the lock-in range, while the mean base pressure is similar to the unforced case, the vortex formation length is shorter when forcing is applied. Comparing the mean base pressure to the magnitude of the peak in horizontal velocity fluctuations in Figure 3.19(b), the lower Reynolds number case shows a stronger dependency between these two characteristics. Near the upper limit of the lock-in range for the higher Reynolds number case and before the phase shift in the lower Reynolds number case, there is a small drop in mean base suction while the formation length continues to decrease. As previously discussed, this is associated with a lower fluctuating component of velocity in the vertical direction. This implies that for the flow to remain locked to the forcing as the frequency is increased, the formation length would have to reduce. The drop in mean base suction and magnitude of the peak in the fluctuating component of the velocity in the horizontal direction prior to dropping out of the lock-in state shows that the flow is less receptive to the forcing. A possible explanation for the flow no longer remaining locked to the forcing as the frequency is increased is that the flow is no longer receptive to the higher frequencies because this would require the formation of more compact vortices associated with the reduced vortex formation length.

Experiments on flow around a rectangular plate ( $c/t = 6$ ) by Bearman (1965) at Reynolds numbers between approximately  $23,000 < Re < 43,000$  has previously shown the relationship between the formation length and base pressure. A splitter plate placed in the wake was used to control the formation length. Using hot-wire probes, these experiments showed that the mean base suction was proportional to the formation length. The data in Figure 3.20 also shows this trend but the proportionality constant varies for the different Reynolds number and aspect ratios. These experiments also traversed the probe across the wake at various positions downstream. The peak in fluctuations in this case represent the vortex centres. The trajectory of these vortices also show a necking as seen in the previous section and they occur approximately at the formation length in these experiments. The simulations show a similar trend in the higher Reynolds number flow but the lower Reynolds number flow shows that the formation length is further downstream of the position where the vortex trajectory necks for the natural and forced shedding cases.

In experiments where the plate was excited in a pitching motion, the formation length increases with increasing forcing frequency within the lock-in range (Lofty & Rockwell, 1993). In those experiments, the flow is also undergoing a phase shift. In these simulations, there is an increase in vortex formation length as the phase shift occurs. The phase shift occurs close to the upper limit of the lock-in boundary in the simulations. Therefore no comparisons with experiments can be made with further increases in forcing frequency. The different observations between the experiments and the simulations concerning vortex formation length is related to if and where the phase shift occurs in the

lock-in range.

### 3.3.4 Circulation

This section attempts to quantify the amount of circulation in the shed vortices and the link to the base pressure. Initially a theoretical approach will show the relationship between the amount of circulation generated and the base pressure. The results from the two different plates will then be compared with the theoretical predictions.

#### 3.3.4.1 Theory

Morton (1984) derived a relationship between the generation of circulation from a solid surface and the pressure gradient along that surface. The derivation stated by integrating around an infinitesimal area at the interface between a solid surface and a fluid. The momentum equation is then applied to eliminate the temporal derivative of velocity. When the surface is stationary and diffusion is neglected (because it does not contribute to the generation of vorticity), the rate of generation of circulation per unit length,  $\gamma_t$ , is equivalent to the pressure drop along the surface, expressed by

$$\frac{d\gamma_t}{dt} = -\frac{\partial p}{\partial S}. \quad (3.1)$$

If we then assume that all the circulation of one sign is generated from one side of the centreline, integrating along the surface of the plate between point 1 and point 2 along the bottom side of the plate shown in Figure 3.22(a) gives :

$$\int_1^2 \frac{d\gamma_t}{dt} dS = - \int_1^2 \frac{\partial p}{\partial S} dS \quad (3.2)$$

and performing the line integral results in,

$$\frac{d\Gamma}{dt} = (p_1 - p_2), \quad (3.3)$$

where here  $\Gamma$  is the total circulation. Integrating along the top surface of the plate gives the rate of generation of negative circulation. The integral on the left hand side of Equation 3.2 which results in the rate of generation of positive circulation,  $\frac{d\Gamma}{dt}$ , refers to the circulation generated in the infinitesimal layer around the plate represented by the gray area in Figure 3.21(b). When the flow is in an asymptotic state, there is no accumulation

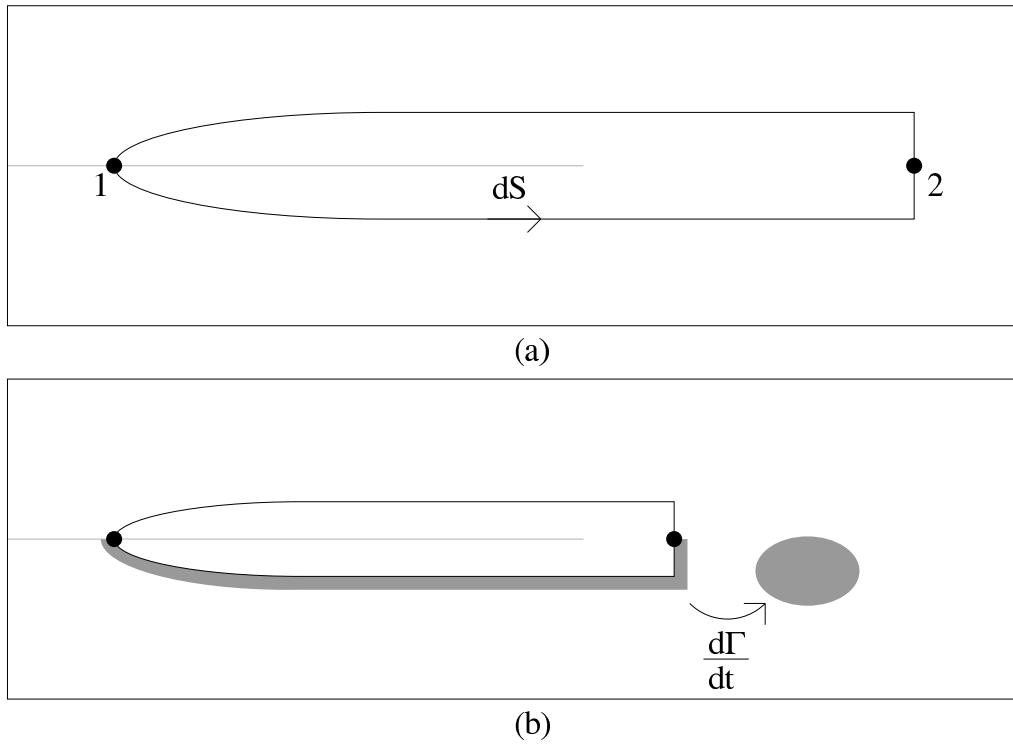


Figure 3.22: A sketch of the elliptical leading-edge plate showing (a) the path of integration from the stagnation point (1) at the leading edge to the centre of the base (2) where the base pressure is evaluated and (b) the circulation generated on the surface of the plate being convected into the wake.

of circulation around the plate and the circulation is convected into the wake. If the flow is periodic, the amount of circulation generated in one period is equivalent to the amount convected into the wake. Therefore, the result of integrating both sides of Equation 3.3 over one complete shedding cycle results in,

$$\Gamma = (\overline{p_1 - p_2})T. \quad (3.4)$$

If point 1 is assumed to be the leading-edge stagnation point, the pressure coefficient at this point is a constant with a value of unity. When all the variables are non-dimensionalised, this gives,

$$\frac{St\Gamma_o}{1 - \overline{c_p}} = 0.5, \quad (3.5)$$

where  $\overline{c_p}$  is the mean base pressure coefficient and the factor on the right hand side is a result of the conversion from kinematic pressure to pressure coefficient. The non-dimensionalised circulation,  $\Gamma_o$  generated in one shedding period, is derived for the positive circulation. The top surface generates an equivalent amount of negative circulation so that the overall amount is zero.

### 3.3.4.2 Comparison with simulations

This relationship between mean base pressure and the circulation generated in one shedding period is investigated for the flow over elliptical leading-edge plates with  $c/t = 7.5$  and  $12.5$  at  $Re = 500$  and  $300$  respectively. The analysis is performed only on cases where the flow is periodic. This includes the natural shedding case and the lock-in range when the forcing amplitude is  $v_{pert} = 2.5\%$ . The positive and negative circulation generated in a period is assumed to be contained in one vortex pair. The technique described in Section 2.4.2 was used to measure the circulation contained within each discrete vortex shed from the plate. The circulation was calculated by taking a closed loop line integral around the vortex. The path was chosen to be where the absolute value of the non-dimensional vorticity is  $0.4$ . This level is less than  $15\%$  of the peak vorticity and is chosen so as to capture as much of the circulation within each vortex patch while isolating each vortex. This was performed on vortices up to  $14$  diameter downstream from the trailing edge. For the flow around a plate with  $c/t = 7.5$  at  $Re = 500$ , Figure 3.23 shows the integral paths used for the unforced case and the forced cases with  $St = 0.175$  and  $0.2025$ . When forcing was applied, these plots were taken at  $0^\circ$  in the forcing cycle. The unforced case is chosen when the phase of the shedding is approximately equivalent to the forced shedding cases.

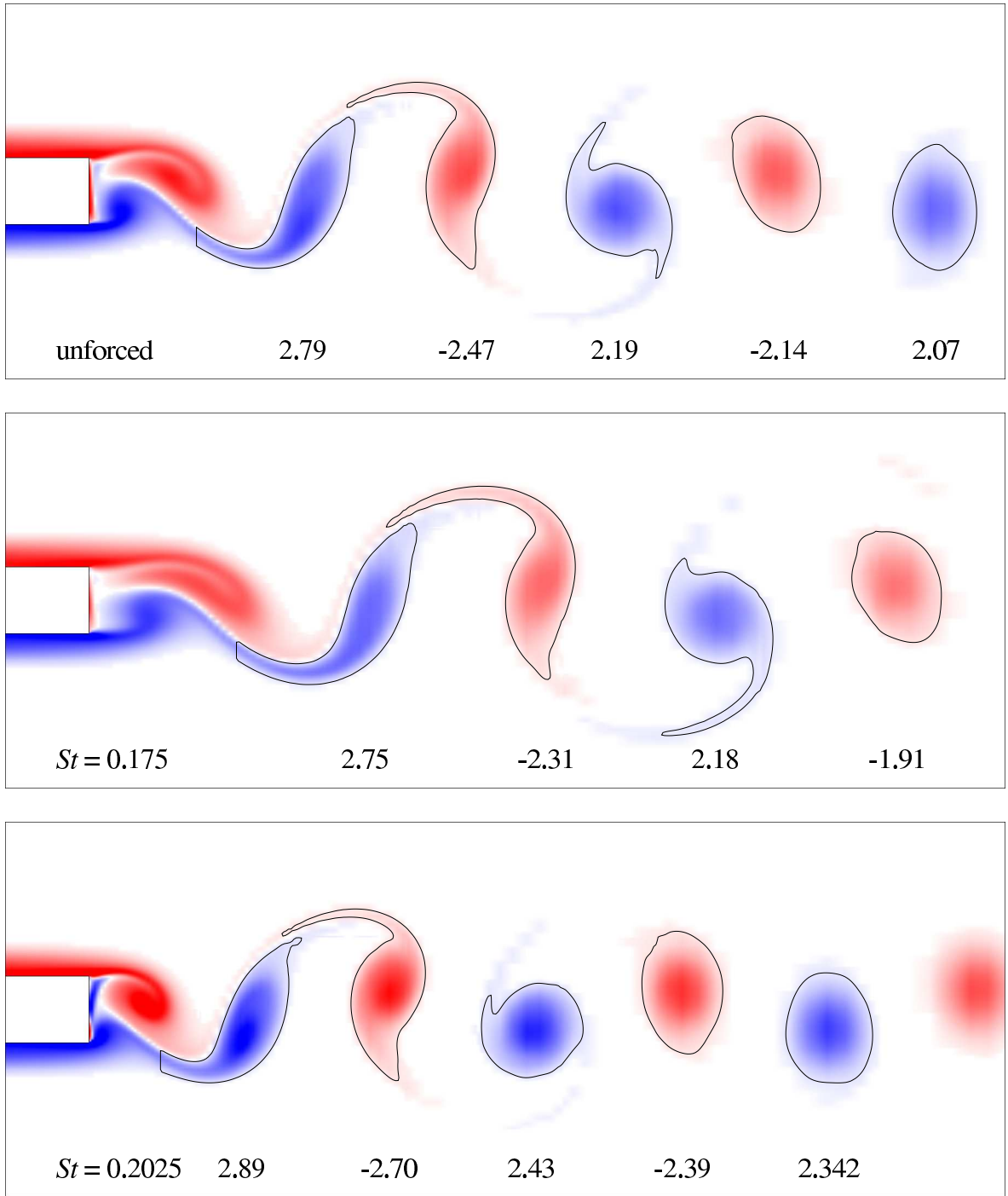


Figure 3.23: Vorticity plots in the wake of an elliptical leading-edge plate with  $c/t = 7.5$  at  $Re = 500$  in the natural and forced shedding cases. In the forced shedding cases, the plots are taken at  $0^\circ$  in the forcing cycle with the forcing frequency at  $St = 0.175$  and  $St = 0.2025$ , and the amplitude at  $v_{pert} = 2.5\%$ . The flow is in a similar shedding phase in the unforced case. The outlines show contours of non-dimensional vorticity having an absolute value of 0.4. These are used as integral paths to calculate the circulation which are shown below the contours.

The contour around the vortex closest to the trailing edge is artificially truncated so as to not include the developing vortex which is forming and the vorticity in the boundary layer of the plate.

From these plots, the amount of circulation in the vortices does not vary significantly between the natural shedding case and the two forced shedding cases (representing the lower and upper limit of the lock-in range). There is only a marginal increase in circulation but a large difference in mean base pressure between the lower and upper limits of the forcing frequency in the lock-in range. The rate of generation of circulation is still higher at the higher forcing frequency because of more vortices being generated in a fixed time period. This together with the marginal increase in circulation causes the higher mean base suction. The decay in circulation is greater nearer to the trailing edge. The vortices are closer and there is likely to be more cross-annihilation of vorticity. The decay is less further downstream where the vortices are further apart. The diffusion dominates the decay there and the high Reynolds numbers result in this low rate. The larger error when the vortices are more diffused also contributes to some of the decay.

These calculations were repeated for the natural shedding case and all frequencies simulated in the lock-in range for the cases with applied perturbation at four regular intervals in the shedding/forcing cycle. For the cases with applied forcing, this corresponded to  $0^\circ$ ,  $90^\circ$ ,  $180^\circ$  and  $270^\circ$ . The local peak in vorticity is used to determine the distance downstream the vortex is from the trailing edge. A selection of these cases for the flow around the plate with  $c/t = 7.5$  at  $Re = 500$  is shown in Figure 3.24. The natural shedding case and all the forced shedding cases showed a steep decrease within the first 6 to 8 diameters from the trailing edge. In this region, there is a smaller difference between the different cases. Further downstream, there is a marked decrease in the decay rate. This trend is more prominent as the forcing frequency is increased and the behaviour of the unforced case is similar to that for an intermediate frequency in the lock-in range. To estimate  $\Gamma_o$ , which is the amount of circulation of one sense generated in a forcing cycle, linear regression on the data obtained near the plate (i.e., 6 to 8 diameters from the trailing edge) is used to extrapolate the value to the trailing edge. The result of this analysis (and the other data required to calculate  $\frac{St\Gamma_o}{1-cp}$ ) is shown in Tables 3.1 and 3.2 for the flow around a plate with  $c/t = 7.5$  at  $Re = 300$  and  $c/t = 12.5$  at  $Re = 300$  respectively.

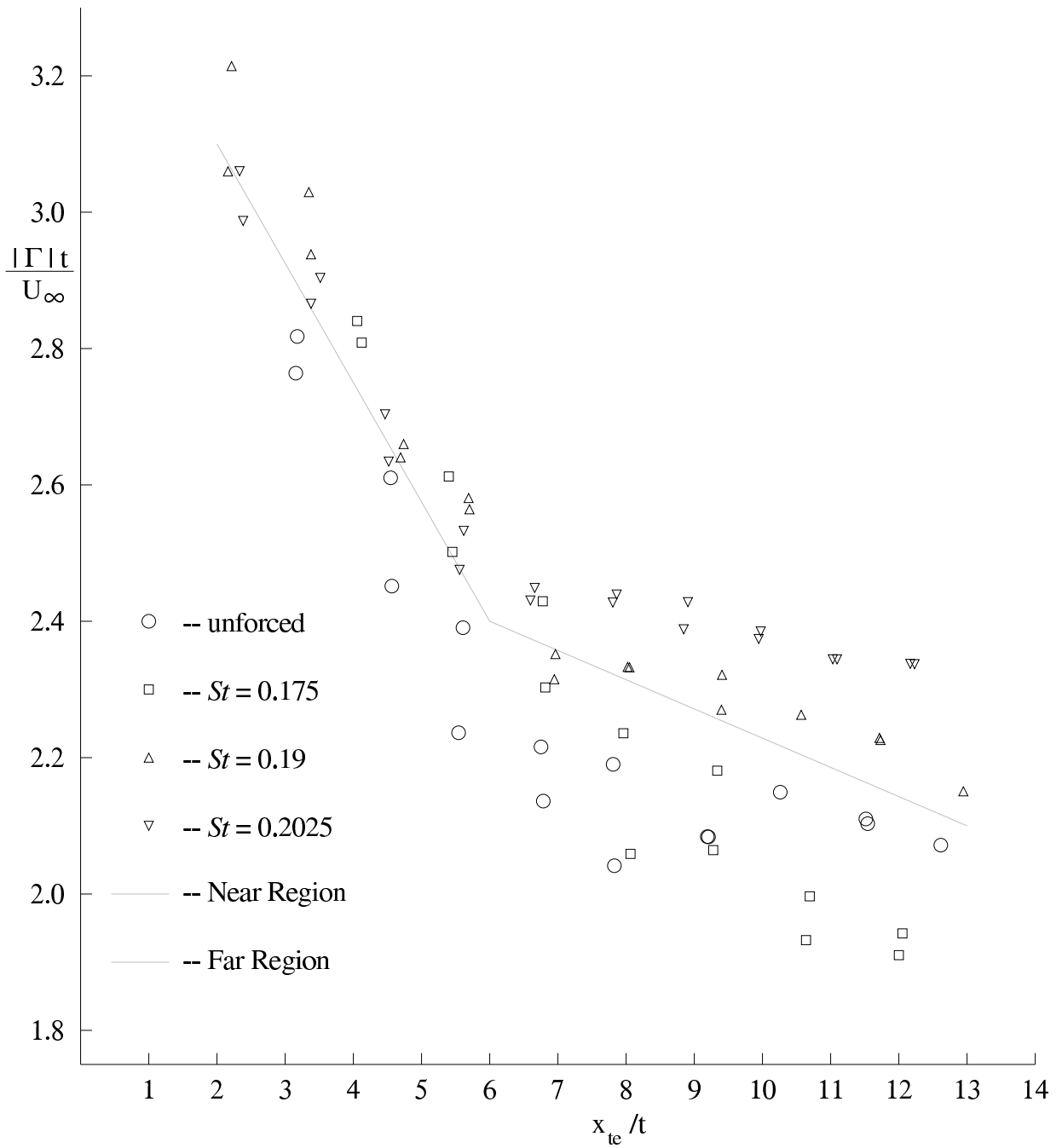


Figure 3.24: The absolute value of the circulation (non-dimensionalised with the plate thickness and free-stream velocity) contained within each vortex taken at four intervals in the shedding/forcing cycle as a function of the distance downstream from the trailing edge. The four cases shown are the natural shedding case and forced shedding cases at  $St = 0.175$ ,  $St = 0.19$  and  $St = 0.2025$ .

$St$	$\Gamma_o$	$1 - \overline{c_p}$	$\frac{St\Gamma_o}{1-c_p}$
0.19 (unforced)	3.215	1.439	0.425
0.175	3.260	1.344	0.424
0.18	3.356	1.400	0.431
0.185	3.379	1.446	0.432
0.19	3.349	1.492	0.426
0.20	3.366	1.579	0.426
0.2025	3.425	1.592	0.436
0.205	3.366	1.587	0.435

Table 3.1 : Computational data for the case with  $c/t = 7.5$ ,  $Re = 500$  and  $v_{pert} = 2.5\%$ .

$St$	$\Gamma_o$	$1 - \overline{c_p}$	$\frac{St\Gamma_o}{1-c_p}$
0.15(unforced)	3.620	1.264	0.430
0.13	4.180	1.253	0.433
0.14	3.798	1.292	0.411
0.145	4.044	1.321	0.444
0.15	3.560	1.350	0.395
0.1525	3.576	1.363	0.400
0.155	3.488	1.374	0.393
0.16	3.522	1.386	0.406
0.1625	3.651	1.378	0.430
0.165	3.004	1.242	0.399

Table 3.2 : Computational data for the case with  $c/t = 12.5$ ,  $Re = 300$  and  $v_{pert} = 2.5\%$ .

In both cases, the value of  $\frac{St\Gamma_o}{1-c_p}$  is approximately 0.42. The higher Reynolds number case has smaller deviations between all the cases ( $\pm 0.015$ ) compared with the lower Reynolds number case ( $\pm 0.03$ ). For most of the data, the circulation,  $\Gamma_o$ , does not vary significantly and the increase in base pressure is more dependent on the increase in frequency. One notable exception is when the phase shift occurs in the lower Reynolds number case. The drop in mean base suction is accompanied by a significant reduction in the circulation,  $\Gamma_o$ . The value of  $\frac{St\Gamma_o}{1-c_p}$  obtained from the simulations can be expected to be below the theoretical value of 0.5 because the value of  $\Gamma$  and therefore  $\Gamma_o$  is likely to be underestimated. The error in  $\Gamma$  is mainly from the exclusion of circulation due to the choice of cut-off level in vorticity. This results in some circulation not being accounted for. As there is more diffusion in the lower Reynolds number case, the larger spread in the data could be from the larger errors associated with this exclusion. Another possible source of error in estimating  $\Gamma_o$  is in the extrapolation of the data from the wake. The

linear regression method used to extrapolate the value of  $\Gamma_o$  may not accurately account for the cross-annihilation of vorticity near the trailing edge of the plate (within the first two diameters) where the effects may be stronger. There is difficulty in obtaining data in this region because it is hard to isolate the circulation produced in one shedding cycle.

An analysis similar to this was previously performed on experimental data by Mills (1998). Mills made measurements in the wake of an aerofoil leading-edge plate with an aspect ratio of  $c/t = 10$  at  $Re = 1,000$ . The results of the natural shedding case were compared to the case where the forcing frequency is approximately equal to the natural shedding frequency. By showing that  $\Gamma_o/(1 - c_p)$  is a constant for both cases, the experimental data successfully linked the increase in mean base suction to the increase in circulation in the wake. When the data presented in Mills (1998) is used to calculate the value of  $\frac{St\Gamma_o}{1-c_p}$ , the result of the natural shedding case and the forced shedding case are 0.476 and 0.450 respectively. This is closer to the theoretical value and is likely because the error due to the finite cut-off levels are smaller when the vortices are more compact and concentrated at higher Reynolds numbers. However, at such high Reynolds numbers, the development of wake three-dimensionality would cause some of the vorticity generated to realign in the spanwise direction. Some circulation may not be accounted for when analysing only a two-dimensional plane.

# Contents

<b>3</b>	<b>Flow Past a Plate with an Elliptical Leading Edge</b>	<b>67</b>
3.1	Natural shedding . . . . .	67
3.2	The effect of applied cross-stream forcing . . . . .	70
3.2.1	Mean base pressure . . . . .	72
3.2.2	Comparison of mean base pressure with experiments . . . . .	78
3.2.3	Base pressure trace . . . . .	81
3.2.4	Lift and drag forces . . . . .	88
3.3	Further analysis . . . . .	89
3.3.1	Shedding phase relative to forcing . . . . .	89
3.3.2	Vortex trajectory . . . . .	93
3.3.3	Vortex formation length . . . . .	98
3.3.4	Circulation . . . . .	104

# Chapter 4

## Flow Past a Long Rectangular Plate

The study of flow around long rectangular plates will be presented in this chapter. The complexity of this relative to the geometry in the previous chapter is increased because there is shedding from both the leading and trailing edges. The interaction between these two processes plays a crucial role in the overall flow. As in the previous chapter, the natural shedding case and the forced shedding case will be studied. The range of aspect ratios that will be studied start from  $c/t = 3$  in the natural shedding case and  $c/t = 6$  for the forced shedding case and reach  $c/t = 16$  in both cases.

Initially, the surface pressure on the plate will be used to gauge the overall characteristics such as shedding frequency, base pressure and forces in both the natural and forced shedding cases. Flow visualisation will then be used to analyse other traits such as shedding modes and phasing. Other features such as the convective velocity of the vortices and the vortex formation length will be evaluated to support the theoretical explanations. The acoustic power generated by the plate in a duct will be modelled using Howe's theory (Howe, 1975, 1980).

### 4.1 Natural shedding

This section studies the flow around rectangular plates in the absence of any external perturbations. This case has been well studied both experimentally and numerically (Nakamura *et al.*, 1991, Ohya *et al.*, 1992). The shedding from the leading edge and trailing edge of a rectangular plate locks to a single shedding frequency at low Reynolds numbers (up to  $Re \approx 3,000$ , Nakamura *et al.*, 1991). This instability relies on the interaction of the leading-edge vortices with the trailing-edge shedding to generate a pressure pulse. This pulse locks the leading-edge shedding and completes the feedback

loop. The pressure pulse is weak and therefore restricts this instability to low Reynolds numbers and limits the range of aspect ratios for which it is observed. It was initially classified as the impinging shear layer instability by Nakamura & Nakashima (1986) and Nakamura *et al.* (1991) because in some cases (where the aspect ratios are low) the shear layer directly interacts with the trailing edge and this has similarities with the instability in the cavity flow. Later studies (Naudascher & Wang, 1993, Naudascher & Rockwell, 1994, Mills *et al.*, (1995), Mills, 1998) prefer the name impinging leading-edge vortex (ILEV) instability because it better describes the process where leading-edge vortices are shed, convect downstream and then interact with the trailing edge. The result of this instability is distinct integer shedding modes ( $n$ ) where the integer represents the number of pairs of vortices along the plate. As the aspect ratio is increased, the Strouhal number based on chord ( $St_c$ ) shows a stepwise response with each increasing step corresponding to a higher shedding mode.

This section intends to validate the techniques used here by reproducing the different shedding modes, as the unforced case is a obvious precursor to the forced shedding cases. Initially, the effects of varying the Reynolds number on plates with aspect ratio of  $c/t = 3$  and 10 will be investigated. Next, simulations starting with an aspect ratio of  $c/t = 3$  will show the various shedding modes. The influence of the shedding modes on the pressure and forces on the plate will also be examined.

#### 4.1.1 Effects of Reynolds number

To study the effects of Reynolds number on the flow around long rectangular plates, simulations were performed for plates with aspect ratios of  $c/t = 3$  and 10 at Reynolds numbers of  $Re = 300, 400$  and 500. The base pressure trace indicates how strongly the flow is locked to a particular shedding mode. The variations in shedding frequency, mean base pressure and forces on the two plates with Reynolds number are also presented.

Figure 4.1 shows typical samples of the base pressure trace for an aspect ratio of  $c/t = 3$  after the flow has reached an asymptotic state for the three Reynolds numbers considered. The signal is strictly periodic at all three Reynolds numbers suggesting that the flow is strongly locked to a particular shedding mode. The period is half that of the shedding because the base pressure is evaluated at the centre of the trailing edge. Any asymmetry in the shedding would be detected when monitoring the pressure at the centre of the trailing face. The mean base suction and the amplitude of the trace both increase with Reynolds number. With less diffusion, the thinner boundary layers and stronger and more compact vortices contribute to this. Results for a longer plate with an aspect ratio of  $c/t = 10$  are presented in Figure 4.2. At a Reynolds number of  $Re = 300$ , a periodic

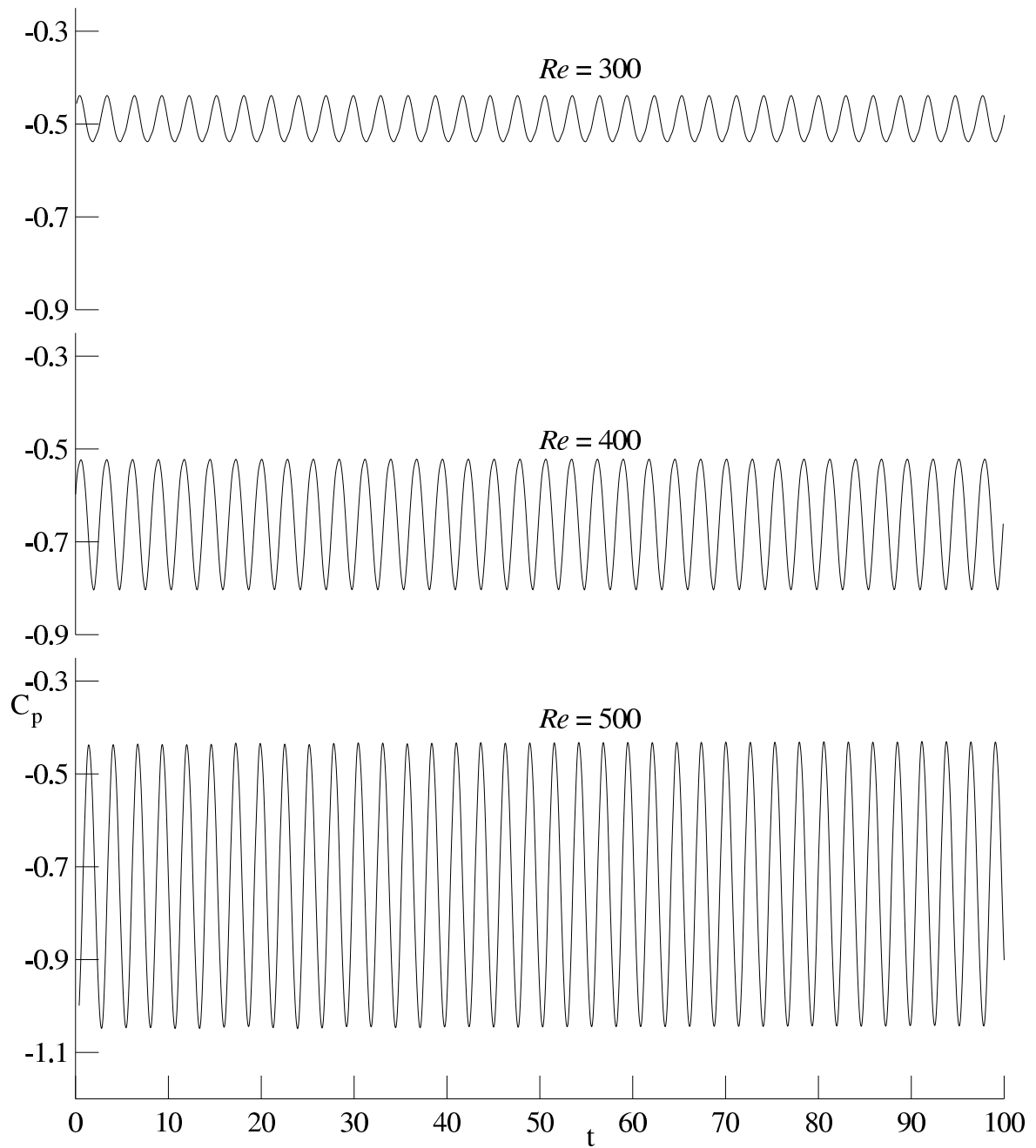


Figure 4.1: A 100 time unit sample of the base pressure trace taken when the flow around a rectangular plate with  $c/t = 3$  has reached an asymptotic state for  $Re = 300$ , 400 and 500.

signal is observed as with the shorter plate. Although there is a clear shedding frequency at a Reynolds number of  $Re = 400$ , there is a small drift in the signal. This signifies that the feedback mechanism has less control on the flow. The base pressure signal at  $Re = 500$  shows a significant amount of randomness in the signal. Although the frequency associated with the shedding mode at this aspect ratio is still dominant in the spectrum, there are also many other frequencies present suggesting that the controlling mechanism can no longer lock the flow. This signal is obtained after the simulation has been evolved for 2000 time units ( i.e.  $\approx 360$  periods at the ILEV frequency) and the flow shows no indication of locking to a particular shedding mode.

This instability that locks the flow to a particular shedding mode is weak since it relies upon a (weak) pressure pulse from the trailing edge to control the leading-edge shedding. With increasing Reynolds numbers (i.e greater randomness) or aspect ratios (i.e. increased distance for pulse to travel), the flow is less likely to lock to a particular shedding mode. Experiments by Nakamura *et al.* (1991) showed that above a Reynolds number of approximately  $Re \approx 3,000$ , the spectrum in the wake became broadband and showed no affinity to a particular shedding mode. Parker & Welsh (1983) observed a distinct frequency in the wake only up to an aspect ratio of  $c/t = 7.6$  in the Reynolds number range of  $1,500 < Re < 3,000$ . This corresponded to the second ( $n = 2$ ) shedding mode. Only a broadband spectrum is observed in the wake for larger aspect ratios. Numerical simulations also show that the instability is no longer able to lock the system to a single frequency past a certain Reynolds number or aspect ratio. Simulations by Ozono *et al.* (1992) at  $Re = 1,000$  showed the presence of several frequencies in the lift coefficient trace past  $c/t = 9$ . In these simulations at  $Re = 500$ , the mean base pressure trace also shows significant random fluctuations when  $c/t = 10$ .

$Re$	$c/t$	$St$	$\bar{c}_p$	$\bar{c}_d$	$\sigma_{c_l}$
300	3	0.170	-0.493	1.25	0.256
400	3	0.180	-0.651	1.40	0.360
500	3	0.188	-0.738	1.59	0.392
300	10	0.151	-0.334	1.11	0.0918
400	10	0.163	-0.483	1.29	0.133
500	10	0.171*	-0.452	1.27	0.123

Table 4.1: Shedding frequency, mean base pressure coefficient, mean drag coefficient and standard deviation of the lift coefficient for the two plates at the three Reynolds numbers simulated. (\* Denotes that other frequencies are present.)

Table 4.1 shows global properties for the cases considered in this section. When the flow is locked to a particular shedding mode, there is only a small (less than 10%)

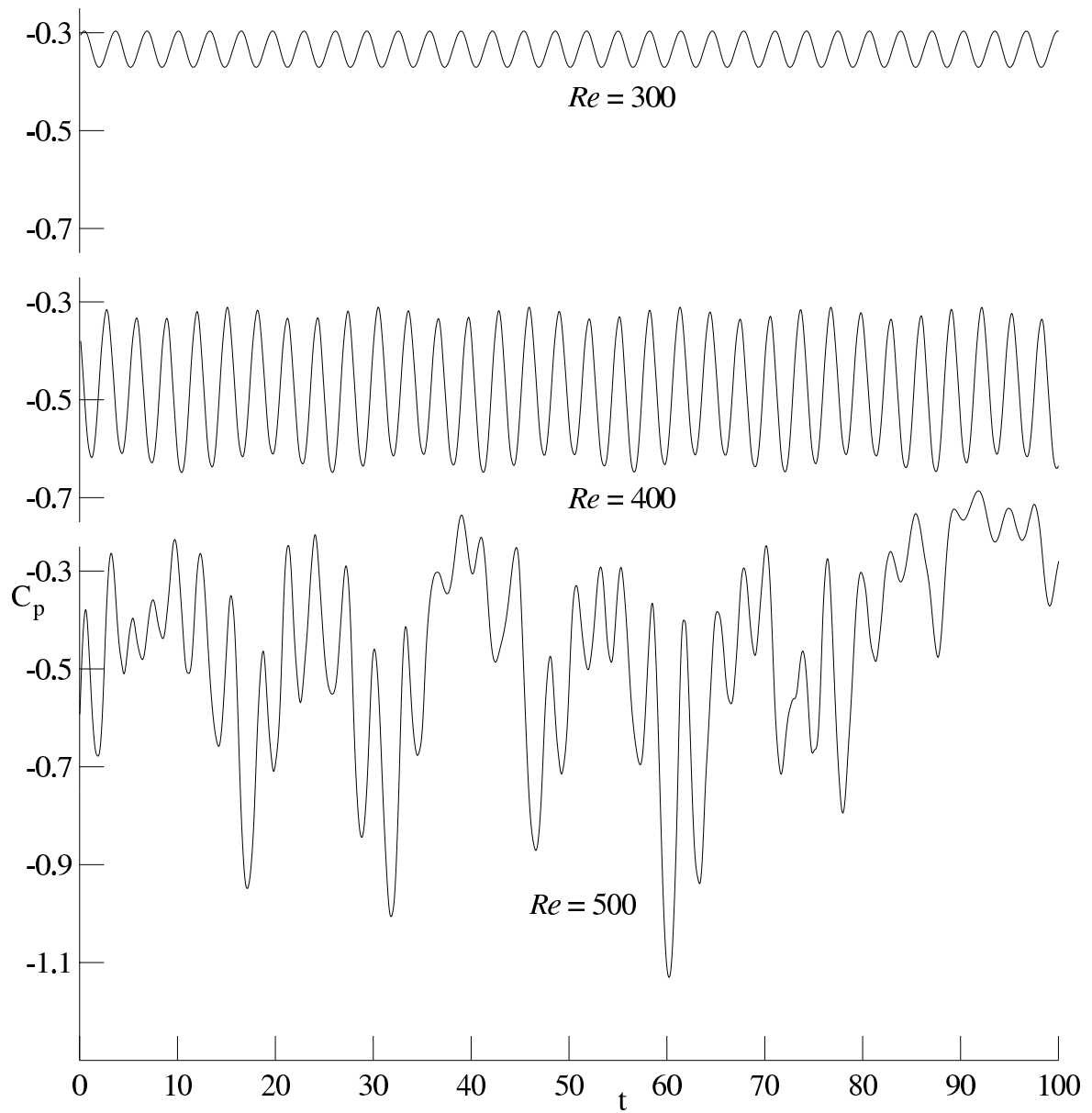


Figure 4.2: A 100 time unit sample of the base pressure trace taken when the flow around a rectangular plate with  $c/t = 10$  has reached an asymptotic state for  $Re = 300$ , 400 and 500.

variation in the shedding frequency as the Reynolds number is varied unlike the elliptical leading-edge plate and short bluff bodies. The frequency selection is less dependent on Reynolds number when the ILEV instability locks the flow. In experimental observations, Nakamura *et al.* (1991) also observed that the shedding frequency is almost independent of Reynolds numbers while the flow was controlled by this instability. In all the cases where the flow is dominated by the instability which synchronises the leading- and trailing-edge shedding, there is an increase in mean base suction, mean drag and fluctuating lift forces. When this instability no longer dominates (i.e. at  $c/t = 10$  and  $Re = 500$ ), there is a drop in these three properties from the lower Reynolds number case ( $Re = 400$ ) indicating that this instability contributes to an increase in the forces experienced by the plate. It is uncertain if this is a general trend because this observation is only based on simulations at three different Reynolds numbers.

### 4.1.2 Shedding modes

In this section, the aspect ratio of the plate is varied while keeping the Reynolds number at  $Re = 400$  with the aim of capturing the various shedding modes. The plates studied range in aspect ratio between  $c/t = 3$  and 16 at intervals of unity. Initially, the shedding frequency estimated from the base pressure trace is presented for those plate lengths that show a distinct shedding frequency resulting from the ILEV instability. Vorticity plots of the flow at these aspect ratios will show the different shedding modes associated with this instability. The base pressure trace will show that there are some random fluctuations between shedding cycles, especially at the longer aspect ratios, for each mode.

The shedding frequencies for the different plates are shown in Figure 4.3. As the plate is lengthened from  $c/t = 3$  to 5, the shedding frequency decreases. It then rises again at  $c/t = 6$  before following the same trend with another jump at  $c/t = 9$ . For plates longer than  $c/t = 10$ , the flow does not show one distinct frequency except for  $c/t = 13$ . When the shedding frequency is normalised with the chord rather than the thickness of the plate, the graph shows distinct steps of approximately  $St = 0.55n$  with each step corresponding to a shedding mode. As discussed in the first chapter, each shedding mode has an integer number of vortices along the plate. As the chord is increased, assuming the convective velocity along the plate is not significantly influenced by the aspect ratio, the vortices shed from the leading edge take longer to reach the trailing edge, thus the reduction in shedding frequency. This continues until the flow is no longer receptive to such a low frequency, then it jumps to the next shedding mode. It is hypothesised that the longer plates fail to lock to a particular shedding mode because the pressure pulse drops below the threshold required to lock the leading-edge shedding. As the pressure pulse travels out radially from the trailing edge, the level at the leading edge decreases as

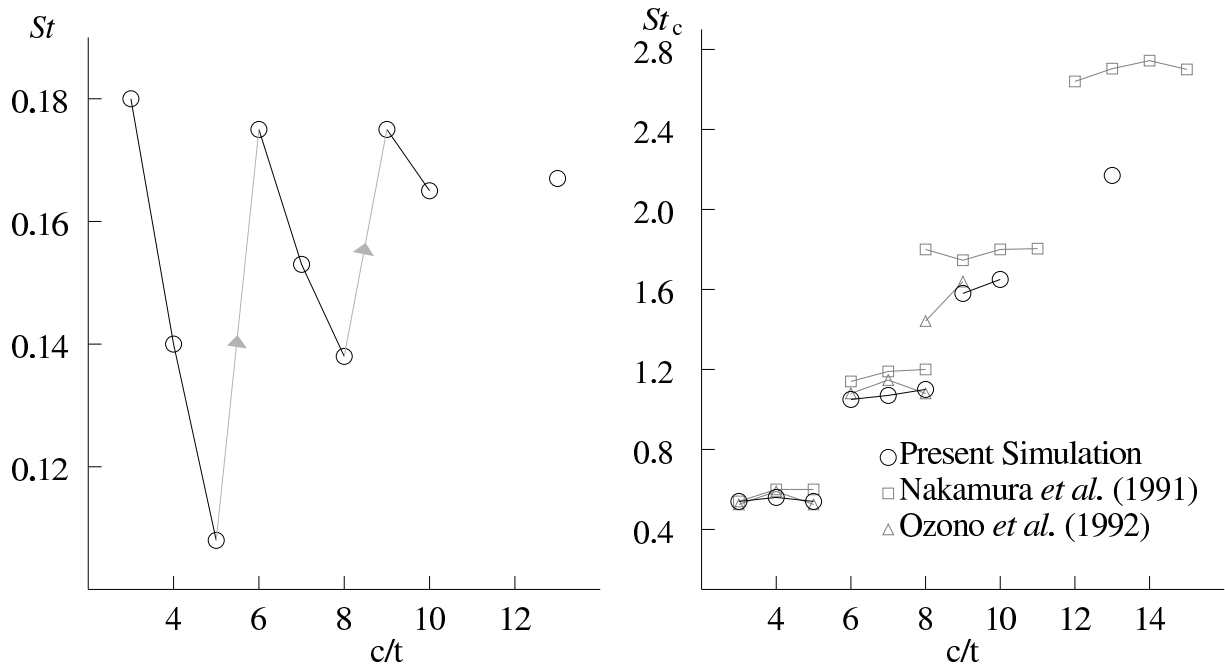


Figure 4.3: Shedding frequency as a function of aspect ratio at  $Re = 400$ . On the left, the Strouhal number is based on thickness while on the right it is based on chord. The graph on the right also shows a comparison of previous numerical and experimental results.

the plate is lengthened.

The non-dimensional frequency based on chord ( $St_c$ ) is the shedding frequency multiplied by the chord and divided by the free-stream velocity (i.e.  $St_c = cf/U_\infty$ ). The different steps (shedding modes,  $n$ ) represent the number of vortices along the plate or the number of shedding periods required for a leading-edge vortex to travel the length of the plate. The average convective velocity of a leading-edge vortex along the plate is therefore the distance travelled by the vortex ( $c/n$ ) in one period ( $1/f$ ) (i.e.  $\overline{V_{conv}} = cf/n$ ). Therefore the Strouhal number based on chord ( $St_c$ ) is the ratio of the average convective velocity of the vortices along the plate and the free-stream velocity, multiplied by the shedding mode (i.e.  $St_c = (\overline{V_{conv}}/U_\infty)n$ ). The stepwise behaviour signifies that the average convective velocity along the plate is approximately constant for all those plates that lock to the instability and equivalent to the height of the steps which is 55% of the free-stream velocity (i.e.  $\overline{V_{conv}}/U_\infty = 0.55$ ).

Also shown in Figure 4.3 are the results from simulations by Ozono *et al.* (1992) and experiments by Nakamura *et al.* (1991). These results are in good agreement with the simulations at a Reynolds number of  $Re = 1,000$  by Ozono *et al.* (1992) suggesting that the two-dimensional simulations are less dependent on Reynolds number. The results differ more, especially for the longer plates, from those of Nakamura *et al.* (1991) because

the shedding frequency in the experiments is approximately  $St_c = 0.6n$ . This difference is likely due to the difference in convective velocity of the vortices along the plate which could be influenced by the three-dimensional flow and higher Reynolds numbers in the experiments.

Figure 4.4 shows the vorticity plots for all the cases where the flow is locked to a particular shedding mode. These plots are taken at approximately the same phase in the shedding cycle. They show that the aspect ratios of  $c/t = 3, 4$  and  $5$ ,  $c/t = 6, 7$  and  $8$ ,  $c/t = 9$  and  $10$ , and  $c/t = 13$  correspond to the shedding modes of  $n = 1, 2, 3$  and  $4$  respectively. The flow around plates at the lower aspect ratio end of each step, which are shedding at higher frequencies (i.e. at  $c/t = 3, 6, 9$  and  $13$ ), show the vortices forming more closely to the trailing edge and a smaller horizontal spacing between the vortices in the wake. At the higher aspect ratio end of each step (i.e. at  $c/t = 5$  and  $8$ ), the lower frequency shedding also results in less regular wake vortices. All these plots are taken at approximately the same phase in the leading-edge shedding cycle. The trailing-edge shedding also appears to be at the same phase in the cycle for all the different plate lengths. Vortices are shed from the trailing edge between the passing of leading-edge vortices. Previous studies assert that the ILEV instability mechanism synchronises the the leading-edge shedding with the passing of these vortices at the trailing edge because the latter generates a pressure pulse (Naudascher & Wang, 1993, Mills, 1998). These simulations show strong base shedding which are also locked in phase by the influence of leading-edge vortices. These would generate stronger pressure fluctuations which influences the leading-edge shedding thus completing the feedback loop. A modification to the ILEV mechanism to incorporate the role of base shedding and better describe this process is proposed in a later section (Section 6.3.3).

For the same feedback mechanism to lock the flow independent of aspect ratio, the phasing between the leading- and trailing-edge shedding would have to be constant. This ensures that the phase in the shedding cycle at which the leading-edge vortices pass the trailing edge and the signal (pressure pulse) from the trailing edge affecting the leading edge is constant for all plate lengths which lock to this instability. This has also been observed in water tunnel experiments by Mills (1998) at  $Re = 490$  and wind tunnel experiments by Nakamura (1991) at  $Re = 1,000$ . The constant phase relationship also ensures a similar shedding cycle within a shedding mode as the chord is varied and a complete pair of vortices along the plate between modes. This has been shown by phase measurements along the side of the plate and in the path of the vortices convecting downstream by Nakamura *et al.* (1991). Besides a similar phase relationship between the leading- and trailing-edge shedding, all the vorticity plots in Figure 4.4 also show both the leading- and trailing-edge shedding to be at approximately the same stage in the shedding cycle. Both leading- and trailing-edge vortices are in the process of forming on

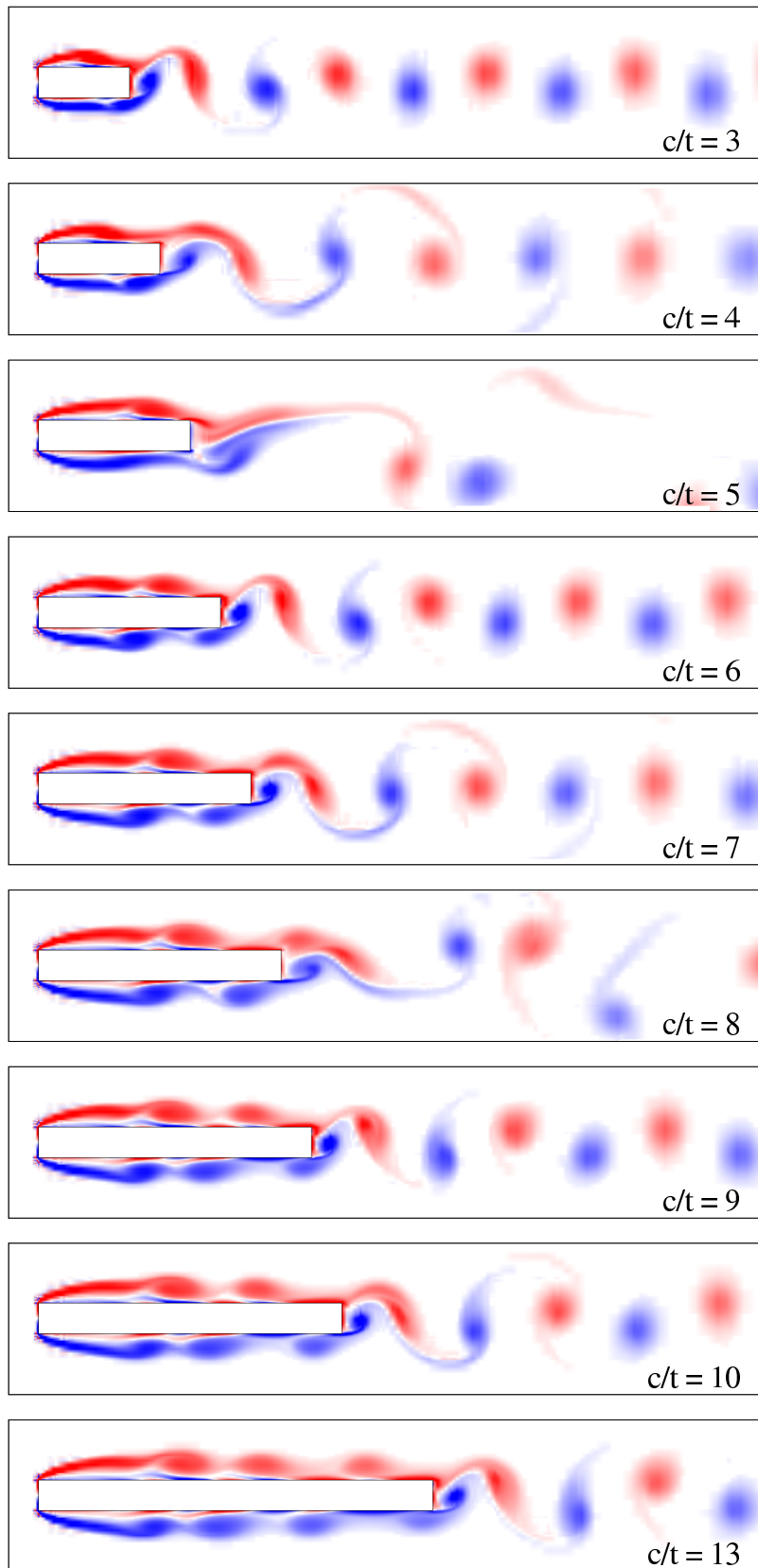


Figure 4.4: Vorticity plots of flow around rectangular plates at  $Re = 400$  taken at approximately the same phase in the shedding cycle for the various aspect ratios.

the bottom side of the plate. On the top side, the leading-edge vortex has just shed and so has the vortex from the trailing edge.

The trace of the base pressure is studied to gauge the temporal behaviour of the flow. Traces of 100 time units of base pressure for plates with  $c/t$  from 7 to 11, and also 13, taken after the flow has reached an asymptotic state are shown in Figure 4.5. At  $c/t = 7$ , the base pressure shows a nearly perfect sinusoidal signal. Although this aspect ratio corresponds to approximately the middle of the step, the moderate aspect ratio allows the instability to lock the flow resulting in a state which is very close to periodic. When the plate length is increased to  $c/t = 8$ , although there is still a distinct shedding frequency, there also appear to be several longer wavelengths present. The low frequency of the shedding results in the flow not being as receptive to the instability. This is reflected in small differences between shedding periods. There is a change in shedding mode and a jump in frequency when the aspect ratio is increased to  $c/t = 9$ . The base pressure trace shows the shedding to be approximately periodic which suggests that the flow is well locked to the instability just after the transition. This behaviour associated with the transition from one shedding mode to another is also evident for the smaller aspect ratios. At  $c/t = 10$  there are small fluctuations between shedding periods suggesting that the control of the instability is weakening. Unlike at  $c/t = 8$ , there are many more random fluctuations at  $c/t = 11$ . This is after the simulations were evolved for 1,000 time units. This is caused by the instability having less control for longer plates and the flow being less receptive at the longer plate end of each step. The base pressure trace for  $c/t = 12$  is similar. At  $c/t = 13$ , the start of the next step, the instability is able to lock the flow but there are already small fluctuations between shedding cycles. Above this aspect ratio, the base pressure trace is not dominated by a single shedding period. Traces of the lift coefficient in simulations by Ozono *et al.* (1992) also showed a similar trend in that the signal was closer to periodic towards the lower aspect ratio within each step. Also note that the mean base suction is higher when the flow is more receptive to the instability (i.e. at the shorter aspect ratio within each step). This aspect will be discussed in the next section (Section 4.1.3).

To gauge the strength of the instability at  $c/t = 11$ , spectral analysis is performed on the base pressure trace of the asymptotic flow state. The spectrum shown in Figure 4.6 is obtained from 1000 time units of data sampled every 0.175 time units. Although there are other frequencies present, the frequency at  $St = 0.300$  which is two times that of the shedding frequency (because it is measured at the centre of the trailing face) corresponds to the third shedding mode (i.e.,  $St = 0.150$  is equivalent to  $St_c = 1.65$ , which is the third shedding mode based on  $St_c = 0.55n$ ). The other shedding frequency of  $St = 0.243$  ( $St_c = 1.33$ ) is a frequency between the second and third mode. The leading-edge shedding from both sides of the plate is no longer synchronised when the flow is not locked to a

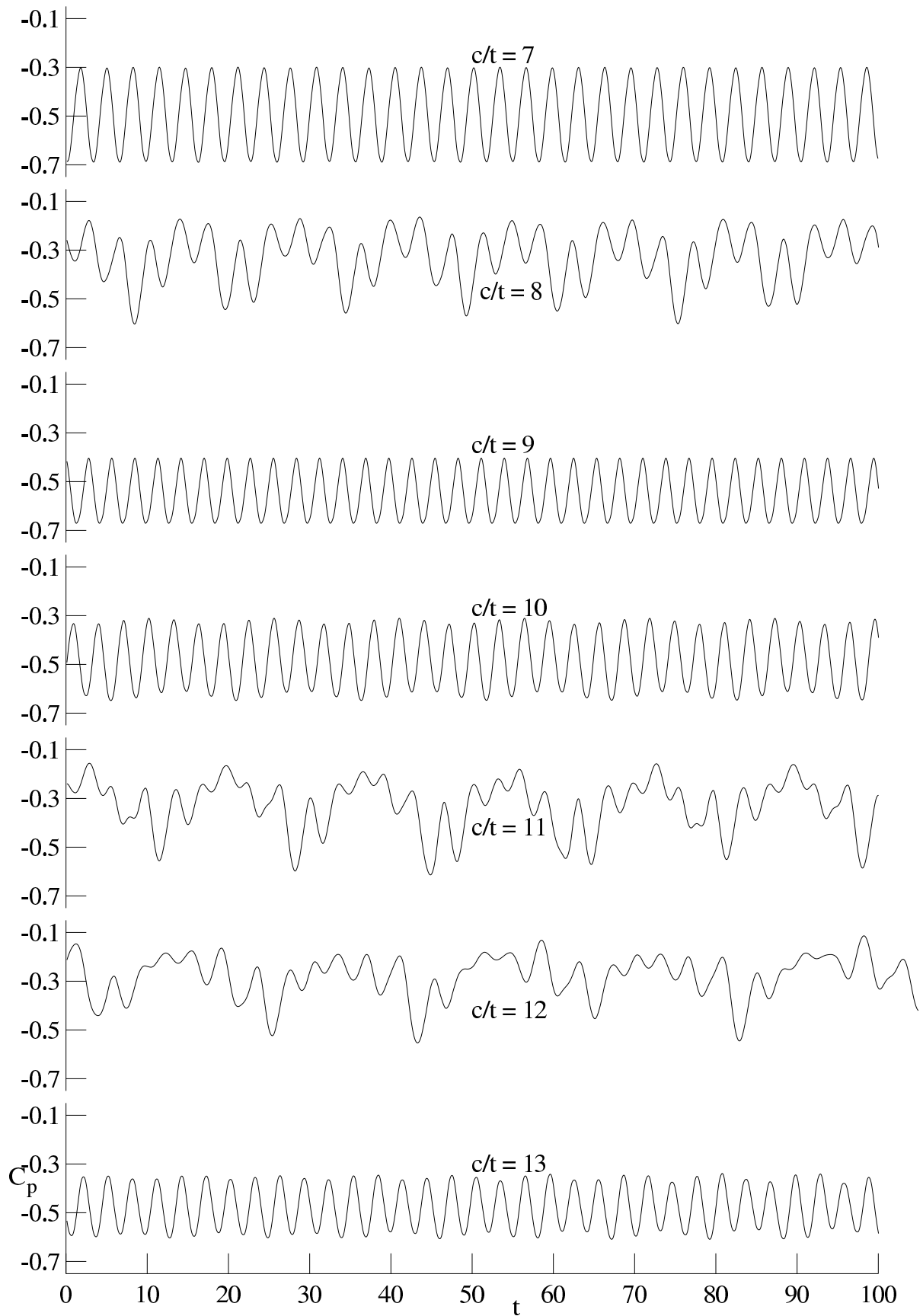


Figure 4.5: A sample of 100 time units of the base pressure trace for flow around rectangular plates at several aspect ratios at  $Re = 400$ .

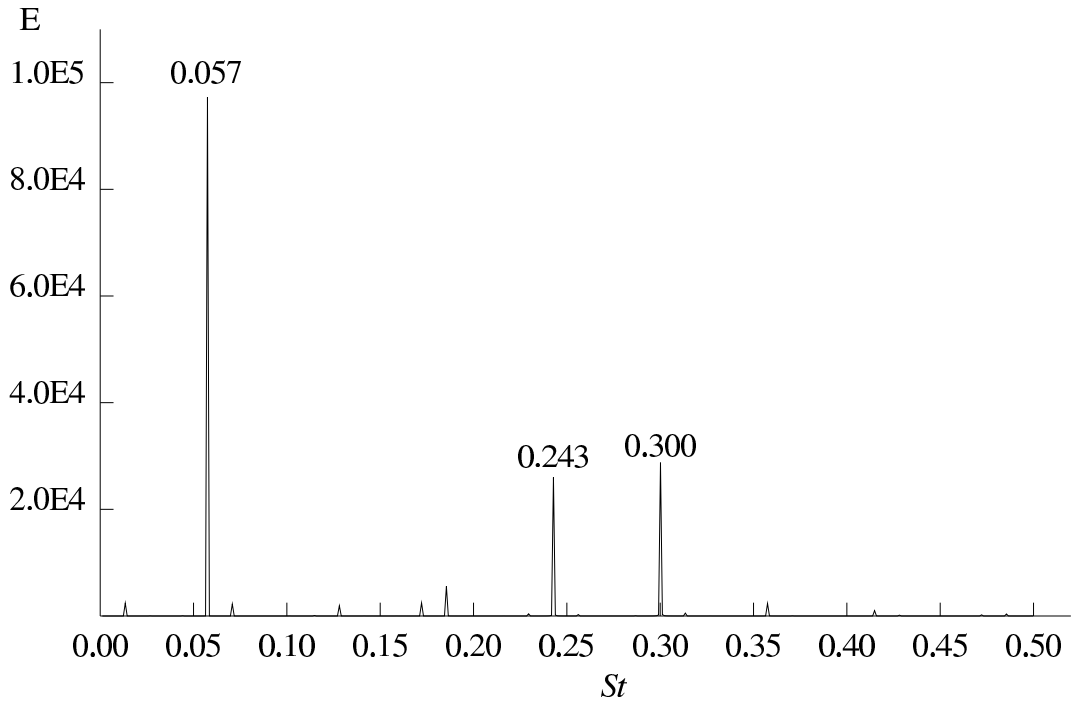


Figure 4.6: A spectral plot of the base pressure trace for a plate with  $c/t = 11$  at  $Re = 400$ .

particular shedding mode. This is likely to cause a mismatch in the number of vortices on both sides of the plate in some periods which would result in an asymmetry between the leading- and trailing-edge shedding. In those periods, the shedding is in between modes (i.e. three vortices on one side and two on the other) and the shedding frequency is at an intermediate level between steps. The lower frequency in the spectrum (i.e. at  $St=0.057$ ) corresponds to the difference in the two shedding frequencies and is caused by the presence of the two signals (associated with the two shedding processes) in the trace. For the longer plates which do not lock to a particular shedding mode, the ILEV frequencies are present in the flow and become relatively weaker as the chord is increased.

### 4.1.3 Base pressure and forces

Plots of the mean base pressure coefficient, mean drag coefficient and fluctuating lift coefficient as a function of aspect ratio are presented in Figure 4.7. Viscous forces are neglected in the calculation of the overall forces because they are expected to be relatively small at these moderate Reynolds numbers. It is evident that the mean base suction and therefore mean drag is higher at the lower aspect ratio end of each step. The possible contributing factors to this behaviour include how strongly the flow is locked by the ILEV instability and the higher receptivity of the trailing edge to the higher frequency.

As discussed in the previous section, the flow is strongly locked at the lower aspect ratio end of each step and the shedding is more regular. The vorticity plots for those aspect ratios show more compact vortices forming closer to the trailing edge. The shedding at the trailing edge is therefore more receptive to the higher frequency and this is reflected in the mean base pressure and drag coefficient. The overall magnitude and the difference between the lower and upper aspect ratios of each step is smaller for the longer plates. The longer plates develop thicker boundary layers at the trailing edge which result in less vigorous shedding. The ILEV instability has less of an influence on the flow at larger aspect ratios. These two factors may contribute to the smaller values and difference within each step for the longer plates. Although the longer plates ( $c/t > 11$  except  $c/t = 13$ ), do not lock to the ILEV shedding frequency, the trends in base pressure and force coefficients associated with this instability are still observed. When the ILEV instability no longer controls the shedding, there is still a significant amount of the energy in that frequency as shown by the spectral plot of base pressure coefficient for  $c/t = 11$  and this still influences the forces on the plate, although less so than for the shorter plate. Mean base pressure measurements by Mills (1988) show that this trend is not present at higher Reynolds numbers ( $Re \approx 9,000$ ) where the instability no longer governs the flow. Okajima (1990) and Okajima *et al.* (1990) presented simulated and experimental results of mean drag force and pressure coefficients up to  $c/t = 8$  at low Reynolds numbers ( $250 < Re < 1200$ ) which also show a small increase at the shorter aspect ratio end of each shedding mode.

There is a decrease in the fluctuating lift force as the plate length is increased. For the rectangular plate, only the top and bottom surfaces contribute to lift forces. The lift forces from pairs of vortices along the plate cancel out. The fluctuating component of the lift is mainly from the alternate shedding from the leading edge and the mismatch at the trailing edge. As these processes occur for all the plates and the coefficient is based on the chord, an inverse relationship with aspect ratio is expected. The data does show an approximate inverse relationship. Further discussion on this will be provided after the fluctuating lift forces in the forced shedding case have been presented. Superimposed on this inverse relationship, although less significant, is an effect similar to that found for the mean drag force in that there is a higher fluctuating lift component at the lower aspect ratio end of each step. The higher frequencies at the lower aspect ratio end of each step also result in more compact leading-edge vortices. The larger fluctuations in lift forces, and the shedding of more compact vortices, indicate that the leading-edge shedding is also more vigorous at higher frequencies.

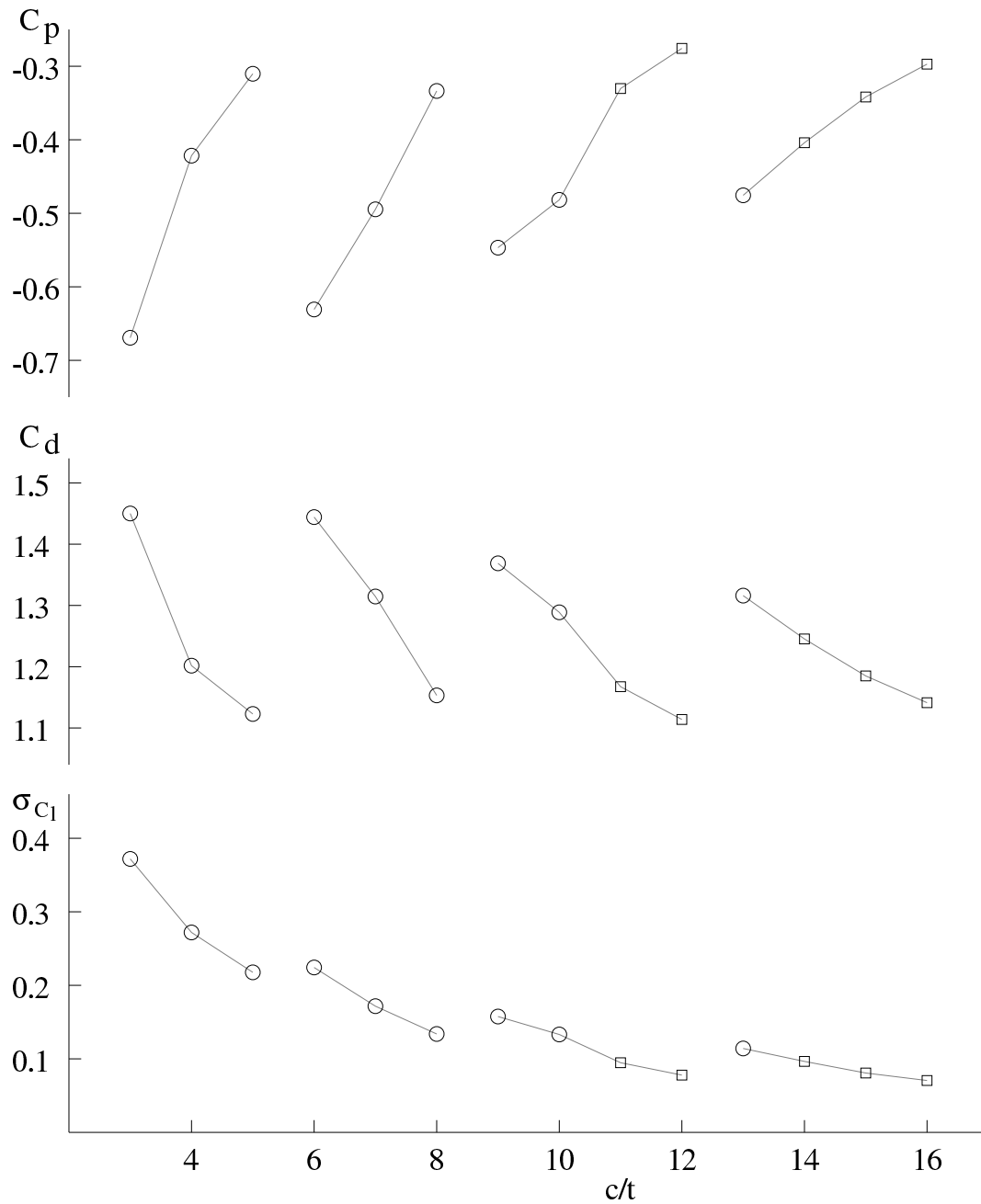


Figure 4.7: Mean base pressure coefficient, mean drag coefficient and standard deviation of lift coefficient as a function of the aspect ratio for flow around rectangular plates at  $Re = 400$ . The circular symbols represent cases where the flow shows an association with a particular shedding mode while the squares represent the cases where the flow is not strictly locked to any shedding mode.

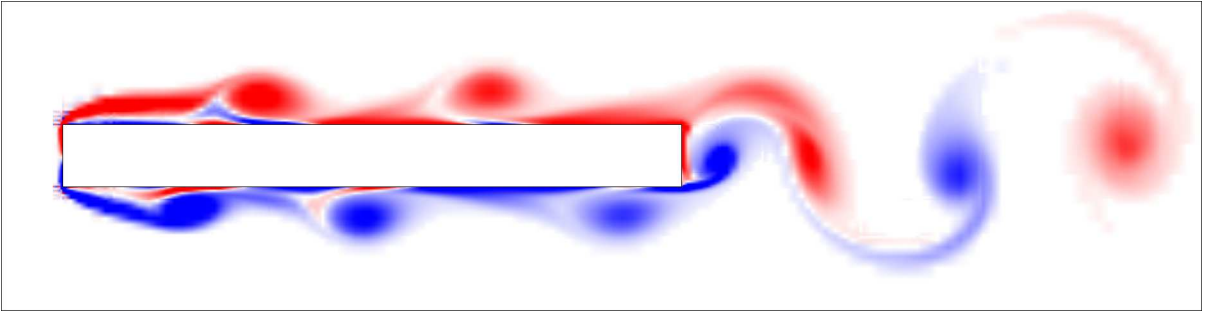


Figure 4.8: A vorticity plot taken at  $90^\circ$  in the forcing cycle for flow over a  $c/t = 10$  plate with an applied forcing at  $St = 0.16$  and  $v_{pert} = 2.5\%$ .

## 4.2 Applied forcing

This section examines how the flow around a long rectangular plate is influenced by a small sinusoidal cross flow oscillation added to the free-stream flow. Initially, the base pressure is used to gauge the response of the flow as it is a good indicator and closely related to the drag force. The effects of Reynolds number, forcing amplitude and aspect ratio are examined. As the forcing amplitude has been measured near the plate in the experimental data used for comparison, several simulations are performed in the absence of the mean flow as in the experiments to determine the level of the forcing near the edges relative to the applied far field amplitude. The overall forces on the plate are also examined in the later part of this section.

To visualise the effect of applied forcing on the flow structure, Figure 4.8 shows a colour contour vorticity plot taken at  $90^\circ$  in the forcing cycle for flow over a plate with  $c/t = 10$ ,  $St = 0.16$  and  $v_{pert} = 2.5\%$ . This forcing frequency results in the strongest mean base suction within the lock-in range. The applied forcing results in several key differences compared with the natural shedding cases. Starting from the leading edge, the shear layer reattaches earlier and more compact vortices are shed. These remain more compact while they convect toward the trailing edge and coalesce with the vortices shed from there. The vortices at the trailing edge are marginally more compact than those in the natural shedding case.

### 4.2.1 Effect of Reynolds number

The effect of Reynolds number is studied for a plate with  $c/t = 10$  and  $v_{pert} = 2.5\%$ . Simulations were performed for Reynolds numbers of  $Re = 300$ ,  $400$  and  $500$ . Each simulation is started with the velocity field from an unforced simulation at the same

Reynolds number after reaching an asymptotic state. In the asymptotic state, the lock-in range of frequencies is larger than for the flow over elliptical leading-edge plates. In this lock-in range, the base pressure trace shows a repeatable signal like those presented in the previous chapter. For this plate and forcing amplitude, the lock-in ranges at  $Re = 300, 400$  and  $500$  are approximately  $St = 0.09 - 0.17, 0.12 - 0.23$  and  $0.11 - 0.24$ , respectively. Within this range, both leading- and trailing-edge shedding lock to a single frequency. The overall study will focus here because the forcing significantly alters the mean base pressure and forces on the plate in this range. As the forcing frequency moves outside this range, the trace shows the influence of other frequencies but no clear longer wavelengths like those found for the elliptical leading-edge plates. The predominantly convective nature of the leading-edge shedding (Soria & Wu, 1992) is likely the main factor for the large frequency range in which the flow locks to the forcing. For small acoustic cross-flow perturbations, Parker & Welsh (1983) found the leading edge to be phase-locked from  $St = 0.05$  to  $0.25$  for  $7.6 < c/t < 16$ . Within this range, the flow locks to the forcing and that is the only frequency prominent in the near wake. Simulations by Okajima & Kitajima (1993) at  $Re = 1,000$  also found a large lock-in region starting from around  $St = 0.07$  to  $St = 0.5$  which was the highest frequency studied. Although these simulations were for shorter plates ( $c/t \leq 3$ ), the flow does reattach to the plate. The wider lock-in range is also a result of the large oscillation amplitude used which was 14% of the thickness of the plate. Based on the perturbation velocity near the plate (which will be studied later), this is between two to three times the forcing amplitude used in the simulations when  $v_{pert} = 2.5\%$ .

The mean base pressure coefficient as a function of the forcing frequency is shown in Figure 4.9. The base pressure coefficient and shedding frequency in the unforced case (also plotted) are from Table 4.1. The responses at the three different Reynolds numbers do not differ significantly. When the forcing frequency is well below the natural shedding frequency, the mean base suction is much less than the natural shedding case. There is a small peak in the mean base suction at approximately  $St = 0.10$  at  $Re = 300$  and  $400$  and a more prominent peak at  $St = 0.12$  at  $Re = 500$ . As the forcing frequency is increased, there is a gradual increase in the mean base suction followed by a more dramatic drop. The forcing frequency where the mean base suction peaks is close to the natural shedding frequency for the flow at  $Re = 300$  and  $400$  and does not vary significantly with Reynolds number. These peaks will be investigated in later sections (Section 4.2.6, 4.3.4, 4.3.6 and 4.3.7). When the forcing frequency is increased further, the mean base suction again reduces to below that of the natural shedding cases. At forcing frequencies away from the natural shedding frequency the flow remains locked to the forcing, and the shedding, especially from the trailing edge, is likely to be less receptive at these frequencies resulting in the lower mean base suction. A limited number of simulations outside the lock-in range

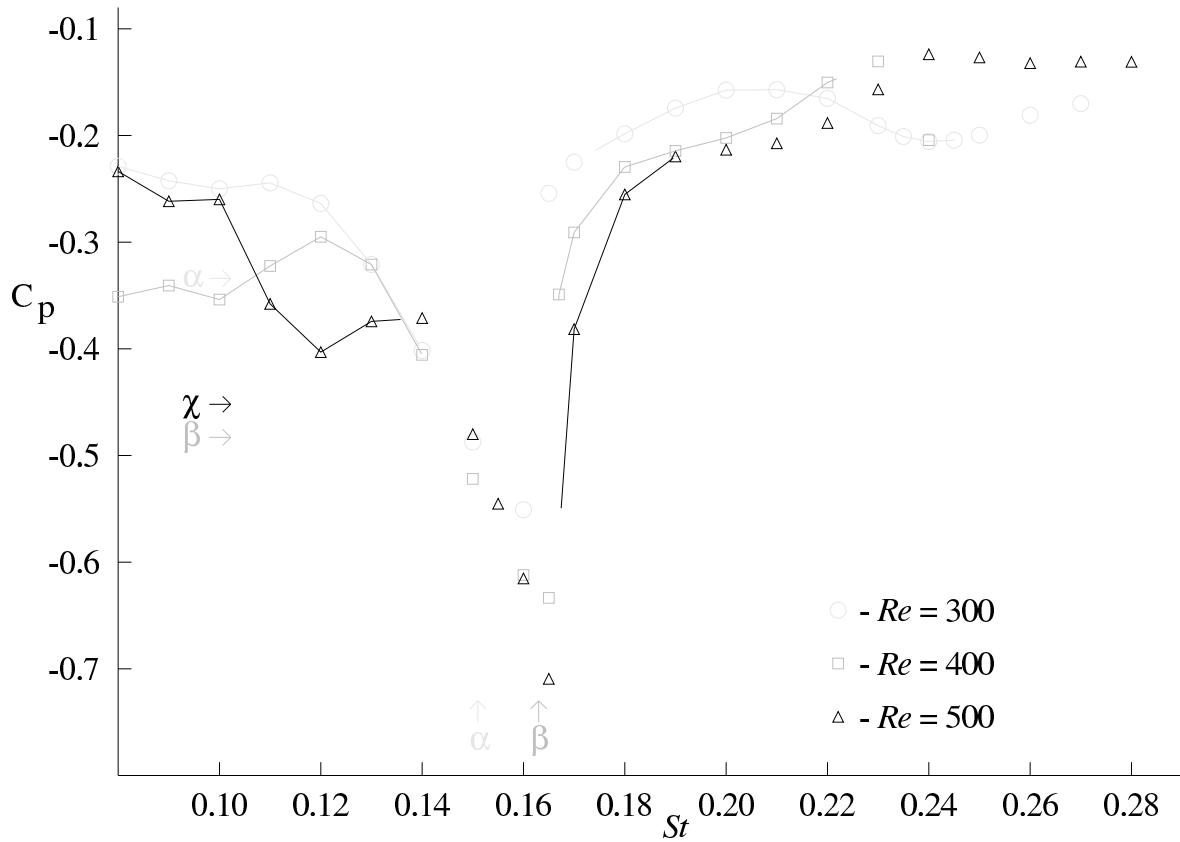


Figure 4.9: Mean base pressure as a function of the forcing frequency for a plate with  $c/t = 10$  and  $v_{pert} = 2.5\%$ . Horizontal and vertical arrows show the mean base pressure and shedding frequency in the unforced cases. The symbols  $\alpha$ ,  $\beta$  and  $\chi$  correspond to  $Re = 300$ ,  $400$  and  $500$ .

also show this trend suggesting that the forcing still has a significant influence on the flow over the feedback mechanism that occurs in the absence of forcing in some cases.

## 4.2.2 Effects of the amplitude of forcing

In this section, simulations with three different levels of forcing are performed to ascertain the effect on the mean base pressure. These are performed for a plate with  $c/t = 10$  at  $Re = 400$ . The mean base pressure coefficient as a function of forcing frequency for forcing amplitudes of  $v_{pert} = 1.25\%$ ,  $2.5\%$  and  $5.0\%$  is shown in Figure 4.10. At the lowest forcing amplitude, the frequency range at which the flow locks to the forcing is marginally narrower. The lock-in range started from  $St = 0.12$  and the flow remained locked until  $St = 0.19$  which was the highest frequency simulated. At the highest forcing amplitude, the flow locked to the forcing in the entire frequency range simulated (i.e.  $0.12 \leq St \leq 0.20$ ).

The different levels of forcing have only a small effect on the mean base pressure compared to the elliptical leading-edge plates. (Further evidence is presented in Section 4.2.3.1). The level of forcing in the cases with an elliptical leading-edge plate governs the frequency range where the flow locks to the forcing (see Figure 3.13). It is within this range where the forcing has a larger influence on the mean base pressure by controlling the shedding frequency. For the flow around elliptical leading-edge plates, an increase in forcing amplitude also leads to larger deviations in mean base pressure relative to the natural shedding case.

For the rectangular plates, the flow is locked to the forcing over a larger frequency range. In this case, the effect of increasing the forcing amplitude is only significant at forcing frequencies near the peak in mean base suction. This is where the trailing-edge shedding of the rectangular plate is more vigorous and the dependence on forcing amplitude is similar to the flow around elliptical leading-edge plates. There is also an increase in the forcing frequency at which the mean base suction peaks as the forcing amplitude is increased, although smaller than the case with an elliptical leading edge. (That is, for the rectangular plate the peaks occurs at  $St = 0.165$  when  $v_{pert} = 5.0\%$  and natural shedding frequency is  $St = 0.163$  while for an elliptical leading-edge plate with  $c/t = 7.5$  the peak is at  $St = 0.21$  when  $v_{pert} = 5.0\%$  and natural shedding frequency is  $St = 0.196$ .)

Wind tunnel experiments by Mills (1988) also recorded mean base pressure coefficients for various plate lengths, forcing amplitudes and Reynolds numbers. The forcing frequency at which the mean base suction peaks is approximately constant when the

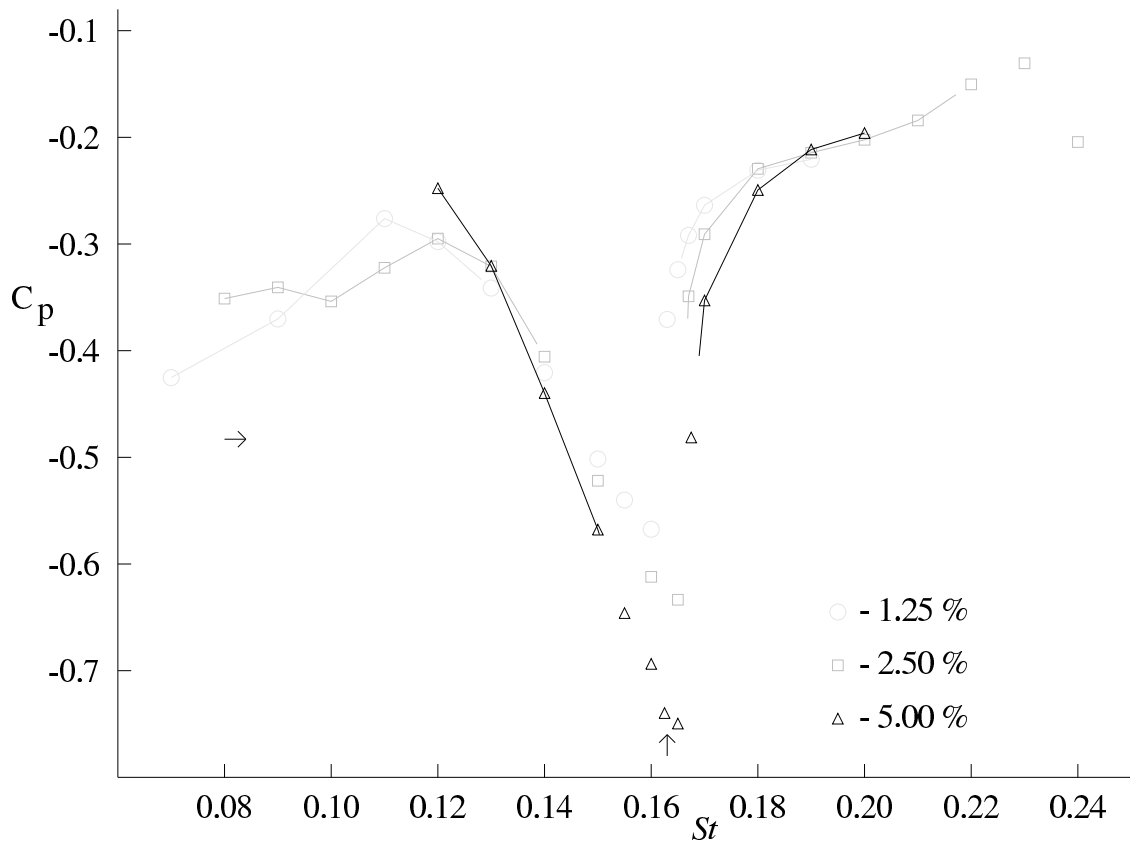


Figure 4.10: Mean base pressure coefficient as a function of forcing frequency for three different forcing amplitudes. The flow parameters were  $Re = 400$  and  $c/t = 10$ .

Reynolds number is varied between 5,  $200 \leq Re \leq 12,130$ . Within this range, the overall magnitude of the mean base suction increases with Reynolds number. Although the simulations are performed only in two dimensions, and at much lower Reynolds numbers, these trends are also present for the various Reynolds numbers simulated with an aspect ratio  $c/t = 10$ .

A set of experiments were also performed at a constant Reynolds number of  $Re = 8,667$  but varying the forcing amplitudes between 3% and 5% of the free-stream velocity. The “forcing amplitude” is measured near the plate and how this relates to the far field forcing amplitude ( $v_{pert}$ ) in the simulations will be discussed in Section 4.2.4. Increasing the forcing amplitude generally increased the mean base suction but larger increases also occurred at forcing frequencies where the mean base suction is stronger (i.e., forcing amplitude behaves like an amplification factor of the base suction). The increase in forcing amplitude also caused the mean base suction to rise over a larger band of forcing frequencies. This suggests that the larger forcing amplitude asserts control over the flow over a larger frequency range. The increase in forcing amplitude does not cause the forcing frequency at which the mean base suction peaks to vary significantly except for aspect ratios of  $c/t = 6$  and 7. Mills (1988) suggested that the exception is likely caused by some influence of the ILEV instability mechanism. Parker & Welsh (1983) observed a distinct shedding frequency for plates with  $c/t \leq 7.6$ , even for  $Re > 2,000$  in the natural shedding case.

As in the experimental observations, the numerical simulations also show a greater rise in mean base suction with forcing amplitude, especially where the mean base suction is strong. Another similarity between the experimental and simulated results is the small variation in the forcing frequency which would result in the peak base suction when the forcing amplitude is varied. Unlike the experimental trend, the frequency band where the forcing causes a significant increase in the mean base suction does not grow significantly with forcing amplitude in the simulations. The lock-in range in the simulations even at the small perturbation amplitude is large and grows only marginally with forcing amplitude. There is uncertainty over the lock-in range in the experiments. The response over a larger frequency range in the experiments could be a result of the lock-in range growing with forcing amplitude.

### 4.2.3 The response at various aspect ratios

Flow over plates with aspect ratios  $6 \leq c/t \leq 16$  are simulated for a range of forcing frequencies at  $Re = 400$  and  $v_{pert} = 2.5\%$ . A large lock-in range was also observed for all the plates which ranged from  $St = 0.13$  to  $St = 0.20$  (highest frequency simulated) for

the shortest plate ( $c/t = 6$ ), and  $0.09 \leq St \leq 0.19$  for the longest plate ( $c/t = 16$ ).

The behaviour of the mean base pressure coefficient as a function of forcing frequency both predicted by the simulations and measured experimentally by Mills (1988) is shown in Figure 4.10. Referring to the simulations, plates with an aspect ratio of  $c/t = 6, 7, 10, 11, 15$  and  $16$  show a single peak in the mean base suction. These peaks are generally larger than for plates with aspect ratios of  $c/t = 8, 9, 12, 13$  and  $14$ . For the second set there are two less prominent peaks although one of them is barely noticeable. There is a distinct trend in the frequency at which the mean base suction peaks. Beginning with  $c/t = 6$ , a local maximum base suction is recorded for  $St = 0.17$ . As the aspect ratio is increased to  $c/t = 7$ , the Strouhal number at which maximum base suction occurs drops to  $St = 0.16$ , then  $St = 0.14$  at  $c/t = 8$  and  $St = 0.12$  for  $c/t = 9$ ; with the last two much less noticeable. Plates with an aspect ratio of  $c/t = 8$  and  $9$ , which show two local peaks, have peaks which start at  $St = 0.174$  for  $c/t = 8$  and reduce to  $St = 0.162$  at  $c/t = 9$ . There is a small jump in frequency when increasing the aspect ratio to  $c/t = 10$  which shows only a single peak at  $St = 0.165$ . Then with increasing aspect ratio, this peak shifts to  $St = 0.155$  at  $c/t = 11$ ,  $St = 0.14$  at  $c/t = 12$ ,  $St = 0.13$  for  $c/t = 13$  and  $St = 0.11$  for  $c/t = 14$  with again the last two being relatively small. Similar to the situation for  $c/t = 8$  and  $9$ , plates with  $c/t = 12, 13$  and  $14$  also show another local peak at a higher frequency which decreases with increasing plate length. For plates with  $c/t = 12, 13$  and  $14$ , these peaks are at  $St = 0.17, 0.157$  and  $0.155$  respectively. Similar to the trend starting at  $c/t = 10$ , there is a single larger peak at  $St = 0.155$  which then decreases to  $St = 0.145$  at  $c/t = 16$ . The experimental data of Mills (1988) also show a similar trend in that some plates peak with a strong mean base suction while others have a weaker peak. As with the simulations, the experimental data does show that the frequency at which the mean base suction peaks decreases with increasing plate length before jumping to a higher frequency. Within each set of peaks in the mean base suction, the experiments show that the magnitude is weaker towards the shorter and longer plate lengths and stronger at the intermediate lengths while in the simulations, the magnitudes of the peaks are smaller at the longer aspect ratio end of each set. The experiments do not show two local peaks in the mean base suction for those plates that have weaker peaks. These trends in the frequency and magnitude of the peak mean base suction with plate length will be further investigated in later sections (Section 4.2.6, 4.3.4, 4.3.6 and 4.3.7).

The predictions from the simulations and experimental results show some significant quantitative differences. Note the difference in range for the horizontal axes and scales for the vertical axes of these plots. The frequency range is chosen so as to fully represent the lock-in range at the applied forcing amplitude of  $v_{pert} = 2.5\%$  in the simulations. The perturbation amplitude was kept at  $5\%$  (measured near the plate) which because of experimental constraints restricted the lowest frequency to be at  $St = 0.13$ .

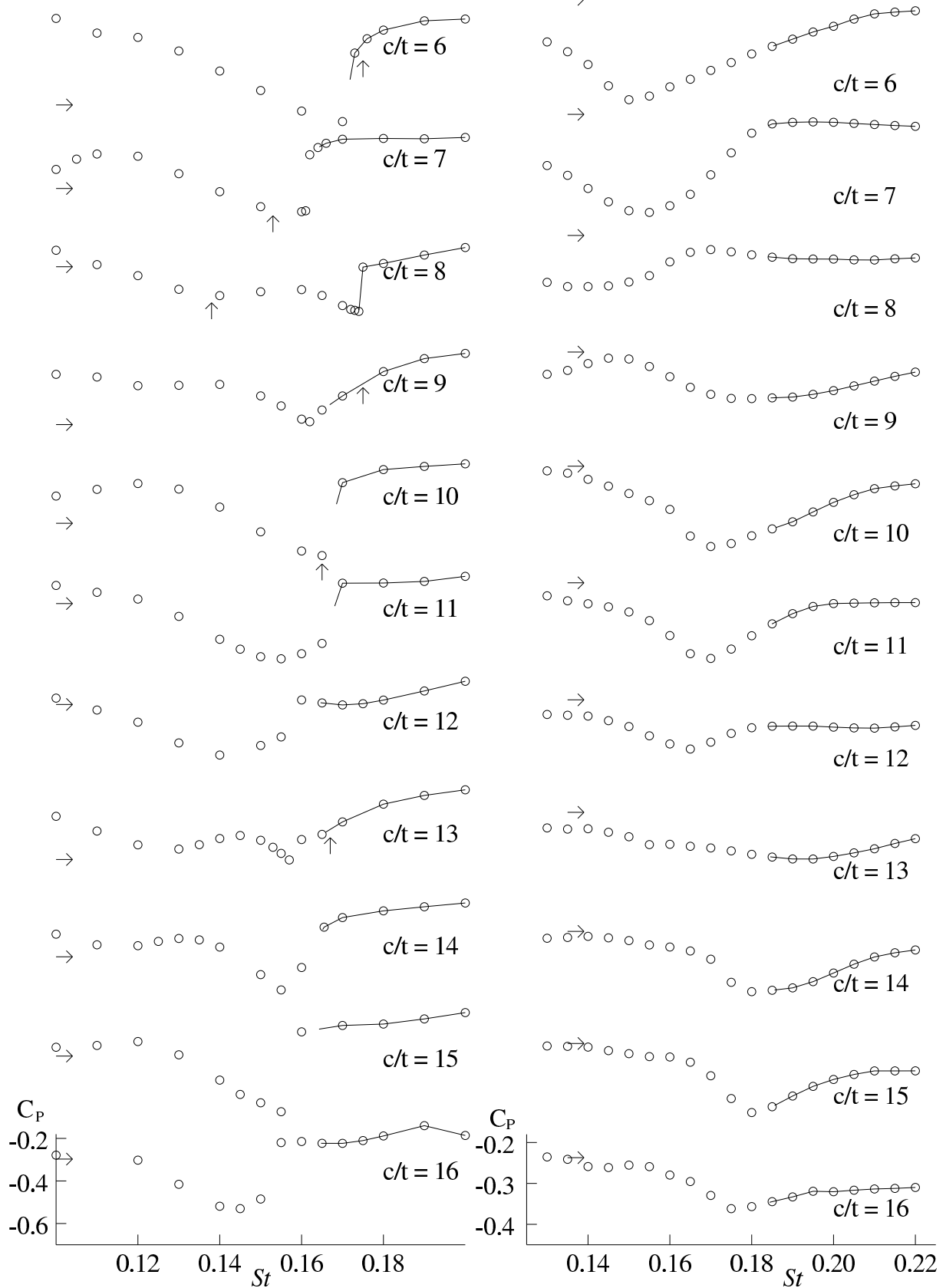


Figure 4.11: Mean base pressure coefficient as a function of forcing frequency for plates ranging from  $c/t = 6$  to  $c/t = 16$ . The simulations (left) are performed at  $Re = 400$  with a forcing amplitude of  $v_{pert} = 2.5\%$ . The mean base pressure without applied forcing is shown by the right arrows and the natural shedding frequency (if applicable) is shown by the vertical arrows. The experiments (right) were performed at  $Re \approx 9,000$  with a forcing amplitude of  $5\%$  of the free-stream velocity.

The experimental data at higher frequencies are not shown here because the forcing at those higher frequencies leads to a small variation in the mean base pressure coefficient relative to the natural shedding case. The simulations were performed in two dimensions at  $Re = 400$  while for the experiments  $Re = 9,000$ . Although the applied forcing suppresses some three-dimensionality in the flow field, it is present at higher Reynolds numbers (Hourigan *et al.*, 1993). The difference in Reynolds number, and the reduction in spanwise correlation in the experiments, result in the significant difference in the mean base pressure coefficient between the simulation and the experiment.

Alongside each plot is an arrow showing the mean base pressure when no applied forcing is present. The natural shedding frequency in the simulated cases which lock to a single frequency is also shown. The mean base pressure approaches that of the natural shedding at the lower and upper limits of the forcing frequency range in the experiments. The mean base pressure in the simulations for the unforced cases is still influenced by the ILEV instability and varies significantly with aspect ratio. In the forced cases, the forcing frequency at which the mean base pressure reaches a minimum (maximum base suction) does not coincide with the natural shedding frequency. The frequency selection for both of these cases will be discussed in Section 4.3.2. The trailing-edge shedding is sensitive to the forcing frequency as shown in Chapter 3. The different frequency of the trailing-edge shedding in the natural and forced shedding cases contributes to the differences in magnitude of the peak in base suction for the forced case and the natural case. Further discussion on the sensitivity of the trailing-edge shedding is included in Section 4.3.6 and 4.3.7. Those plates with relatively smaller peaks in the mean base suction, especially  $c/t = 9$  and  $c/t = 13$ , show that only at the peak mean base suction does the value in the forced shedding case approach the natural shedding case. In these cases, the natural shedding is locked strongly to the ILEV instability and sheds at a higher frequency. The forcing frequency at which the mean base suction peaks is lower and the trailing-edge shedding may not be as responsive to that frequency.

In general, there are large frequency subranges, especially away from the maxima, where the mean base suction is less than in the natural shedding case. In these subranges, the flow either locked to the forcing or was strongly influenced by it. The low mean base suction is a result of the trailing-edge shedding not being responsive to these frequencies. Vorticity plots in Section 4.3.3 will show that the trailing-edge shedding is suppressed at high forcing frequencies. Experiments by Bearman & Obasaju (1982) and Ongoren & Rockwell (1988) also observed that flow around short bluff bodies oscillated at higher frequencies can reduce the base suction to less than that without forcing. The suppression of the shedding at the trailing edge of the plate is likely to be similar to the mechanism controlling the base pressure in the cases involving the short bluff bodies. The experiments on the plate do not show any clear subrange in forcing frequency where the mean base

suction is below that of the natural shedding cases. The high Reynolds numbers and the three-dimensional nature of the flow may reduce the effect of the forcing which leads to less control of the flow especially at the upper and lower extremes of the forcing frequency range. In that situation, the mean base pressure will approach the unforced case.

#### 4.2.3.1 Smaller forcing amplitude

A set of simulations is performed with a lower forcing amplitude of  $v_{pert} = 1.25\%$  to verify that the trends observed in the previous section are relatively independent of the level of forcing. The Reynolds number is kept at  $Re = 400$  and the plate lengths simulated ranged from  $c/t = 6$  to  $c/t = 13$ . As a result of the smaller forcing amplitude, the lock-in range is expected to be smaller. The lock-in range for the shortest plate ( $c/t = 6$ ) is between  $St = 0.165$  and  $0.20$  (upper limit of forcing frequency) while for the longest ( $c/t = 13$ ) between  $St = 0.11$  and  $0.20$ . In the latter case these are the limits of the forcing frequencies examined. Plots of the mean base pressure coefficient as a function of the forcing frequency are shown in Figure 4.12 for the various plates. The plots contain predictions of mean base pressure when the forcing amplitude is at  $v_{pert} = 1.25\%$  and  $2.5\%$  for comparison. The results are very similar to those from the previous section for most plates. There are some more obvious variations for plates with aspect ratios of  $c/t = 7$ ,  $8$  and  $13$ . At  $c/t = 8$ , the value of the peak mean base suction at a forcing frequency of  $St = 0.18$  is larger than for the case with a higher forcing amplitude. At  $c/t = 7$ , there is also a strong peak at  $St = 0.18$  and the peak at  $St = 0.16$  is smaller. For the plate with  $c/t = 13$ , the peak at  $St = 0.16$  is larger when the forcing amplitude is smaller. The similarity in all these cases is that these aspect ratios show two local peaks in base suction. At the lower forcing amplitude, the peak in base suction at the higher forcing amplitude is larger and dwarfs the lower frequency peak. At the extreme case of  $c/t = 7$ , the higher forcing amplitude does not show the higher frequency peak. Further discussion on the high frequency peaks will be presented in Section 4.3.3 and 4.3.4. Besides this difference, overall trends are similar between the two forcing amplitudes.

#### 4.2.4 The applied forcing without the mean flow

A more detailed and quantitative description of the applied forcing field, especially near the plate, is presented in this section. The forcing field is examined in more detail because it is the control mechanism used to influence the flow in these studies. As described earlier, the global applied perturbation is a sinusoidally oscillating velocity component in the cross-flow direction added to the velocity at all free-stream boundaries (equivalent to adding to the free-stream flow). To study the applied forcing only, the flow is examined

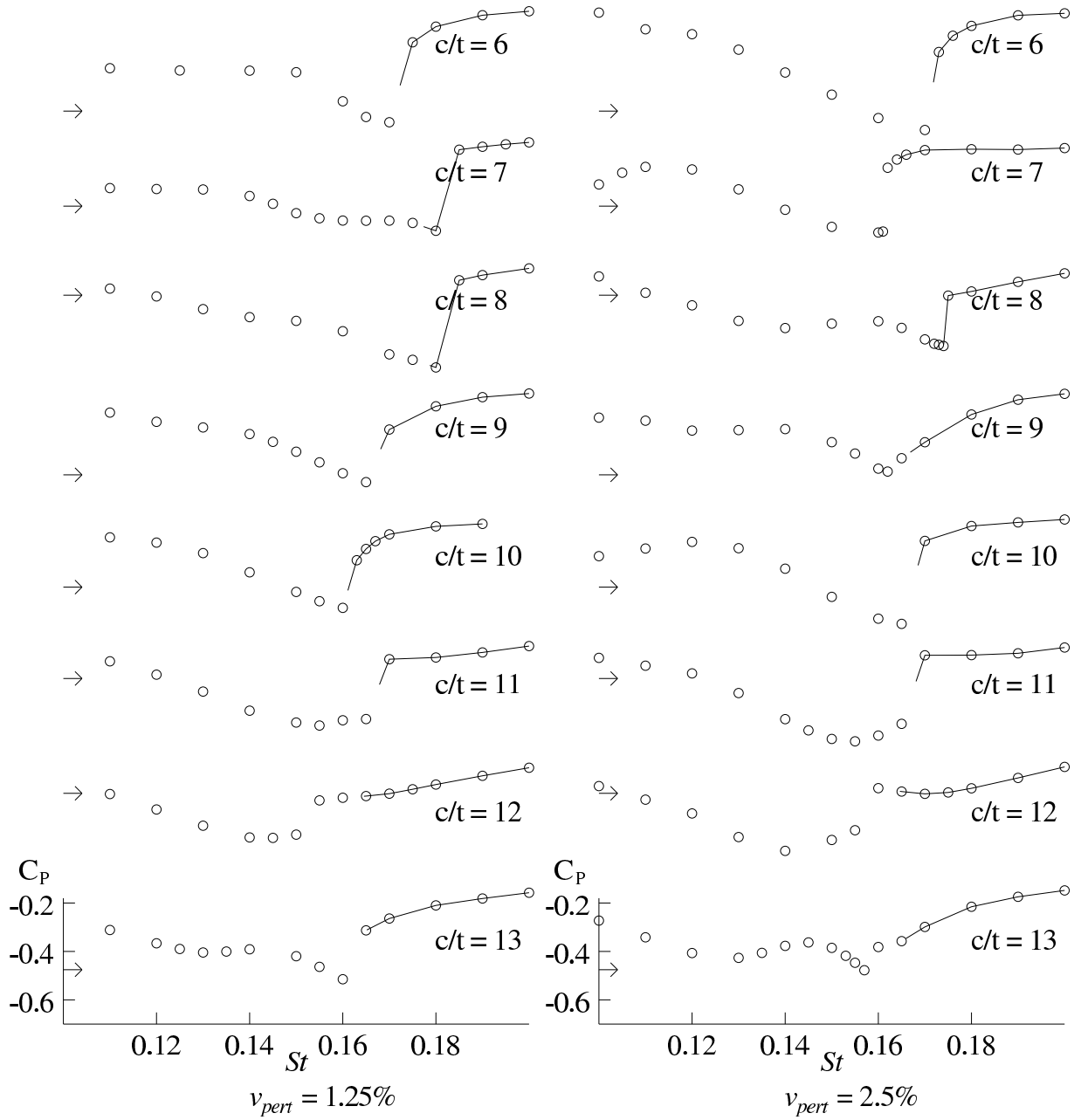


Figure 4.12: Mean base pressure coefficient as a function of forcing frequency for plates ranging from  $c/t = 6$  to  $c/t = 13$  simulated at  $Re = 400$  with a perturbation amplitude of  $v_{pert} = 1.25\%$  (left) and  $2.5\%$  (right).

in the absence of the mean free-stream flow. A similar method was used by Mills (1988) to determine the effective forcing amplitude near the receptive regions i.e., the leading and trailing edges. In that case the mean flow was turned off to allow the sound pressure level of the speakers to be calibrated.

These simulations are performed on the same grids as used in the previous simulations and all parameters such as plate dimensions, viscosity and the forcing amplitude remain the same as those in the previous simulations. The Reynolds number of the flow is  $Re = 400$  and the forcing amplitude is  $v_{pert} = 2.5\%$  with both scaled to a free-stream velocity of one unit. In the simulations, the free-stream velocity is set to zero but the scaling is based on the previous velocity scale of one unit. These simulations are started with the fluid at rest and the flow is simulated for several forcing cycles until all transients have decayed and the field appears periodic.

The velocity field near the plate with an aspect ratio of  $c/t = 10$  taken at  $90^\circ$  in the forcing cycle (i.e. applied forcing is maximum in the upward direction) is shown in Figure 4.13. The velocity vector plot shows the flow accelerating around the plate. As the forcing amplitude is small (effectively a small Reynolds number), the flow approaches a potential flow away from the plate while there is a thick boundary layer around the plate.

Although the global applied perturbation amplitude is constant, the amplitude near the plate is dependent on the location and the aspect ratio of the plate. This is investigated in the initial parts of this section. The amplitude of the perturbation (from the time trace of the velocity magnitude) is monitored at three points near the plate so that a quantitative comparison can be made at different aspect ratios. These three locations are shown in the schematic diagram in Figure 4.14. Although they are relative to the top leading edge of the plate, due to the symmetry in the geometry and the periodic nature of the forcing, the amplitude is the same for the equivalent locations at the respective positions from any edge. These locations are chosen to be near the plate but outside the boundary layer. The boundary layer is avoided because the steep gradients and the non-linear effects there would cause difficulties when comparing the different aspect ratios. The points are chosen to be at 0.5 plate thicknesses vertically and horizontally away from the edge and another point which is both 0.5 plate thicknesses vertically and horizontally away from the edge.

The velocity magnitude showed a sinusoidal signal at the three monitoring locations for all the plates examined. The amplitudes at these three points for plates with  $c/t = 6, 10$  and  $16$  are plotted in Figure 4.15. The forcing frequency of  $St = 0.17$  is chosen because it is an intermediate forcing frequency. The levels measured at these points are up to several times larger than the forcing amplitude of  $v_{pert} = 2.5\%$ . Points 2 and 3 show very similar amplitudes while the amplitude at point 1 is larger because it is in line

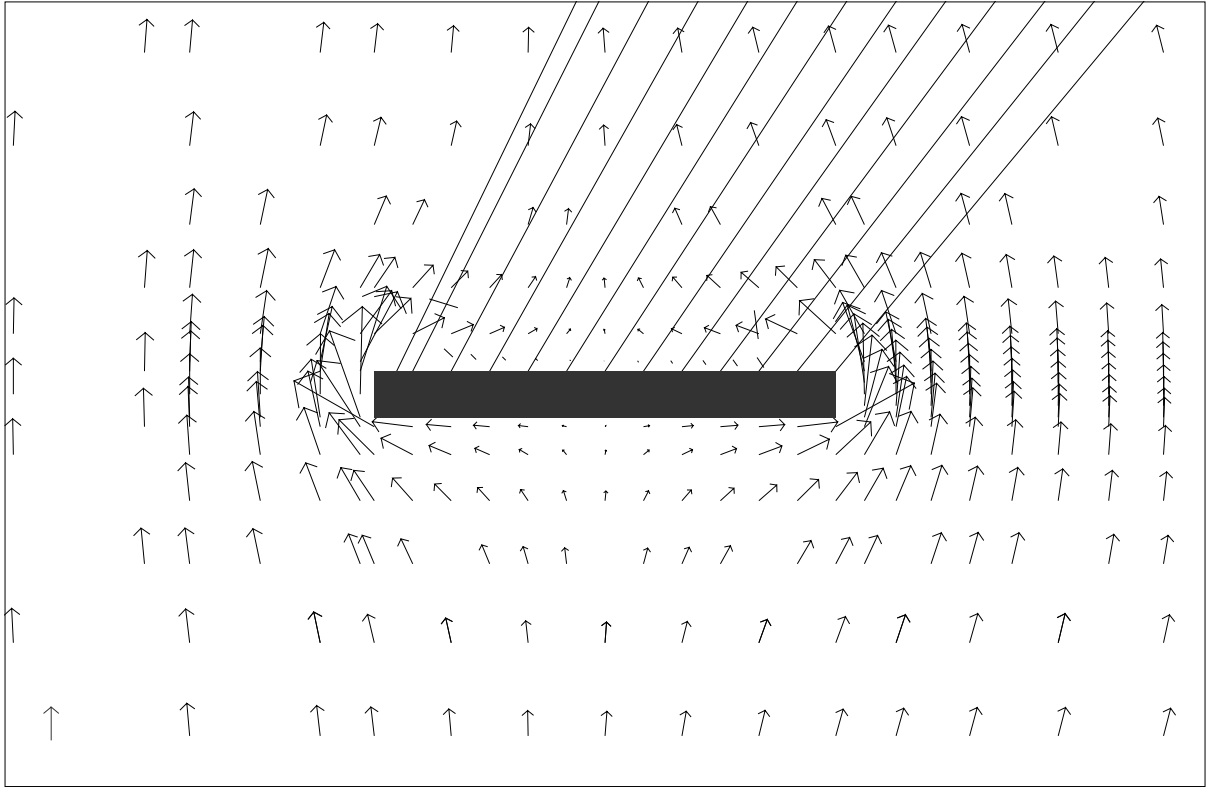


Figure 4.13: A velocity plot taken at  $90^\circ$  in the forcing cycle for flow around a plate with  $c/t = 10$  at  $Re = 400$  (based on free-stream velocity) with a forcing amplitude of  $v_{pert} = 2.5\%$  with no mean flow. The plot is drawn to scale with the gray arrow at the bottom left of the diagram showing the perturbation amplitude far away from the plate ( $v_{pert} = 2.5\%$ ).

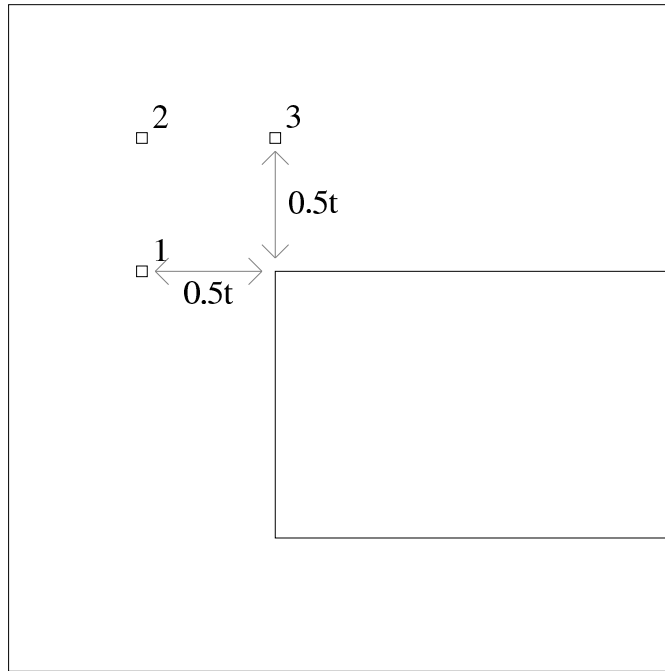


Figure 4.14: Schematic of the leading/trailing edge of the plate showing the locations where the perturbation amplitude is measured.

with the plate and influenced by the blockage which results in the fluid being accelerated more. As the plate length is increased, all the amplitudes show a linear increase. The flow is effectively at a small Reynolds number because of the small amplitude. Since the positions are outside the boundary layer, the flow is almost irrotational and behaves in a linear fashion. Therefore the choice of forcing frequency will not have much influence on the variation of amplitude near the plate.

While the forcing amplitude near the plate is increasing with aspect ratio, the strength relative to the overall flow must also be considered. The potential flow model is used to gauge the effect of aspect ratio on the magnitude of the velocity at points 1, 2 and 3. The potential flow model is used to avoid any influence from vortical structures. The potential flow field approaches one unit far away from the plate and is in the direction of the mean flow in the simulations. Table 4.2 shows that the variations in velocity amplitude are less than 2% between the shortest and longest plate. The small difference is expected because the plates are long and the aspect ratio has only a small influence on the velocity near the edges when the flow is in the streamwise direction. With the flow field velocity approximately constant, the increase in forcing amplitude with aspect ratio is an increase relative to the flow field velocity.

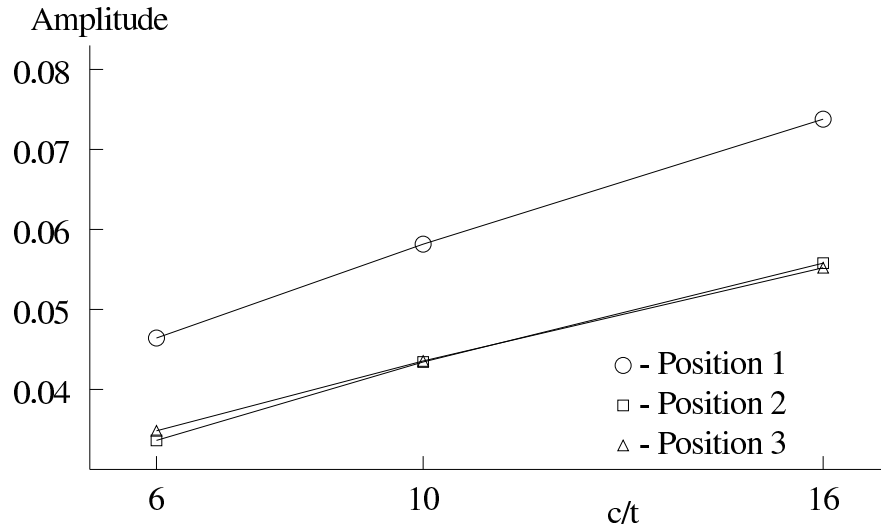


Figure 4.15: Effective perturbation amplitude relative to free-stream velocity evaluated at positions 1, 2 and 3 for plates with  $c/t = 6, 10$  and  $16$  experiencing a cross-flow harmonic perturbation. Here  $St = 0.17$  and  $v_{pert} = 2.5\%$ . There is no mean flow but  $Re = 400$  is based on a unit of free-stream velocity.

$c/t$	Velocity Magnitude		
	Point 1	Point 2	Point 3
6	0.8197	0.9857	1.1306
10	0.8137	0.9784	1.1213
16	0.8099	0.9738	1.1156

Table 4.2: Velocity magnitude at points 1,2 and 3 from the potential flow model with a free-stream velocity of one unit.

To verify that the rise in effective amplitude with plate length does not significantly alter the results in the previous section, a lower forcing amplitude of  $v_{pert} = 2.0\%$  is applied on the longest plate studied ( $c/t = 16$ ). With no mean flow, the velocity amplitudes at the three points are close to that of a plate with an aspect ratio of  $c/t = 10$  and a forcing amplitude of  $v_{pert} = 2.5\%$ . At  $v_{pert} = 2.0\%$  and  $c/t = 16$ , the levels at points 1,2 and 3 are 5.7%, 4.3% and 4.3% respectively while at  $v_{pert} = 2.5\%$  and  $c/t = 10$ , the levels are 5.8%, 4.3% and 4.4% with all measurements relative to one unit of free-stream velocity. Figure 4.16 shows the mean base pressure coefficient as the forcing frequency is varied for a plate with  $c/t = 16$  and  $Re = 400$  at the two levels of forcing. The plot shows there is only a marginal difference in the mean base pressure variations confirming that the variation in forcing levels near the plate as the aspect ratio is varied has only a small influence on the overall results. This is because there is only a marginal difference in the levels of forcing near the plate between  $c/t = 10$  and  $16$  when the far-field forcing

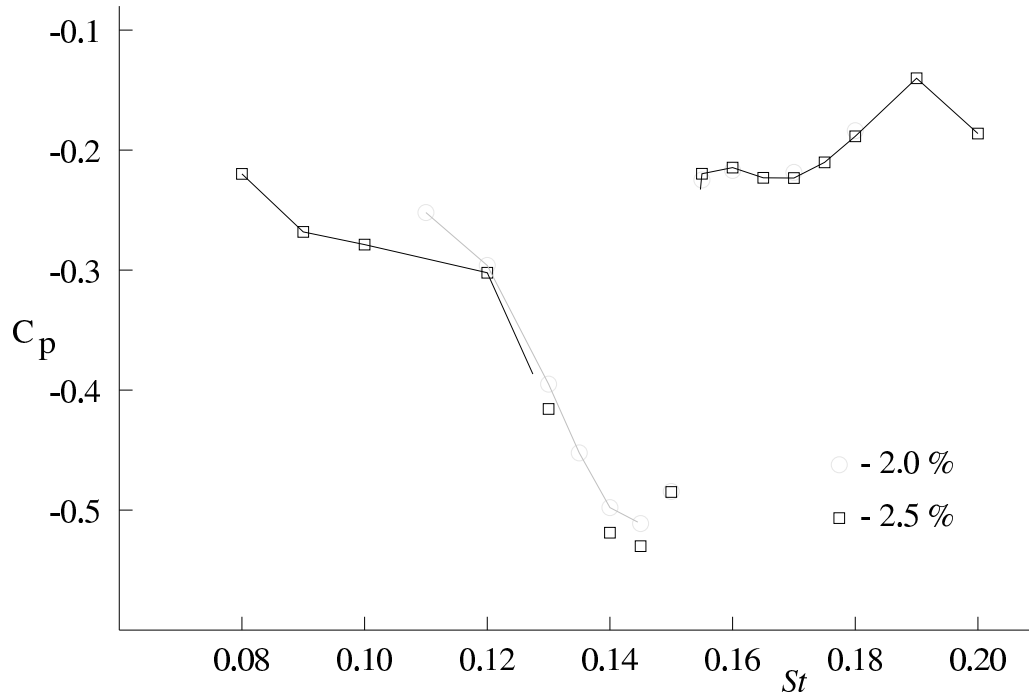


Figure 4.16: Mean base pressure coefficient as a function of forcing frequency for flow over a plate with  $c/t = 16$  at  $Re = 400$  under applied forcing at amplitudes of  $v_{pert} = 2.0\%$  and  $2.5\%$ .

amplitude is constant.

As many of the results, especially those related to mean base pressure, are compared with those of Mills (1998), it is useful to relate the forcing amplitude measured in the experiments and that for the simulations. As discussed earlier, to measure the perturbation amplitude in the wind tunnel, the fan is turned off and the sound pressure level of the speakers is calibrated for a plate having an aspect ratio of  $c/t = 10$ . The level of the perturbation is measured at a point similar to point 3 but only  $0.077t$  from the edge. The experiments are done in air where the viscosity is less and the boundary layer is thinner. This location is not used to measure the forcing amplitude in the simulations because this point would be within the boundary layer and the large gradients and the sensitivity to plate lengths and viscosity would make it difficult for comparisons: therefore points outside the boundary layer are chosen. The levels in the experiments ranged from  $3\%$  to  $5\%$  of the free-stream velocity while those in the simulation ranged from  $v_{pert} = 1.25\%$  to  $5\%$  of the free-stream velocity although measured or evaluated at different locations. The maximum amplification observed in the simulations due to the presence of the plate is about 4 times at  $c/t = 10$ . The measured amplitudes in the experiments are around the range of amplitudes observed near the plate and therefore the levels used in both cases are of the same order. Differences due to other factors are expected to be more dominant

such as the Reynolds number and the three-dimensionality of the experiments.

### 4.2.5 Lift and drag forces

In the previous sections, the focus was on the pressure at one point on the plate. Here the overall forces are examined for flow over a plate with applied forcing. The mean drag coefficient and the standard deviation of the lift coefficient, which is a measure of the fluctuating lift force, are examined for a range of plates lengths and forcing frequencies. Only the pressure forces are considered because the viscous forces are expected to be relatively small at these moderate Reynolds numbers. It is relatively simple to calculate the forces on a rectangular plate as only the leading and trailing faces contribute to drag and the top and bottom faces contribute to lift forces. In this section and also in preceding sections, the Reynolds number is chosen to be  $Re = 400$  and the forcing amplitude to be  $v_{pert} = 2.5\%$ . The trends observed at these parameters are characteristic of the parameter range studied and the investigation of a larger set of data at these parameters led to this choice.

The mean drag coefficient and the fluctuating lift coefficient are plotted in Figure 4.17 for an aspect ratio between  $6 \leq c/t \leq 16$  over the range of forcing frequencies. As expected, the mean drag force coefficient closely mimics the mean base pressure coefficient. As the contribution from the leading face is close to constant for all cases, the variation in mean drag force coefficient is a result of the trailing face contribution (i.e., the mean frontal drag coefficient varied between  $\overline{C_D} = 0.774 - 0.851$  for  $c/t = 10$  and,  $\overline{C_D} = 0.808 - 0.833$  for  $c/t = 13$ , for all the forcing frequencies simulated). The mean base pressure coefficient (which is recorded at the centre of the trailing face of the plate) is strongly related to the pressure force acting on the back face of the plate. The trends in the local maxima in the mean drag coefficient as the aspect ratio is varied are similar to those of the mean base suction and are shown by the broken lines. These peaks, which start with plates that only show a single peak, occur at a lower forcing frequency with increasing aspect ratio until the frequency is too low to be receptive and lies outside the lock in range. At the next increment in plate length, a peak develops at a higher forcing frequency and continues the trend. For the plates that have two local peaks, the higher peak also usually occurs at a lower forcing frequency when the plate is lengthened.

The plots of fluctuating lift forces show some quantitative difference in behaviour compared to the mean drag forces. Overall, there is a gradual rise in the fluctuating lift force with frequency similar to flow around elliptical leading-edge plates. This is also due to the (cross-stream) applied forcing acting directly on the plate which results in a larger fluctuating component at higher frequencies. Compared with the mean drag or mean base

pressure plots, the standard deviation in the lift coefficient shows a local maximum when there is a larger mean drag or base suction. For those plates that have two local peaks in mean base suction or drag, the one at the lower frequency is associated with a maximum local peak, while the one at the higher frequency, to a minimum local peak. Similar to the mean drag, these local maxima or minima are marked by broken lines. The trends here are clearer and continuing for between one and two plate lengths outside those trends for the mean drag coefficient. An explanation for these observations will be discussed in a following section (Section 4.3.5). It involves the relative phase of the leading-edge shedding and the phase when the vortices pass the trailing edge. An investigation into the phase relationship will be presented first.

Also shown in these plots by the arrows are the mean drag coefficient and standard deviation of the lift coefficient when there is no applied forcing. As with the mean base pressure, comparing the mean drag coefficient in the natural case with the forced shedding case is difficult because the natural shedding case is controlled by the ILEV instability while the applied forcing controls the flow in the forced shedding cases. This will be revisited in a later section (Section 4.3.6 and 4.3.7). The fluctuating lift force is generally smaller in the natural shedding case than in the forced shedding case; especially for longer plates. The forcing results in added pressure fluctuations on the plate surface. Although the scaling on chord when calculating the lift coefficient helps maintain some uniformity between plates, the increase in cross-flow blockage and the higher effective perturbation amplitudes near the plate result in a larger fluctuating component for the longer plates. In Section 4.1.3, the reason for the declining value of the standard deviation of the lift coefficient with increasing aspect ratio is discussed. These factors account for the large difference, especially for longer plates, in the standard deviation of lift coefficient between the natural and forced shedding cases.

## 4.2.6 Peaks in mean base suction

In the previous two sections, it is shown that the local peak in mean base suction or drag coefficient occurred at a lower forcing frequency as the aspect ratio is increased until the forcing frequency is too low and no longer locks the flow. At this stage another peak develops at a higher forcing frequency and continues this trend. For those aspect ratios where there are two local peaks, the peak at the higher forcing frequency also occurs at a lower forcing frequency as the aspect ratio is increased until the single larger peak dominates. Using the data on the mean base pressure for various forcing frequencies and plate lengths (Figure 4.10), the Strouhal number based on chord ( $St_c$ ) of the forcing at which these local peaks occur from both the present simulation and experimental data of Mills (1998) is plotted in Figure 4.18. Similar to the behaviour of the natural shedding

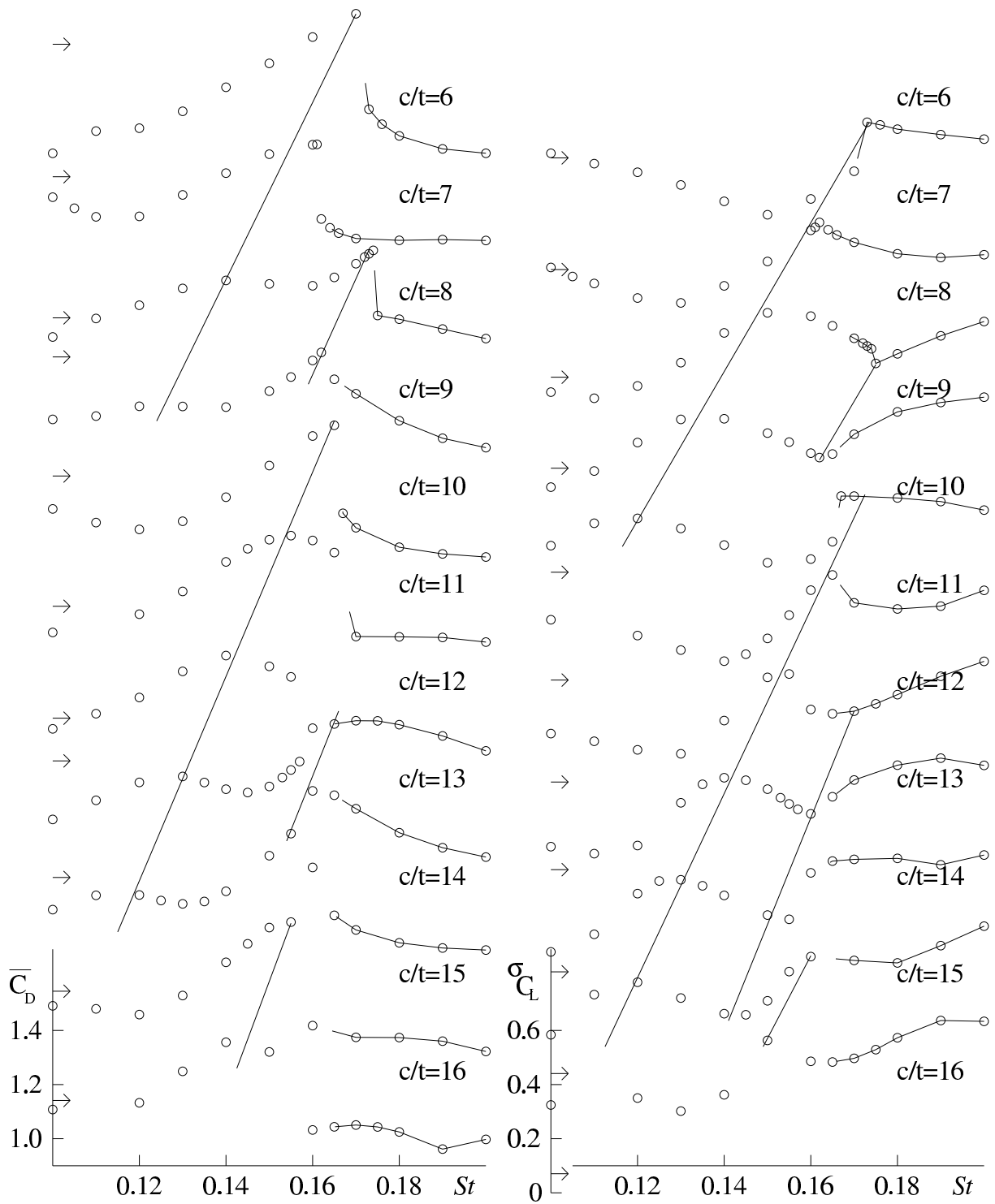


Figure 4.17: Mean drag coefficient (left) and standard deviation of the lift coefficient (right) as a function of forcing frequency for plates with  $6 \leq c/t \leq 16$  at  $Re = 400$  and  $v_{pert} = 2.5\%$ . The arrows on the left show the mean drag coefficient and the standard deviation of the drag coefficient when no forcing is applied.

frequency, these plots also show a stepwise increase with chord. The local peak which occurs at the higher frequency in the simulation for plates with aspect ratios of  $c/t = 8, 9, 12, 13$  and  $14$  appear to be at an intermediate step. The following sections (Section 4.3 especially Section 4.3.4) will further investigate this stepping behaviour.

Within each step, the local peaks are generally greater at the lower aspect ratio end of each step when forcing is applied. This is consistent with the natural shedding cases where the mean base suction and drag are higher at the lower aspect ratio end of each step. On the other hand, within each step, the experiments show the magnitude of the peak reaching a maximum around the intermediate aspect ratio. The peak that occurs at the intermediate level between steps in the simulations may have suppressed the local peak which would correspond to the next higher step. This could therefore restrict the lower limit in aspect ratio of each step resulting in each step starting with a larger magnitude peak.

Comparing the two sets of data, the heights of each step (i.e., the values of  $St_c$ ) are closer for shorter plates but differ for longer plates with the experimental data showing a higher level. This also occurs when comparing the natural shedding frequency between the simulations and the experiments. As in the natural shedding case, the steps in the simulation are approximately  $St_c = 0.55n$  while in the experiments they are approximately  $St_c = 0.6n$ . As in the natural shedding cases, the difference in convective velocity is likely to cause this.

### 4.3 Dynamics of the flows

In this section, further investigation of the flow fields is performed with the aim of relating the trends in the overall observations to the flow characteristics. The Reynolds number of the flow is at  $Re = 400$  and the forcing amplitude at  $v_{pert} = 2.5\%$  as in previous sections.

The characteristic stepping in Strouhal number corresponding to the local peaks in mean base suction for the case where forcing is applied will be examined first. Hourigan *et al.* (1993) have proposed that the interaction of the leading- and trailing-edge vortices has a controlling influence on the strength of the mean base suction. This mechanism involves the phase in the forcing cycle when the leading-edge vortex passes the trailing edge and thereby influences the phase of shedding there. More data and further discussion in Mills (1998) supported this vortex interaction hypothesis. To address this issue through the numerical simulations, the phasing at the leading edge relative to the forcing, the convective velocity of the vortices along the plate, and finally the resulting phase of the shedding relative to the forcing, will be examined. This will then provide strong support

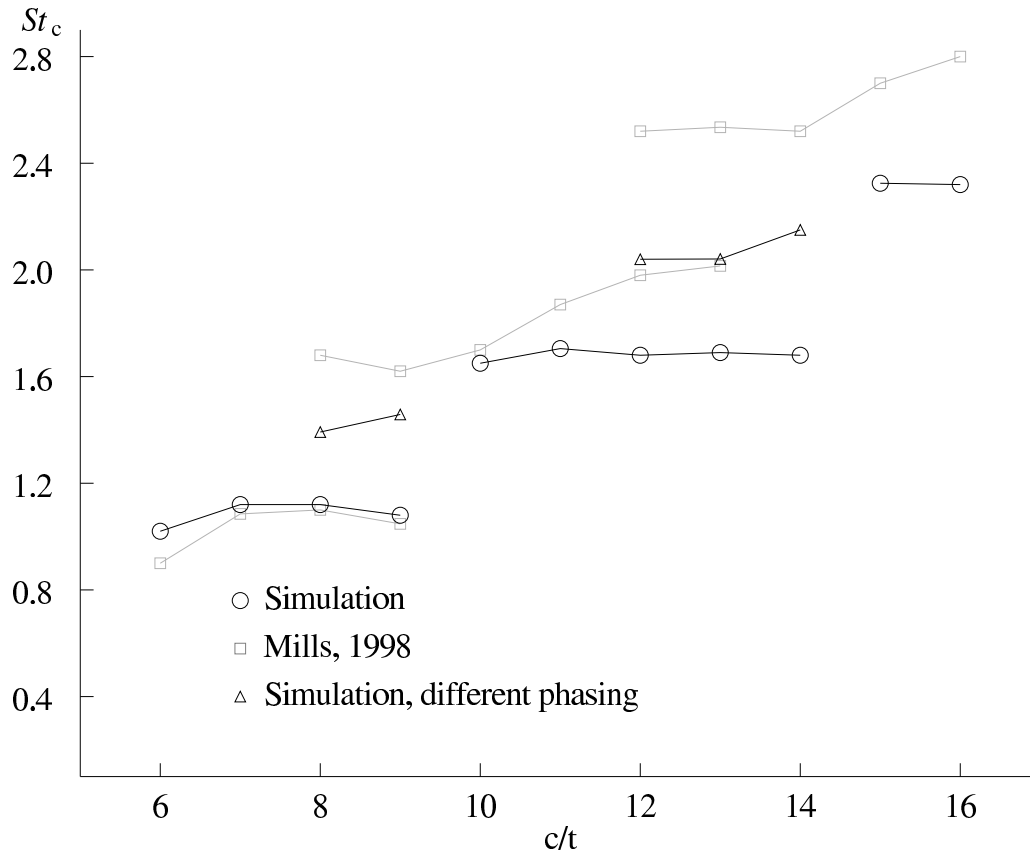


Figure 4.18: Forcing frequency (non-dimensionalised with chord) which results in a local peak in the mean base suction as a function of the aspect ratio for the present simulations and experiments by Mills (1998).

for this hypothesis from the simulated results.

A secondary question that will be investigated is the variation in the magnitude of the local peaks in mean base suction. The simulations and the experiments both show that certain plate aspect ratios have a larger magnitude in the local peak in mean base suction than others. The sensitivity of the trailing-edge shedding to frequency is hypothesised to be the controlling mechanism. To further investigate this, the vortex formation length downstream of the trailing edge will be analysed and compared with the flow over elliptical leading-edge plates. The similarities between these two cases will be examined to test this hypothesis. The implications of this for the natural shedding case where the ILEV instability controls the flow will also be discussed.

### 4.3.1 Phase of leading-edge shedding

In the cases where the flow is locked to the forcing, the leading-edge shedding is phase locked. The phase of shedding relative to the forcing also appears to be constant for all plate lengths and forcing frequencies investigated. To show this, three diverse cases are chosen: a shorter plate at a lower frequency ( $c/t = 8$  and  $St = 0.11$ ); a longer plate at an intermediate frequency ( $c/t = 16$  and  $St = 0.15$ ); and an intermediate plate length at a higher forcing frequency ( $c/t = 10$  and  $St = 0.20$ ). Figure 4.19 shows the leading-edge shedding of these three cases at  $0^\circ$ ,  $90^\circ$ ,  $180^\circ$  and  $270^\circ$  in the forcing cycle. When the forcing frequency is increased, the shear layer rolls up closer to the leading edge but the relative phase of shedding to the forcing in each case is approximately the same.

For all cases, the top shear layer is in the initial stages of forming a vortex at  $180^\circ$ . This vortex then gains more circulation from the shear layer at  $270^\circ$ . It starts to detach at  $0^\circ$  and by  $90^\circ$ , it is almost completely shed from the shear layer. The shedding from the bottom is  $180^\circ$  out of phase with the top. In all cases, the vortex on the top of the plate forms between  $90^\circ$  and  $270^\circ$  in the forcing cycle. This is when the perturbation velocity is accelerating in the downward direction. The forcing is therefore causing a more compact vortex to form closer to the leading edge (relative to the natural shedding case). During the other half of the cycle, the acceleration upward helps shed the vortex. This phase relationship is likely to be the most beneficial to the shedding process. The constant phase relationship between the shedding and the forcing for all the cases is a result of this.

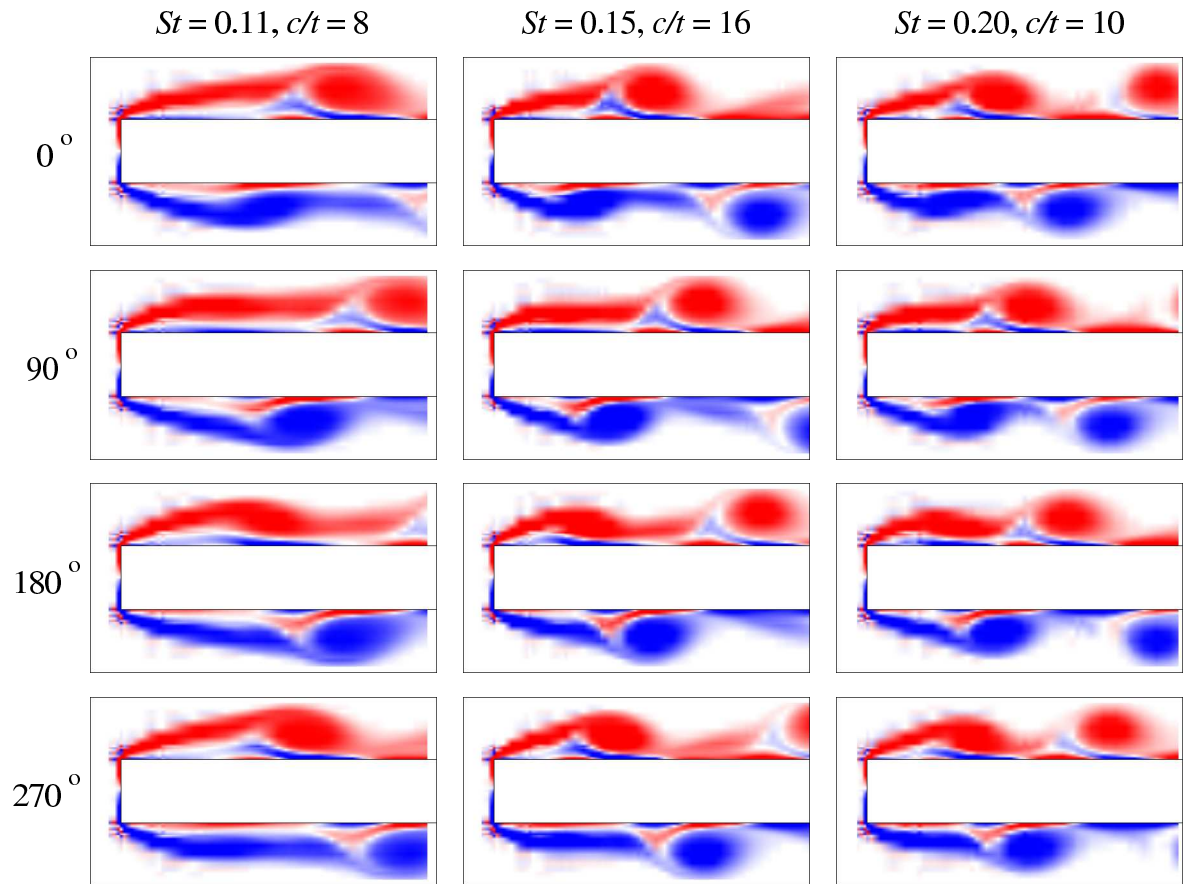


Figure 4.19: Vorticity plots of the leading-edge shedding for flow over rectangular plates at  $Re = 400$  and  $v_{pert} = 2.5\%$  Vorticity plots taken at  $0^\circ$ ,  $90^\circ$ ,  $180^\circ$  and  $270^\circ$  in the forcing cycle for plates with  $c/t = 8$ ,  $16$  and  $10$  at applied forcing frequencies of  $St = 0.11$ ,  $0.15$  and  $0.20$  respectively.

### 4.3.2 Convective velocity

The streamwise component of velocity of the vortices as they convect along the plate is investigated in this section. This feature is crucial because it governs the time taken for a leading-edge vortex to pass the trailing edge thereby affecting the phasing there. The investigation will cover (1) different plate lengths for the natural shedding case, (2) various forcing frequencies for a fixed plate length and, (3) various plate lengths for a constant forcing frequency.

To evaluate the convective velocity of the vortices, their locations are determined at regular time intervals. The local peak vorticity, which is found using the Newton-Raphson method as in the previous chapter, is used to define the location of the vortex. The velocity is evaluated using central differencing between these locations. The sampling is performed every 0.21 time units over 8 to 10 time units, which is more than one shedding period. The convective velocities of the vortices on both sides of the plate are calculated.

Figure 4.20 shows the convective velocity of the vortices as they traverse the length of the plate for the three classes studied. Figure 4.20(a) shows the convective velocity for flow over plates with aspect ratios of  $c/t = 6, 8, 10$  and  $13$  with no external forcing. Shown in Figure 4.20(b) is the convective velocity for an aspect ratio of  $c/t = 8$  at forcing frequencies of  $St = 0.11, 0.14, 0.165, 0.174$  and  $0.19$ . The forcing frequency is fixed at  $St = 0.16$  in Figure 4.20(c) and the convective velocities for  $c/t = 7, 9, 11, 13$  and  $15$  are shown. In all these cases studied, the convective velocity reaches a minimum close to the time it is fully formed. After separating from the shear layer, it then accelerates and reaches saturation at approximately 70% of the free-stream velocity.

#### 4.3.2.1 Natural Shedding

In the natural shedding case, the behaviour is similar for all the plate lengths except for the shortest ( $c/t = 6$ ). Compared to the other plates, the plot for the shortest plate appears to have been translated approximately  $1t$  upstream. This is likely due to the close proximity of the trailing edge to the leading-edge shedding. The rest of the plates show a minimum in convective velocity at about  $4t$  from the leading edge. At the aspect ratio of  $c/t = 8$ , there is some scatter in the plot because the flow is not perfectly periodic (i.e. every period is not exactly identical) and over the duration of the sampling there is some difference between the two sides of the plate.

#### 4.3.2.2 Fixed aspect ratio, variable forcing frequency

When the aspect ratio is fixed at  $c/t = 8$ , the convective velocity does not show a significant dependence on the forcing frequency except at the lowest frequency ( $St = 0.11$ ). The low forcing frequency which results in the vortices forming further downstream causes the convective velocity plot to be effectively translated downstream by approximately  $0.75t$ . The rest of the plates show a minimum in the convective velocity at about  $2t$  from the leading edge. Note that this is much less than for the natural shedding case and is a result of the applied forcing which causes the reattachment length to shorten significantly. This earlier reattachment when forcing is applied has been shown experimentally by Mills (1998).

#### 4.3.2.3 Forcing frequency constant, aspect ratio varies

When the forcing frequency is kept constant at  $St = 0.16$ , the various plate lengths show a similar convective velocity history along the plate. There are some differences near the trailing edge due to the influence of the trailing-edge shedding. Again, the minimum in convective velocity also occurs at about 2 plate thicknesses from the leading edge. The overall behaviour of the convective velocity along the plate is similar for all the cases studied. Perhaps this is not surprising given the low level of forcing. The main influence of forcing is that it reduces the reattachment length. The average convective velocity for all the cases studied is approximately the same.

### 4.3.3 Phase of trailing-edge shedding

The next obvious step is to investigate the trailing-edge shedding and how this relates to the mean base pressure. Firstly, the flow over a plate with an aspect ratio of  $c/t = 10$  is investigated closely. Next the plate with an aspect ratio of  $c/t = 8$  is investigated because it is typical of the plates that have two local peaks in the mean base suction within the lock-in range. Finally vorticity plots for the whole range of plates studied will show the similarities at the trailing edge when the mean base suction peaks.

Figure 4.21 shows vorticity plots for flow around a plate with an aspect ratio of  $c/t = 10$  at  $St = 0.12, 0.15, 0.165$  and  $0.18$  together with the plot of mean base pressure as a function of the forcing frequency. Only plots taken at  $0^\circ$  and  $90^\circ$  in the forcing cycle are shown. The other half of the cycle mirrors these plots because the flow is locked to the shedding and is therefore periodic.

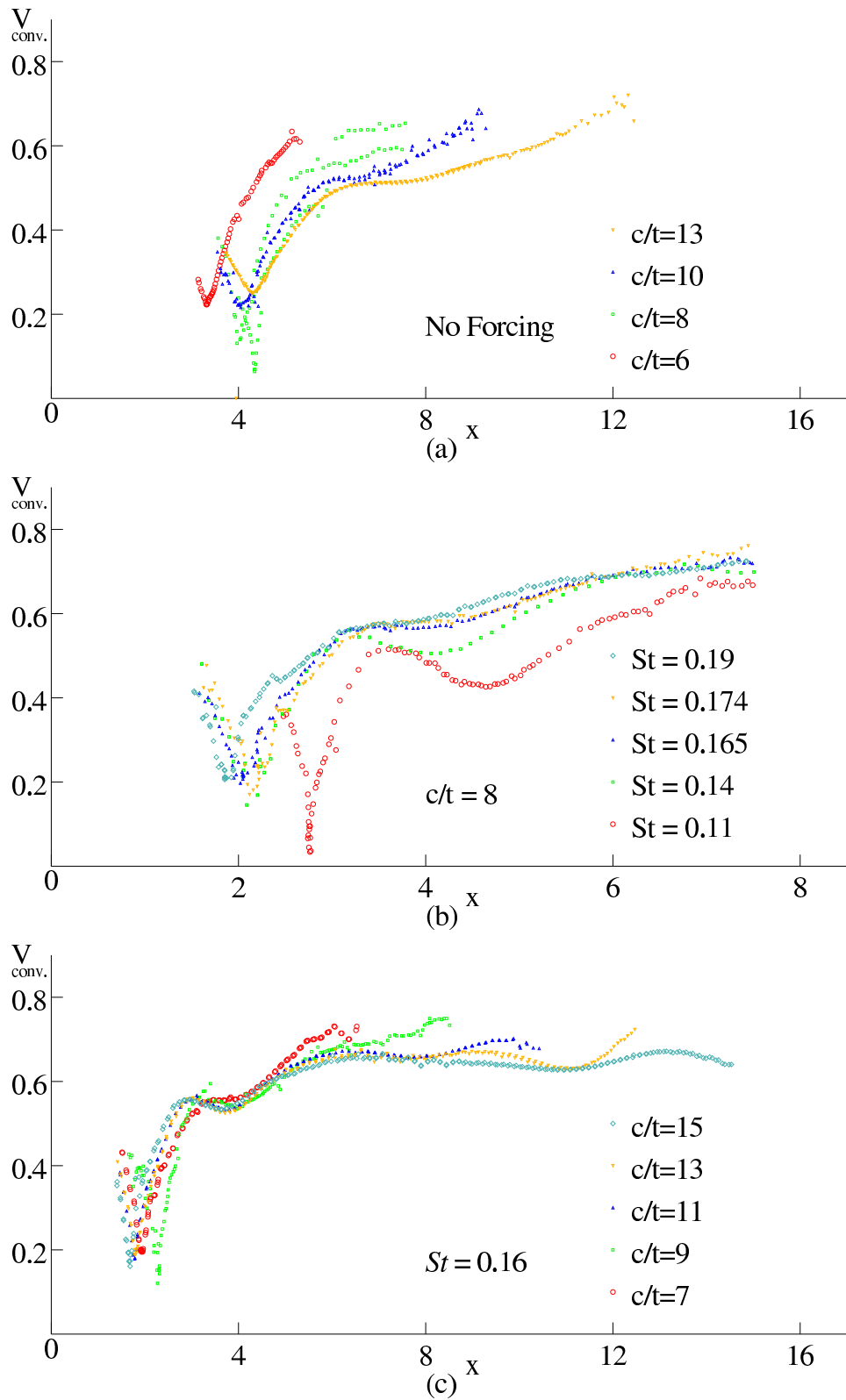


Figure 4.20: Streamwise component of the convective velocity of the vortices along the plate as a function of distance downstream from the leading edge. (a) Various aspect ratios in the natural shedding case. (b) Various forcing frequencies at an aspect ratio of  $c/t = 8$ . (c) Various plate lengths with forcing frequency at  $St = 0.16$ . The flow is at  $Re = 400$  and the applied forcing amplitude at  $v_{pert} = 2.5\%$

As in the previous section, all these plots show the same relative phase of the leading-edge shedding to the forcing at all forcing frequencies. These vortices convect downstream and control the shedding at the trailing edge (as the trailing-edge vortices are formed between the passing of leading-edge vortices.) As the forcing frequency is gradually increased from  $St = 0.12$  to  $St = 0.15$  and  $St = 0.165$ , the gradual increase in mean base suction is associated with a gradual change in the phase of the trailing-edge shedding relative to the forcing. When the mean base suction peaks ( $St = 0.165$ ), there are similarities between the phases of the leading- and trailing-edge shedding relative to the forcing. At  $0^\circ$  in the forcing cycles, both the leading- and trailing-edge vortices are forming on the top side of the plate while on the bottom of the plate, the vortices have been shed from both the leading and trailing edges. At  $90^\circ$  in the forcing, both shedding processes are still at a similar phase in that the vortices on the bottom side are just forming while the top ones are about to be shed. As discussed previously, the applied forcing is most conducive to shedding at the leading edge at this relative phase. The similarities at the forcing frequency that results in the mean base suction peaking also suggest that the forcing is conducive to the shedding. This is seen by the bottom vortex also developing between approximately  $270^\circ$  and  $90^\circ$  when the perturbation velocity is accelerating upwards. In this case, the forcing will cause the vortex to form closer to the base. In the other half of the cycle, the downward acceleration would help shed the vortex while the one on the other side forms. This phenomenon could cause the strong mean base suction and will be revisited later in this section. As the forcing frequency is incremented to  $St = 0.18$ , there is a more drastic decrease in the mean base suction. The vorticity plot shows that the higher forcing frequency suppresses the trailing-edge shedding. This is consistent with the low mean base suction.

Figure 4.22 shows the vorticity plot for flow around a plate with  $c/t = 8$  at forcing frequencies of  $St = 0.14$  and  $St = 0.174$ , which correspond to the two local peaks in the mean base suction. Also shown is the plot of the mean base pressure as a function of forcing frequency. Again the relative phase of the leading-edge shedding is fixed and consistent with all the previous cases. At the forcing frequency of  $St = 0.14$ , the phase of the trailing-edge shedding relative to the forcing is similar to the case where the aspect ratio is  $c/t = 10$  and the forcing frequency is  $St = 0.165$ . As both cases show a peak in the mean base suction, the similar process discussed earlier for the plate with an aspect ratio of  $c/t = 10$  also applies here.

When the forcing frequency is at  $St = 0.174$ , the shedding from the trailing edge appears to be  $180^\circ$  out of phase from the shedding at the lower forcing frequency ( $St = 0.14$ ). This also induces a local peak in the mean base suction. As the shedding in this case is only half a cycle ahead of the previous case and not a complete cycle ahead, these frequencies correspond to the intermediate step between shedding modes shown in

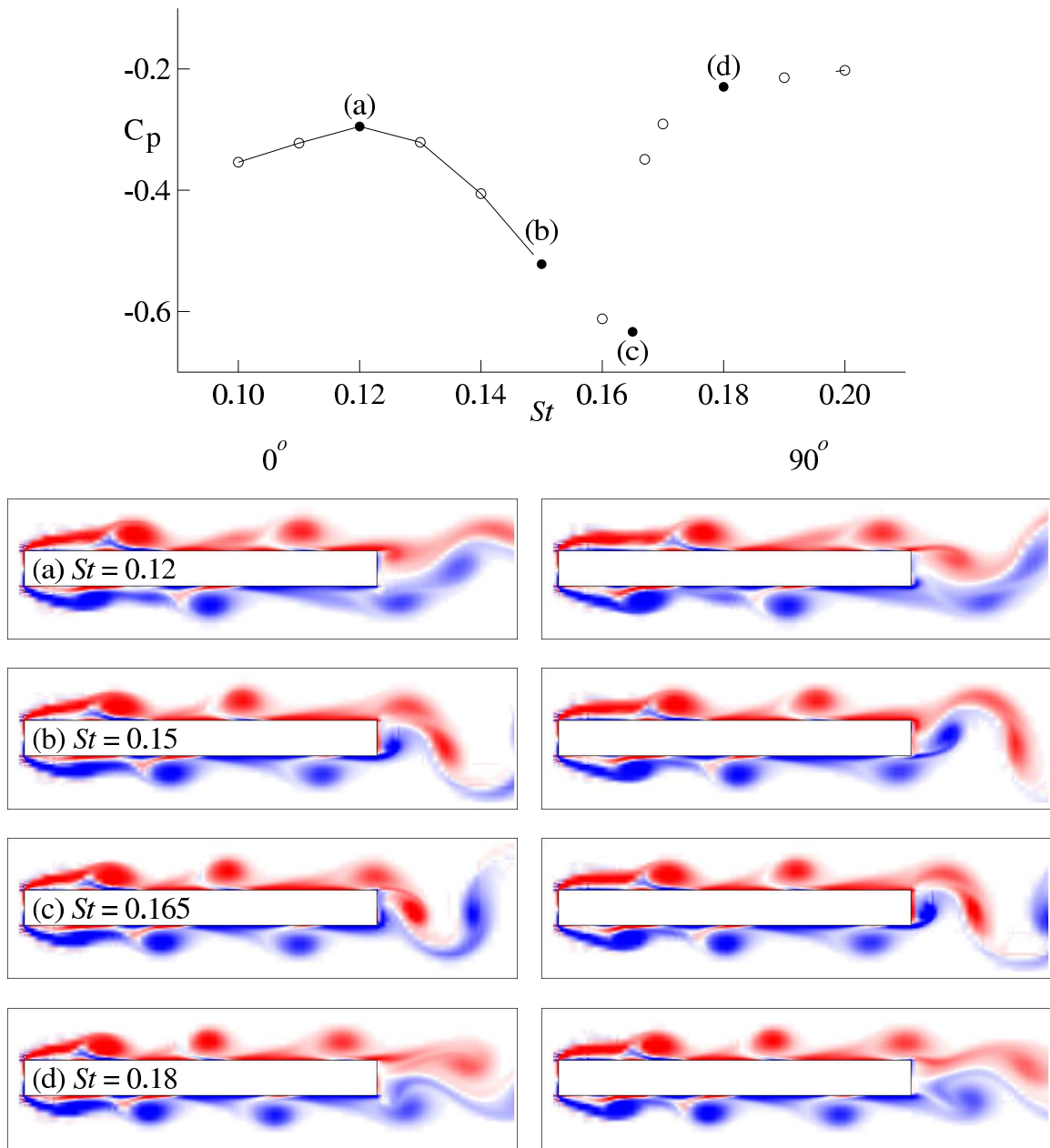


Figure 4.21: Vorticity plots for flow over a plate with  $c/t = 10$  at  $Re = 400$  taken at  $0^\circ$  and  $90^\circ$  in the forcing cycle at forcing frequencies of  $St = 0.12, 0.15, 0.165$  and  $0.18$  with an amplitude of  $v_{pert} = 2.5\%$ . At the top is a plot of the mean base pressure coefficient as a function of forcing frequency.

Figure 4.18. In this case there is not an additional pair of vortices along the plate but only one half of a pair. Although the local peaks in mean base suction are generally weaker at these intermediate steps, there is still some resonance that causes the strong mean base suction. The leading-edge vortices are also passing the trailing edge at  $180^\circ$  out of phase compared with the lower forcing frequency. The forcing may influence the leading-edge vortices as they pass the trailing edge as it does the trailing-edge vortices at the lower forcing frequency. It appears the forcing causes the leading-edge vortices to move closer to the base. Together with the trailing-edge shedding, the result is a stronger mean base suction. As shown by mean base pressure plots in Figure 4.12 and discussed in Section 4.2.3, the magnitude of the peak mean base suction which occurs at the higher forcing frequency reduces as the forcing frequency is increased. The trailing-edge shedding, which is still the major contributor to base suction in this case, is influenced by the applied forcing. Contrary to the other case (peak mean base suction occurring at the lower forcing frequency), the trailing-edge vortex is forming on the top side of the plate between  $270^\circ$  and  $90^\circ$  (approximately) in the forcing cycle while the perturbation velocity is accelerating in the upwards direction. This vortex is shed off the plate in the other half of the forcing cycle while a vortex from the other side forms. The direction of the acceleration therefore induces the vortex to form further away from the centreline of the plate. Vortices which form further away from the centreline should contribute less to the mean base suction. It follows that an increased forcing amplitude would therefore reduce the mean base suction by inducing trailing-edge vortices to form further away from the centreline.

To show that the observations are applicable to all the plates studied, every local peak in mean base suction is examined. Figure 4.23 shows vorticity plots taken at  $0^\circ$  in the forcing cycle for all plate lengths studied at forcing frequencies which result in local peaks in the mean base suction. These are the same plate aspect ratios and forcing frequencies that are plotted in Figure 4.18 showing the stepwise behaviour. Again the phase of the leading-edge shedding is consistent with all the previous cases. All plates that have a single local peak in the mean base suction and the lower forcing frequency peak for those plates that have two local peaks have approximately the same phase of shedding relative to the forcing at the trailing edge. In those cases where two local peaks in base suction are present, the one occurring at the higher forcing frequency shows the base shedding to be  $180^\circ$  out of phase to those occurring at the lower forcing frequency and those cases where there is only a single peak in base suction. The vorticity plots clearly show the different shedding modes that correspond to the stepping in the Strouhal number based on chord in Figure 4.10. The peaks at aspect ratios of  $c/t = 6, 7$  and the lower forcing frequencies at 8 and 9 show two vortices along the plate ( $n = 2$ ). At forcing frequencies where the base suction peaks when  $c/t = 10$  and 11, and the lower forcing

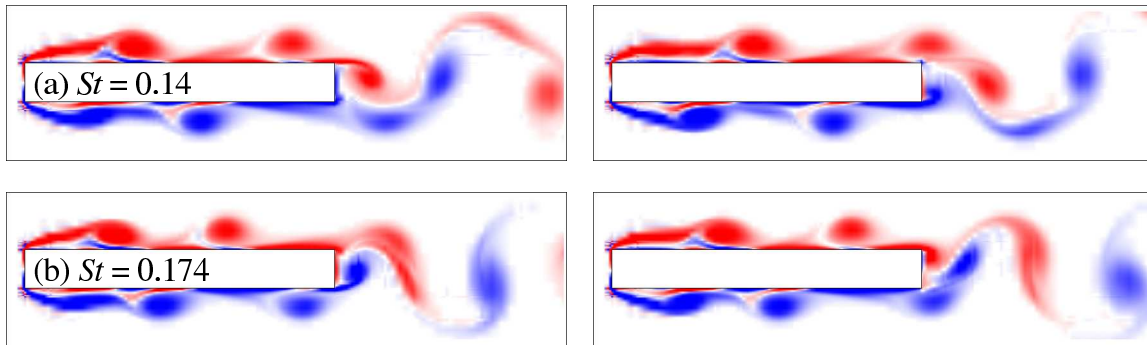
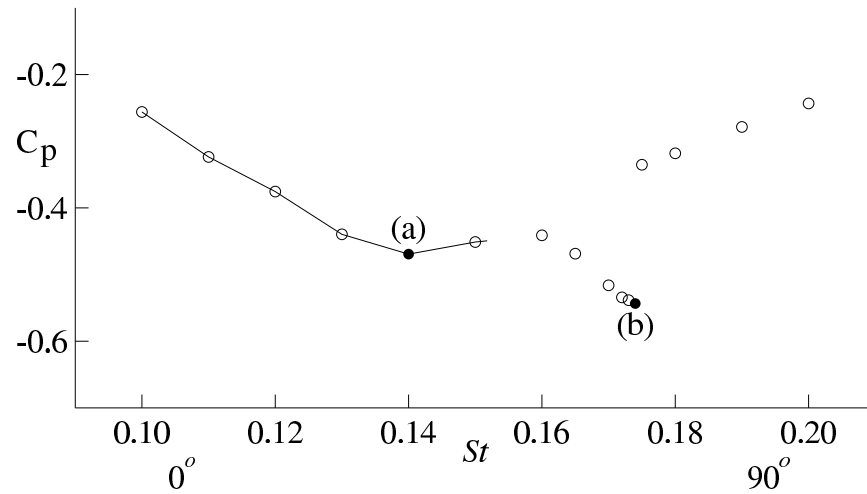


Figure 4.22: Vorticity plots for flow over a plate with  $c/t = 8$  at  $Re = 400$  taken at  $0^\circ$  and  $90^\circ$  in the forcing cycle at forcing frequencies of  $St = 0.14$  and  $0.174$  with an amplitude of  $v_{pert} = 2.5\%$ . At the top is a plot of the mean base pressure coefficient as a function of forcing frequency.

frequencies of these peaks when  $c/t = 12, 13$  and  $14$ , all correspond to the third mode of shedding ( $n = 3$ ). Finally, aspect ratios of  $c/t = 15$  and  $16$  show 4 vortices along the plate ( $n = 4$ ). The higher forcing frequency peaks at aspect ratios of  $c/t = 8, 9, 12, 13$  and  $14$  are shedding at an intermediate mode which shows up as frequencies between the major steps. The phase of shedding of the trailing edge relative to the forcing for all plates with a single local peak in the mean base suction, and the local peak at the lower forcing frequencies for the plates that have two peaks, are all similar to the local peak for the plate with an aspect ratio of  $c/t = 10$  which was studied earlier. This suggests that the same mechanism described earlier is also causing the strong mean base suction for all plate lengths. The remainder of the local peaks in mean base suction are all shedding  $180^\circ$  out of phase at the trailing edge.

#### 4.3.4 On the stepping in the natural and forced shedding cases

In the natural shedding case, the impinging leading-edge vortex instability (ILEV) not only locks both the leading- and trailing-edge shedding to one frequency but also maintains the same relative phase between the two processes. This ensures the same phase relationship between the interaction at the trailing edge, and the arrival of the upstream travelling signal (pressure pulse) that locks the leading-edge shedding. Therefore the same mechanism is controlling the flow for all the cases where the flow is locked to this instability. Although previously assumed, the behaviour of the convective velocity along the plate has been shown by the data presented in Figure 4.20(a) to be fairly independent of the aspect ratio. Therefore, to maintain the same phase relationship, as the aspect ratio is increased, the shedding frequency decreases to allow more time for the vortex which is shed from the leading edge to arrive at the trailing edge. This continues until the frequency is too low and the system is no longer receptive to that frequency. At that stage there is a jump in frequency allowing another period for the vortex to traverse the plate. This results in an extra pair of vortices along the plate which corresponds to the next higher shedding mode.

When forcing is applied, the forcing directly locks the flow and does not require the feedback from the trailing edge. In the simulations, the level of forcing used is strong enough to lock the flow over a wide range of frequencies and overpowers the natural instability. The local peaks in the mean base suction also show a stepwise increase with chord. Similar to the natural shedding case, each step also corresponds to an integer number of vortices along the plate as for the shedding modes in the unforced case. In the forced shedding cases, the leading-edge shedding appears to be phase locked to the applied forcing. Again the convective velocity is only weakly dependent on the aspect ratio and the forcing frequency. For a given aspect ratio, the forcing frequency controls

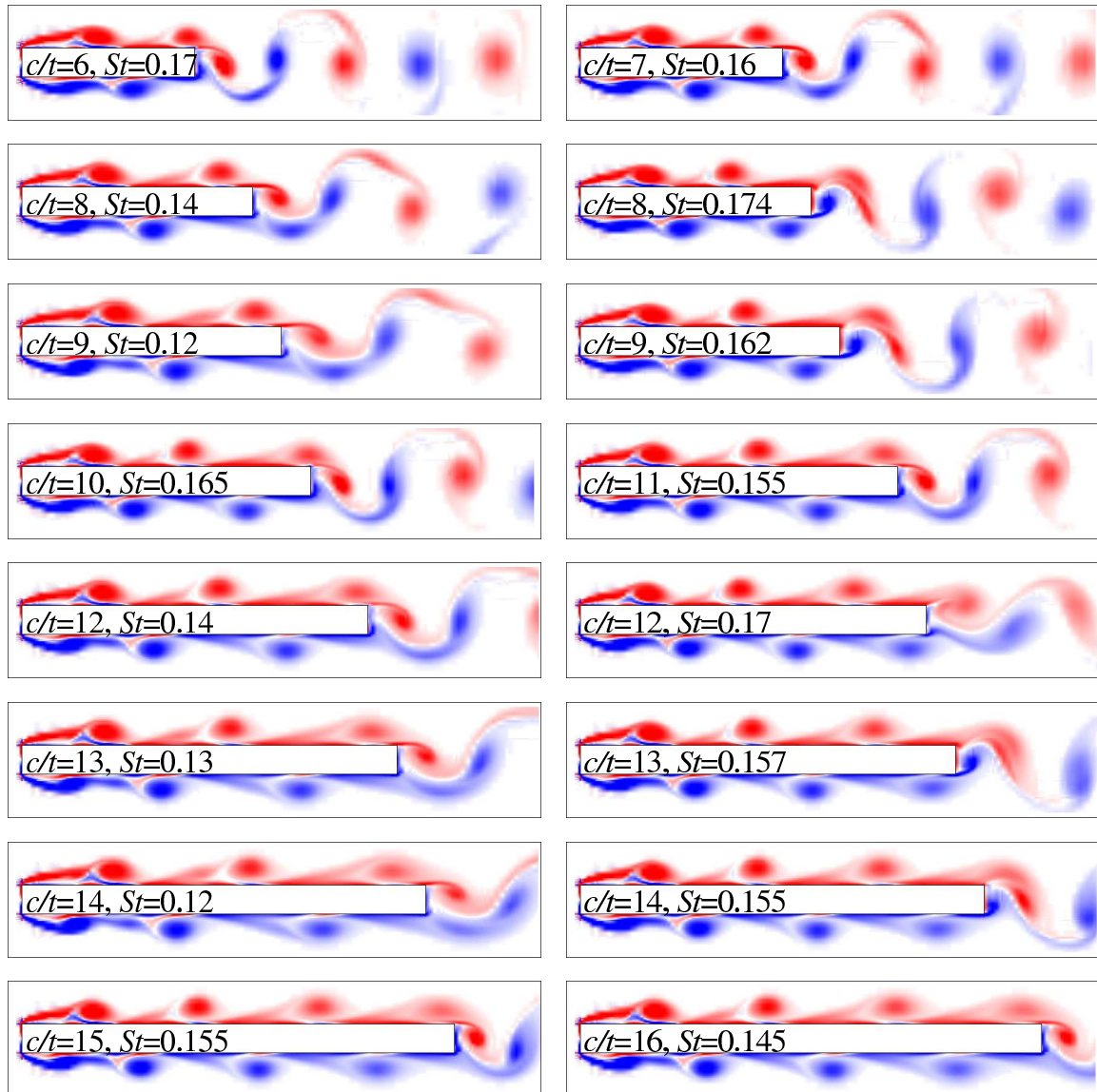


Figure 4.23: Vorticity plots for plates ranging from  $c/t = 6$  to 16 with forcing frequencies chosen so as to result in local peaks in the mean base suction as a function of forcing frequencies. The plots are taken at  $0^\circ$  in the forcing cycle, the flow is at  $Re = 400$  and the perturbation amplitude is  $v_{pert} = 2.5\%$ .

the phase of the trailing-edge shedding relative to the forcing by controlling when the leading-edge vortex passes the trailing edge. The vorticity plots in Figure 4.23 show that the phase of the trailing edge relative to the forcing is approximately constant for all plate lengths and frequencies which result in a strong mean base suction and correspond to the major shedding modes or steps in Figure 4.18. The relative phase between the forcing and the trailing-edge shedding, for the reason described earlier, controls the mean base pressure. The stepwise increase in Strouhal number (based on chord) with aspect ratio in the forced shedding case also maintains the same phase relationship between the trailing- and leading-edge shedding. As the phase of the shedding at the trailing edge is controlled by the passing of the leading-edge vortices at the trailing edge, the hypothesis by Hourigan *et al.* (1993) which states that the mean base pressure is due to the interference of the leading-edge vortices at the trailing edge is also applicable to this case.

In the forced shedding cases, the simulations show some plates displaying a second local peak in the mean base suction at a higher frequency. In these cases, the shedding at the trailing edge is about  $180^\circ$  out of phase relative to the forcing compared with the local peak at the lower forcing frequency or those plates with only a single local peak in the mean base suction. As these are only half a mode higher ( $180^\circ$  is half a cycle), the forcing frequencies of these cases correspond to an intermediate step between the modes as shown by the broken lines in Figure 4.18. The vorticity plots for these cases show not an extra pair of vortices along the plate but one half of a pair. It is likely that some resonance is occurring at these frequencies but the generally smaller peaks suggest that they are not as strong as the other local peaks. As the forcing amplitude is increased, the magnitudes of these peaks decrease (see Figure 4.12). As the leading-edge shedding remains phase locked, the increase in forcing amplitude therefore opposes the trailing-edge shedding in these cases. The experiments (Mills, 1998) do not show any excitation at these modes. They may not be present or be too weak to be detected. The differences are likely due to the large differences in Reynolds number and the three-dimensionality of the experimental flow. As an analogy to short bluff body flows, some geometries such as a square section show a  $180^\circ$  phase shift in the shedding when the forcing frequency is increased past the resonant point in some experiments (Bearman & Obasaju, 1982, Nakamura & Mizota, 1975) and not in others (Ongoren & Rockwell, 1988). This is also likely due to the differences in experimental parameters.

In the natural shedding case, the leading- and trailing-edge shedding is locked to a single frequency and relative phase by the ILEV instability. This is achieved via a feedback loop consisting of (i) the leading-edge vortices passing the trailing edge which control when the trailing-edge vortices form and, (ii) the passing of leading-edge vortices and the formation of vortices at the trailing edge which send pressure pulses upstream which then control when further leading-edge vortices form. For the forced shedding

cases, the first part of the feedback loop of the natural shedding case is still in effect but the forcing phase locks the leading-edge shedding, leaving no role for the second part. At the forcing frequencies that result in local peaks in base suction, there is also the same synchronisation between the leading- and trailing-edge shedding which in this case is controlled by the forcing. In fact, the relative phase difference between the leading- and trailing-edge shedding in these two cases is also similar (i.e., in the forced and unforced cases, when a leading-edge vortex is forming or detaching, so is the trailing-edge vortex on the same side). To maintain this condition for both the cases, the frequency reduces as the chord is increased until the overall flow system is no longer receptive to the low frequency and jumps to the next shedding mode, allowing for another period for the leading-edge vortex to traverse the plate, and resulting in another pair of vortices along the plate. The convective velocity of the vortices is not strongly influenced by the chord or frequency. All these factors lead to the stepwise response in the frequency for both cases.

In both the natural and forced shedding cases, the steps in frequency correspond to approximately  $St_c = 0.55n$ . The Strouhal number based on chord is the frequency multiplied by the chord and divided by the free-stream velocity. Let us consider the first mode ( $n = 1$ ). The frequency is the inverse of the time taken by the leading-edge vortex to travel the chord. Therefore the Strouhal number based on chord,  $St_c$ , is the streamwise component of the convective velocity of the leading-edge vortex averaged over the chord and scaled with the free-stream velocity. For the higher modes, the factor  $n$  is the number of periods required for the leading-edge vortex to pass the trailing edge. From Figure 4.20, both natural and forced shedding cases show the convective velocity initially reaching a minimum before rising to saturate at about 70% of the free-stream velocity. From the level of the steps, 55% of the free-stream velocity is a good estimate of the average convective velocity. Both the experiments for the natural shedding case (Nakamura, 1991) and the forced shedding case (Mills, 1998) show a step height of about  $St_c = 0.6n$ . Differences such as in Reynolds number and three-dimensionality in the experiments may cause a slightly higher average convective velocity.

### 4.3.5 Relating the fluctuating lift forces to the flow field

The fluctuating lift forces on the plate, shown in Figure 4.17, also show the stepwise nature with local maxima corresponding to the major steps and local minima associated with the half steps. The lift force is dependent on the pressure on the top and bottom surfaces. The leading-edge vortices result in a low pressure region on the surface near the vortex. Therefore the fluctuations in the lift force come from the mismatch in vortices on both sides of the plate. The leading edge sheds vortices alternately contributing to some of the fluctuating lift force. As this occurs similarly for all plates and frequencies,

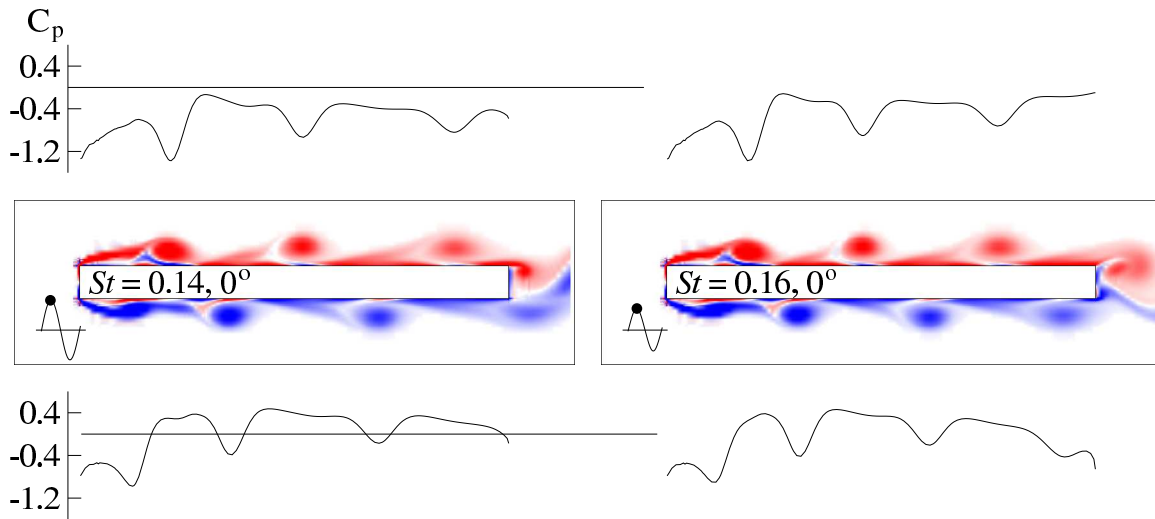


Figure 4.24: Plots of vorticity (centre) and surface pressure coefficient (above and below) for flow around a plate with  $c/t = 13$  at  $Re = 400$  taken at  $0^\circ$  in the forcing cycle with  $v_{pert} = 2.5\%$ . The plot on the left is when  $St = 0.14$  and the right when  $St = 0.16$ . The trace at the bottom left of each plot is the time trace of lift coefficient and the dot on the trace corresponds to when these plots are taken. The surface pressure plot above/below corresponds to the pressure coefficient on the top/bottom surface of the plate.

it cannot account for the variations in fluctuating lift forces as the forcing frequency is varied. The effects of the pairs of vortices along the plate approximately cancel each other. Once these vortices pass the trailing edge, their effect on the plate is significantly diminished. Therefore there is a mismatch at the trailing edge as the pairs of vortices from the top and bottom pass the trailing edge at  $180^\circ$  out of phase. For a given plate length, the forcing frequency controls the phase relative to the forcing as the vortices pass the trailing edge while the phase of the leading-edge shedding relative to the forcing is fixed. The magnitude of the fluctuating lift force is controlled by the relative phase between the leading-edge shedding and vortices passing the trailing edge because, like the superposition of two signals, they can either sum together or cancel each other depending on the relative phase. As the forcing frequency is varied, for those plates that show two local peaks in their mean base suction, the peak that is associated with the lower frequency shows a local maximum in the fluctuating lift force (maximum positive superposition), while the peak that occurs at a higher forcing frequency, where the passing of the leading-edge vortices and trailing-edge shedding is  $180^\circ$  out of phase relative to the earlier case, shows a local minimum (maximum cancellation) in the fluctuating lift forces. Therefore the fluctuating lift force is also dependent on the phasing of the leading-edge vortices as they pass the trailing edge.

The case where  $c/t = 13$ ,  $Re = 400$  and  $v_{pert} = 2.5\%$  is used to illustrate the

relationship between the vortices passing the trailing edge and the fluctuating lift force. Figure 4.24 shows vorticity plots taken when the forcing is at  $St = 0.14$  and  $0.16$ , which correspond to local maxima and minima in the standard deviation of lift coefficient. These plots are taken at  $0^\circ$  in the forcing cycle. The time trace of the lift coefficient in both plots is sinusoidal and shows that the lift coefficient reaches a maximum (maximum lift force in the upward direction) at  $0^\circ$  in the forcing cycle. The leading-edge shedding is approximately at the same shedding phase in both forcing frequencies shown. At the trailing edge, the plot shows that the flows are approximately  $180^\circ$  out of phase. As a result, there are three pairs of vortices when  $St = 0.16$  but only two pairs and a single vortex on the top side when  $St = 0.14$  (neglecting the partially formed vortex on the bottom side of the leading edge in both cases). In the case when  $St = 0.14$ , the extra vortex on the top side increases the lift coefficient (in the upward direction) because each vortex is associated with a low pressure region. When  $St = 0.16$ , the vortices are paired and this results in a lower lift coefficient. Naturally, the amplitude of the lift force is directly related to the standard deviation of lift coefficient. As these two cases are the extreme cases with respect to the fluctuating lift force, other forcing frequencies would result in a situation which is between these two.

In the natural shedding case, the leading-edge shedding also contributes to fluctuating lift forces. The number of vortices along the plate (shedding mode) is less significant because the forces from a pair of vortices cancel each other. The ILEV instability locks the relative phase of the leading- and trailing-edge shedding. Therefore the vortices pass the trailing edge at the same phase relative to the leading-edge shedding for all plates that lock to this instability. As shown in Figure 4.7, although the flow is no longer locked to one frequency, the larger aspect ratio plates continue the trends in mean base pressure, mean drag and fluctuating lift forces. The constant relative phase between the leading-edge shedding and the vortices passing the trailing edge would result in approximately a constant fluctuating lift force for all plates. As the fluctuating lift coefficient is scaled with the aspect ratio, an inverse relationship with aspect ratio is expected. For the data presented in Figure 4.7 with the flow at  $Re = 400$ , the relationship is approximately  $\sigma_{Cl} \approx 1.2/(c/t)$ .

### 4.3.6 On the variation in magnitude of the peak mean base suction

Also of interest is the magnitude of the local peaks in mean base suction as the forcing frequency is varied. Some aspect ratio peaks are of larger magnitude than others. This is also observed in the experimental data of Mills (1998). Certain aspect ratios in the natural

shedding case also show larger mean base suction than others. For both situations, the lower aspect ratio end of each step generally has a larger mean base suction.

The previous sections discussed the mechanism which controls the frequency selection for both these cases. In the previous chapter, the trailing-edge shedding on its own has been shown to be very sensitive to frequency in the lock-in range. In this chapter, the shedding frequency decreases towards the higher aspect ratio end of each step (constant  $St_c$ ). The base pressure is strongly controlled by the trailing-edge shedding because of its proximity. It is likely that the trailing-edge shedding is also sensitive to frequency as in the previous chapter.

To show the similarities between the two different geometries, the vortex formation length at the trailing edge is calculated. The mean base pressure and the vortex formation length are both measures of the state of the flow and are likely to be related. This is because the core of the vortex is a region of low pressure and larger base suction results if it develops nearer to the trailing face. Although this does not directly show the sensitivity of the trailing-edge shedding to (forcing) frequency, this analysis hopes to show the similarities between the trailing-edge shedding of the flow around the elliptical leading-edge plate and the rectangular plate. The trailing-edge shedding has been shown to be sensitive to frequency in the previous chapter. As this controls the strength of the mean base suction, a similar process may also occur for the rectangular plate.

#### 4.3.6.1 Vortex formation length

The vortex formation length will be calculated for plates with aspect ratios of  $c/t = 8$  and 10. These two plates are chosen because the shorter one is characteristic of plates that show two generally smaller local peaks in the mean base suction, while the longer one shows only a single dominant peak in the lock-in range. The method used to determine the vortex formation length is the same as that used in the previous chapter. The standard deviation of the cross-flow component of velocity is determined along the centreline downstream of the trailing edge of the plate. The vortex formation length is the distance downstream where the fluctuating component of the velocity in the cross-flow direction reaches a maximum.

Figure 4.25 shows the standard deviation of the cross-flow component of velocity as a function of distance downstream of the plate for several forcing frequencies and for the natural shedding case. Similar to the flow around elliptical leading-edge plates, all cases show a steep rise before peaking and then a more gradual decay. Upstream of the peak is the near wake where the velocities are small and downstream of the peak is where diffusion and cross-annihilation of the vorticity becomes important. The leading-

edge shedding does not significantly alter these processes. Compared with the natural shedding cases, the applied forcing generally increases the level of the fluctuations. This increase is due to a combination of more vigorous shedding and the additive contribution of the forcing.

The behaviour at an aspect ratio of  $c/t = 8$  is more complex. As the forcing frequency is increased from  $St = 0.12$  to  $0.14$ , which is at a local peak in the mean base suction, the formation length shortens and the level of the fluctuation rises. Both these observations suggest more vigorous shedding. As  $St$  is increased to  $0.16$ , the formation length increases and the levels drop off again. Then at  $St = 0.174$ , there is a larger increase and the formation length decreases again. At  $St = 0.18$ , both the fluctuation level decreases and the formation length increases drastically because the high forcing frequency suppresses trailing-edge shedding.

At an aspect ratio of  $c/t = 10$ , as the forcing frequency is increased from  $St = 0.12$  through  $0.14$  to  $0.165$ , there is a gradual decrease in the vortex formation length and an increase in the level of the fluctuations. This is a sign of a gradual increase in the intensity of the shedding at the trailing edge. There is a significant increase in the formation length and decrease in the level of fluctuation as the forcing frequency is increased to  $St = 0.167$  and then to  $0.19$ . As with the shorter plate, this is also the result of the shedding at the trailing edge being suppressed at high forcing frequencies.

Plots of the vortex formation length and mean base pressure as a function of forcing frequency for the two aspect ratios studied are shown in Figure 4.26. For most of the frequency range, there is almost a linear relationship between the vortex formation length and the mean base pressure. This is similar to the flow around elliptical leading-edge plates. This relationship is not maintained at high forcing frequencies where the trailing-edge shedding is suppressed. Compared with the natural shedding case, there is a greater increase in the mean base suction than there is a decrease in the vortex formation length when forcing is applied. Other factors such as more compact leading-edge vortices and the periodic nature of the forced cases may also contribute to the increased mean base suction when forcing is applied. The fluctuations between periods in the natural shedding cases at these aspect ratios and Reynolds numbers will reduce the synchronisation between the flow structures on both sides of the plate and lead to less base suction.

For flow around the rectangular plate with applied forcing, two major factors influence the mean base pressure. The phase of the trailing-edge shedding relative to the forcing has been shown in Section 4.3.3 to govern the forcing frequency where the mean base suction is the strongest. The magnitudes of these peaks are in turn related to the forcing frequency at which they occur. The magnitude of the peak base suction is higher when the forcing frequency at which it occurs is higher. The vortex formation length

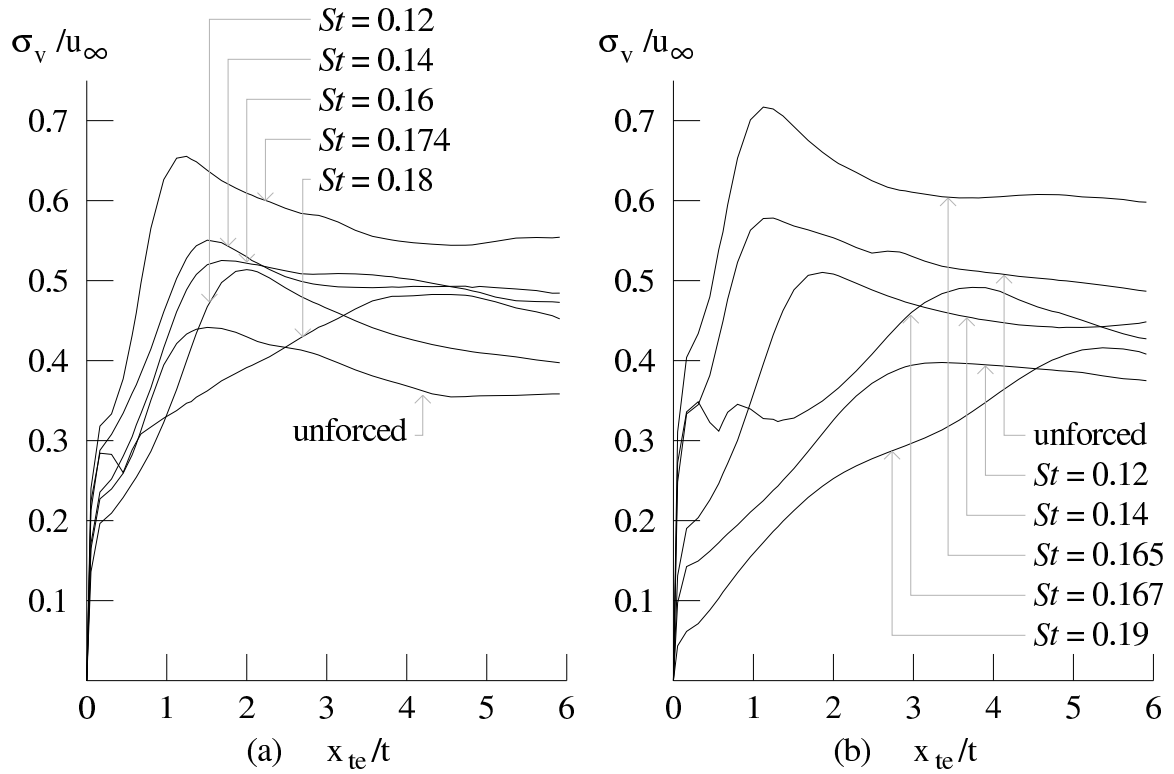


Figure 4.25: The standard deviation of the vertical component of the flow velocity measured along the centreline of the plate as a function of the downstream distance from the trailing edge for the unforced case and at selected forcing frequencies. The two cases shown have aspect ratios of (a)  $c/t = 8$  and (b)  $c/t = 10$  respectively. The flow is at  $Re = 400$  and the forcing amplitude is  $v_{pert} = 2.5\%$

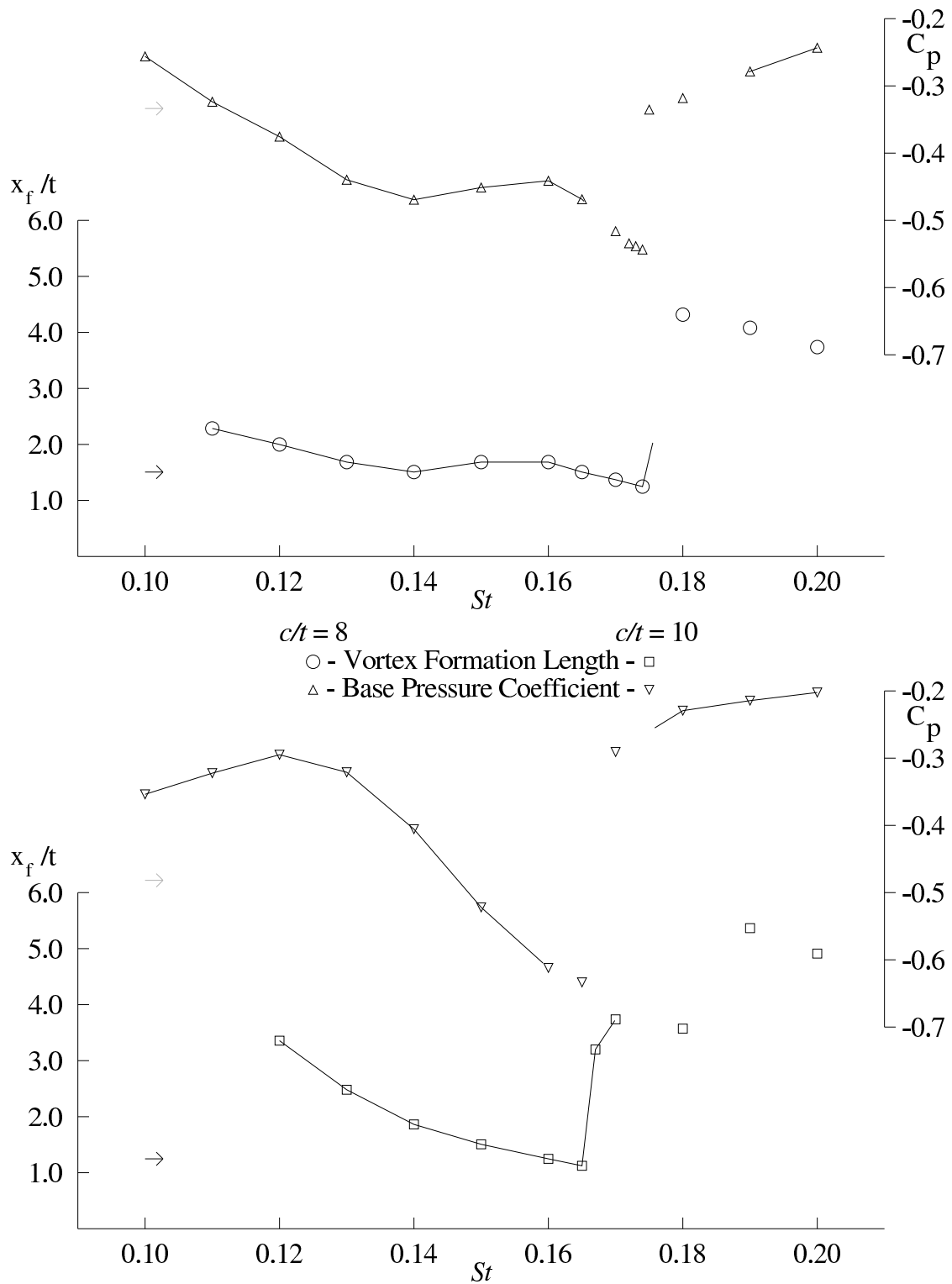


Figure 4.26: Vortex formation lengths and mean base pressure coefficient as a function of forcing frequency for flow over plates with  $c/t = 8$  and  $c/t = 10$  at  $Re = 400$  and  $v_{pert} = 2.5\%$ . Black and gray arrows show the vortex formation length and the mean base pressure respectively when there is no applied forcing.

decreases as the frequency increases and higher base suction are recorded when vortices form closer to the plate. There is a critical frequency above which the trailing-edge shedding is suppressed. In conclusion, the frequency selection of the peaks is a function of the aspect ratio (see Section 4.3.4) and the magnitudes of these peaks in turn depend on the forcing frequency at which these peaks occur.

As discussed in Section 4.2.3, there appears to be no relationship between the magnitude of the mean base suction in the natural shedding case and magnitude of the peak mean base suction in the forced shedding case. The frequency selection in both cases has been discussed in Section 4.3.4. Generally, there are small differences between the natural shedding frequency and the forcing frequency where the peak base suction occurs (See Figure 4.11). This is due to the small differences in the convective velocities of the vortices along the plate (see Figure 4.20). The different frequencies excited in the natural shedding case and the forced shedding case result in the different magnitudes in mean base suction. This is because the response of the trailing-edge shedding (which strongly influences base suction) is dependent on frequency.

## 4.4 Duct acoustic resonance

The interest in acoustic resonance controlling the flow around rectangular plates results from its application in cross-flow heat exchangers (Welsh & Gibson, 1979). The tandem arrangement of these plates was simplified to a single plate placed in a duct with solid walls in subsequent studies (Welsh *et al.*, 1984 and Stokes & Welsh, 1986). These experiments found that resonance occurred only around the natural shedding frequency when the plate had an aerodynamic leading edge but around several distinct ranges with a rectangular plate.

In this section, the flow around a plate confined within a solid walled duct will be studied. Experimentally, it is found that the sound generated by the vortex shedding from the plate may feed into resonant acoustic modes in the duct which then further interact with the flow leading to a strong acoustic resonance. The acoustic part of the problem will be modelled using Howe's acoustic theory (Howe, 1975, 1980) which is described in Section 2.4.3. An objective of this study is to compare the predictions with the experimental observations of Stokes & Welsh (1988) and to determine the phasing required for resonance. The source of the resonance will also be examined.

This model decouples the velocity field into an incompressible field and an acoustic field. It is assumed that there is already a sound field present to lock the flow. In this case, this is introduced by the cross-flow oscillations added to the free-stream velocity

as in the previous section. It turns out that, depending on the relative phasing of the vortex shedding and pre-existing acoustic cross mode, energy can be either transferred from the flow to the acoustic fields or vice versa (also described in Section 1.3.3 under Duct acoustic resonance). The rationale of the investigation is to determine whether a hypothetical acoustic field will enable energy transfer from the flow to the acoustic field so allowing maintenance of the resonance. This case can then be compared and contrasted with the natural and forced cases. This approach is used instead of treating both the flow and sound field simultaneously in a compressible flow simulation because the latter is much more computationally expensive. This is because for low Mach number flow, the time scale of the flow field is much greater than the sound field and consequently an extremely small timestep is required with an explicit integration scheme. Even so, the decoupled approach also allows the physics to be investigated more deeply through an ability to adjust the (hypothetical resonant) acoustic field independently of the flow field. The model attempts to determine the time-averaged transfer of acoustic energy between the flow field and the sound field. A positive time-averaged transfer of energy from the flow field to the sound field is a necessary condition for resonance because the energy is required to sustain the resonance. These simulations treat an ideal model but in reality there will be some (acoustic) damping which may narrow the resonance range. In effect, the approach tries to find a necessary but not a sufficient condition for resonance to occur. Only the first  $\beta$ -mode (i.e. cross-mode) in the duct will be considered in this study.

#### 4.4.1 Applying Howe's theory

In this study the flow around plates with aspect ratios between  $6 \leq c/t \leq 16$  at a Reynolds number of  $Re = 400$  will be examined. The amplitude of the perturbation used to lock the flow is  $v_{pert} = 2.5\%$ . The frequencies used in these analyses are chosen so that the flow is locked to the forcing. The flow is judged to be locked to the forcing (or periodic) when the mean base pressure trace is repeatable from one cycle to another and fluctuations between periods are negligible. The time averaging is done by sampling every 0.21 time units over one period which results in between 24 and 48 points per period.

The model also requires the acoustic particle velocity field to be determined. This is obtained by solving the wave equation (Equation 2.17). As described in section 2.4.3, the wave equation is decoupled into a product of the space and time dependent parts. The spatial dependence is solved on the same grid as used to simulate the flow to obtain the nodal variation of the  $\beta$ -mode. The size of the domain (duct) is therefore the same as that used in the flow simulation. Velocity nodes of the standing wave at the top and bottom boundaries in the simulation occur at the solid duct walls. This simulates a plate in a duct with a blockage ratio of 2.4%. This is close to the levels in the experiments

of Stokes & Welsh (1988) which were between 2.5% and 5%. The time-dependent factor consists of a sinusoidal oscillating component which is at the same frequency and is in phase with the forcing.

In the application of the model, the direction of the average energy transfer is crucial to determining whether resonance is possible. That is, is there nett transfer of energy from the flow to the acoustic field or vice versa, for any particular set of flow parameters? To maintain consistency between the different cases, some variables and parameters are kept constant. The mean ambient density,  $\rho_o$ , is set to one unit. The amplitude of the acoustic particle velocity can be arbitrarily scaled and still satisfy the wave equation and the boundary conditions. This ambiguity is removed by setting the amplitude of the acoustic particle velocity at the centre of the upstream (or downstream because of symmetry) face of the plate to one unit. The magnitudes of the velocity fields and the vorticity fields are determined by the free-stream velocity and the thickness of the plate which are both set to one unit. The only free parameter is viscosity which is used to control the Reynolds number.

The next hurdle is to determine the bounds of the volume integral which reduces to an area integral in the two-dimensional simulations. Although the entire region has to be included, from equation 2.15, only regions of non-zero vorticity contribute to the acoustic power. The vorticity several plate thicknesses away from the plate upstream of the leading edge and in the cross-flow direction is negligible. Therefore it is safe to set the integration boundaries about three plate thicknesses away from the plate in these directions. As the vorticity in the wake extends arbitrarily far downstream, formally the downstream integration boundary should be an infinite distance downstream. However, far downstream of the plate the transfer of energy between the flow and acoustic field is zero because each vortex contributes positive transfer for half the cycle and negative for the other half. Only regions near the plate have a nett contribution. If the downstream boundary is set a fixed distance downstream, a vortex crossing this boundary would only be a source/sink for part of a cycle. This would result in a bias in the calculation of overall average acoustic energy transferred. To overcome this, the time average acoustic energy is calculated with the integration boundary set at various downstream locations. This would result in a cumulative plot in the streamwise direction of the time average acoustic energy. The asymptotic value far downstream can then be estimated by extrapolating this cumulative plot.

## 4.4.2 Results from Howe's model

Figure 4.27 shows the cumulative plots for the plate with an aspect ratio of  $c/t = 10$  as a function of downstream distance for several duct frequencies. There are some aspects of the general behaviour which are applicable to all plates. The amount of acoustic power from upstream of the plate is very small because the amount of vorticity there is negligible. There is only a small amount of acoustic power generated along the plate because the acoustic particle velocity is deflected from a cross-flow direction to a streamwise direction in this region. This results in a small value of the cross product between the velocity and acoustic fields which is used to calculate the acoustic power. There are large contributions to the time average acoustic power just downstream of the trailing edge. At the trailing edge, shedding occurs and also passing of the leading-edge vortices. In this region, the acoustic particle velocity is approximately in the cross flow direction. These two factors cause the cross product to have a much larger value. Note the sudden change at the trailing edge: upstream of it there is only a small amount of acoustic power generated but there are large contributions just downstream. The cumulative time average acoustic power behaves similarly to a decaying sinusoid further downstream of the plate. The sinusoidal behaviour is due to pairs of shed vortices of opposite sign approximately nullifying the contribution of each other and the decay is due to cross-annihilation of the vortices.

The flow and geometry at the trailing-edge region results in a nett positive or negative transfer of energy and the cumulative total oscillates about a finite mean reflecting the nett transfer as it decays downstream. This mean is the asymptotic value the cumulative plot will reach far downstream. The plots show that for some frequencies the mean asymptotes to a positive value and for others it asymptotes to a negative value. Where the nett transfer is positive (i.e. from the flow to the sound field), resonance is possible. The wavelength of the oscillations further downstream of the plate decreases as the forcing frequency is increased. This wavelength represents the distance between shed vortices from the same side of the plate and this behaviour is expected if the convective velocity is approximately independent of forcing frequency. Also, as the forcing frequency is increased, the sinusoidal signal is phase shifted in the upstream direction. This is due to the variation in the phase of the leading-edge vortices passing the trailing edge and therefore also the trailing-edge shedding relative to the acoustic field or applied forcing. This process has been discussed in the previous sections (Section 4.3.3).

To demonstrate clearly that the source of acoustic power is mainly from the region just downstream of the trailing edge, an attempt is made to remove the downstream oscillations. Firstly, the wavelength of the downstream oscillation for each frequency is determined by averaging the distance between both peaks and troughs, ignoring the nearest cycle immediately downstream of the plate. This wavelength is then used to perform

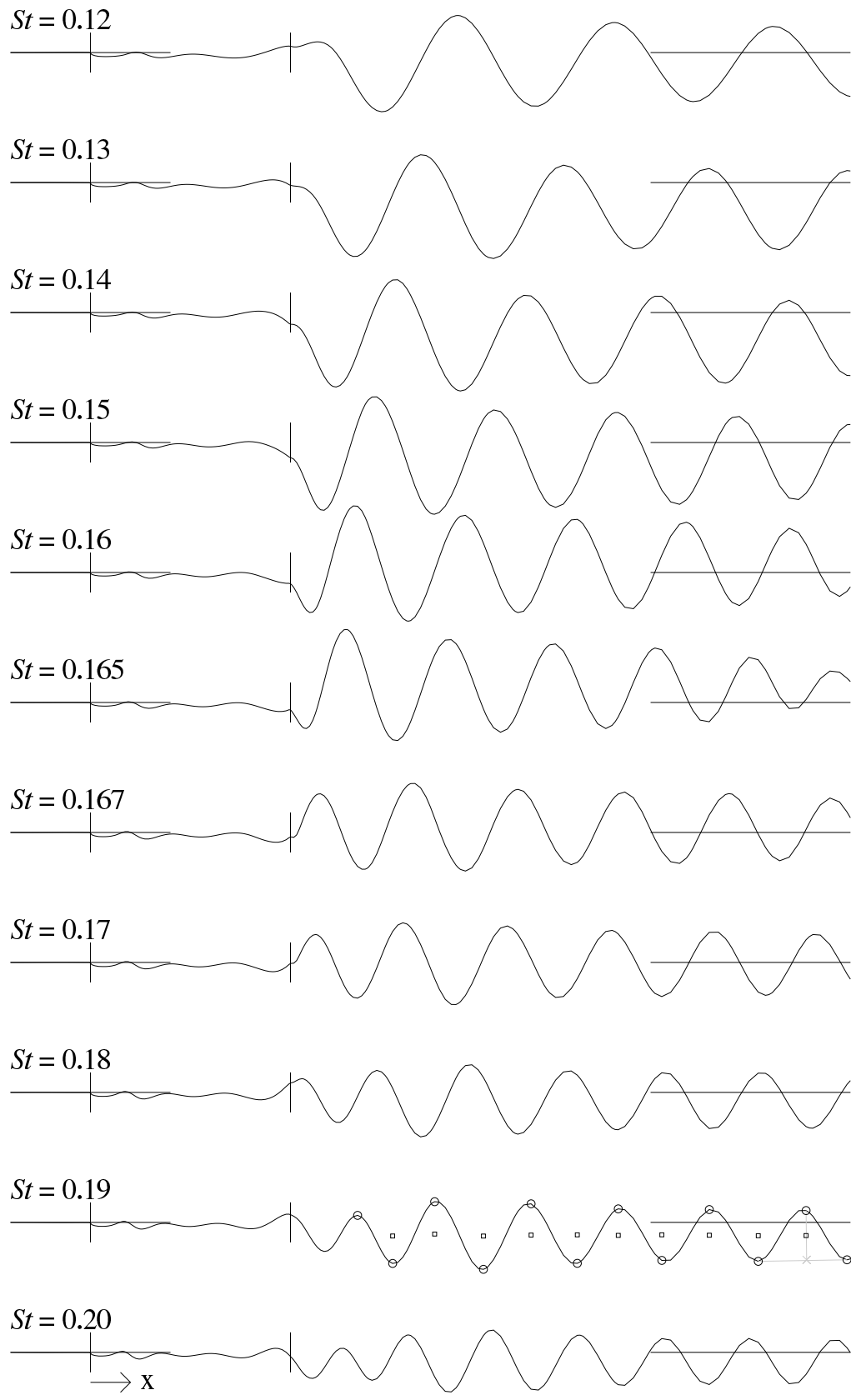


Figure 4.27: Cumulative total in the downstream direction of the time averaged acoustic power for a plate with  $c/t = 10$  at various frequencies. Vertical lines represent the leading and trailing edge of the plate while the dotted line is the zero value of the cumulative total.

a running average over the cumulative time average acoustic power thereby eliminating most of the downstream oscillations. The downstream oscillations are insignificant because contributions from each wake pair effectively cancel out resulting in a negligible net result. This analysis isolates the source of the acoustic power. Performing this on the plate with an aspect ratio of  $c/t = 10$  at the same set of forcing frequencies as in Figure 4.27 results in the plots shown in Figure 4.28. This exercise successfully isolates the source region of the acoustic power. In all cases, there is only a small value upstream of the trailing edge and this approaches a constant value downstream of the trailing edge. Therefore the main contribution is from just downstream of the trailing edge. This supports the argument that the source of acoustic power is from the mismatch at the trailing edge of the plate resulting from the change in direction of the acoustic particle velocity (i.e upstream of the edge it is approximately in the streamwise direction and downstream of the plate it is approximately in the cross-flow direction as seen in Figure 4.13 showing the forcing field).

At a forcing frequency of  $St = 0.165$  in Figure 4.28, the fluctuations in the running average further downstream in the wake, although small, are larger than in the other cases. The strongest mean base suction and the shortest reattachment length are observed at this duct (forcing) frequency. Compact trailing-edge vortices form close to the plate. As they convect downstream, they also accelerate. This results in small variations in the distance between the vortices as they convect downstream. These variations would be largest when the vortices form closest to the plate. This would explain the larger fluctuations downstream for the case with  $St = 0.16$ .

These plots show the asymptotic value further downstream of the plate. This value would correspond to the time average acoustic energy generated by the flow. Duct acoustic resonance is possible for those cases where this asymptotes to a positive value. The cumulative sum of the time average acoustic power would have to be evaluated far downstream to obtain the asymptotic value. This is not possible because of the finite computational domain. Instead, the asymptotic value is estimated from the cumulative plot downstream of the plate. This is done by analysing the sinusoidal decay. Symbols in Figure 4.27 when the frequency is at  $St = 0.19$  are used to illustrate these calculations. The troughs and peaks in the plot are shown by the circular symbols. The first three plate thicknesses downstream of the plate are ignored because this region is where there is a net generation or absorption of acoustic energy. For the rest of each cumulative plot, the average value between each two troughs is calculated (shown by the cross) and then averaged with the value at the peak for every cycle (resulting in the square). The same is done between each two peaks and the intermediate trough. Finally all these values (squares) are averaged to obtain the asymptotic value.

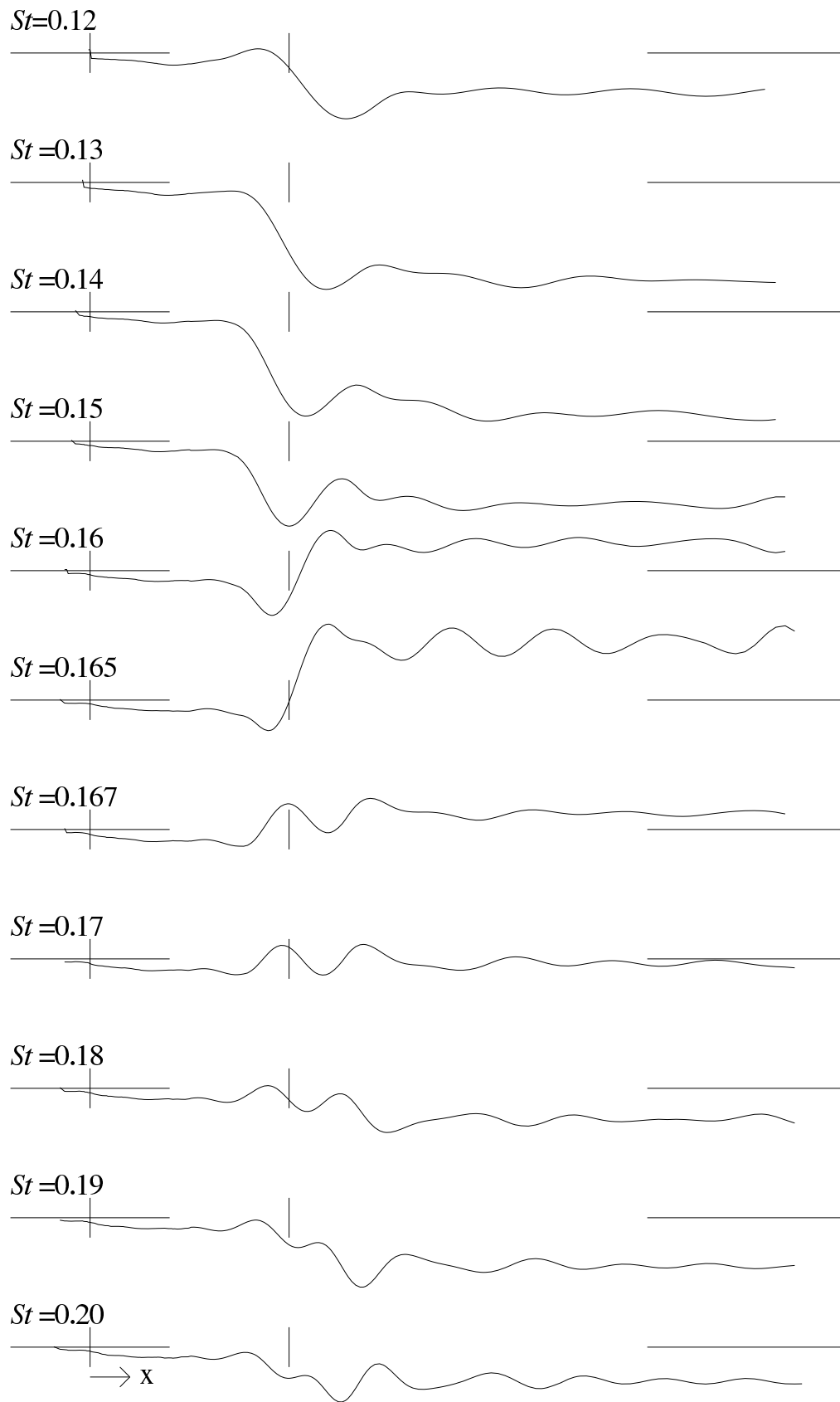


Figure 4.28: A running average of the cumulative sum in the downstream direction of the time averaged acoustic power for a plate with  $c/t = 10$  at various frequencies. The running average is taken over approximately one wavelength of the oscillations downstream of the plate.

This type of analysis is performed for all the plate lengths over the forcing frequency ranges that lock the flow. Plots of the asymptotic value of the time-averaged acoustic energy as a function of forcing frequency and plate length are shown in Figure 4.29. The vertical bars represent the maximum and minimum values obtained when analysing the peaks and troughs and are therefore representative of the errors associated with the extrapolation technique. For each plate this shows that there are ranges in the duct frequency where there is a positive transfer of energy from the flow field to the acoustic field. Some plates even show two distinct frequency ranges where this occurs. These ranges also show the similar trend of decreasing duct frequency as the aspect ratio is increased until the forcing frequency is no longer in the lock-in range. As this happens, another set forms at a higher frequency. This trend can be followed with the dashed lines crossing the plots in Figure 4.29.

### 4.4.3 Resonant ranges

The range of frequencies for each plate that could result in duct resonance is plotted in Figure 4.30. In this plot, the frequency is scaled with the chord ( $St_c$ ) and the results of Stokes & Welsh (1988) are plotted in the background and in colour (red and yellow). The simulations clearly show that the duct acoustic resonance frequencies also show a stepwise increase with chord. The experimental data also shows this trend. There is a larger deviation at longer aspect ratios because the level of the steps in the experimental data is about 10% larger than in the simulations. This is also observed when comparing the simulations with the experimental data in the natural shedding and the forced shedding cases. Again this is likely due to the difference in the convective velocity and is likely a result of the large difference in Reynolds number and the three-dimensional nature of the experiments.

### 4.4.4 Flow dynamics

To investigate further the source of the acoustic power, this section will examine more closely the region near the trailing edge where there is a large nett contribution to the acoustic power. Plots of vorticity from the flow field, the instantaneous acoustic power intensity (the value of the term within the integral in equation 2.15) and the time-average acoustic power intensity from the acoustic model will be used to explain the interaction between the flow and the sound field. The plate with an aspect ratio of  $c/t = 10$  at a low, moderate and high forcing frequency will be examined to show the differences caused by varying the forcing frequency. The plate with an aspect ratio of  $c/t = 16$  will be used to

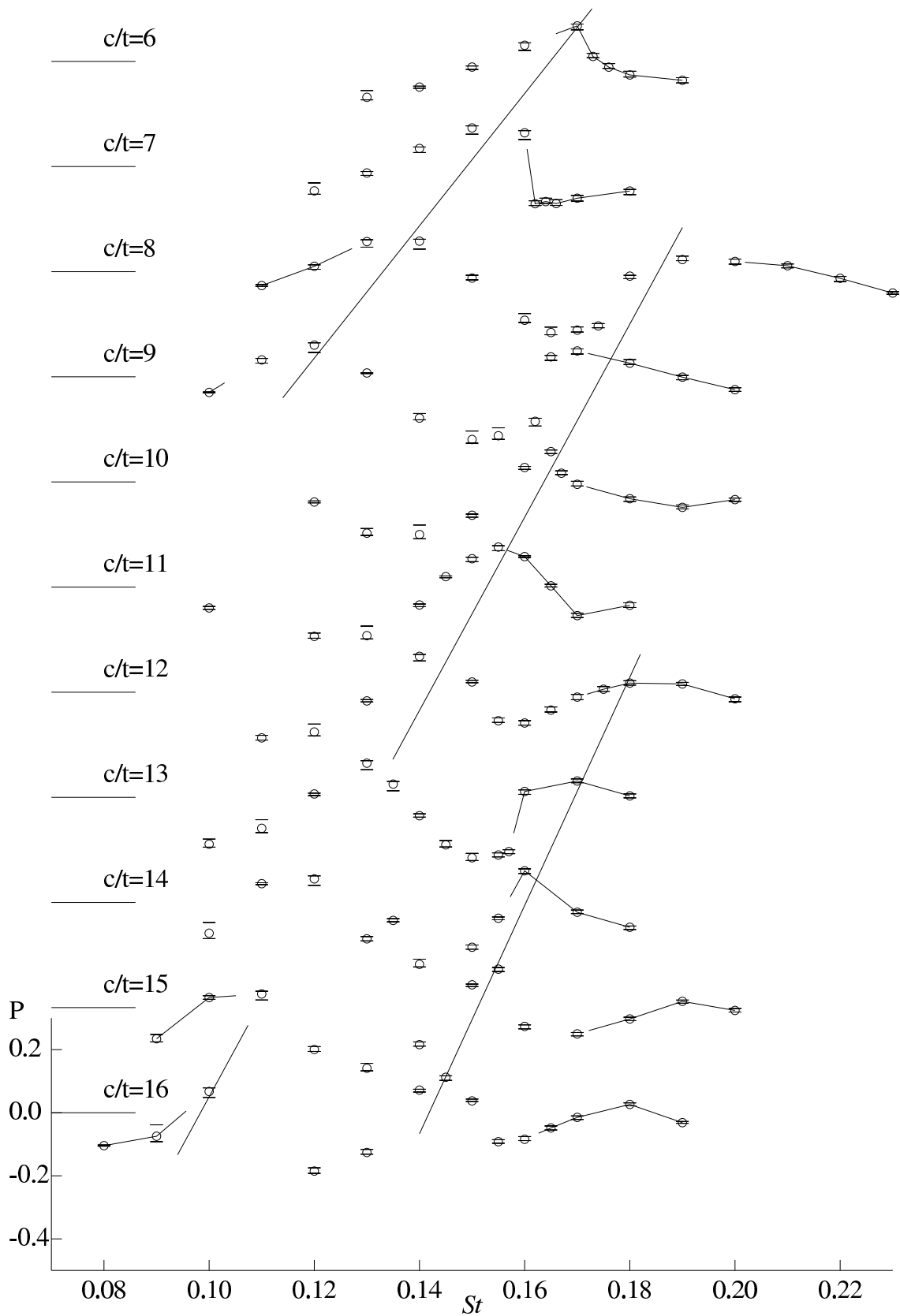


Figure 4.29: Time average acoustic power transferred between the flow field and the sound field for plates ranging from  $c/t = 6$  to 16 at various duct frequencies. The vertical bars represent the errors in extrapolating the time average acoustic power far downstream of the plate.

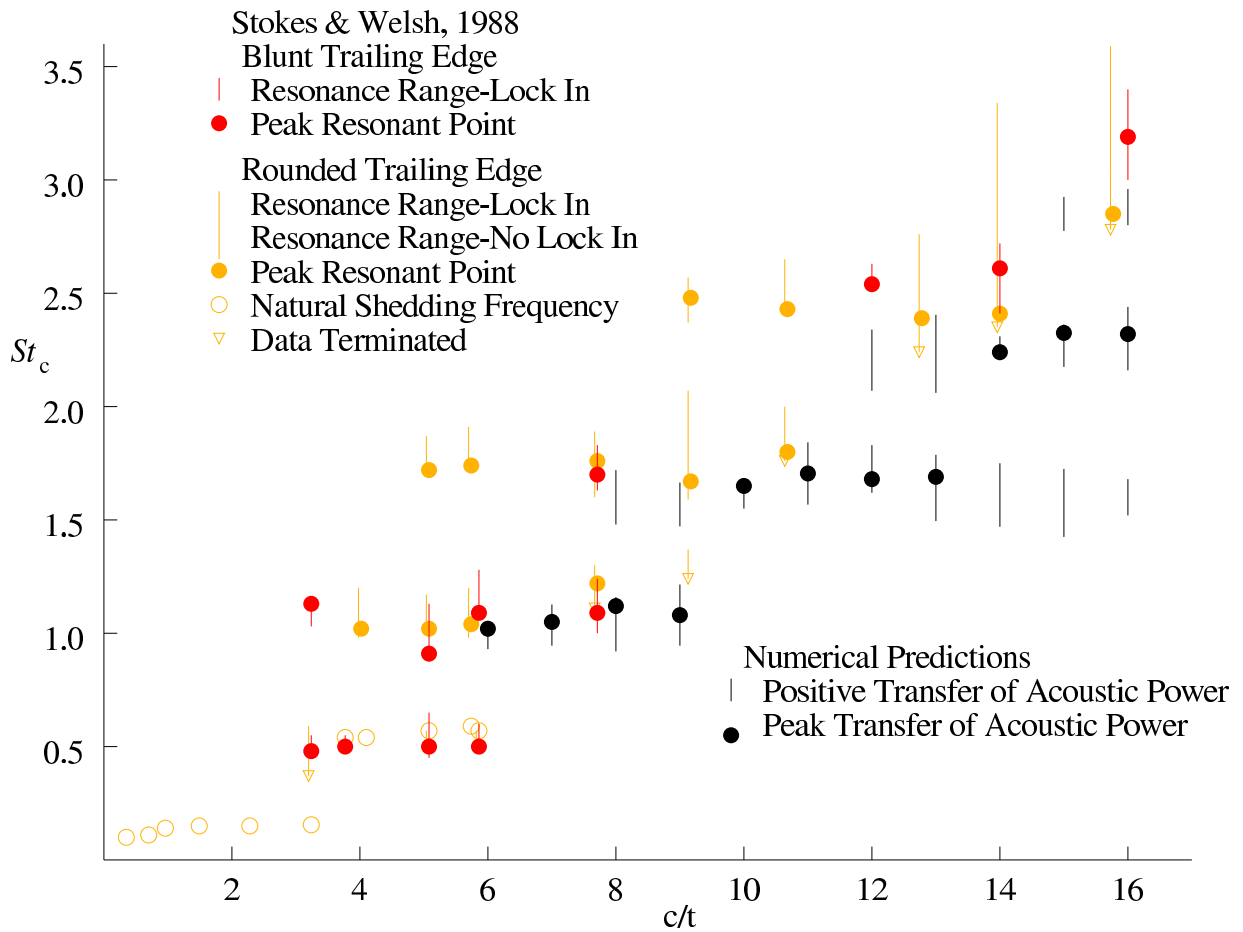


Figure 4.30: A plot of the frequency range (Strouhal number based on chord) where there is a positive transfer of energy between the flow field and the sound field. The results of Stokes & Welsh (1988) are plotted in red (rectangular plate) and yellow (plate with blunt leading edge and rounded trailing edge) for comparison.

show how resonance is generated at high frequencies even when trailing-edge shedding is suppressed.

Figure 4.31, 4.32 and 4.33 are taken at forcing frequencies of  $St = 0.14$ ,  $0.165$  and  $0.19$  respectively for flow over a plate with  $c/t = 10$ . In each plot, vorticity plots taken at  $0^\circ$ ,  $90^\circ$ ,  $180^\circ$  and  $270^\circ$  in the cycle are shown in (a) through to (d). Part (e) shows the time-averaged acoustic power intensity while plots (f) and (g) show the instantaneous acoustic power intensity at  $90^\circ$  and  $270^\circ$  in the duct resonance cycle. The instantaneous power at  $0^\circ$  and  $180^\circ$  in the forcing cycle is non-existent because the acoustic particle velocity is zero everywhere at that time. The time-average acoustic power intensity in each case shows a negligible amount of power upstream of the trailing edge and a large contribution just downstream of the trailing edge. As previously discussed in Section 4.4.2, this mismatch is the main contributor to the overall acoustic energy transfer. Further downstream are pairs of vortices that do not contribute a significant net amount. These correspond to the decaying sinusoid in the cumulative time-average acoustic power plots in Figure 4.27.

To understand better the mechanism involved in the generation of acoustic power, the discussion will focus on the timing of the shedding at the trailing edge for a plate with an aspect ratio of  $c/t = 10$ . Consider the case with a forcing frequency of  $St = 0.14$ . At  $90^\circ$  in the cycle, vortices from the bottom side of the plate are being shed into the wake (positive vorticity, out of the page). The acoustic particle velocity,  $\mathbf{v}$ , is in the upward direction and the flow velocity,  $\mathbf{u}$ , is predominantly in the streamwise direction. The cross product of these two vector fields would result in a positive vector (into the page). This is illustrated in the top right of Figure 4.35. The resulting dot product with the (positive) vorticity field would result in a region of negative power transfer between the flow field and the acoustic field (because the instantaneous power transfer is  $P = -\rho_0 \int \omega \cdot (\mathbf{u} \times \mathbf{v}) dV$ ). This is shown by the red (negative) region in the instantaneous plot at  $90^\circ$  in the cycle. At  $270^\circ$  in the cycle, which mirrors the plot at  $90^\circ$  in the cycle, (negative) vortices are being shed from the top side of the plate. Now the acoustic particle velocity is in the downward direction and therefore the cross product is now negative (bottom right of Figure 4.35). The result of the dot product would therefore be positive and this would again lead to a negative region in the instantaneous plot. These two phenomena lead to the negative region just downstream of the trailing edge in the time-average plot and therefore an overall negative transfer of power between the flow field and the acoustic field.

The situation is quite the opposite when the forcing frequency is at  $St = 0.165$ . At  $90^\circ$  and  $270^\circ$  in the cycle (see left column of Figure 4.35), vortices are being shed from the top (negative vorticity) and bottom (positive vorticity) surfaces of the plate respectively while the cross product is positive and negative respectively (as with the previous case with  $St = 0.14$ ). Although there is a small amount of vorticity forming on

the opposite side, the shedding of these larger vortices results in a positive (blue) region near the trailing edge of the plate in both the instantaneous and time-average plots of acoustic power. This leads to an overall positive transfer of power between the flow field and the acoustic field.

At the higher forcing frequency of  $St = 0.19$ , although the trailing-edge shedding is suppressed, the passing of the leading-edge vortices into the wake also results in a nett transfer of acoustic power. Like at the lower forcing frequency  $St = 0.14$ , vortices from the top and bottom side of the plate are being convected into the wake at  $90^\circ$  and  $270^\circ$  in the forcing cycle respectively. Again this results in the negative region downstream of the trailing edge in both the instantaneous and time-average plots of acoustic power intensity and an overall nett transfer of power from the acoustic field to the flow field.

At higher forcing frequencies, although trailing-edge shedding is suppressed, acoustic resonance is possible if the timing of the leading-edge vortices is conducive. The range of positive power transfer at the higher frequencies in Figure 4.29 and the higher level steps for several of the plates in Figure 4.30 display this phenomenon. To show this mechanism, the case where the aspect ratio is  $c/t = 16$  and the duct frequency at  $St = 0.18$  is chosen. Figure 4.34 shows this case in the same format as the previous three diagrams. The top and bottom vortices passing the trailing edge at  $90^\circ$  and  $270^\circ$  in the cycle result in the positive region near the plate in both the instantaneous and time-average plots of acoustic power intensity. This leads to a nett positive transfer of power between the flow field and the acoustic field.

#### 4.4.5 Discussion on the duct acoustic resonance

The main points in this section will now be reviewed. This includes the source of the acoustic power, the generation mechanism and the stepwise response of the resonance ranges.

It is not essential for there to be development of strong trailing-edge vortices for the development of resonance in the duct (as shown by the case with  $c/t = 16$  and  $St = 0.18$ ). The main controlling factor is the phase in the acoustic cycle when the leading-edge vortices pass the trailing edge (which also controls the phase of the trailing-edge shedding if it is present). When strong trailing-edge vortices develop at the trailing edge, they form before the arrival of a leading-edge vortex and these vortices coalesce in the wake. The increased circulation in the combined vortex would only serve to amplify the overall acoustic power transfer. The other regions of the flow provide a negligible contribution to the nett acoustic power. There is only a small amount generated upstream

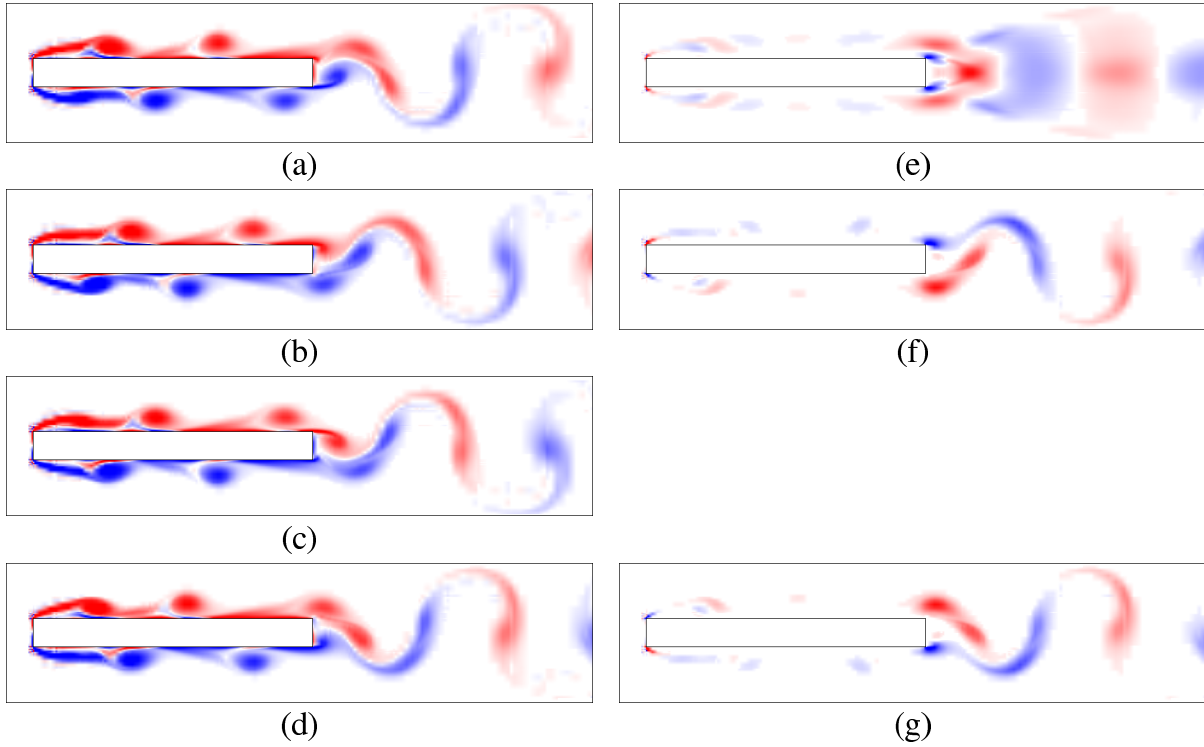


Figure 4.31: Left : Vorticity plots taken at (a)  $0^\circ$ , (b)  $90^\circ$ , (c)  $180^\circ$ , (d)  $270^\circ$  in the cycle ( $c/t = 10$  and  $St = 0.14$ ). Right : Extracted from the acoustic model are (e) the time-average acoustic power intensity, and instantaneous acoustic power at (f)  $90^\circ$  and (g)  $270^\circ$  in the cycle. In the time-average plot, the colour intensity range is  $[-0.4, 0.4]$ , and for the instantaneous plots, the range is  $[-1.5, 1.5]$ . Blue and red represent positive and negative respectively in all plots. Levels below a magnitude of 0.02 and 0.1 for the average and instantaneous plots are not coloured and levels outside the range are coloured with the maximum intensity.

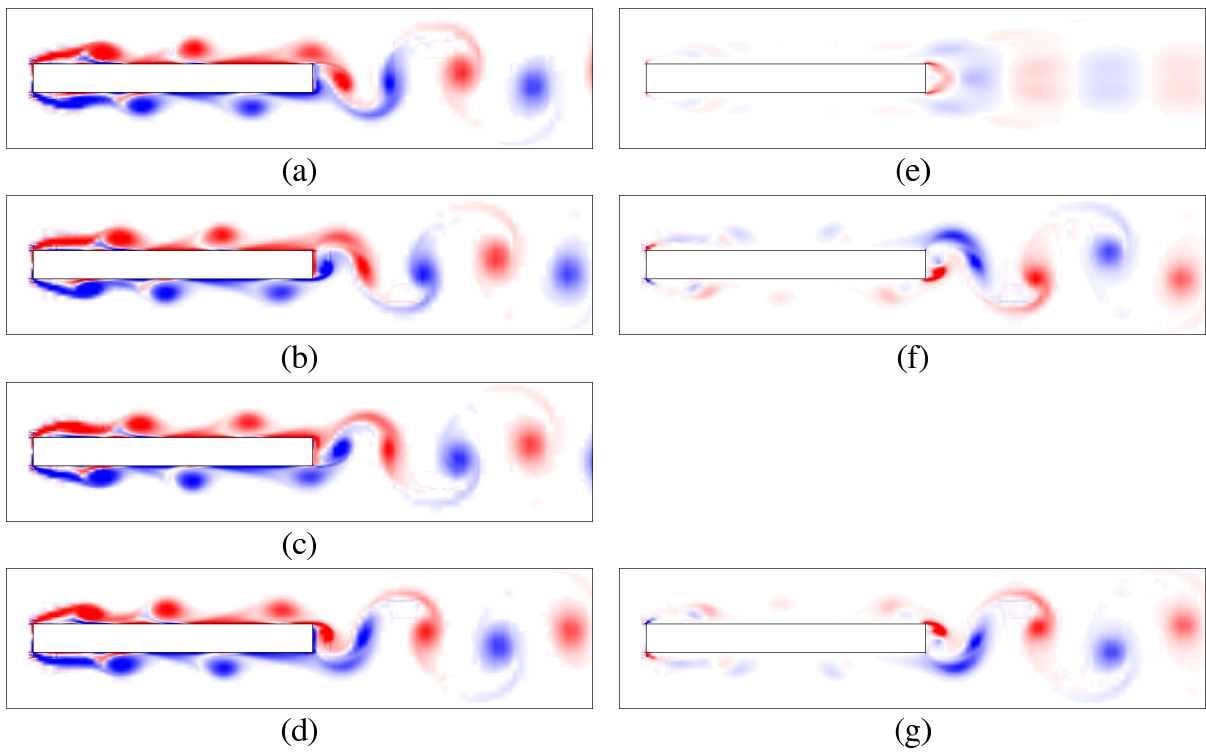


Figure 4.32: As for Figure 4.31, except for  $St = 0.165$

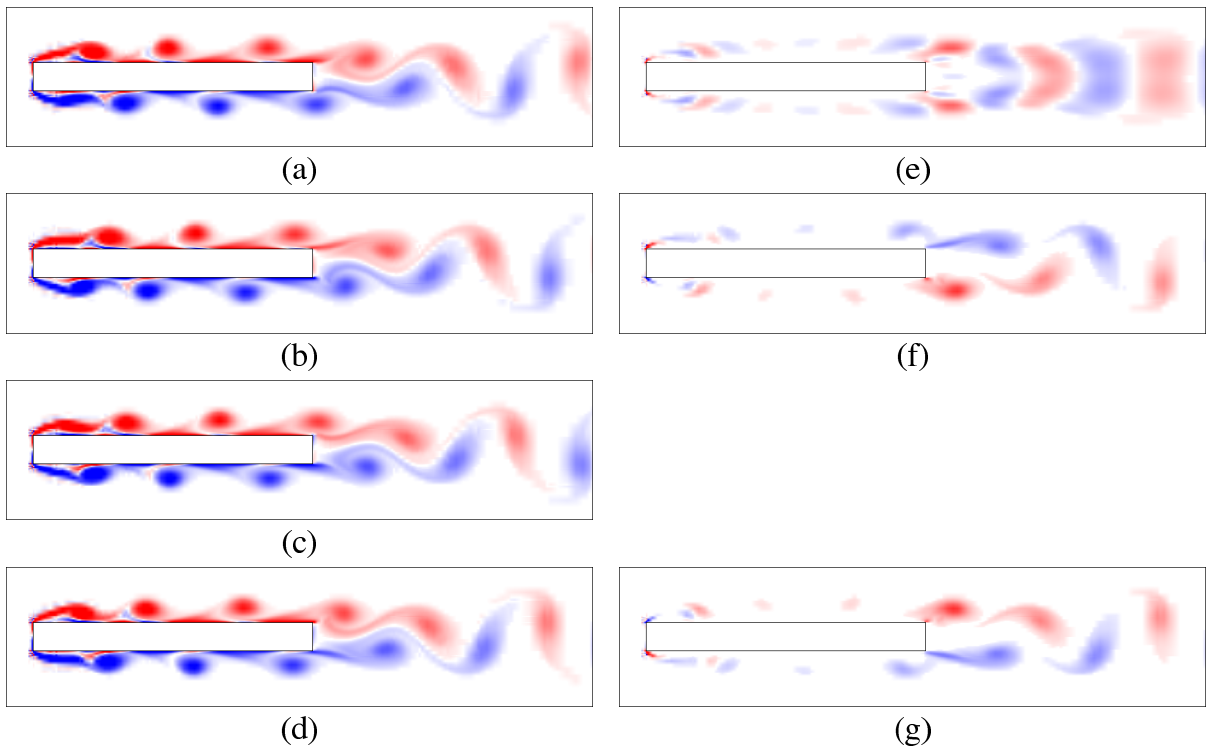


Figure 4.33: As for Figure 4.31, except for  $St = 0.19$

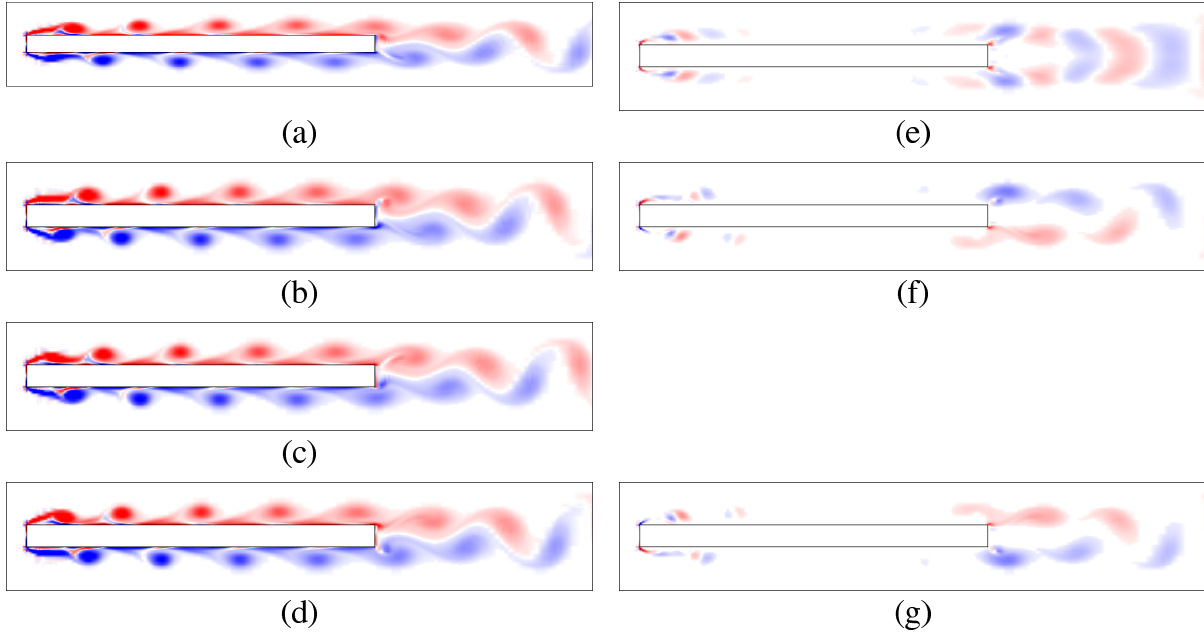


Figure 4.34: As for Figure 4.31, except for  $c/t = 16$  and  $St = 0.18$

of the trailing edge and the pairs of vortices further downstream nullify the effects of each other.

The phase in the cycle as the leading-edge vortices enter the wake or influence the formation of the trailing-edge vortices is crucial in determining whether resonance can occur. Figure 4.35 shows the two extreme cases with regard to the transfer of energy. Energy is transferred to the acoustic field when a vortex with a negative sign (clockwise) enters the wake when the acoustic particle velocity is in the upward direction, and a positive vortex (anti-clockwise) enters the other half of the cycle when the acoustic particle velocity is in the downward direction. Energy is transferred in the opposite direction if the vortices entering the wake at these times are of the opposite signs. Most cases would be between these two extremes and the amount and overall direction of energy transfer would depend on which case it is closer to.

Again the resonance range shows a stepwise increase in Strouhal number based on chord,  $St_c$ , with aspect ratio. The phase of the vortices entering the wake has been shown to govern the range where resonance is possible. As discussed in relation to the forced shedding case, the phase of the trailing-edge shedding (which forms vortices between the passing of leading-edge vortices) relative to the forcing is related to the aspect ratio and frequency. This same relationship also applied here except the forcing simulates the presence of an acoustic field. As with the forced shedding case, to maintain this

favourable phase at the trailing edge, a lower frequency is required as the aspect ratio is increased thereby resulting in a constant Strouhal number based on chord. As in the forced shedding case, this is a result of the approximately constant average convective velocity of the vortices along the plate at various frequencies and aspect ratios. The next higher or lower step would correspond to either an addition or a reduction in the number of pairs of vortices while again maintaining the favourable conditions at the trailing edge. These factors lead to the stepwise response in resonance ranges. The upper and lower limits in aspect ratio of each step are mainly governed by the lower and upper limits in forcing frequencies which lock the flow.

Point vortex models used by Stokes & Welsh (1986) and Stoneman *et al.* (1988) also predicted the relationship between the resonance range and the timing of vortices entering the wake (or impinging on the downstream plate for the tandem plate arrangement also studied in Stoneman *et al.*, 1988). A limited set of results by Thompson *et al.* (1987) using the vortex cloud method to simulate the flow field and the same treatment for the acoustic modelling as these simulations also came to this conclusion. A boundary layer model is used in these vortex methods and difficulties arise because the acoustic predictions are sensitive to these models. Although previous studies were able to capture the physics of the problem, they are less accurate because of the flow models used. In the simulations presented here, the flow field is directly simulated and the acoustic particle velocity field is accurately represented by the wave equation. This work has also extended the previous studies by covering a broad range of aspect ratios and frequencies.

#### 4.4.6 On the modelling of the acoustic particle velocity

As a side study, the sensitivity of the predictions from this model is examined when different approximations are used for the acoustic particle velocity. Besides the wave equation used in the previous section, two other models of the acoustic particle velocity will be considered.

The first alternative is to use a potential flow field solution to approximate the variation of the acoustic particle velocity around the plate. This results in the acoustic particle velocity consisting of a sinusoidally varying potential flow solution. The assumption of acoustic particle velocity is justifiable when the source region (of acoustic power) is small relative to the acoustic wavelength (in this case the size of the duct) so compressible effects can be ignored. This poor approximation away from the plate is acceptable because the source of acoustic power is mainly concentrated in regions near the plate. This method is examined because it has been used in previous analyses by Welsh *et al.* (1984) and Stokes & Welsh (1986).

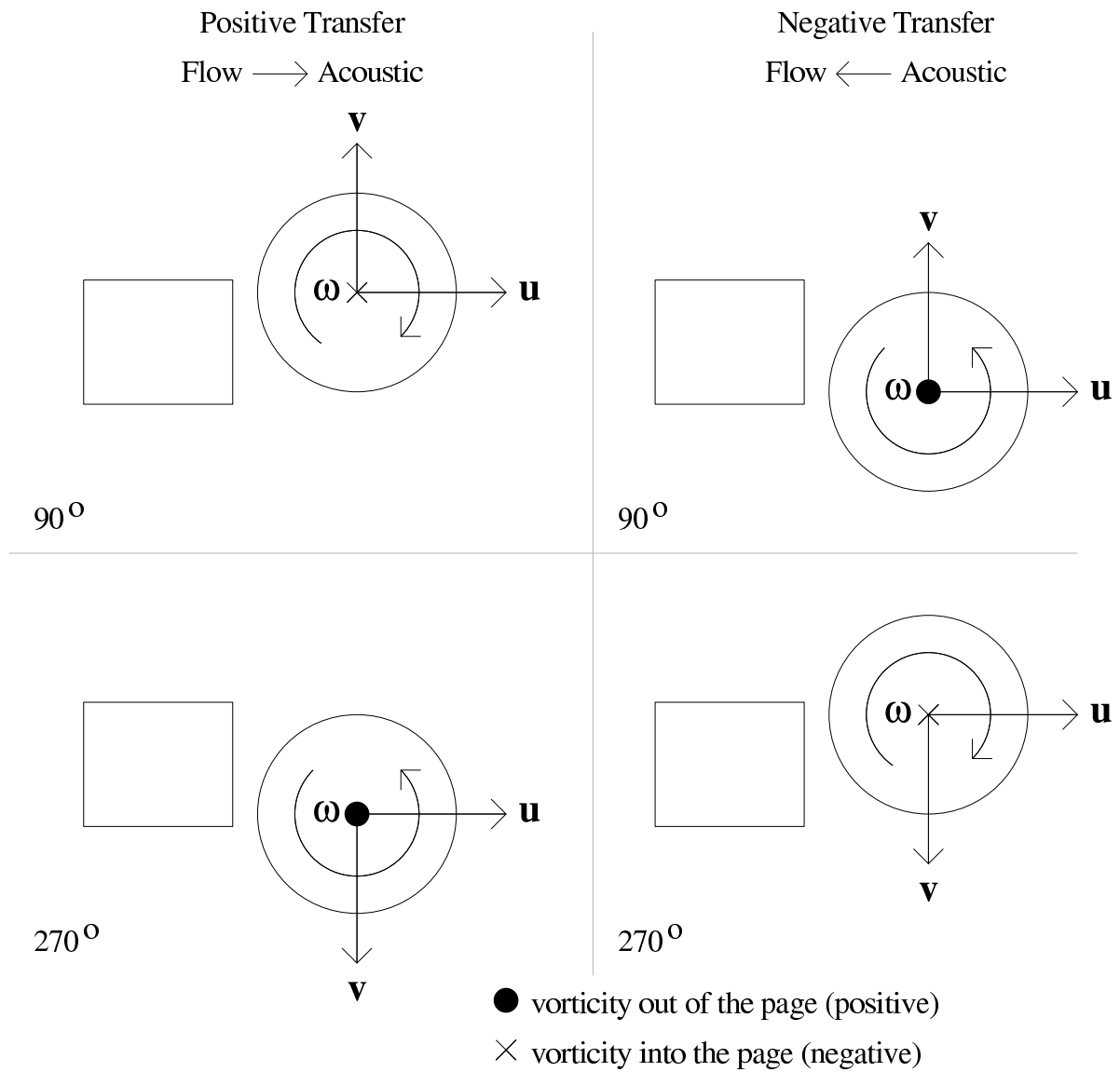


Figure 4.35: A schematic diagram showing the direction of the vorticity, flow velocity and acoustic particle velocity at  $90^\circ$  and  $270^\circ$  when power is transferred from/to the flow field to/from the acoustic field.

There are various methods for finding the potential flow around a plate. Here the following approach is used. Firstly the potential flow around a cylinder is solved analytically. Then the space around the cylinder is transformed to that around a plate using the Schwarz-Christoffel transformation (Churchill *et al.*, 1974). The velocity field around the cylinder can then be transformed to the space around the plate for any aspect ratio.

The second model for the acoustic particle velocity field is for an infinite duct. For the acoustic field approximation used in the rest of Section 4.4, the same computational grid is used as for the flow. The distance between the plate and the upstream boundary is  $l_1 = 24t$  while the downstream boundary is  $l_3 = 28t$  from the plate. The constraints imposed on the upstream and downstream acoustic velocity field are zero normal gradients on the acoustic particle velocity potential. Although these boundaries are far away from the plate, the boundary conditions that are imposed here artificially constrain the solution of the wave equation. Physically, this means that no energy (from the acoustic particle field) is transferred across the boundaries. To evaluate the effect of this constraint, the acoustic particle velocity from an infinite length duct (extreme case) will be used for comparison. Although the ducts used in the experiments are long, they are of a finite length and methods used to condition the flow may constrain the acoustic particle velocity differently. As it is difficult to quantify and model these conditions, this exercise only examines the effects the computational constraints have in the computation.

To determine the solution of the wave equation for an infinite duct, the wave equation is solved with the same boundary conditions but with various duct lengths. The amplitude of the acoustic particle velocity is solved with the boundary being at  $56t$ ,  $112t$  and  $224t$  away from the plate. Then (together with the original domain size) the four velocity fields are used to extrapolate the amplitude of the acoustic particle velocity for an infinite duct.

These three different approximations for the acoustic particle velocity are then used in the calculations. The longest plate ( $c/t = 16$ ) is used in this test because the various approximations differ more as the aspect ratio is increased. To show the differences between the various approximations, horizontal velocity profiles are taken of the cross-flow component of the acoustic particle velocity. Figure 4.36 shows these velocity profiles at several locations vertically displaced from the plate centreline. As all these amplitudes can be arbitrarily scaled, the potential flow with unit free-stream velocity is used as a reference. The other two velocity fields are scaled so that all fields are the same at a point one diameter horizontally away from the plate (shown by the circle). The comparisons are only shown for one quarter of the plate because the flow is symmetric or anti-symmetric in all the other quadrants. The length scale in the plot ( $x$ ) is the distance from the leading

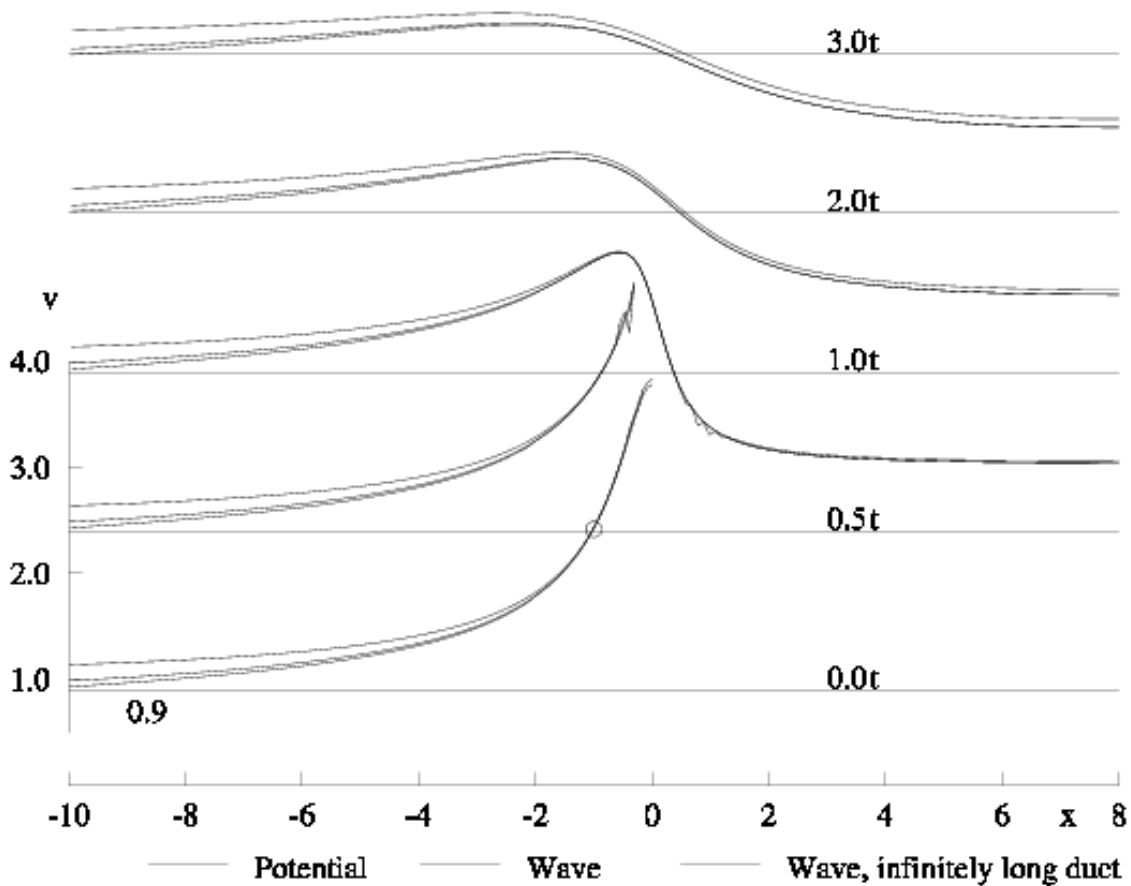


Figure 4.36: Horizontal velocity profiles of the cross-stream component of the amplitude of the acoustic particle velocity at several vertical positions from the centreline of the plate. The different approximations are found using the potential flow model and the wave model with a finite and infinite duct.

edge normalised by the thickness of the plate.

These plots show that the three approximations to the acoustic particle velocity differ more further away from the plate. This trend is insignificant as only the region near the plate is crucial in accurately determining the nett generation of acoustic power. The potential model approaches one unit far away from the plate as expected. Both the wave models decay away from the plate, in line with the physics. The solution for the finite duct decays less than for the infinite duct because of the constraints imposed at the boundaries. The amplitude for the infinite duct approaches zero far away from the plate while for the finite duct the imposed zero normal gradients of the velocity potential do not force the cross-flow velocity component to be zero.

Despite the fact that different approximations clearly give similar quantitative results, for completeness they are used to calculate the time-average transfer of acoustic

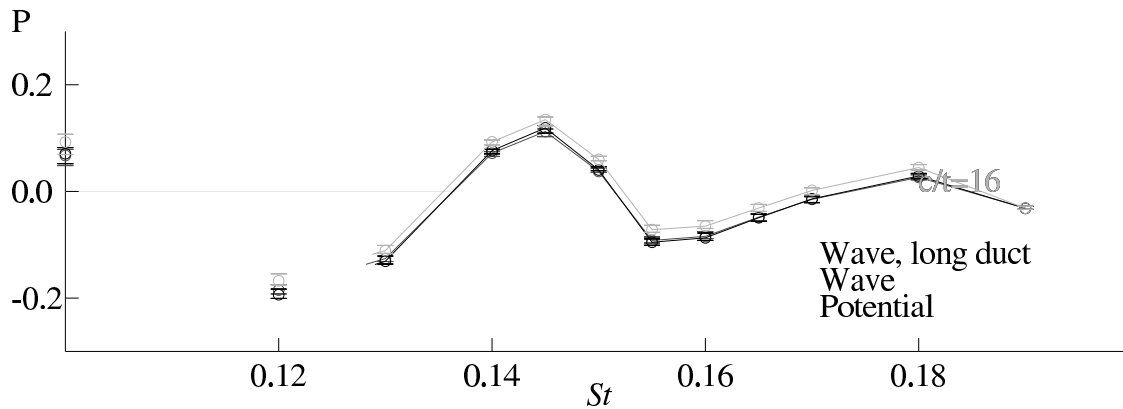


Figure 4.37: Time-average acoustic power intensity as a function of duct frequency for a plate with  $c/t = 16$ . The three results are for three different acoustic particle velocity models: (i) For the wave equation extrapolated to an infinitely long duct, (ii) for the wave equation for a duct the length of the computational domain, and (iii) for potential flow.

power from the flow field to the acoustic field. The same method as in the previous sections is used on the flow around the plate with  $c/t = 16$ . The time-average acoustic power as a function of duct frequency is plotted in Figure 4.37. There is only a small difference of less than 3% of the largest magnitude in energy transfer between the results when using the three different approximations. Using different approximations for the acoustic field does not alter the trend but only shifts the result by an approximately constant value. The technique used here only predicts a necessary but not a sufficient condition for resonance. A small error in the predicted range where resonance is possible is less significant because resonance would occur in an even narrower range as there is some damping in the physical system. The potential flow model shows a larger transfer because the velocity does not decay to zero. To conclude, the overall predictions are not sensitive to the model used for the acoustic particle velocity.

# Contents

<b>4</b>	<b>Flow Past a Long Rectangular Plate</b>	<b>112</b>
4.1	Natural shedding . . . . .	112
4.1.1	Effects of Reynolds number . . . . .	113
4.1.2	Shedding modes . . . . .	117
4.1.3	Base pressure and forces . . . . .	123
4.2	Applied forcing . . . . .	126
4.2.1	Effect of Reynolds number . . . . .	126
4.2.2	Effects of the amplitude of forcing . . . . .	129
4.2.3	The response at various aspect ratios . . . . .	131
4.2.4	The applied forcing without the mean flow . . . . .	135
4.2.5	Lift and drag forces . . . . .	142
4.2.6	Peaks in mean base suction . . . . .	143
4.3	Dynamics of the flows . . . . .	145
4.3.1	Phase of leading-edge shedding . . . . .	147
4.3.2	Convective velocity . . . . .	149
4.3.3	Phase of trailing-edge shedding . . . . .	150
4.3.4	On the stepping in the natural and forced shedding cases . . . . .	156
4.3.5	Relating the fluctuating lift forces to the flow field . . . . .	159

4.3.6	On the variation in magnitude of the peak mean base suction . . .	161
4.4	Duct acoustic resonance . . . . .	166
4.4.1	Applying Howe's theory . . . . .	167
4.4.2	Results from Howe's model . . . . .	169
4.4.3	Resonant ranges . . . . .	173
4.4.4	Flow dynamics . . . . .	173
4.4.5	Discussion on the duct acoustic resonance . . . . .	177
4.4.6	On the modelling of the acoustic particle velocity . . . . .	181

# Chapter 5

## Three Dimensional Flow Simulations

Three-dimensional simulations of flow around long plates with both elliptical and blunt leading-edge geometry are presented in this chapter. For the elliptical leading-edge plates, the focus will be on the flow structures that develop in the wake. These will be compared to those observed in the wake of short bluff bodies such as circular cylinders. The development of three dimensionality in the leading-edge structures will be studied for flow around rectangular plates. These will then be compared with experimental observations. Simulations are concentrated around Reynolds numbers where transition from two- to three-dimensional flow occurs.

### 5.1 Flow around elliptical leading-edge plates

As discussed in Chapter 1, the transition from two to three-dimensional flow around short bluff bodies, especially circular cylinders, has been well documented. The experimental observations of Williamson (1988) were the first detailed study of the two stage transition in the wake of a circular cylinder. Floquet stability analysis by Barkley & Henderson (1996) showed the critical Reynolds numbers for *Mode A* and *Mode B* shedding were  $Re = 188.5 \pm 1.0$  and 259 respectively. At transition, the spanwise wavelengths were  $3.96 \pm 0.02$  and 0.822 diameters for these two modes. Williamson (1996) suggested that *Mode A* is an instability of the main two-dimensional vortex rollers and *Mode B* is a result of an instability in the braid region between these vortices. The nature of these instabilities leads to different topologies in the wake. In particular, the vorticity of the streamwise vortical structures connecting the predominantly two-dimensional shed vortices are of opposite signs on each side of the wake for *Mode A* shedding and the same sign for *Mode B* shedding.

These instabilities have also been observed in the wake of other short bluff bodies such as square sections. Again using the Floquet stability analysis, Robichaux *et al.* (1999) predicted the transitions for the flow around a square section to be at  $Re = 161$  and 190. In this case, the spanwise wavelength for *Mode A* and *Mode B* shedding are  $5.2t$  and  $1.2t$  respectively. The analysis also predicted another mode above  $Re = 200$  called *Mode S*, which had a spanwise wavelength of  $2.8t$ . Unlike the first two modes, this mode is a subharmonic with a period twice that of the vortex shedding.

Above a critical Reynolds number, and in the absence of leading-edge shedding, the boundary layer on a long plate rolls up and sheds vortices at the trailing edge similar to short bluff bodies. In this section, the three-dimensional flow over elliptical leading-edge plates is simulated to investigate the effect of the longer body. The differences are likely caused by the thicker boundary layer at the trailing edge and the blunt trailing-edge geometry.

The method used to simulate the three-dimensional flow is described in Chapter 2. It involves expanding from a two-dimensional plane into the spanwise direction using a Fourier Galerkin method. The boundary conditions applied to the two-dimensional simulations are now extended throughout the span. The free stream and solid boundaries have no velocity component in the spanwise direction and the outflow boundary enforces zero normal gradients on all components of velocity. The Fourier expansion (artificially) imposes a periodic condition in the spanwise direction. This means that the spanwise dimension should be chosen to be sufficiently large to capture the relevant spanwise wavelength. The pressure boundary condition incorporates the spanwise velocity component to ensure that continuity is satisfied near the solid boundary and the overall scheme formally maintains second-order temporal accuracy.

To reduce the computational cost of the simulations, the two-dimensional domain is reduced relative to the domain size used in the two-dimensional simulations. This enables more Fourier planes to be used and a larger spanwise domain to be simulated. This is desirable as some spanwise modes may have long wavelengths. Although this will quantitatively affect the surface pressure on the plate (up to 10%), the interest is mainly on flow topology in this section which is assumed to be less sensitive to the size of the computational domain. The computational domain is still kept large enough to avoid any significant influence on the flow structures. For the simulations of the flow over an elliptical leading-edge plate, the same leading-edge geometry is used as before which is an ellipse with a 5:1 axes ratio. The outflow, side and inflow boundaries are positioned at  $l_3 = 18t$  and  $l_1 = l_2 = 10t$  away from the plate respectively. The resolution near the plate within each plane is kept approximately the same as in the two-dimensional simulations. As the Reynolds numbers for these simulations do not exceed those used for the two-

dimensional cases, and the two-dimensional simulations resolve the flow, it is assumed that this resolution is sufficient. The same timestep of  $\Delta t = 0.07$  non-dimensional time units are used for these simulations.

The spanwise domain is set to  $2\pi t$  wide. This is approximately two *Mode A* wavelengths observed for a circular cylinder wake. The spanwise resolution is varied between 24 to 48 Fourier planes to verify that resolution is sufficient to resolve the (spanwise) flow. This allows discrete resolution of spanwise wavelengths between  $2\pi/24t$  and  $2\pi t$  ( $\approx [0.25t, 6t]$ ). The resolution of longer wavelengths is more limited (i.e.  $2\pi t$ ,  $2\pi/2t$ ,  $2\pi/3t$ , ...). This limits the modes that can appear in the simulations, and thus can have an impact on the results.

The simulations are started with the velocity field from a two-dimensional simulation (in the asymptotic state) mirrored onto every plane. The simulations at higher Reynolds numbers are started with the flow field from the next lower Reynolds number. A small amount of noise is added to the velocity field at the start of the simulations to excite any spanwise instabilities that may be present. The noise consists of a random field at three orders of magnitude below the free-stream velocity. Between 150 to 200 non-dimensional time units (approximately 30 to 50 shedding cycles) are simulated in each case before any conclusions are drawn. The velocity is monitored at several points near the trailing edge of the plate. A flow is classified as two-dimensional if the spanwise component of the velocity shows a clear decay. If a three-dimensional instability develops, the flow is simulated until there is some repeatability in the flow structures over several shedding cycles and the mean base pressure over several shedding cycles does not show large drifts normally associated with changes in shedding modes.

### 5.1.1 Natural shedding case

#### 5.1.1.1 $c/t = 7.5$

Initially the same aspect ratio of  $c/t = 7.5$  as studied in the two-dimensional cases was chosen. The simulations were performed using 24 Fourier planes in all cases except at  $Re = 500$  where strong streamwise vortices developed and 48 Fourier planes were used. Simulations at a Reynolds number of  $Re = 250$ ,  $Re = 300$  and  $400$  showed no three-dimensional instabilities and the noise introduced at the start of the simulations decays to levels corresponding to round off error. Simulations at  $Re = 500$  showed the development of three-dimensional flow. Figure 5.1 shows the case where the Reynolds number is  $Re = 500$ . This iso-surface plot and all the subsequent visualisations in this section show double the actual computational domain for clarity. As can be seen from the contouring levels

of streamwise vorticity ( $\pm 0.3$ ), the magnitude of the streamwise vorticity is of the same order as the vorticity levels in the spanwise direction (peak vorticity of around 2 non-dimensional units in the shed vortices).

The streamwise vortices diffuse rapidly resulting in poorer visualisation past three or four of the two-dimensional rollers downstream of the plate. Nearer the plate, the iso-surface plots shows that the streamwise vortical structures connecting the two-dimensional rollers are of opposite signs on both sides of the wake. There is some distortion of the two-dimensional rollers especially nearer to the plate. The topology of the wake in this case is consistent with *Mode A* shedding in the wake of a circular cylinder. The predominant wavelength in this case is half the domain width which is  $\pi t$ . There is some excitation of the longest wavelength in the domain ( $2\pi t$ ) which is more noticeable further downstream. As these are the two longest wavelength that can be captures in this domain, there is some uncertainty in the wavelength of the dominant mode. This is discussed further after studying the shorter plate ( $c/t = 2.5$ ).

Preliminary results from a Floquet stability analysis by Thompson (2000) have shown that the first transition for this geometry occurs at approximately  $Re \approx 470$  which is consistent with these simulations. Relative to the circular cylinder wake transition, the transition Reynolds number for this geometry is significantly higher probably because of the thicker boundary layer and the shedding of more diffused vortices at the trailing edge. No simulations were performed above  $Re = 500$  in search of the next transition because of computational constraints.

### 5.1.1.2 $c/t = 2.5$

The flow over a shorter plate with aspect ratio of  $c/t = 2.5$  is simulated to bridge the difference between the long plate and a short bluff body. At this aspect ratio, the elliptical leading-edge geometry spans the entire chord. Simulations were performed at Reynolds numbers of  $Re = 300, 350$  and  $380$ . The spanwise resolution was varied between 36 planes and 48 planes to verify the accuracy of the predictions.

At a Reynolds number of  $Re = 300$ , the instability that develops has a wavelength that spans the entire computational domain. After the flow has reached an asymptotic state, there is some variation in the spanwise mode which occurs over several shedding cycles. Figure 5.2 and 5.3 shows the flow at approximately the two extreme cases. Figure 5.2 shows mainly the presence of the longer wavelength while Figure 5.3 show the presence of a shorter wavelength as well. This mode-mode interaction is similar to that found in the wake of a circular cylinder simulated by Henderson (1997). The flow shows a significant distortion to the two-dimensionality of the Strouhal vortices and the streamwise vortices

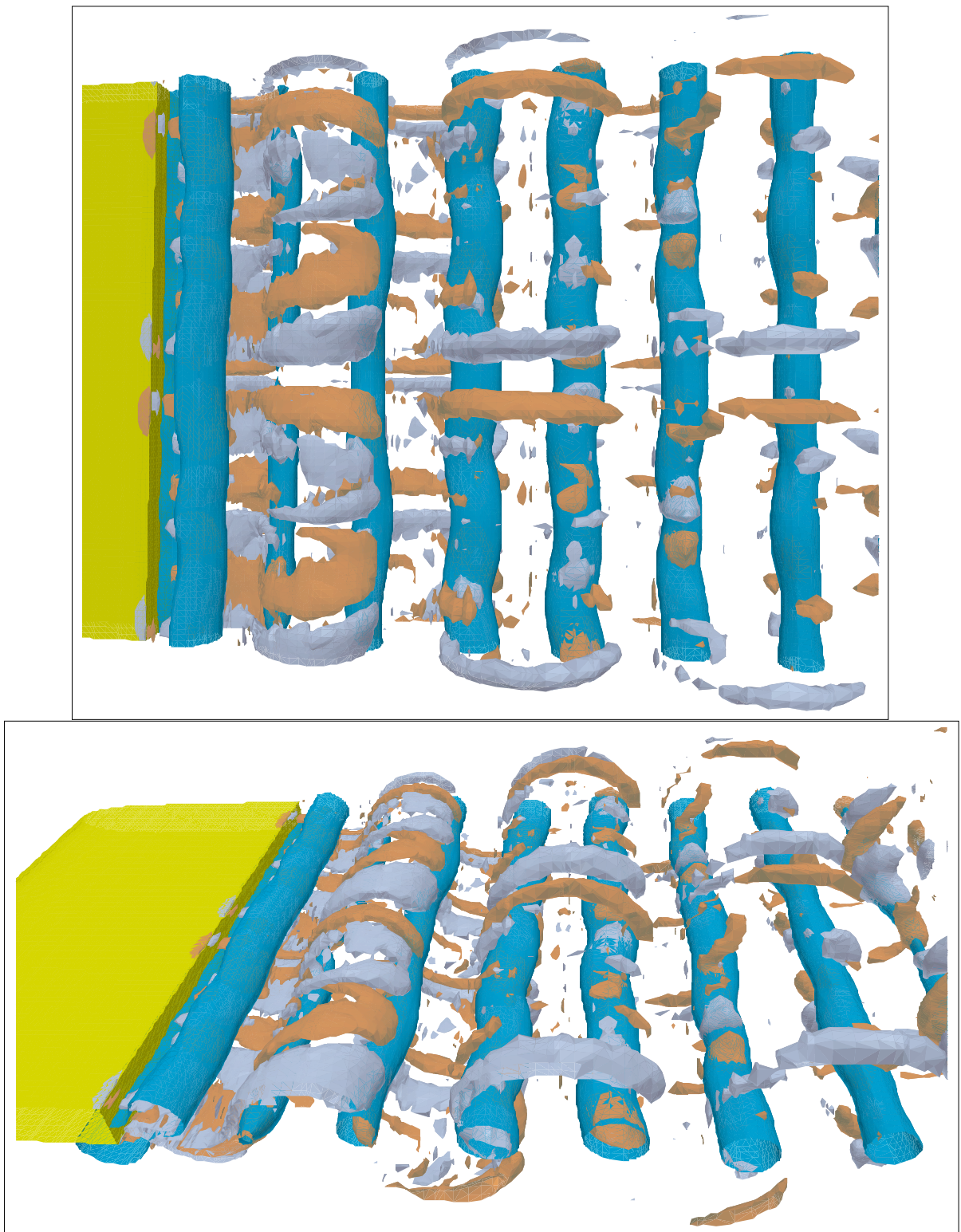


Figure 5.1: Iso-surface plot for flow around an elliptical leading-edge plate with  $c/t = 7.5$  at  $Re = 500$  viewed from the top (above) and side (below). The plate is shown in yellow, the positive and negative iso-surfaces of vorticity are coloured light blue and orange respectively; and the iso-surfaces of pressure are in dark blue. The value of the iso-surface of kinematic pressure is at  $-0.2$  and streamwise vorticity  $\pm 0.3$ . These values are non-dimensionalised with the free-stream velocity and plate thickness. This colour scheme is used in all subsequent three-dimensional visualisations.

are aligned with opposite signs between the two sides of the wake consistent with *Mode A* shedding observed in a circular cylinder wake. The different viewpoint used in the separate plots highlights the behaviour of the streamwise vortices. This shedding mode excites the longest wavelength in the domain ( $2\pi t$ ) with sporadic bursts of shorter wavelengths. The spanwise wavelength of this shedding process together with that of the longer plate will be further discussed in the following section.

Figure 5.4 shows a visualisation of the flow taken for the simulation at a Reynolds number of  $Re = 350$ . Competition between the two different shedding modes is observed at this Reynolds number. While there is significantly less distortion to the two-dimensional vortex tubes, the braid region between the tubes shows the presence of a smaller wavelength with a topology similar to *Mode B* shedding. This behaviour is similar to that observed for a circular cylinder wake at  $Re = 260$ . At that Reynolds number the wake is particularly “clean” in that the *Mode B* shedding is reasonably regular, while the *Mode A* shedding has mostly died out. At higher or lower Reynolds numbers, the circular cylinder wake is observed to be more chaotic. The increased correlation in the two-dimensional shedding results in a recovery in base pressure from the *Mode A* shedding similar to the flow around circular cylinders (Williamson, 1988). Overall, this competition between the two modes is consistent with the flow around circular cylinder in which there is a gradual decay (in the mean energy) of one mode and the growth of another as the Reynolds number is increased.

When the Reynolds number is increased still further to  $Re = 380$ , as seen in Figure 5.5, the flow is dominated by shedding similar to *Mode B* shedding. This has a wavelength of approximately  $0.8t$  and the vortex filaments are of the same sign as matching filaments on opposite sides of the wake consistent with *Mode B* shedding in the wake of a circular cylinder (Williamson, 1988). There is also less distortion to the two-dimensional vortex tubes like the case at  $Re = 350$ .

### 5.1.1.3 Wavelength of *Mode A* shedding

In these simulations, the domain size restricts the allowable wavelengths to be  $2\pi t$ ,  $\pi t$ ,  $2\pi/3t$  ... . In the case with  $c/t = 7.5$  and  $Re = 500$ , the most excited wavelength is  $\pi t$ , while at  $c/t = 2.5$  and  $Re = 300$ , it is  $2\pi t$  with the sporadic presence of some smaller wavelengths. To estimate the most unstable wavelength, assume that it scales linearly with the thickness of the plate plus two times the displacement thickness at the trailing edge. The circular cylinder with a thin boundary layer has a *Mode A* wavelength of 3.96 diameters at transition. When the displacement thickness is included, the length scale for the shorter plate is  $1.2t$  and the longer plate is  $1.3t$  at their respective Reynolds numbers.

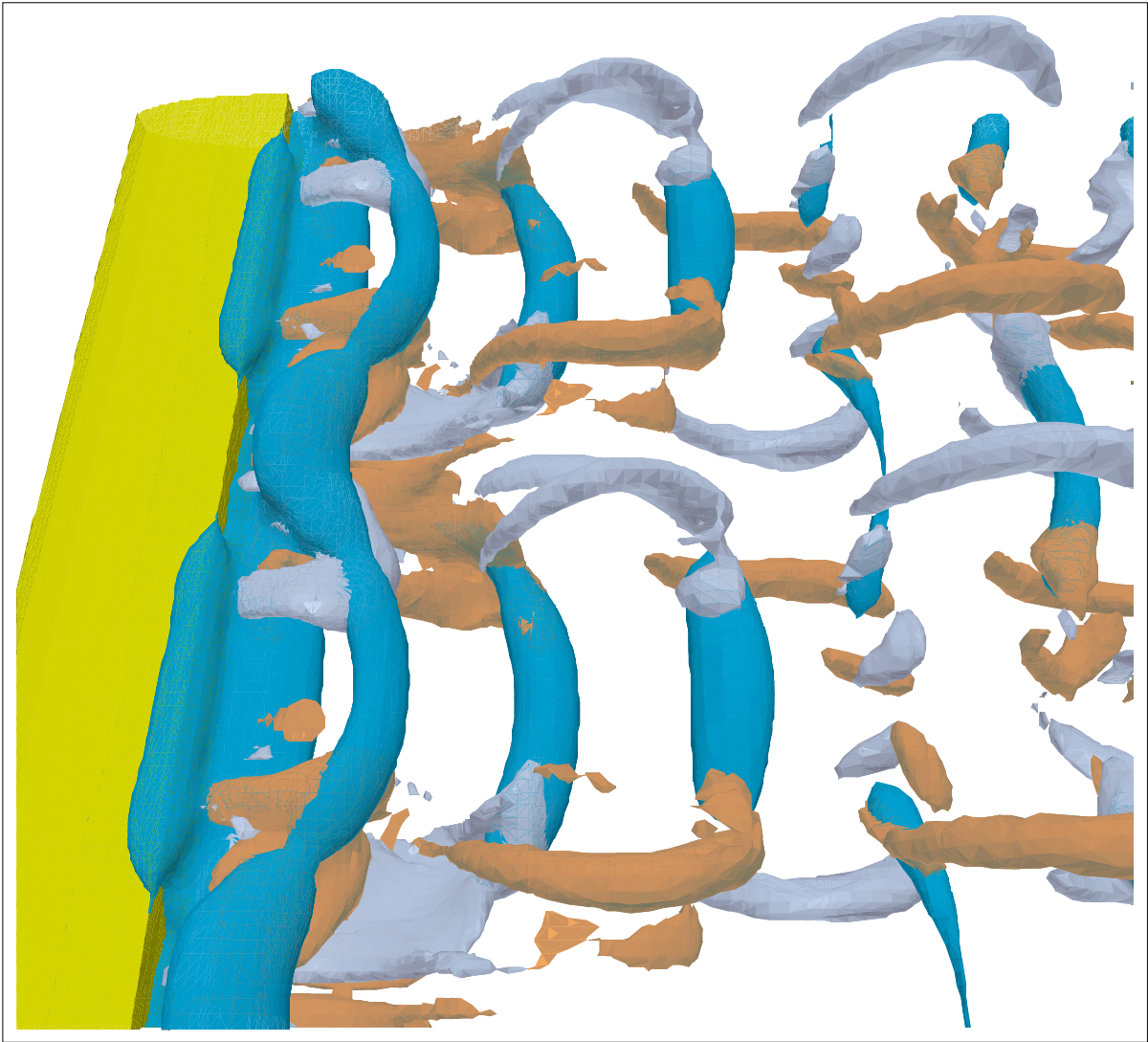


Figure 5.2: Iso-surface plot for flow around an elliptical leading-edge plate with  $c/t = 2.5$  at  $Re = 300$  viewed from the side in a state where only the long wavelength is present. The value of the iso-surface of kinematic pressure is at  $-0.25$  and streamwise vorticity is at  $\pm 1.0$ .

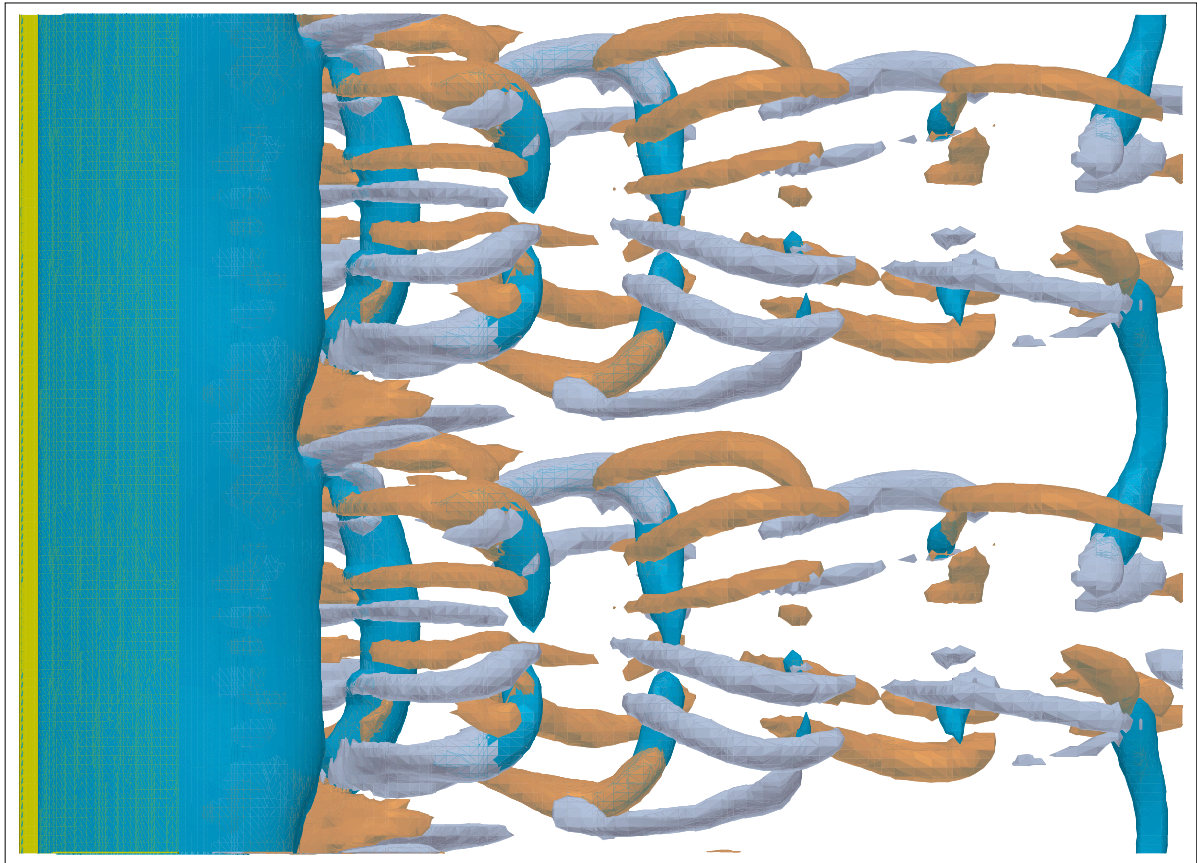


Figure 5.3: Iso-surface plot for flow around an elliptical leading-edge plate with  $c/t = 2.5$  at  $Re = 300$  viewed from the top in a state where there is also the presence of shorter wavelength. The value of the iso-surface of kinematic pressure is at  $-0.25$  and streamwise vorticity is at  $\pm 1.0$ .

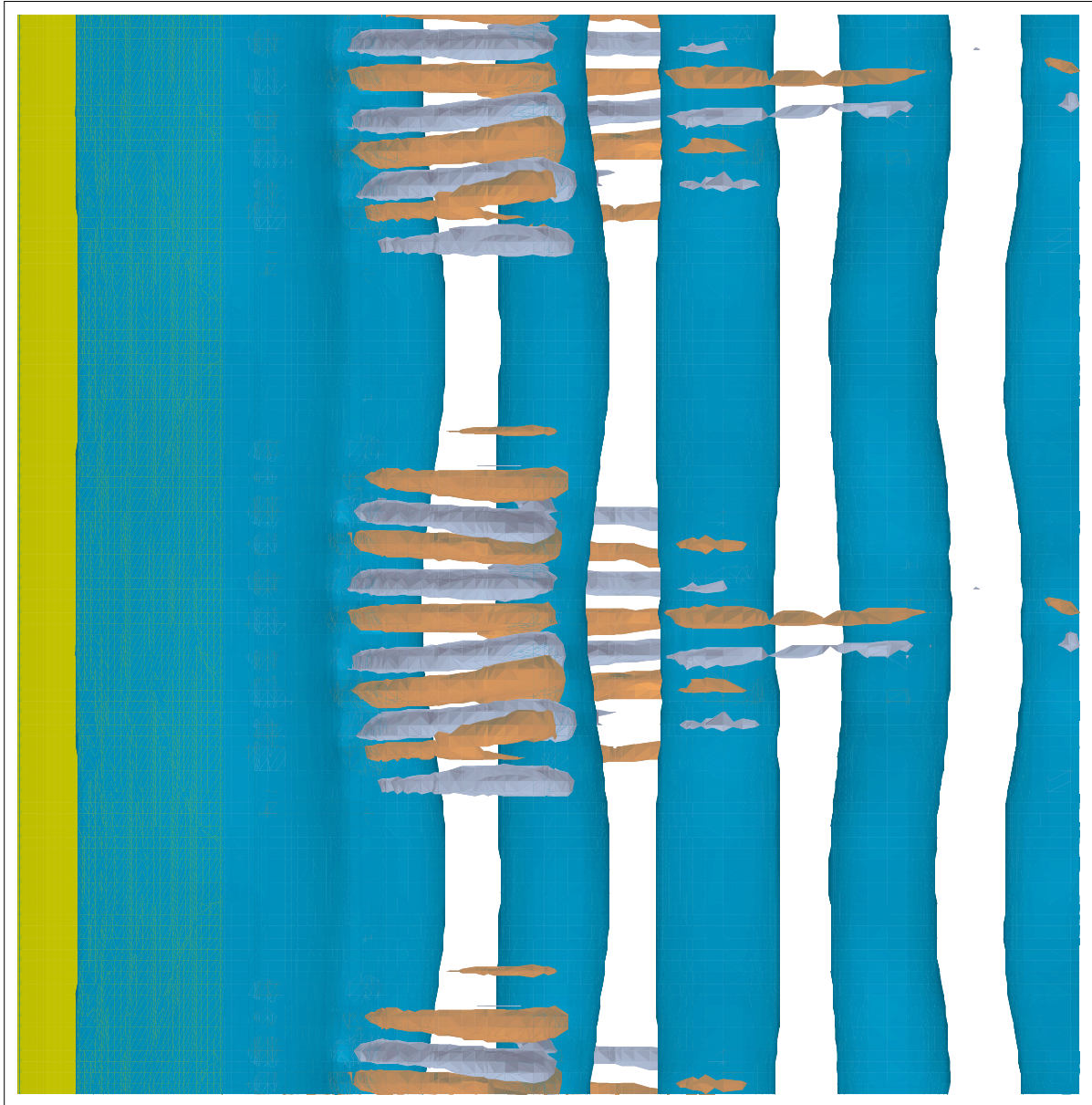


Figure 5.4: Iso-surface plot for flow around an elliptical leading-edge plate with  $c/t = 2.5$  at  $Re = 350$  viewed from the top. The value of the iso-surface of kinematic pressure is at  $-0.2$  and streamwise vorticity is at  $\pm 1.0$ .

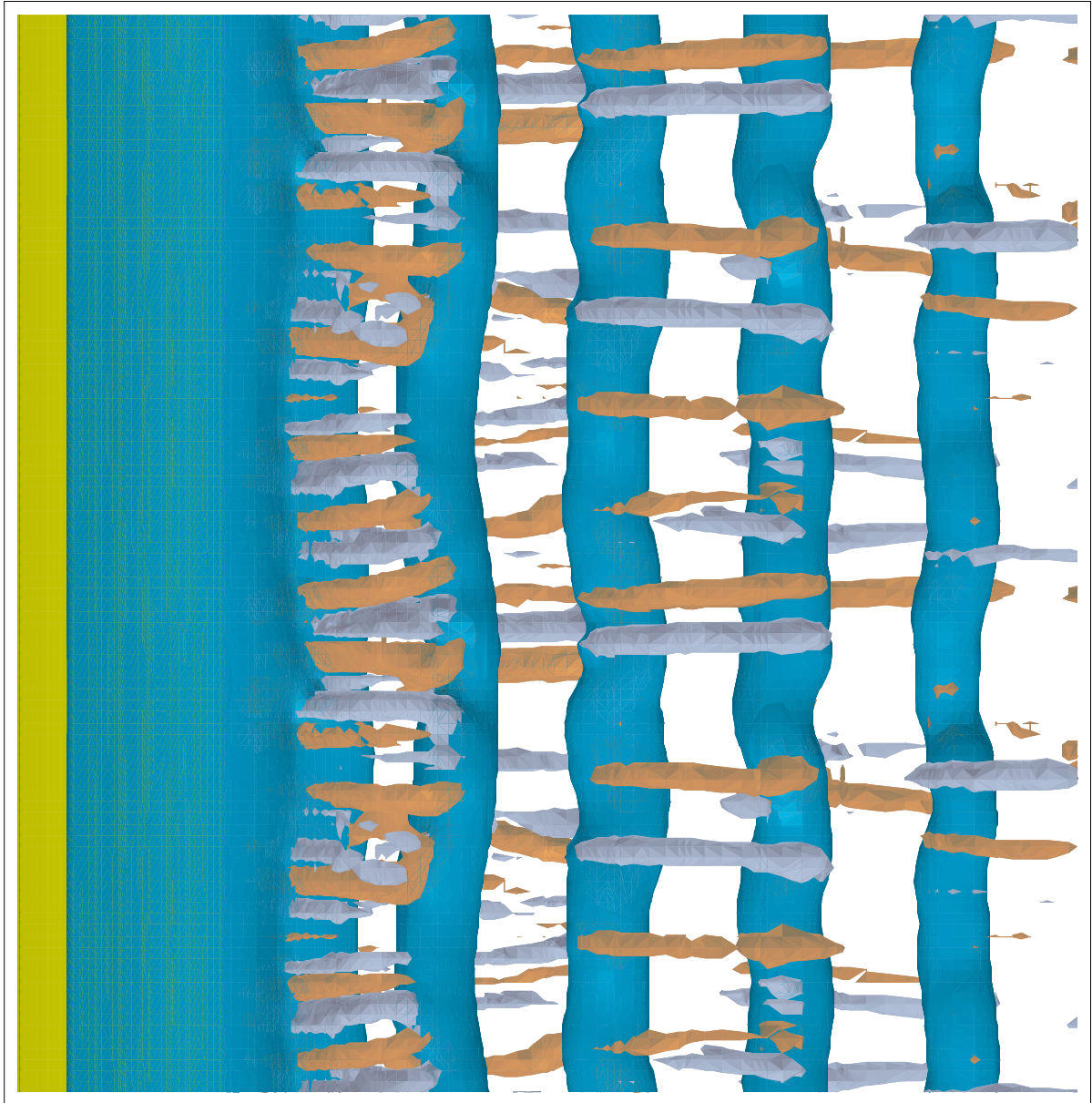


Figure 5.5: Iso-surface plot for flow around an elliptical leading-edge plate with  $c/t = 2.5$  at  $Re = 380$  viewed from the top in a state where there is also the presence of shorter wavelength. The value of the iso-surface of kinematic pressure is at  $-0.2$  and streamwise vorticity is at  $\pm 1.2$ .

It therefore might be expected that the wavelengths of *Mode A* are  $4.8t$  and  $5.1t$  for  $c/t = 2.5$  and  $7.5$  respectively. Both of these are between the two largest wavelengths that can be captured in this simulation (i.e  $3.1t$  and  $6.3t$ ). As expected, the simulations show either one of these modes being dominant in each case. To accurately predict the most unstable mode, a much larger domain size that can simulate numerous wavelengths or a stability analysis is required.

The simulations have shown that the wake transition for long plates with streamlined leading edges show many similarities with wake transition for circular and square cross-sectioned cylinders. As the Reynolds number is increased, the transition from two-dimensional shedding to *Mode A* and then *Mode B* shedding has been observed for the shorter plate ( $c/t = 2.5$ ) and the transition from two-dimensional to *Mode A* shedding for the longer plate ( $c/t = 7.5$ ). The *Mode A* wavelength may be larger because of the thicker boundary layer at the trailing edge which sheds more diffused vortices. As only discrete wavelengths can be captured in these simulations, it is uncertain if these simulations have captured the most unstable mode. However, the *Mode A* wavelength instability band is relatively broad in the circular cylinder wake transition for Reynolds numbers not too much greater than the critical values, so it is likely that the wake topology is qualitatively correct. Henderson (1997) has shown that to capture the wake dynamics successfully requires the domain size to allow many *Mode A* wavelengths. This appears important to predict the mean base pressure (Mittal & Balchandar, 1996), and for the interaction leading to dislocations (Williamson, 1996, Henderson, 1997).

### 5.1.2 Forced shedding

The transition from two- to three-dimensional flow in the forced shedding case has received much less attention than the natural shedding case. Applied external forcing has been known to increase the spanwise correlation and suppress (but not completely) the spanwise structures in bluff body wakes even at high Reynolds numbers (Wu *et al.*, 1993). Therefore it is expected that the transition Reynolds numbers would be higher in the forced shedding case. Note that the forced shedding case is also relevant to the free oscillation case since the wake induces a sinusoidal forcing on the bluff body. This can lead to natural oscillations of structures if damping is insufficient.

The plate with an aspect ratio of  $c/t = 7.5$  shows spanwise instabilities developing at  $Re = 500$  in the natural shedding case. This simulation is close to the upper limit of the Reynolds number range that can be successfully simulated. No three-dimensional simulations of the flow around elliptical leading-edge plates with applied forcing have been attempted because of the restriction in Reynolds number with the present resolution.

Three-dimensional simulations of flow around rectangular plates with applied forcing is attempted in the following section. There are difficulties in reaching the Reynolds numbers required for transition in those cases also.

## 5.2 Flow around rectangular plates

A limited number of three-dimensional simulations were performed on the flow around long rectangular plates. Compared with short bluff bodies, and especially circular cylinders, there have been fewer investigations on the three-dimensional transition for this geometry. In this section, the intent is to study the transition for this geometry and compare with experimental observations, namely the natural shedding cases studied by Sasaki & Kiya (1991) and forced shedding cases examined by Hourigan *et al.* (1993). Sasaki & Kiya (1991) concentrated on the structures formed by the leading-edge vortices along the plate. Two different flow topologies were observed in the transition process, namely *Pattern A* and *Pattern B*. *Pattern A* developed above  $Re = 320$  and consisted of  $\wedge$ -shaped structures with both the spanwise and streamwise wavelengths being between  $2t$  and  $2.5t$ . When the flow is above  $Re = 380$ , hairpin vortices classified as *Pattern B* are observed. The main difference is that these vortices have a staggered arrangement in the streamwise direction and both the spanwise and streamwise wavelengths are between  $3t$  and  $4t$ . As the Reynolds number is increased, the hairpin structures are less clear and regular with of the development of finer scale structure. Applied forcing when the flow is at  $Re = 1,300$  showed the presence of staggered hairpin vortices which were not clearly visible without forcing (Hourigan *et al.*, 1993).

The approach used for these simulations is the same as those used in the previous section. For most cases, 32 Fourier planes were used for the simulations which span  $2\pi t$ . As discussed in the previous chapter, only discrete wavelengths can be captured within the domain (i.e., in this case they are  $2\pi t$ ,  $\pi t$ ,  $2/3\pi t$ ,  $1/2\pi t$ , ...). This domain size is chosen because it is able to capture spanwise wavelengths which are within the range observed experimentally ( $\pi t$  and  $2/3\pi t$  are within the range observed for *Pattern B* and *Pattern A* respectively).

As for the simulations in the previous section, the size of the domain in each two-dimensional plane is reduced relative to the two-dimensional simulations. Again, this is to reduce the computational resource requirements to a size that is manageable. For aspect ratios of  $c/t = 6$  and  $10$ , the distance from the plate to the boundaries,  $l_1$ ,  $l_2$  and  $l_3$ , are  $10t$ ,  $10t$  and  $18t$  respectively. For the longer plate,  $c/t = 13$ , the distance to the outflow boundary,  $l_3$ , is reduced further to  $10t$ . The resolution near the plate is

similar to that used in the two-dimensional simulations. This allows the same timestep of  $\delta t = 0.007$  to be used (which gives approximately between 700 to 1,200 timesteps in a shedding period).

### 5.2.1 The unforced case

The flows around rectangular plates with aspect ratios of  $c/t = 6, 10$  and  $13$  are simulated without any external excitation. Most of the simulations are performed at Reynolds numbers of  $Re = 350$  and  $400$ .

#### 5.2.1.1 $c/t = 6$

These simulations at both  $Re = 350$  and  $400$  showed no development of any spanwise structures. After approximately 150 time units, the monitoring points in the simulations still showed the decaying of the noise introduced initially. At this stage, the noise had decreased by between two to three orders of magnitude. It appears likely that a higher Reynolds number is required for three-dimensional transition at this aspect ratio. However, it is possible that the reduced spanwise domain has an effect.

At this aspect ratio, the shedding mode has only two pairs of vortices along the plate ( $n = 2$ ). This may not be sufficient to trigger the spanwise instability in the leading-edge vortices. As described by Sasaki & Kiya (1993), the mechanism appears to require the downstream vortices to trigger the upstream vortices to sustain the instability. The experiment only studied plates with aspect ratios greater than  $c/t \geq 10$ . The vortices in this case reach the trailing edge before any instabilities develop. The trailing-edge shedding does not develop any spanwise instabilities at these Reynolds numbers. Therefore the overall flow remains two-dimensional.

#### 5.2.1.2 $c/t = 10$

The flow over a plate with this aspect ratio displays the third shedding mode ( $n = 3$ ). This appears to be adequate to trigger spanwise instabilities at both the Reynolds numbers simulated (i.e.  $Re = 350$  and  $400$ ). The traces show that after 150 time units (approximately 25 shedding cycles), the flow has approached an asymptotic state. A 50 time unit trace of the base pressure coefficient (averaged across the span) taken when the flow has reached an asymptotic state is included in Figure 5.6.

At a Reynolds number of  $Re = 350$ , the flow is nearly periodic. The fluctuations

between cycles are due to small drifts of the three-dimensional structures in the spanwise direction (i.e. the pattern is not at an identical location for each period). Figure 5.6 and Figure 5.7 shows the flow structures from the side and top view. As in the previous chapter, the plots show twice the simulated domain for clarity. The plots show some waviness in the vortex roller that is developing from the shear layer at the leading edge. The next roller is strongly distorted in the streamwise direction and the development of streamwise vortices is clear. The resulting structure has been described as hairpin-like by Sasaki & Kiya (1991). The staggered nature of these vortices in the streamwise direction is a result of the vortices downstream triggering the instability in the upstream roller. The argument used was elucidated by Sasaki and Kiya (1991). The structures here are similar to those classified as *Pattern B* in their experiments. Both the spanwise and streamwise wavelength of these instabilities is about  $3t$ . The finite size of the domain allows only discrete spanwise wavelengths to form. These simulations show that this spanwise instability prefers a wavelength of  $\pi t$  rather than its neighbouring values ( $2\pi t$  and  $2/3\pi t$ ). The wavelengths in the simulation are within the range of those observed by Sasaki and Kiya (1991) (which were between  $3t$  and  $4t$  for both wavelengths) although the experiments generally used much longer plates where the trailing-edge shedding becomes less significant. These three-dimensional structures interact with the trailing-edge shedding and result in a less coherent structure in the wake.

Similar large scale structures are present in the flow at  $Re = 400$ . Also present are smaller scale structures which are less coherent. Therefore, the large scale structures cannot be visualised as clearly as in the previous case.

### 5.2.1.3 $c/t = 13$

Simulations at  $Re = 350$  and  $400$  also show similar large-scale spanwise structures at this aspect ratio. The top view of the flow at  $Re = 350$  is shown in Figure 5.8. The shedding has not switched to the next mode because of the higher blockage ratio. The latter causes a small increase in the convective velocity and this results in the flow being more receptive to the third ( $n = 3$ ) shedding mode. The spanwise wavelength in this case remains at  $\pi t$ . However, in this case, the larger spacing between the vortices shed from the leading edge results in a larger streamwise wavelength of about  $4t$ .

At  $Re = 400$ , the flow no longer locks to a particular shedding mode. Together with the presence of smaller scales structures, the large scale structures are less clearly defined and the flow losses (periodic) repeatability.

Several simulations were performed in an attempt to capture *Pattern A* as described by Sasaki and Kiya (1991). These are wedge shaped hairpin vortices which are

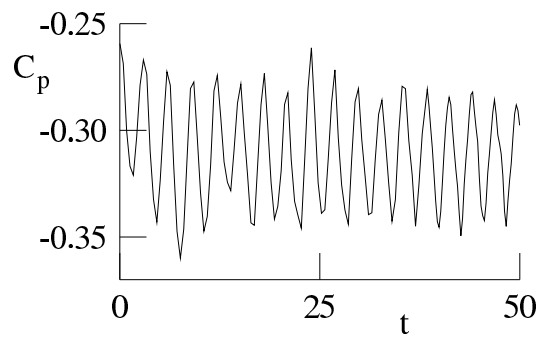
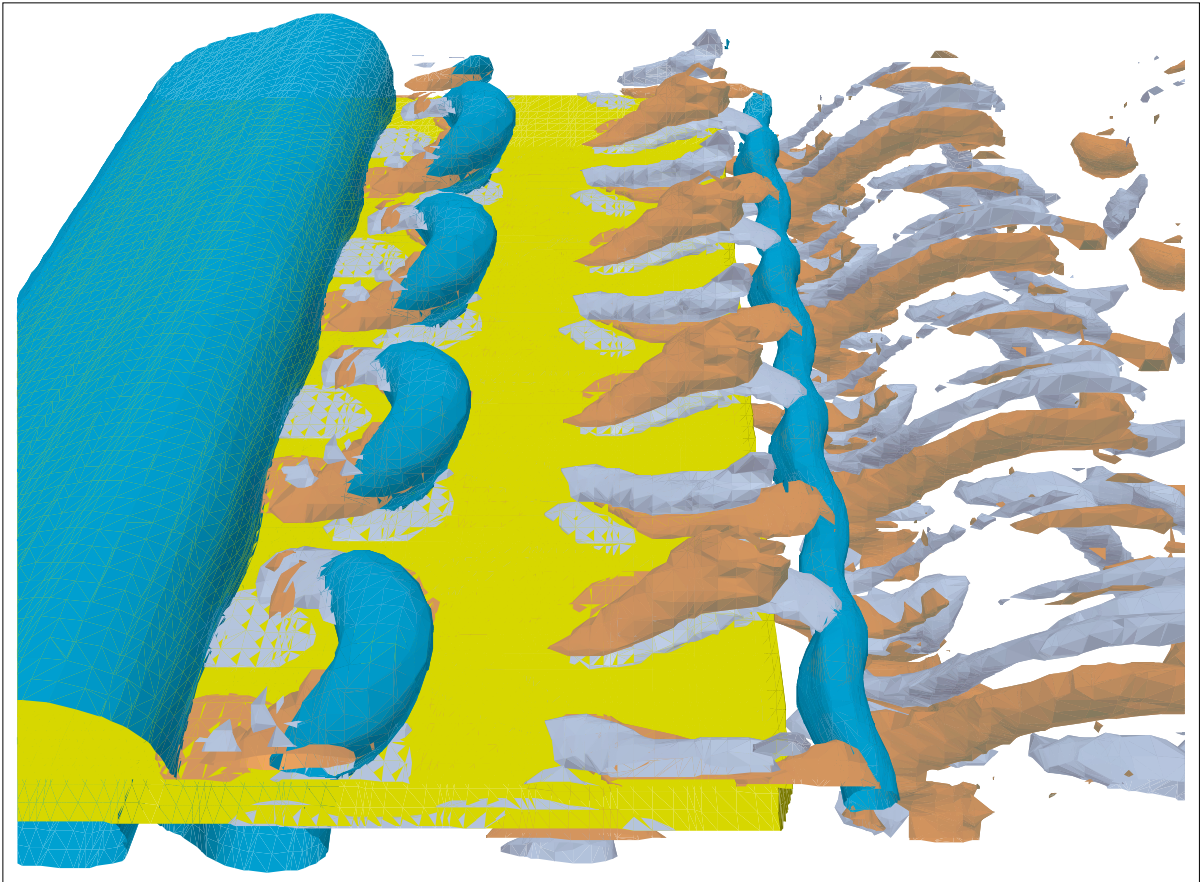


Figure 5.6: Above: Iso-surface plot for flow around a rectangular plate with  $c/t = 10$  at  $Re = 350$  viewed from the side. The value of the iso-surface of kinematic pressure is at  $-0.25$  and streamwise vorticity is at  $\pm 1.2$ . Below: A trace of the base pressure coefficient taken when the flow has reached an asymptotic state.

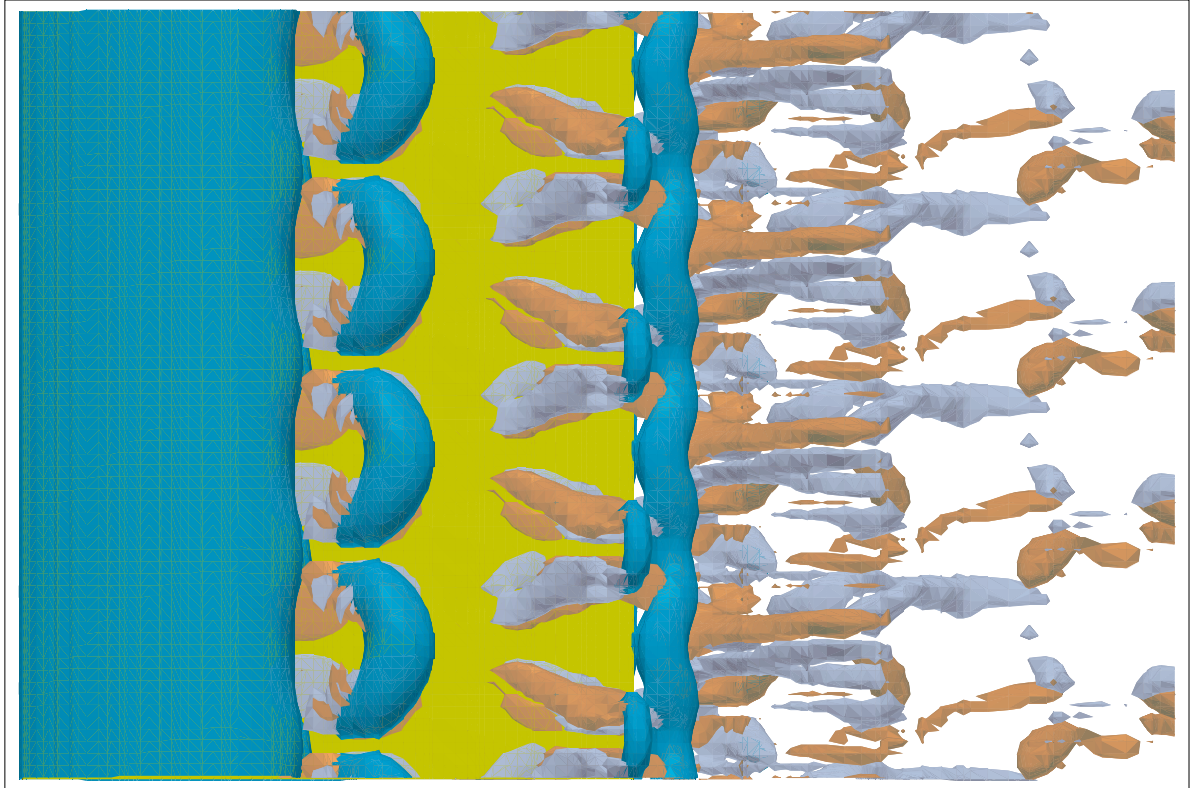


Figure 5.7: Iso-surface plot for flow around a rectangular plate with  $c/t = 10$  at  $Re = 350$  viewed from the top. Same iso-surface levels as in Figure 5.6.

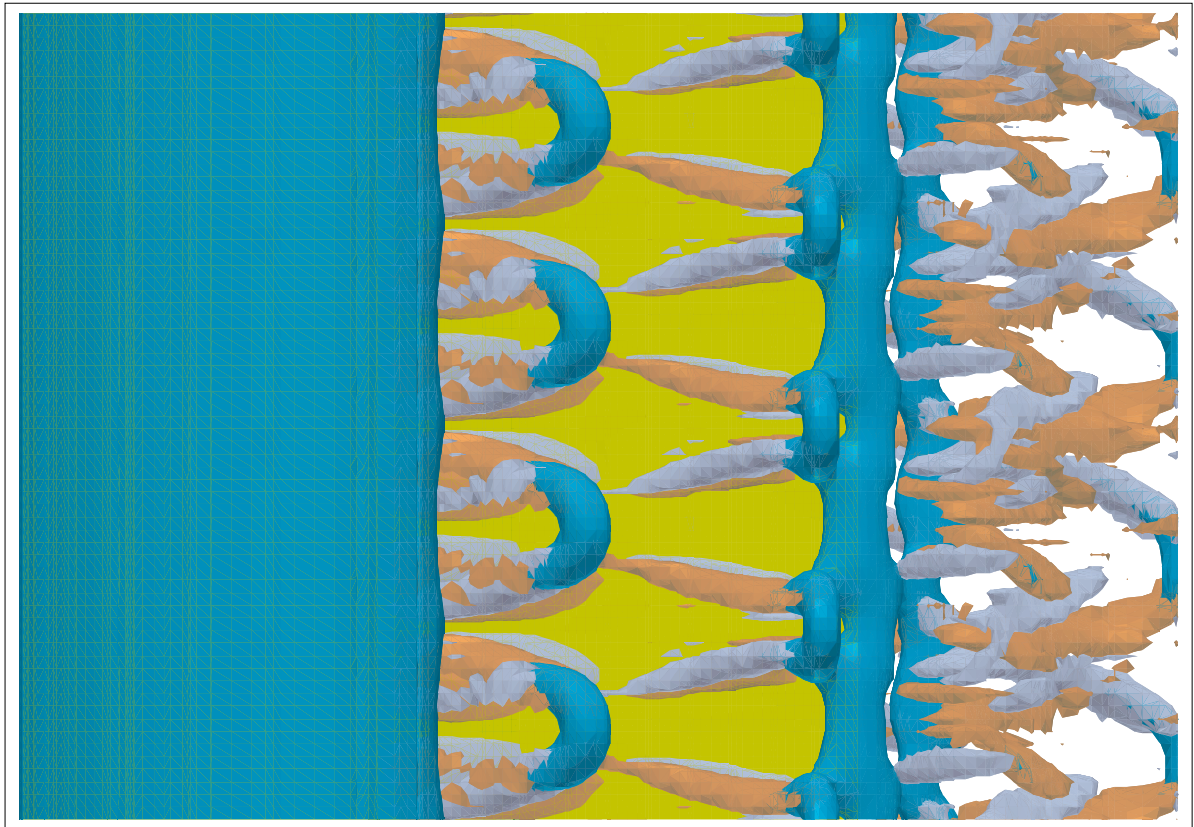


Figure 5.8: Iso-surface plot for flow around a rectangular plate with  $c/t = 13$  at  $Re = 350$  viewed from the top. The value of the iso-surface of kinematic pressure is at  $-0.15$  and streamwise vorticity is at  $\pm 0.8$

not staggered. In those experiments, *Pattern A* is observed between  $320 < Re < 380$  and *Pattern B* above  $Re > 380$ . Vortical structures similar to *Pattern B* are observed in the simulations at  $Re = 350$ . The discrepancies in Reynolds numbers where these transitions occur will be discussed later in this section. As *Pattern A* is expected to occur at a lower Reynolds number than *Pattern B*, simulations are performed with this aspect ratio at Reynolds numbers of  $Re = 300, 325$  and  $340$ . After 200 time units of simulation, the monitoring points in all three simulations only showed the decay of the introduced noise. Only one spanwise wavelength which is within  $2t$  and  $2.5t$  (experimental spread of wavelengths observed for *Pattern A*) can be captured in these simulations. This wavelength is  $2/3\pi t$  and is near the lower end of the experimental spread. To encourage the growth of this mode, a spanwise domain of  $5t$  wide was also simulated. This would allow a spanwise instability with a wavelength of  $2.5t$  to develop (which is at the upper limit). No spanwise instabilities developed in this simulation either. A similar structure has been observed during the transient startup before the development of *Pattern B* but it is not present in the asymptotic state.

There are two major differences between the simulation and the experimental observations. Firstly, *Pattern B* is observed in the experiments above  $Re > 380$  while in the simulations, *Pattern B* is observed at  $Re = 350$  but no spanwise instabilities at  $Re = 340$ . The other issue is concerns the presence of *Pattern A*. This instability is observed between  $320 < Re < 380$  in the experiments but the simulations so far have not been able to simulate it except as a transient mode. There are some obvious differences between the methods used for studying the flow and limitations in the numerical simulations. The experiments were carried out on plates which have much larger aspect ratios ( $10 \leq c/t \leq 40$ ) and therefore the influence of the trailing-edge shedding on the leading-edge flow structures is diminished. For flow around a circular cylinder, Williamson (1989) has shown that varying the end conditions strongly influenced the spanwise structures in the wake. In these experiments, no end plates were used. In the simulations, due to prohibitive computational requirements, only moderate spanwise domains are used. The nature of the technique used here only allows an integer number of spanwise structures to develop and this limits the possibilities especially at longer wavelengths. The simulations performed in this section have only one wavelength within the spread of experimental data. The inability to capture certain modes may be because the discrete wavelengths which are able to be captured in the simulations are not within the range of unstable wavelengths. In conclusion, the differences in observations between the experimental and numerical simulations are likely to be due to the geometry, end conditions and the limitations of the numerical technique.

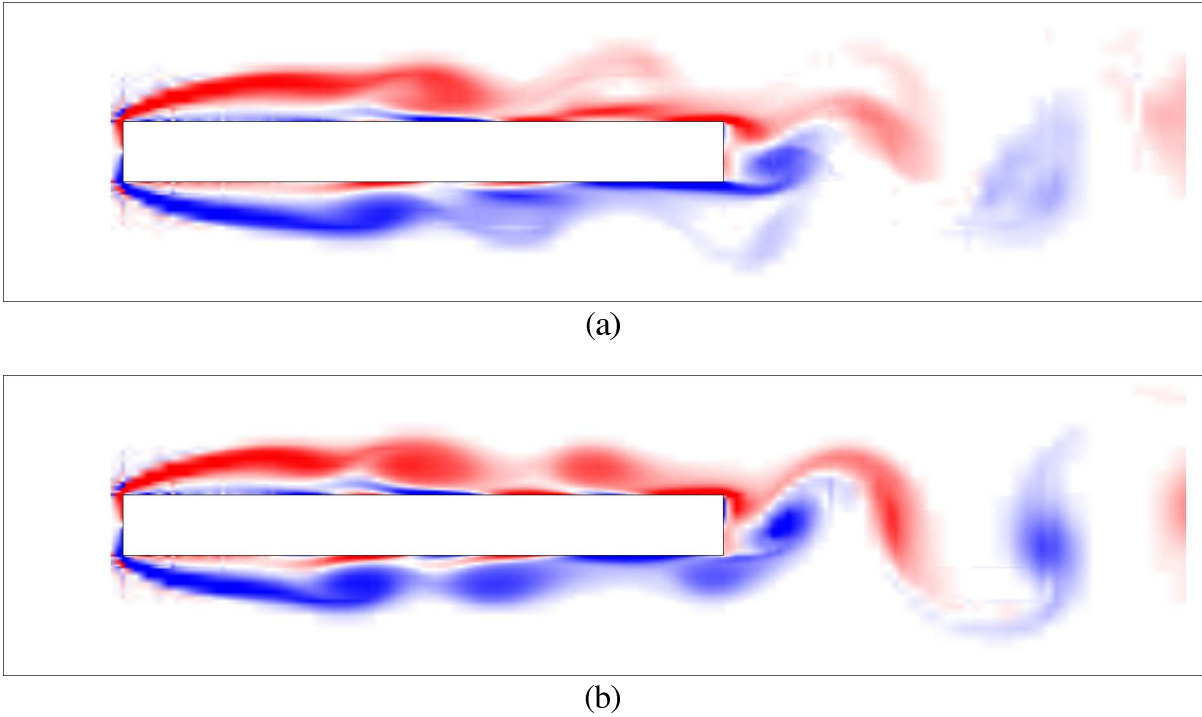


Figure 5.9: Vorticity plots of flow past a rectangular plate with  $c/t = 10$  and  $Re = 350$ . The top plot, (a), is a span averaged from the three-dimensional simulation. The bottom plot, (b), is a two-dimensional simulation.

#### 5.2.1.4 Comparison with two-dimensional simulation

In this section, several flow characteristics of the two- and three-dimensional simulations are compared. The case considered here is the rectangular plate with  $c/t = 10$  and  $Re = 350$ . The computational domain and resolution on a two-dimensional plane is identical in both cases. Firstly the shedding frequency is compared. The Strouhal numbers,  $St$ , in the two- and three-dimensional cases are  $St = 0.170$  and  $0.174$  respectively. The shedding frequency in the three-dimensional simulation is marginally higher because the vortices along the plate have a higher convective speed. This increase in speed is due to these vortices being stretched further away from the plate by the extra Reynolds stresses due to the spanwise instability to where the flow velocity is greater. When the Strouhal number is based on chord, the shedding frequency in both the two- and three-dimensional cases are  $St_c = 1.70$  and  $1.74$  respectively. The simulations in Chapter 4 have shown that at this aspect ratio, the flow locks to the third shedding mode ( $n = 3$ ). The Strouhal number based on chord is in good agreement with the larger set of two-dimensional simulations (i.e.  $St_c = 1.65$  when  $n = 3$  and  $St_c = 0.55n$ ). The marginal increase here is due to the more restrictive domain with the blockage increasing the convective velocity of the vortices.

Figure 5.9 shows a comparison of the two-dimensional flow structures between the two- and three-dimensional simulations. The three-dimensional simulation is reduced to a two-dimensional plane by averaging across the span. The vorticity plots clearly show that both cases are locked to the third,  $n = 3$ , shedding mode. The main difference between the plots is the more diffuse leading-edge vortices in the three-dimensional case. This is especially true closer to the trailing edge where they have been significantly stretched in the streamwise direction. As with the two-dimensional simulation, strong base shedding is also observed with trailing-edge vortices forming between the passing of leading-edge vortices.

## 5.2.2 Applied Forcing

Some attempts were made to simulate transition in the forced case. Initially, the flow around a plate with  $c/t = 10$  at  $Re = 400$  was examined. The applied forcing ranged in frequency between  $St = 0.13$  to  $0.18$  and had an amplitude of  $v_{pert} = 2.5\%$ . Spatial resolution of up to 48 planes were used in some of the simulations. The simulations were started with the unforced three-dimensional flow (*Pattern B* present). The applied forcing suppressed all spanwise instabilities in all the cases examined. The flow remained two-dimensional. The mean base pressure behaviour in these simulations was close to that in the two-dimensional simulations in previous sections. The differences were presumably due only to reduced domain size.

It is likely that higher Reynolds numbers are required for three-dimensional transition in the forced cases. Attempts were made at  $Re = 500$  and  $600$  with some difficulties due to increased resolution and consequently larger computational resource requirements and there is uncertainty about the resolution at these Reynolds numbers in the forced shedding case. Hourigan *et al.* (1993) observed these instabilities at  $Re = 1000$  and so the transition for the forced shedding case would be in this range. More resolution is required to simulate at higher Reynolds numbers and capture these instabilities. Unfortunately, the computational resources are not available for this exploration.

There are several projects running concurrently or being planned to investigate further the spanwise instabilities for both the elliptical leading-edge and the rectangular plate case. Floquet analysis is currently being performed (outside the scope of this project) on flows around these geometries to obtain more accurately the transition Reynolds numbers and the spanwise wavelengths. Experimental work is also planned with the fabrication of a water tunnel currently in progress. This facility will provide more information on the transition Reynolds numbers and the effects of different end conditions.

# Contents

<b>5</b>	<b>Three Dimensional Flow Simulations</b>	<b>186</b>
5.1	Flow around elliptical leading-edge plates . . . . .	186
5.1.1	Natural shedding case . . . . .	188
5.1.2	Forced shedding . . . . .	196
5.2	Flow around rectangular plates . . . . .	197
5.2.1	The unforced case . . . . .	198
5.2.2	Applied Forcing . . . . .	205

# Chapter 6

## Summary and Conclusions

This chapter reviews the issues covered in this study and conclusions are drawn from the work presented both here and in previous studies. The numerical techniques employed and their use in the study of flow around long plates is described. In relation to the simulation techniques, the topics covered include benchmarking, testing of a modified temporal scheme, domain and resolution testing, and procedures used for post-processing. The plates considered either had an elliptical or blunt leading edge and a blunt trailing edge. The cases considered include natural and forced shedding in two-dimensional space and a limited number of cases in three dimensions. For the rectangular plate, the duct acoustic resonance case is also investigated.

### 6.1 Computational aspects

The approach to this problem involves numerically simulating the flow around the bluff bodies. As the problem being studied involves receptivity and feedback mechanisms, a high-order method is preferable because it is able to accurately capture the relatively weak and sensitive features within the flow.

#### 6.1.1 Numerical technique

The time-dependent Navier-Stokes equations in primitive variables are the governing equations used in this solver. The spatial scheme consists of a spectral-element/Fourier method as outlined by Karniadakis & Triantafyllou (1992). The spectral-element method is used for spatial discretisation on a two-dimensional plane. This technique is similar to a

Galerkin finite element method except that high-order Lagrangian polynomials (although others could be used) are used to interpolate within each element. This technique has the ability to handle geometries like the finite element method and can achieve high orders of accuracy if the solution is continuous. A global Fourier expansion is used for discretisation in the spanwise direction. This scheme is chosen because it is relatively simple to implement and is efficient on computational resources. A classical three-step time-splitting scheme (Karniadakis *et al.*, 1991) is used to evolve the solution in time. This technique splits a timestep into convective, pressure and diffusion sub-steps. The convective step is handled by an explicit third-order Adam-Bashforth scheme. Continuity is enforced to solve for pressure which results in a Poisson equation. The diffusion is performed using an implicit second-order Crank-Nicholson scheme which results in a Helmholtz equation. The latter two steps are solved by matrix inversion. To reduce the splitting errors, a first-order pressure boundary condition is enforced and the overall scheme is second-order accurate in time.

### 6.1.2 Benchmark test

Two commonly used benchmark problems are used for validation, namely the driven cavity flow and the flow over a backward facing step. These two are chosen because they are distinct problems with the flow over a backward facing step involving continuous inflow and outflow while the driven cavity flow is in a closed system.

In the flow over a backward facing step problem, simulations are performed at various Reynolds numbers and the reattachment length is recorded. The results at  $Re = 10, 100, 200$  and  $400$  are compared with those of Kim & Moin (1985) and the result at  $800$  with Gresho *et al.* (1993). All these cases including at  $Re = 800$  asymptotes to a steady state as predicted by Gresho *et al.* (1993). The reattachment length for all the cases simulated were within 2% of the previous published data. The scheme used in these simulations can therefore reproduce steady-state results of previous simulations.

Simulations on the driven cavity flow problem were performed over a large Reynolds number range which resulted in asymptotic states that were either steady or time dependent. A small amount of regularisation to the lid profile was needed to maintain the spectral convergence. Simulations at  $Re = 100, 400, 1000, 3200, 5000$  and  $7500$  which asymptote to a steady state were compared with those of Ghia *et al.* (1982). Velocity profiles taken vertically and horizontally across the centre of the cavity were used for comparison. Plots of velocity profiles showed that the two sets of simulations are visually indistinguishable. This scheme is therefore able to consistently reproduce results in the steady regime and the small difference in lid profile is negligible. The asymptotic state

was steady in time below  $Re \leq 8000$  in these simulations.

A code using a global spectral technique for spatial discretisation was developed independently to validate the time dependent results produced and investigate the feasibility of using a Runge-Kutta scheme to advance the convective step. This is a Global-Galerkin technique which uses Chebyshev polynomials to interpolate the flow variable in both spatial dimensions. Again, spectral convergence is achievable if the solution is continuous. The time-stepping scheme is modified from the classical three-step time-splitting scheme to facilitate the use of a fourth-order Runge-Kutta scheme for the convective step.

Simulations were performed with both numerical schemes at Reynolds numbers ranging from  $Re = 8,000$  to  $17,000$ . The global spectral scheme also predicted that the flow reaches a steady state at  $Re = 8,000$ . The total kinetic energy was used to monitor the flow. The mean kinetic energy differed by less than 1% between the two techniques used for simulation. The difference in the standard deviation were also in that range except at  $Re = 16,000$  and  $17,000$  where the difference is larger (less than 10%). This larger difference is due to many frequencies present in the trace and a much larger sampling time is required to reduce this uncertainty. There is an overall agreement in the results produced by the independently developed codes using different schemes.

No three-dimensional flow problem was performed to validate the code. This technique is limited to two-dimensional geometries and periodic boundary conditions in the spanwise direction. This further limits the number of problems where accurate solutions have been published. No detailed validation was performed because of the computational cost and the limited number of accurate flow simulations for comparison. This is the same code used by Thompson *et al.* (1994, 1996) and has accurately simulated the two stage transition for flow around a circular cylinder.

### **6.1.3 On using the Runge-Kutta scheme for the convective sub-step**

The time-stepping algorithm has been modified to enable the Runge-Kutta scheme to be used for the convective step. This temporal scheme together with the global spectral scheme for spatial discretisation has been tested by simulating the driven cavity flow. This investigation is carried out because implicit schemes (such as the Adam-Bashforth and Runge-Kutta schemes) have stability limits which restrict the size of the timestep. The aim of this investigation is to determine if the Runge-Kutta scheme is more efficient and stable than the current scheme.

To implement correctly the Runge-Kutta scheme for the convective step, the pressure and diffusive step also has to be advanced within each sub-step of the Runge-Kutta scheme. In terms of operation count, using the fourth-order Runge-Kutta scheme would be approximately equivalent to four discrete timesteps with the Adam-Bashforth scheme. The benefit of using the fourth-order Runge-Kutta scheme is that timestep could be six times larger than the third-order Adam-Bashforth scheme (close to theoretical predictions). In term of storage requirements, the third-order Adam-Bashforth scheme requires four levels of velocity fields while the Runge-Kutta scheme (any order) would require only three levels when using the memory efficient algorithm.

Beside operation count and storage requirements, the order of accuracy of the overall scheme must also be considered. The original scheme and the modified scheme are both second-order accurate in time because both are limited by the pressure boundary condition and the order of the diffusive step. Attempts to increase the order of accuracy either by using higher-order pressure boundary conditions or higher-order implicit schemes for the diffusive step have resulted in a significant decrease in the allowable timestep. (Note that the third-order Adams-Moulton scheme is not unconditionally stable unlike the Crank-Nicholson scheme.)

It was decided that accuracy was more important than the higher operation count ( $\approx 25\%$ ) required to achieve the same simulation time. Therefore the third-order Adam-Bashforth scheme is maintained for all subsequent simulations. The main constraint on accuracy in these schemes is the pressure boundary condition and the Runge-Kutta scheme would be more favourable if a more stable high-order pressure boundary condition could be formulated.

#### 6.1.4 Simulation of flow around plates

Before the detailed investigation into flow around long plates was undertaken, some preliminary simulations were performed to determine the adequate domain size and resolutions. For flow around bluff bodies, the predictions of surface pressure can be significantly altered if the boundaries are too close to the body (Barkley & Henderson, 1996). The two-dimensional simulations are intended to produce quantitative predictions of base pressure and forces on the plate and therefore some preliminary simulations are performed to determine the adequate domain size. Simulations with various domain sizes are performed for an elliptical leading-edge plate (5:1 axes ratio) with  $c/t = 7.5$  at  $Re = 300$  and a rectangular plate with  $c/t = 10$  at  $Re = 300$  and  $400$ . The mean and the level of fluctuation in the base pressure is used to gauge the effect of the domain size. The domain size is considered adequate when predictions with larger domains differ by less than 2%. These

simulations show that this is achieved when the distance from the plate to the upstream domain ( $l_1$ ) and to the side boundary ( $l_2$ ) is  $20t$  and the distance from the plate to the outflow boundary ( $l_3$ ) is  $28t$ .

To check if the resolution is adequate, simulations were performed with higher spatial and temporal resolution. Again the elliptical leading-edge plate ( $c/t = 7.5$ ) and the rectangular plate ( $c/t = 10$ ) were simulated at  $Re = 500$  (upper limit). Simulations of the natural and forced shedding cases are performed on the same grid using  $7 \times 7$  ( $N = 7$ ) and  $9 \times 9$  ( $N = 9$ ) noded elements. The increased resolution required the timestep to be reduced from  $\Delta t = 0.007$  to  $0.004$ . Again the properties of the base pressure trace is used for comparison and the difference between resolutions in all cases were less than 2%. This shows that the lower resolution is adequate and therefore all the simulations maintained this resolution around the plate. The higher resolution used for simulating the flow around the elliptical leading-edge plate ( $c/t = 7.5$ ) at  $Re = 700$  was also shown to be adequate.

## 6.2 Flow around elliptical leading-edge plates

In this case, there is no leading-edge shedding with the aerodynamic leading edge. This reduces the complexity and is a natural precursor to studying the flow around rectangular plates. This geometry shares some similarities with short bluff bodies because vortices are only shed in the wake.

### 6.2.1 Natural shedding

The shedding frequency predicted by the simulation is compared with the results obtained experimentally by Eisenlohr & Eckelmann (1988). Simulations are performed for a plate with  $c/t = 7.5$  between  $Re = 200$  and  $700$ . As with most of the aerodynamic leading-edge plates, the leading edge is an ellipse with a 5:1 axes ratio. The shedding frequency is extracted from the base pressure trace which in all these cases asymptote to a periodic state.

Eisenlohr & Eckelmann (1988) found a correlation between the reduced shedding frequency ( $F_{\nu}$ ) and the Reynolds number ( $Re_{\nu}$ ) if the characteristic length is the plate thickness plus two times the displacement thickness at the trailing edge. The simulations are in good agreement with these results. The plots show that the rate of increase of  $F_{\nu}$  with  $Re_{\nu}$  is visually indistinguishable. All but the lowest Reynolds number simulated are

within the range of experimental uncertainty.

### 6.2.2 Forced shedding

Simulations of flow around elliptical leading-edge plates ranging from  $c/t = 3.5$  to  $12.5$  at Reynolds numbers between  $300 \leq Re \leq 500$  are performed. The forcing is in the form of a sinusoidal oscillating velocity component in the cross-flow direction added to the free stream. The amplitude of these oscillations are small relative to the free-stream velocity (i.e. forcing amplitudes simulated were at  $v_{pert} = 1.25\%, 2.5\%$  or  $5.0\%$ ).

The base pressure was used initially to gauge the response of the system. The forcing only alters the mean base pressure at frequencies close to the natural shedding frequency. This range approximately corresponds to the lock-in range where the shedding is locked to the forcing and the base pressure trace shows a periodic oscillation with a frequency matching that of the forcing (twice the forcing frequency, because taken at the centre). The lock-in range varies between cases (i.e  $Re$  and  $c/t$ ) but grows with increasing forcing amplitude. This is illustrated in Figure 3.13 which is the state selection diagram for the case where  $c/t = 7.5$  and  $Re = 500$ . The state selection diagram for this geometry is similar to that described for a circular cylinder in Karniadakis & Triantafyllou (1989). For this geometry, as the forcing amplitude is increased, the lower limit of the lock-in range grows faster than the upper limit. The natural shedding frequency is closer to the upper limit of the lock-in range. Outside the lock-in regime, the mean base pressure is approximately equivalent to that of the natural shedding case and the spectrum showed a typical 'beating' process (i.e. the two dominant frequencies present were the natural shedding frequency and a low frequency corresponding to the difference between the forcing and the natural shedding frequency).

In all the cases studied, there is a linear increase in mean base suction with forcing frequency for most of the lock-in range. The main difference is the behaviour nearer the lower and upper limits of the lock-in range. These can be classified into two typical cases, one that occurs at longer plates or lower Reynolds numbers and the other at shorter plates or higher Reynolds numbers. It is expected that these two parameters govern the behaviour because they control the thickness of the boundary layer at the trailing edge of the plate. At these Reynolds numbers, there was also no shedding from the leading edge when the nose geometry was rounded. Changing the nose geometry increases the overall boundary layer thickness along the plate. For the trailing-edge shedding, this is equivalent to a marginally longer plate.

The behaviour generic to the higher Reynolds number or shorter aspect ratio

cases is described next. At the lower limit of the lock-in range, there is a decrease in mean base suction as the flow locks to the forcing. This is followed by linear increases in mean base suction with forcing frequency. The mean base pressure gradually approached that of the natural shedding case as the forcing frequency increases pass the upper limit of the lock-in boundary. There is a distinct difference for the cases where the Reynolds number is lower or the aspect ratio shorter. At the lower forcing frequency limit of the lock-in range, the drop in mean base suction associated with the onset of lock-in is less significant than the earlier case. Again, this is followed by a linear increase in mean base suction with forcing frequency which dominates the lock-in range. Towards the upper limit of the lock-in range, there is a drastic drop in mean base suction to below that of the natural shedding case as the forcing frequency is increased and approaches the upper limit of the lock-in range. The mean base pressure approaches that of the natural shedding with further increase in forcing frequency. The sudden drop in mean base suction (rise in mean base pressure) is associated with a change in the relative phase between the forcing and the shedding. While the relative phase between the forcing and the shedding is approximately constant for the rest of the lock-in range, a phase shift of approximately  $90^\circ$  in the shedding relative to the other forcing frequencies has been observed in conjunction with the drastic drop in mean base suction when  $c/t = 12.5$  and  $Re = 300$ .

Further analysis is performed on two cases which typify the two distinct behaviour. The case with  $c/t = 7.5$  and  $Re = 500$  is representative of the higher Reynolds number or shorter aspect ratio cases, and the case with  $c/t = 12.5$  and  $Re = 300$  is for the the lower Reynolds number or longer aspect ratio. The level of applied forcing is at  $v_{pert} = 2.5\%$ . The focus will be in the lock-in range where the forcing has more influence on the pressure and forces on the plate.

The behaviour of the drag force as a function of forcing frequency mimics that of the mean base pressure. This can be expected as the forcing has an insignificant effect on the forces at the leading edge and the base pressure is monitored at the trailing face. As the drag force increases in the lock-in range, the fluctuating lift force decreases. Plots of vortex trajectories have shown that the vortices form and remain closer to the centre line in these cases. The narrower wake would account for the increase in drag force and the decrease in fluctuating lift force. Experiments on flow around bluff bodies have recorded an increase in fluctuating lift force when forcing is applied (Staubuli, 1981, Bearman & Obasaju, 1982). In those situations, the flow is three-dimensional in nature and the applied forcing increases the spanwise correlation and thus the overall forces.

The narrowing of the wake can be related to the phase of the shedding relative to the forcing. Within the lock-in range, excluding the narrow region where the phase shift

occurs, the vortices are encouraged by the forcing to form closer to the centreline. This is supported by visualisation which shows vortices forming on the top side of the plate between  $90^\circ$  and  $270^\circ$  in the forcing cycle where the perturbation is accelerating in the downward direction and the opposite occurs in the other half of the cycle.

The vortex formation length is evaluated for both cases (i.e.  $Re = 500$ ,  $c/t = 7.5$  and  $Re = 300$ ,  $c/t = 12.5$ ) at forcing frequencies that lock the flow and also the natural shedding case for comparison. In general, the vortex formation length is proportional to the mean base pressure. As expected, stronger mean base suction is recorded when the vortices are more compact and form closer to the base of the plate. In determining the vortex formation length, the standard deviation of the vertical velocity component along the centreline is also calculated. The analysis shows that the magnitude of the peak standard deviation also influences the mean base pressure. When both the natural and forced shedding cases are considered, the mean base pressure is more closely related to the magnitude of the peak standard deviation for the case where the Reynolds number is lower and the aspect ratio is greater. In both cases, as the forcing frequency is increased past the frequency at which the peak base suction occurs, there is a small drop in mean base suction, a further reduction in vortex formation length and a reduction in the magnitude of the peak standard deviation of the vertical component of flow velocity. A possible explanation for this behaviour is that the vortex formation length is controlled by the forcing (increased frequency resulting in a reduction in vortex formation length) but the wake is not as receptive to the higher frequency (shown by the decrease in the peak value of standard deviation, decrease in mean base suction and approaching the upper limit of the lock-in range). A further increase in forcing frequency for the lower Reynolds number and longer aspect ratio case results in a drastic increase in vortex formation length in conjunction with a phase shift in the shedding and a drastic reduction in mean base suction.

Theoretical predictions have shown that there is a direct relationship between the mean base pressure and the amount of circulation of one sign generated in one period (i.e. Equation 3.5,  $\frac{St\Gamma_o}{1-c_p} = 0.5$ ). The circulation contained within the vortices in the wake were examined in both representative cases. Only the periodic cases were examined which were the natural shedding case and the lock-in range for the forced shedding cases. Extrapolating the amount of circulation in the wake to the base of the plate, all the simulations were within,  $\frac{St\Gamma_o}{1-c_p} = 0.42 \pm 0.03$ . The lower values are mainly due to the under estimation of the circulation contained in each vortex. The region of integration used to calculate the circulation is arbitrarily truncated at about 15% of the peak vorticity level within the vortex so as to isolate individual vortices. Another source of error could be from the linear extrapolation technique used which may not accurately model the high levels of cross-annihilation that occur near the trailing edge.

Earlier in the study, the mean base pressure as a function of forcing frequency for all cases studied display either one of two distinct characteristics. Further analysis has shown that there are differences in the wake. In general, the observations at higher Reynolds number or shorter aspect ratio show a higher natural shedding frequency and associated lock-in range, smaller length scales (shorter vortex formation length and more compact vortices), and stronger vortices shed (larger fluctuations in base pressure and vertical velocity component in the wake) than the cases observed at lower Reynolds number or longer aspect ratio. The natural cases already show these quantitative differences. The aspect ratio and Reynolds number govern the thickness of the boundary layer at the trailing edge. This in turn determines whether compact or diffuse vortices are shed from the trailing edge. This is indirectly measured by evaluating the vortex formation length and vortex trajectories in the wake. The small applied forcing has only a limited control on the flow in a narrow band of frequencies. The simulations have shown that the flow with the different characteristics in the wake respond differently to the external forcing.

The simulations are performed at Reynolds number below or around where transition to three-dimensional flow occurs. These two-dimensional simulations in the natural shedding case are therefore only accurate at these low Reynolds numbers before transition occurs. As applied forcing suppress the three-dimensionality of the flow, these cases are valid to a higher Reynolds number. In this study, some comparisons were made with experiments, in particular those of Mills (1988) which were performed at  $Re \approx 9,000$ . In that situation, the flow is three-dimensional even with applied forcing. As a result, there are differences between the experimental observations and the numerical predictions which have been previously discussed.

### 6.3 Flow around rectangular plates

The study of flow around rectangular plates has increased complexity when compared to the previous section with the additional interaction of leading- and trailing-edge shedding. This study involves three different flow situations, namely the natural shedding case, the forced shedding case and the duct acoustic resonance case. Firstly, the main points of observations in each situation will be reviewed. Next, the mechanism in each case will be described and related to the predictions. Finally, the similarities between the three cases are highlighted.

## 6.3.1 Results from simulations

### 6.3.1.1 Natural shedding

At moderately low Reynolds numbers, studies in the past have shown that the flow around rectangular plates lock to distinct shedding modes depending on the aspect ratio (Okajima *et al.*, 1990, Nakamura *et al.*, 1991 and Ohya *et al.*, 1992). Only  $n$  (integer) pairs of vortices can develop along the sides of the plate when the flow is locked to a particular mode. The increasing number of vortex pairs along the plate also result in the Strouhal number based on chord ( $St_c$ ) of the shedding to show a stepwise increase with aspect ratio  $c/t$  with each step corresponding to a particular shedding mode ( $n$ ). The mechanism that locks the flow to the different modes has been classified as the impinging leading-edge vortex instability (ILEV) by Naudascher & Wang (1993). Simulations of the natural shedding cases are performed in the lead up to the forced shedding and duct acoustic resonance case to study the relationship between cases.

Firstly several simulations are performed to study the effect of Reynolds number. Flow around plates with aspect ratios of  $c/t = 3$  and  $c/t = 10$  are simulated at  $Re = 300$ , 400 and 500. All simulations with  $c/t = 3$  locked to the first shedding mode ( $n = 1$ ) while at  $c/t = 10$ , the flow locked to the third shedding mode ( $n = 3$ ) when  $Re = 300$  and 400. At  $Re = 400$ , there are small fluctuations between periods in the base pressure trace and at  $Re = 500$ , the flow no longer locked to a particular shedding mode and there are several frequencies present in the base pressure trace. When the flow is locked to a particular mode, varying the Reynolds number has only a small influence on the shedding frequency (i.e. less than 10%). Nakamura *et al.* (1991) also found that the shedding frequency is independent of Reynolds number when this mechanism locks the flow. The base pressure trace showed that the mean and fluctuating levels increasing with Reynolds number for all cases where the flow is locked. There is a drop in the mean and fluctuating levels when the Reynolds number is increased and the flow no longer locked to a shedding mode.

Next, the aspect ratio is varied between  $c/t = 3$  to 16 at  $Re = 400$  to study the effect of varying the aspect ratio. The flow locked to a shedding mode between  $c/t = 3$  to 10 and also at  $c/t = 13$ . Vorticity plots showed that  $c/t = 3, 4$  and 5 locked to  $n = 1$ ,  $c/t = 6, 7$  and 8 to  $n = 2$ , 9 and 10 to  $n = 3$ , and  $c/t = 13$  to  $n = 4$ . The shedding frequency (Strouhal number based on chord) approximately corresponds to  $St_c = 0.55n$  for all these cases. The base pressure trace showed more fluctuations between periods towards the higher aspect ratio end of each shedding mode. The spectrum taken from the base pressure trace when  $c/t = 11$  (not locked) showed the presence of two frequencies, one corresponding to the  $n = 3$  shedding mode and another to a frequency which is in the middle of the  $n = 2$  and 3 shedding mode.

The effect of the ILEV instability is also seen in the base pressure and forces on the plate. The mean base suction and drag forces are generally higher at the lower aspect ratio end of the step and decrease with aspect ratio. This trend continues even to aspect ratios that no longer lock to a single frequency. The standard deviation of lift coefficient is approximately inversely proportional to aspect ratio.

### 6.3.1.2 Forced shedding

At higher Reynolds numbers where the wake only shows a broad band of frequencies, experiments with applied external forcing have shown that the system is more receptive at particular frequencies (Mills *et al.*, 1995 and Mills, 1998). These experiments showed that the forcing frequency ( $St_c$ ) which excited the peak base suction also showed a stepwise increase with aspect ratio. Applied forcing is introduced into the simulations with the aim of simulating these observations and further study the mechanism involved.

Initially, several simulations are performed using  $c/t = 10$  to examine the effect of varying Reynolds number and forcing amplitude. The lock-in range in these cases are much larger than the cases with the aerodynamic leading-edge plates. Firstly, the Reynolds number is varied from  $Re = 300$  to  $500$  while the forcing is fixed at  $v_{pert} = 2.5\%$ . The mean base pressure as a function of forcing frequency shows a similar trend. The forcing frequency where the peak base suction occurred varied by  $0.05$  in Strouhal number. The magnitude of the peak increases with Reynolds number. Next, the forcing amplitude is varied between  $v_{pert} = 1.25\%$  and  $v_{pert} = 5.0\%$  while the Reynolds number is fixed at  $Re = 400$ . Again the overall behaviour in mean base pressure is similar between forcing levels. The increase in mean base suction with forcing levels is greater at forcing frequencies that result in strong base suction.

Next, flow around plates ranging between  $c/t = 6$  to  $16$  are simulated at  $Re = 400$  with a forcing level of  $v_{pert} = 2.5\%$ . The forcing frequency at which the mean base suction peaks also displays a stepwise increase with aspect ratio. These steps corresponds to  $St_c = 0.55n$  with  $c/t = 6$  to  $9$  at  $n = 2$ ,  $c/t = 10$  to  $14$  at  $n = 3$ , and  $c/t = 15$  and  $16$  at  $n = 4$ . In some cases where these peaks occurred at lower forcing frequencies, another peak developed at a higher frequency within the lock-in range. The mean base suction showed another local peak in cases with aspect ratios of  $c/t = 8, 9, 12, 13$  and  $14$ . The forcing frequency at which these peaks occur correspond to a frequency which is between the major steps (i.e. for  $c/t = 8$  and  $9$ , it is between  $n = 2$  and  $3$  and for  $c/t = 12, 13$  and  $14$ , it is between  $n = 3$  and  $4$ ). When the forcing amplitude is decreased to  $v_{pert} = 1.25\%$ , the peaks corresponding to the major steps decreased in magnitude but the magnitude of the peaks associated with the intermediate steps increased.

The stepwise nature of the peaks in base suction is also seen in the mean drag and fluctuating lift forces. The mean drag force shows a similar trend to that observed for the mean base pressure. The standard deviation of lift coefficient showed local maxima corresponding to the cases associated with the major steps while the intermediate steps showed local minima.

Vorticity plots showed that the major steps corresponding to the peak in mean base suction has the same  $n$  integer pairs of vortices along the plate as the level of the steps. The second peaks that occurs at a higher frequency have an extra vortex present along the plate compared with the major step at that aspect ratio. As a result the trailing-edge shedding is  $180^\circ$  out of phase compared with the lower frequency peak.

### 6.3.1.3 Duct acoustic resonance

Sound generated from flow around a plate placed in a duct can excite resonant modes in the duct which in turn locks the flow. Stokes & Welsh (1986) found it possible to generate that resonance at several distinct frequency bands. These bands also showed a stepwise increase with aspect ratio. Previous theoretical and computational models (Welsh *et al.*, 1984, Stokes & Welsh, 1986, Stoneman *et al.*, 1988) have proposed the mechanism for the sound generation. The current simulations improve on the previous work by accurately simulating the flow (i.e. no flow and boundary layer models). The flow field and the acoustic field are decoupled and the acoustic field is modelled using Howe's acoustic theory (Howe 1975, 1980).

These simulations are performed at  $Re = 400$  and the applied forcing used to lock the flow is  $v_{pert} = 2.5\%$ . The acoustic model predicts distinct frequency ranges where there is a nett transfer of energy from the flow field to the acoustic field. This is a necessary condition for acoustic resonance. The ranges of  $St_c$  where resonance is possible also showed a stepwise increase with aspect ratio. Again these steps are approximately at  $St_c = 0.55n$ . Further investigations showed that the predictions were not sensitive to the different approximations used for the acoustic particle velocity. The different approximations tested are the potential flow model and the wave model with different duct lengths.

## 6.3.2 On the controlling mechanism

In this section, the proposed controlling mechanism involved in each of the three cases is reviewed and supported by further analysis. Figure 6.1 shows a sketch of the essential

components involved. The underlying mechanism in each case was used to explain the behaviour of the flow predicted by the simulations. The relationship and similarities between the mechanisms involved in each case will be highlighted.

### 6.3.2.1 Natural shedding

In the natural shedding case, it is generally agreed that the impinging leading-edge vortex instability (ILEV) which locks the flow at low and moderate Reynolds numbers consists of a feed back loop (Nakamura *et al.*, 1991, Ohya *et al.*, 1992, Naudascher & Wang, 1993). As shown in Figure 6.1(a), this mechanism consists of leading-edge vortices convecting downstream. These vortices interact with the trailing-edge vortices and pressure fluctuations develop with the passing of the leading-edge vortices and the development of discrete vortices at the trailing edge. These pressure fluctuations radiate out and if they are strong enough at the leading edge to lock the shedding, it completes the feed back loop. This results in a synchronisation between the leading- and trailing-edge shedding. Vorticity plots taken from the simulations have shown that in all cases where this mechanism locks the flow, there is a constant relative phase between the leading- and trailing-edge shedding. To maintain this synchronisation, the possible modes can either increase or decrease by an integer pair of vortices. Again as shown by vorticity plots, there can be only  $n$  integer pairs of discrete vortices along the plate. With only a pair generated each period, this means that a flow structure would require  $n$  periods to convect from the leading edge to the trailing edge.

This mechanism is also responsible for the frequency selection. When the flow is periodic and a flow structure requires  $n$  periods to traverse the plate, then the Strouhal number based on chord,  $St_c$  (which is  $cf/U_\infty$ ), divided by the shedding mode  $n$ , is the average convective velocity of these structures. The calculations have shown that the behaviour of the convective velocity of the vortices are approximately uniform for plates with different aspect ratio. It follows then that the shedding frequency of  $St_c = 0.55n$  means that the average convective velocity is 55% of the free-stream velocity for all the aspect ratios tested that lock to the flow.

As the aspect ratio is increased, the shedding frequency,  $St$ , would have to decrease to allow more time for the vortices to traverse the plate. This continues until the system is no longer receptive to such a low frequency that it jumps to the next step. This is seen in the reduction in mean base suction and drag force as the aspect ratio is increased within a shedding mode. The lower frequency shedding also results in the base pressure trace showing some random fluctuations between periods. After the step jump in frequency, these trends continue with further increases in aspect ratio. The trend in

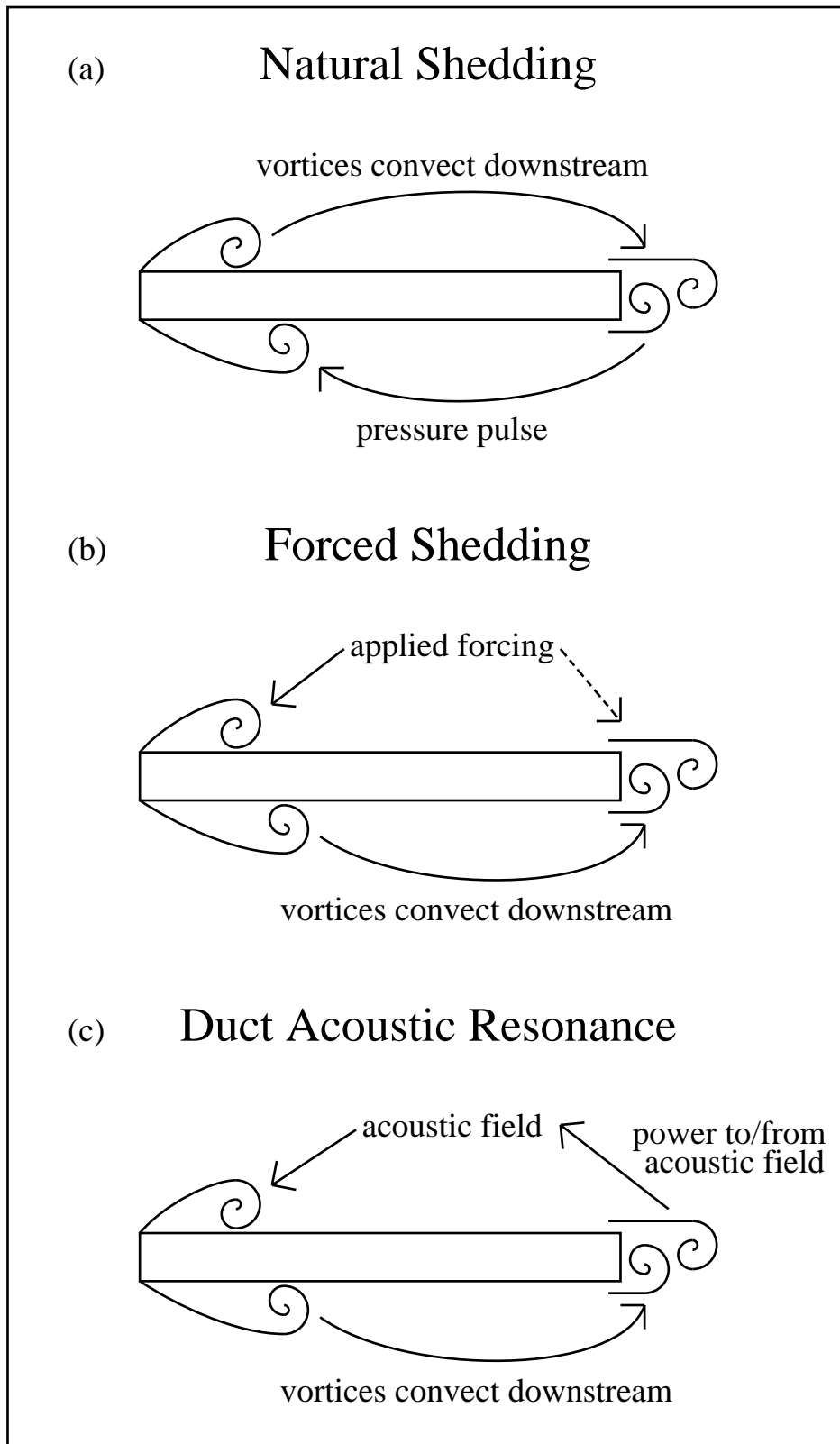


Figure 6.1: Schematic representation of the mechanism involved in the (a) natural shedding, (b) forced shedding and (c) duct acoustic resonance cases.

base pressure and drag force continue even when the flow no longer locks to the shedding. This is not surprising as spectral plots of the base pressure trace shows that the ILEV frequency is still significant for the case with  $c/t = 11$  and  $Re = 400$  which does not lock to the single frequency due to a competition between this shedding mode ( $n = 3$ ) and a lower intermediate mode (between  $n = 2$  and  $n = 3$ ).

The synchronisation between the leading- and trailing-edge shedding also results in a more uniform fluctuating lift force with aspect ratio. Pairs of vortices along the plate approximately cancel the effect of each other. The leading-edge shedding and the passing of vortices at the trailing edge are the main contributors to the fluctuating lift forces. As these two processes are synchronised, the the levels of the fluctuation in the lift force is approximately constant and the standard deviation in the fluctuating lift coefficient (based on chord) would therefore be inversely proportional to the aspect ratio.

The receptivity range of the system is a combination of the receptivity at the leading and trailing edges. In the case where the trailing-edge shedding is suppressed, such as the  $\vdash$  section at  $Re = 300$ , Nakamura (1996) found the first shedding mode ( $n = 1$ ) occurred between  $c/t = 3$  to 10 and the second shedding mode ( $n = 2$ ) occurred between  $c/t = 11$  to 15(limit of experiment),  $n = 2$ . In that case, where only the leading-edge shedding is significant, the shedding frequency ( $St$ ) range is much larger compared to the rectangular plate. The presence of the trailing-edge shedding, although influenced by the passing of the leading-edge vortices, reduces the receptivity range of the system an leads to transition between shedding modes at shorter intervals in aspect ratio.

This feedback mechanism relies on a relatively weak pressure pulse from the trailing edge to synchronise the leading-edge shedding. With increasing distance (larger aspect ratios), the pressure pulse which propagates radially would be weaker at the leading edge. The leading-edge shedding would not lock if the strength of this pulse falls below a critical level. As the Reynolds number increases, any disturbances from upstream and due to flow structures would experience less damping. The level of “background” noise levels due to chaos and turbulence also grows with increasing Reynolds number. Since the pressure pulse does not grow as rapidly with Reynolds number, these disturbances would drown the signal at higher Reynolds numbers. This would explain the upper limit in aspect ratio and Reynolds number where the flow no longer locks to a single frequency.

### 6.3.2.2 Forced shedding

Although not present in the natural shedding case at higher Reynolds number, this mechanism can be excited if there is some external influence (Nakamura *et al.*, 1991). This is seen in the forced shedding and the duct acoustic resonance cases. Hourigan *et al.* (1993)

proposed the forcing frequency where the mean base suction peaks is determined by the interference of leading-edge vortices at the trailing edge. Further refinements by Mills (1998) showed that the phase in the forcing cycle at which the leading-edge vortex arrives at the trailing edge determines the frequency selection. These simulations also show this to occur and builds on these observations.

The key components in the forced shedding cases is shown in Figure 6.2(b). The simulations have shown that the leading-edge shedding is phase-locked to the forcing in all cases where the flow is locked to the forcing. As in the natural shedding case, they convect downstream and the trailing-edge vortices form between the passing of leading-edge vortices. This locks shedding of both the leading- and trailing-edge vortices to one frequency which is the applied forcing frequency. The phase of the trailing-edge shedding relative to the forcing or the leading-edge shedding is therefore determined by these leading-edge vortices. The behaviour of the trailing-edge-shedding, which also experiences the global forcing, would be governed by its relative phase to the forcing as well.

For all aspect ratios tested, at the forcing frequency that corresponds to the peak base suction, or the lower frequency peak in those cases where there are two local peaks, the phase of shedding at the trailing edge relative to the forcing is constant. To maintain this phase relationship, as in the natural shedding case, there can be only an increase or decrease in a complete pair of vortices along the plate. The vorticity plots also show that there are  $n$  (integer) number of vortices along the plate with integer increases at critical aspect ratios. At this relative phase, the direction of the acceleration in the perturbation velocity induces the vortices forming at the trailing edge towards the centreline of the plate. Vortices forming closer to the base and the narrower wake results in the stronger base suction predicted by the simulations.

The frequency selection also depends on the convective velocity of the leading-edge vortices. Calculations have shown that the behaviour of the convective velocity of these vortices is not significantly influenced by the aspect ratio and the forcing frequency. One difference under forcing is that the leading-edge vortex is more compact and the minima in convective velocity occurs closer to the leading edge suggesting that they form closer to the leading edge compared with the natural shedding case. Based on the synchronisation of the trailing-edge shedding and the behaviour of the convective velocity of the leading-edge vortices, the stepwise response in the forcing frequency  $St_c$  where these peaks in mean base suction occur would therefore also show a stepwise response as in the natural shedding case. The number of vortices along the plate ( $n$ ) correspond to the level of the steps. Again the level of the steps at  $St_c = 0.55n$  would signify that the average convective velocity of the vortices along the plate is 55% of the free-stream velocity.

At some aspect ratios, where the peak in base suction occurs at a low forcing frequency, another local peak develops at a higher forcing frequency within the lock-in range. These cases show that the trailing-edge shedding is  $180^\circ$  out of phase relative to the cases corresponding to the major steps. These cases have only one extra vortex along the plate, and as a result, the forcing frequency ( $St_c$ ) is at an intermediate level between steps. Simulations at a different level of forcing show that the magnitude of these peaks decrease with increasing forcing levels. As the trailing-edge shedding is out of phase relative to the major steps, the applied forcing is actually suppressing the mean base suction by inducing the trailing-edge vortices to form further from the centreline of the plate.

The mechanism excited by the forcing can also explain other observations found in the simulations. The forcing frequency at which the base suction peaks is not significantly altered by variations in Reynolds number and forcing amplitude. These parameters do not significantly alter the behaviour of the convective velocity of vortices along the plate. As the same mechanism is involved, the forcing frequency at which the peak base suction occurs would not vary significantly. The effect of increasing the forcing amplitude is to increase the mean base suction with larger increases at forcing frequencies which result in strong mean base suction. At these forcing frequencies, there is strong base shedding, and as in the case where the nose is aerodynamic, the base suction grows with forcing amplitude. Even with a small forcing amplitude, the lock-in range of frequencies is large. This is caused by the leading-edge shedding locking to the large range of frequencies. The vortices from the leading edge have a strong influence on the trailing-edge shedding thereby locking the entire system over a large band of frequencies.

As in all previous cases, the behaviour of the drag force mimics that of the mean base pressure. The fluctuating lift force shows local maximums corresponding to the major steps and local minimums corresponding to the intermediate steps. This is a result of the phase at which the leading-edge vortices pass the trailing edge. They can either add or oppose the fluctuating component resulting from the leading-edge shedding. The magnitude of the peak in base suction and drag force is higher for cases with aspect ratios closer to the lower end of each step. In these cases, the forcing frequency is higher. The simulations have shown that the vortex formation length decreases with increasing frequency. Therefore the vortices form closer to the trailing edge in these cases and this results in stronger base suction. If the forcing frequency is increased further, the simulations show that the trailing-edge shedding is suppressed and this results in a lower mean base suction.

### 6.3.2.3 Duct acoustic resonance

In this case, the sound field resonating in the duct completes the feed back loop. Figure 6.1(c) shows the essential components in this particular case once resonance occurs. The predictions in this study and previous studies have shown the region near the trailing edge to be the main source of sound (Stokes & Welsh, 1986, Thompson *et al.*, 1987). Energy transferred from the flow to the sound field will then sustain the resonant field. The resonant sound in turn locks the leading-edge shedding. The final result is a feed back loop with the sound field, trailing- and leading-edge shedding locking to the resonant frequency.

The technique used in this study assumes the flow is close to incompressible and decouples the flow field and the acoustic field. A resonant acoustic field is assumed to be present and the flow is locked to that frequency by the external applied forcing. Howe's acoustic theory is then used to determine if there is a nett transfer of energy form the flow field to the acoustic field. This is a necessary but not a sufficient (because energy losses are neglected) condition to sustain the resonance.

The acoustic model predicts only a negligible amount of sound generated between the leading and trailing edge because the acoustic particle velocity is approximately tangential to the flow. Upstream of the plate, a negligible acoustic power is generated because the amount of vorticity is negligible. Further downstream of the plate, vortex pairs cancel the effect of each other. Nett acoustic energy is generated when vortices are shed at the trailing edge or leading-edge vortices pass the trailing edge and enter the wake. Contour plots of acoustic power and analysis of the shedding process have shown that the phase in the resonance cycle these vortices are introduced into the wake govern the direction of average energy transfer.

As the leading-edge shedding is phase-locked to the resonant sound, the phase of the leading-edge vortices passing the trailing edge and the trailing-edge shedding is again dependent on aspect ratio and resonant (forcing) frequency as for the forced shedding cases. It is not surprising then that the frequency bands where resonance is possible also shows steps approximately corresponding to  $St = 0.55n$ . In the plates simulated, some plates showed two or three frequency bands where resonance is possible. In these cases, each increasing band corresponds to an additional pair of vortices along the plate. Even when trailing edge shedding is suppressed at higher forcing frequencies, resonance is possible with acoustic power generated from leading-edge vortices entering the wake.

#### 6.3.2.4 Similarity between cases

One common feature in all three cases is the frequency selection which in each case shows stepwise increases of  $St = 0.55n$  with aspect ratio. After reviewing each case, it was found that they all rely on a synchronisation between the leading- and trailing-edge shedding. In all cases the leading-edge vortices convect downstream and this controls the trailing-edge shedding. The difference is the way the leading-edge shedding is synchronised to shed alternately. In the natural shedding case, there is a pressure pulse from the the trailing edge. In the cases with applied forcing or duct resonance, the leading-edge shedding is phase-locked to the applied forcing or sound field. These triggers (pressure pulse, applied forcing or acoustic fields) travel much faster than the flow velocity in these cases because the flow field is almost incompressible. The frequency selection is therefore based on the role of the leading-edge vortices which take a finite time to travel the length of the plate. This study has shown that the behaviour of the convective velocities of these vortices is not significantly influenced by aspect ratio and forcing frequency (when applied). The stepwise increase with aspect ratio is therefore a result of the system maintaining the synchronisation between the leading- and trailing-edge shedding.

The simulations have shown that in each case the steps in frequency are approximately  $St = 0.55n$ . This is a result of the convective velocity of the flow structures between the leading and trailing edges being 55% of the free-stream velocity. The independent experiments in each case show that the steps are closer to  $St = 0.6n$  (Nakamura *et al.*, 1991 in the natural shedding case, Mills, 1988 in the forced shedding case and Stokes & Welsh, 1986 in the acoustic resonance case). In these experiments, the Reynolds numbers are generally higher and the flow three dimensional (Nakamura *et al.*, 1991 at  $Re = 1,000$ , Mills, 1988 at  $Re \approx 9,000$  and Stokes & Welsh at  $Re \approx 15,000 - 30,000$ ). As a result, the average convective velocity of flow structures along the plate in the experiments may be higher than in the simulations.

Although these simulations are two dimensional, they have captured the major mechanism controlling the flow. Physically at these Reynolds numbers, there is some three-dimensionality in the flow, the mechanism is two dimensional and the vortex rollers are still predominantly two dimensional with some spanwise distortions. This allows the flows to be simulated with a reasonable amount of accuracy in two dimensions.

#### 6.3.2.5 On the feedback mechanism in the natural shedding cases

The flow around long bodies with bluff leading edges can lock to a particular shedding mode thereby synchronising the leading-edge shedding with the flow structures at the

trailing edge. To achieve this, a feedback loop is established between the leading and trailing edges. There are some differences in several parts of the feedback loop as shown in Figure 6.2. This diagram builds on previous works (see Section 1.2.4) and the observations in this study. The selection is dependent mainly on aspect ratio and the trailing-edge geometry. The common component is the separated leading-edge shear layer and the pressure pulse generated around the trailing edge which feeds back and controls the shear layer thus completing the loop. Small aspect ratio geometries where the vortices from the leading edge are shed directly into the wake are not considered here.

The first of three cases considered here is where the leading-edge shear layer directly interacts with the trailing edge (shown in blue, Figure 6.2). This has been classified by Nakamura (1986) as the impinging shear layer instability. That study involved geometries with rectangular, H and  $\vdash$  cross-sections ranging between  $c/t = 2$  and 5. Here, the shear layer interacts directly with the trailing edge which in turn sends a pressure pulse to lock the leading-edge shedding. This classification of impinging shear layer instability has been used previously in other cases to describe the situation where the shear layer interacts with a solid boundary downstream which send a pressure pulse upstream influencing the shear layer (Rockwell & Naudascher, 1978).

The term impinging leading-edge vortex instability (ILEV) was proposed by Naudascher & Wang (1993) to incorporate the shedding of leading-edge vortices in those cases where the leading-edge shear layer does not reach the trailing edge (i.e.  $n = 2, 3, \dots$ ). The earlier case ( $n = 1$ ) could be included in this classification because vortices are shed from the leading edge although the shear layer does periodically reach the trailing edge. This process is highlighted in red (Figure 6.2). The shear layer at the leading edge rolls up into discrete vortices and convect along the body. As these vortices pass the trailing edge, a pressure pulse is generated. This pulse travels upstream to lock the leading-edge shedding. Examples of where this occurs include the  $\vdash$  section and a wide variety of bluff bodies such as cylinders and square sections fitted with splitter plates (Nakamura, 1996).

Previous studies and classification associated with the flow around long rectangular plates did not highlight the important role of shedding from the trailing edge (Nakamura *et al.*, 1991, Ozono *et al.*, 1992, Naudascher & Wang, 1993). In these simulations, although pressure fluctuations do occur when the leading-edge vortices pass the trailing edge, strong base shedding is also observed. The pressure fluctuations associated with the formation of trailing-edge vortices are larger in these simulations. This is seen in the large mean and fluctuating components in base pressure. A description of the feedback process occurring in these simulations is shown in green (Figure 6.2). Vortices are shed from the shear layer at the leading edge. These vortices convect along the plate and interact with the shedding at the trailing edge (i.e., trailing-edge vortices forms be-

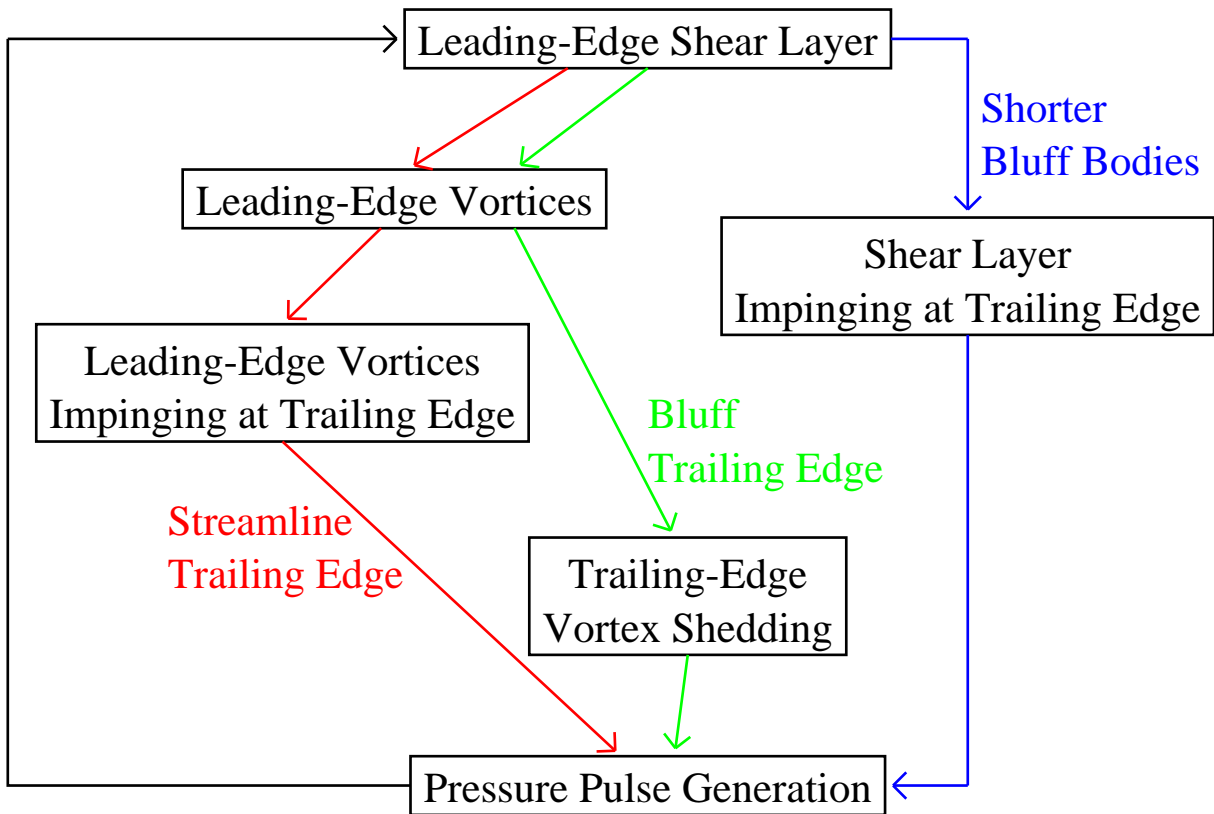


Figure 6.2: A schematic showing the possible feedback mechanisms for flow around a long body with a bluff leading edge experiencing no external excitation.

tween the passing of leading-edge vortices). The pressure pulse from the base shedding then feeds back upstream and controls the leading-edge shedding. As discussed earlier in Section 6.3.2.1, the added influence of the trailing-edge shedding compared with those cases without is the more limited range of shedding frequencies in each shedding mode. Previous description of this feedback mechanism such as the impinging shear layer or the impinging leading-edge vortex instability does not discriminate between trailing-edge geometries. As a result, the trailing-edge shedding has been excluded from the feedback mechanism. In the case of a rectangular plate, the simulations show strong base shedding which would dominate the effect of leading-edge vortices passing the trailing edge. The description proposed here to incorporate the base shedding is therefore more applicable to cases with significant base shedding.

## 6.4 Three-dimensional simulations

A limited number of three-dimensional flow simulations are performed to study the transitional states for flow around elliptical leading-edge and rectangular plates. The Reynolds numbers in these simulations are chosen around where transition from two- to three-dimensional flow occurs. In the case where the leading edge is aerodynamic, the transition in the wake is examined. The spanwise instability of leading-edge vortices is the focus in simulations involving rectangular plates. The nature of the technique used here enforces periodic boundary conditions on the spanwise boundaries. This allows only discrete spanwise wavelengths (more limited at longer wavelengths) to be captured and therefore may influence the results.

### 6.4.1 Elliptical leading-edge plate

Simulations are performed for the flow around elliptical leading-edge plates with a 5:1 axes ratio and aspect ratios of  $c/t = 7.5$  and  $2.5$ . Two spanwise shedding modes have been observed similar to *Mode A* and *Mode B* in the wake of a circular cylinder. The spanwise wavelengths in these simulations are generally larger because of the thicker boundary layers near the trailing edge and the resulting vortices being more diffused.

The simulations were able to capture three-dimensional vortical structures with topology similar to *Mode A* at  $Re = 500$  and  $c/t = 7.5$ . Two wavelengths of this shedding were simulated in the computational domain resulting in a spanwise wavelength of  $\pi t$ . It is uncertain if the most unstable mode is captured because only discrete wavelengths can be simulated. No spanwise instabilities were observed in simulations at  $Re = 400$  and below. *Mode B* shedding is expected to dominate at higher Reynolds number but no simulations were attempted due to computational constraints.

Simulations with  $c/t = 2.5$  have captured two shedding modes in the transition process. The simulation captured a long wavelength flow structure at  $Re = 300$  with topology consistent with *Mode A* shedding. As only one wavelength of this flow structure was captured within the domain ( $2\pi t$ ), there is some uncertainty as to which is the most unstable wavelength. There are smaller wavelengths that develop in certain shedding cycles. This could be either a competition between shedding modes or a result of the restrictive domain. At  $Re = 350$ , *Mode A* shedding is suppressed and the presence of some flow structures consistent with *Mode B* shedding is present. The wavelength of these structures is uncertain because they are sporadic and not uniform across the span. When the Reynolds number is increased to  $Re = 380$ , these structures become stronger and more regular. These flow structures have a spanwise wavelength of approximately

0.8t.

Simulations with applied external forcing are not attempted for this geometry because of the difficulty in simulating at higher Reynolds number to capture the transition. Some simulations with applied forcing are attempted with the rectangular plate.

## 6.4.2 Rectangular plate

The flow around plates with  $c/t = 6, 10$  and  $13$  is simulated at  $Re = 350$  and  $400$ . No spanwise instability was observed in the simulations with  $c/t = 6$ . Flow structures similar to those classified as *Pattern B* by Sasaki & Kiya (1991) are observed when  $c/t = 10$  and  $13$  at both  $Re = 350$  and  $400$ . These were hairpin-like structures arranged in a staggered manner on both sides of the plate. In all cases, two wavelengths were captured in the domain and therefore the spanwise wavelength is approximately  $3t$ . The streamwise wavelength is approximately  $3t$  when  $c/t = 10$  and  $4t$  when  $c/t = 13$ . Both streamwise and spanwise wavelengths are within the range of experimental uncertainty.

Further simulations to capture *Pattern A* have not been successful. These were performed with  $c/t = 13$  at several Reynolds number below  $Re < 350$  and with different spanwise domain sizes. Simulations with applied forcing for plates with  $c/t = 10$  and  $Re = 400$  all resulted in the flow reaching a two-dimensional state. The forcing amplitude was at  $v_{pert} = 2.5\%$  and the frequency ranged between  $St = 0.13$  and  $0.19$ . To capture transition in these cases would require simulations with higher Reynolds number.

# Contents

<b>6</b>	<b>Summary and Conclusions</b>	<b>206</b>
6.1	Computational aspects . . . . .	206
6.1.1	Numerical technique . . . . .	206
6.1.2	Benchmark test . . . . .	207
6.1.3	On using the Runge-Kutta scheme for the convective sub-step . . .	208
6.1.4	Simulation of flow around plates . . . . .	209
6.2	Flow around elliptical leading-edge plates . . . . .	210
6.2.1	Natural shedding . . . . .	210
6.2.2	Forced shedding . . . . .	211
6.3	Flow around rectangular plates . . . . .	214
6.3.1	Results from simulations . . . . .	215
6.3.2	On the controlling mechanism . . . . .	217
6.4	Three-dimensional simulations . . . . .	227
6.4.1	Elliptical leading-edge plate . . . . .	227
6.4.2	Rectangular plate . . . . .	228

# Chapter 7

## References

Barkley D. & Henderson R.D. 1996 Three-dimensional Floquet Stability Analysis of the Wake of a Circular Cylinder. *J. Fluid Mech.* **322**, 215-241.

Bearman P.W. 1965 Investigation of the Flow behind a Two-dimensional Model with a Blunt Trailing Edge and Fitted with Splitter Plates. *J. Fluid Mech.* **21**, 241-255.

Bearman P.W. & Currie I.G. 1979 Pressure Fluctuation Measurements on an Oscillating Circular Cylinder. *J. Fluid Mech.* **91**, 661-677.

Bearman P.W. & Davies M.E. 1977 The Flow about Oscillating Bluff Structures. *Proceedings of the Fourth International Conference on Wind Effects on Buildings and Structures*, Heathrow, (Ed K.J. Eaton) pp. 285-295. Cambridge University Press.

Bearman P.W. & Obasaju E.D. 1982 An Experimental Study of Pressure Fluctuations on Fixed and Oscillating Square-Section Cylinders. *J. Fluid Mech.* **119**, 297-321.

Bearman P.W. 1984 Vortex Shedding from Oscillating Bluff Bodies. *Ann. Rev. Fluid. Mech.* **16**, 195-222.

Blackburn H. & Henderson R. 1996 Lock-In in Simulated Vortex-Induced Vibration. *Exp. Thermal Fluid Sci.* **12**, 184-189.

Canuto C., Hussaini M.Y., Quarteroni T.A. & Zang T.A. 1988 Spectral Methods in Fluid Dynamics. New York : Springer-Verlag.

Cherry N.J., Hillier R. & Latour M.E.M.P. 1984 Unsteady Measurements in a Separated and Reattaching Flow. *J. Fluid Mech.* **144**, 13-46.

Churchill R.V., Brown J.W. & Verhey R.F. 1974 Complex Variables and Applications.

(Third Edition) McGraw-Hill.

Cooper P.I., Sheridan J.C. & Flood G.J. 1986 The Effect of Sound on Forced Convection Over a Flat Plate. *Int. J. Heat & Fluid Flow* **7**, (1), 61-68.

Deniz S. & Staubli Th. 1997 Oscillating Rectangular and Octagonal Profiles: Interaction of Leading- and Trailing-Edge Vortex Formation. *J. Fluids Struct.* **11**, 3-31.

Deniz S. & Staubli Th. 1998 Oscillating Rectangular and Octagonal Profiles: Modelling of Fluid Forces *J. Fluids Struct.* **12**, 859-882.

Eisenlohr H. & Eckelmann H. 1988 Observations in the Laminar Wake of a Thin Flat Plate with a Blunt Trailing Edge. *Proc. Expt. Heat Transfer, Fluid Mech. and Thermodynamics* 4-9 Sept., Dubrovnik, Yugoslavia, (Ed R.K. Shah, E.N. Ganic & K.T. Yang) pp. 264-268.

Ghia U., Ghia K.N. & Shin C.T. 1982 High-Re Solutions for Incompressible Flow Using the Navier-Stokes Equations and a Multigrid Method. *J. Comput. Phys.* **48**, 387-411.

Gresho P.M., Gartling D.K., Torczynski J.R., Cliffe K.A., Winters K.H., Garratt T.J., Spence A. & Goodrich J.W. 1993 Is the Steady Viscous Incompressible Two-dimensional Flow over a Backward-Facing Step at  $Re = 800$  Stable? *Int. J. Num. Methods Fluids* **17**, 501-541.

Hama F.R. 1957 Three-dimensional Vortex Pattern behind a Circular Cylinder. *J. Aeronaut. Sci.* **24**, 156-158.

Hannemann K. & Oertel H. Jr. 1989 Numerical Simulation of the Absolutely and Convectively Unstable Wake. *J. Fluid Mech.* **199**, 55-88.

Head M.R. & Banyopadhyay P. 1981 New Aspects of Turbulent Boundary-Layer Structure. *J. Fluid Mech.* **107**, 297-338.

Henderson R.D. & Barkley D. 1996 Secondary Instability in the Wake of a Circular Cylinder. *Phys. Fluids* **8**(6), 1683-1685.

Henderson R.D. 1997 Nonlinear Dynamics and Pattern Formation in Turbulent Wake Transition. *J. Fluid Mech.* **352**, 65-112.

Hourigan K., Mills R., Thompson M.C., Sheridan J., Dilin P. & Welsh M.C. 1993 Base Pressure Coefficients for Flows around Rectangular Plates. *J. Wind Eng. Ind. Aerodyn.* **49**, 311-318.

Howe M.S. 1975 Contributions to the Theory of Aerodynamic Sound, with Applications

- to Excess Jet Noise and the Theory of the Flute. *J. Fluid Mech.* **71**, 625-673.
- Howe M.S. 1980 The Dissipation of Sound at an Edge. *J. Sound Vib.* **70**, 407-411.
- Huerre P. & Monkewitz P.A. 1990 Local and Global Instability in Spatially Developing Flows. *Ann. Rev. Fluid. Mech.* **22**, 473-537.
- Kachanov Yu.S. & Levchenko V.Ya. 1984 The Resonant Interaction of Disturbances at Laminar-Turbulent Transition in a Boundary Layer. *J. Fluid Mech.* **138**, 209-247.
- Karniadakis G.E. & Triantafyllou G.S. 1989 Frequency Selection and Asymptotic States in Laminar Wakes. *J. Fluid Mech.* **199**, 441-469.
- Karniadakis G.E. 1989 Spectral Element Simulations of Laminar and Turbulent Flows in Complex Geometries. *Appl. Numer. Math.* **6**, 85-105.
- Karniadakis G.E. 1990 Spectral Element-Fourier Methods for Incompressible Turbulent Flows. *Comput. Methods Appl. Mech. Eng.* **80**, 367-380.
- Karniadakis G.E., Israeli M. & Orszag S.A. 1991 High-Order Splitting Methods for the Incompressible Navier-Stokes Equations. *J. Comput. Phys.* **97**, 414-443.
- Karniadakis G.E. & Triantafyllou G.S. 1992 Three-dimensional Dynamics and Transition to Turbulence in the Wake of Bluff Objects. *J. Fluid Mech.* **238**, 1-30.
- Kim J. & Moin P. 1985 Application of a Fractional-Step Method to Incompressible Navier-Stokes Equations. *J. Comput. Phys.* **59**, 308-323.
- Koch W. 1985 Local Instability Characteristic and Frequency Determination of Self-Excited Wake Flows. *J. Sound Vib.* **99**, 53-83.
- Liffman K. 1996 Comments on a Collocation Spectral Solver for the Helmholtz Equation. *J. Comput. Phys.* **128**, 254-258.
- Lofty A. & Rockwell D. 1993 The Near-Wake of an Oscillating Trailing Edge: Mechanisms of Periodic and Aperiodic Response. *J. Fluid Mech.* **251**, 173-201.
- McCormick D.C., Lessmann R.C. & Test F.L. 1984 Heat Transfer to Separated Flow Regions from a Rectangular Prism in a Cross Stream. *J. Heat Transfer* **106**, 276-283.
- Mills R., Sheridan J., Hourigan K. & Welsh M.C. 1995 The Mechanism Controlling Vortex Shedding from Rectangular Bluff Bodies. *12th Australasian Fluid Mechanics Conference* 10-15 Dec., Sydney, Australia, (Ed R.W. Bilger) pp. 227-230.
- Mills R.H. 1998 Vortex Interaction in Flows over Bluff Bodies. Ph.D. Thesis, Dept. of

Mechanical Engineering, Monash University, Melbourne, Australia.

Mittal R. & Balchandar S. 1996 Direct Numerical Simulation of Flow Past Elliptic Cylinders. *J. Comput. Phys.* **124**, 351-367.

Monkewitz P.A. & Nguyen L.N. 1987 Two-dimensional Bluff Bodies. *J. Fluids Struct.* **1**, 165-184.

Morton B. R. 1984 The Generation and Decay of Vorticity. *Geophys. Astrophys. Fluid Dynamics* **28**, 277-308.

Najjar F.M. & Balchandar S. 1998 Low-Frequency Unsteadiness in the Wake of a Normal Flat Plate. *J. Fluid Mech.* **370**, 101-147.

Nakamura Y. & Mizota T. 1975 Unsteady Lifts and Wakes of Oscillating Rectangular Prisms. *J. Engng. Mech. Div.* **6**, 855-871.

Nakamura Y. & Nakashima M. 1986 Vortex Excitation of Prisms with Elongated Rectangular, H and  $\vdash$  Cross-Sections. *J. Fluid Mech.* **163**, 149-169.

Nakamura Y., Ohya Y. & Tsuruta H. 1991 Experiments on Vortex Shedding from Flat Plates with Square Leading and Trailing Edges. *J. Fluid Mech.* **222**, 437-447.

Nakamura Y. 1996 Vortex Shedding from Bluff Bodies with Splitter Plates. *J. Fluids Struct.* **10**, 147-158.

Nakayama R., Nakamura Y., Ohya Y. & Ozono S. 1993 A Numerical Study of the Flow around Flat Plates at low Reynolds Numbers. *J. Wind Eng. Ind. Aerodyn.* **46 & 47**, 255-264.

Naudascher E. & Wang Y. 1993 Flow-Induced Vibration of Prismatic Bodies and Grids of Prisms. *J. Fluid Struct.* **7**, 341-373.

Naudascher E. & Rockwell D. 1994 Flow-Induced Vibrations : An Engineering Guide. Rotterdam; Brookfield : A.A. Balkema.

Norberg C. 1994 An Experimental Investigation of the Flow around a Circular Cylinder: Influence of Aspect Ratio. *J. Fluid Mech.* **258**, 287-316.

Ohya Y., Nakamura Y., Ozono S., Tsuruta H. & Nakayama R. 1992 A Numerical Study of Vortex Shedding from Flat Plates with Square Leading and Trailing Edges. *J. Fluid Mech.* **236**, 445-460.

Okajima A. 1982 Strouhal Numbers of Rectangular Cylinders. *J. Fluid Mech.* **123**,

379-398.

Okajima A., Mizota T. & Tanida Y. 1983 Observations of flow around rectangular cylinders. *Proc. 3rd Int. Symp. on Flow Visualisation*, Michigan, 193-199.

Okajima A. 1990 Numerical Simulation of Flow Around Rectangular Cylinders. *J. Wind Eng. Ind. Aerodyn.* **33**, 171-180.

Okajima A., Nagahisa T. & Rokugoh A. 1990 A Numerical Analysis of Flow around Rectangular Cylinders. *JSME Int. J. Ser. II* **33**(4), 702-711.

Okajima A., Ueno H. & Sakai H. 1992 Numerical Simulation of Laminar and Turbulent Flows Around Rectangular Cylinders. *Int. J. Num. Methods Fluids* **15**, 999-1012.

Okajima A. & Kitajima K. 1993 Numerical Study on Aeroelastic Instability of Cylinders with a Circular and Rectangular Cross-Section. *J. Wind Eng. Ind. Aerodyn.* **46 & 47**, 541-550.

Ongoren A. & Rockwell D. 1988 Flow Structure from an Oscillating Cylinder Part 1. Mechanisms of Phase Shift and Recovery in the Near Wake. *J. Fluid Mech.* **191**, 197-223.

Ota T. & Kon N. 1979 Heat transfer in a Separated and Reattached Flow over Blunt Flat Plates - Effects of Nose Shape. *Int. J. Heat Mass Transfer* **22**, 197-206.

Ozono S., Ohya Y., Nakamura Y. & Nakayama R. 1992 Stepwise Increase in the Strouhal Number for Flows Around Flat Plates. *Int. J. Num. Methods Fluids* **15**, 1025-1036.

Parker R. 1966 Resonant Effects in Wake Shedding from Parallel Plates: Some Experimental Observations. *J. Sound Vib.* **4**, 62-72.

Parker R. & Welsh M.C. 1983 Effects of Sound on Flow Separation from Blunt Flat Plates. *Int. J. Heat Fluid Flow* **4**(2), 113-127.

Patera A.T. 1984 A Spectral Element Method for Fluid Dynamics: Laminar Flow in a Channel Expansion *J. Comput. Phys.* **54**, 468-488.

Perry, A.E., Lim T.T. & Teh E.W. 1981 A Visual Study of Turbulent Spots. *J. Fluid Mech.* **104**, 387-405.

Petrusma M.S. & Gai S.L. 1994 The Effect of Geometry on the Base Pressure Recovery of Segmented Blunt Trailing Edges. *Aeronaut. J.* **98**, 267-273.

Pierrehumbert R.T. 1984 Local and Global Baroclinic Instability of Zonally Varying

- Flows. *J. Atmos. Sci.* **41**, 2141-2162.
- Poliashenko M. & Aidun C.K. 1995 A direct method for computation of simple bifurcations. *J. Comp. Phys.* **121**, 246-260.
- Robichaux J., Balachandar S. & Vanka S.P. 1999 Three-dimensional Floquet Instability of the Wake of Square Cylinder. *Phys. Fluids* **11**(3), 560-578.
- Rockwell D. & Naudascher E. 1978 Review - Self Sustaining Oscillations of Flow Past Cavities. *J. Fluids Engng.* **100**, 152-165.
- Rockwell D. & Naudascher E. 1979 Self-Sustained Oscillations of Impinging Free Shear Layers. *Ann. Rev. Fluid. Mech.* **11**, 67-94.
- Rockwell D. 1990 Active Control of Globally-Unstable Separated Flows. *Proceedings of the ASME Symposium on Unsteady Flows* 3-9 June, Toronto, Canada.
- Roshko A. 1954 On the Development of Turbulent Wakes from Vortex Streets. *Technical Report 1191*, NACA.
- Roshko A. 1961 Experiments of Flow Past a Circular Cylinder at Very High Reynolds Number. *J. Fluid Mech.* **10**, 345-356.
- Saric & Thomas 1984 Experiments on the Subharmonic Route to Turbulence in Boundary Layers. In *Turbulence and Chaotic Phenomenon in Fluids*, (ed. T. Tatsumi) pp. 117-122. Amsterdam; North-Holland : Elseviers.
- Sasaki K. & Kiya M. 1991 Three-dimensional Vortex Structure in a Leading-Edge Separation Bubble at Moderate Reynolds Numbers. *J. Fluids Engng.* **113**, 405-410.
- Shen J. 1991 Hopf Bifurcation of the Unsteady Regularized Driven Cavity Flow. *J. Comput. Phys.* **126**, 329-347.
- Sigurdson L.W. 1995 The Structure and Control of a Turbulent Reattaching Flow. *J. Fluid Mech.* **298**, 139-165.
- Sohankar A., Norberg C. & Davidson L. 1999 Simulation of the Three-dimensional Flow around a square Cylinder at Moderate Reynolds Numbers. *Phys. Fluids* **11**(2), 288-306.
- Soria J. & Wu J. 1992 The Character of the Instability of the Separated Shear Layer from a Square Leading Edge Flat Plate. *11th Australasian Fluid Mechanics Conference* 14-18 Dec., Hobart, Australia, (Ed M.R. Davies & G.J. Walker) pp. 391-394.
- Soria J., Sheridan M. & Wu J. 1993 Spatial Evolution of the Separated Shear Layer from

- a Square Leading-Edge Plate. *J. Wind Engng. Indust. Aero.* **49**, 237-246.
- Stansby P.K. 1976 Base Pressure of Oscillating Circular Cylinders. *J. Engng. Mech. Div.* **4**, 591-600.
- Staubli Th. 1981 Calculation of the Vibration of an Elastically Mounted Cylinder using Experimental Data from Forced Oscillation. *ASME Symp. Fluid Struct. Interactions Turbomachinery* pp. 19-24.
- Stokes A.N. & Welsh M.C. 1986 Flow-Resonant Sound Interaction in a Duct Containing a Plate, II: Square Leading Edge. *J. Sound Vib.* **104**(1), 55-73.
- Stoneman S.A.T., Hourigan K., Stokes A.N. & Welsh M.C. 1988 Resonant Sound caused by Flow Past Two Plates in Tandem in a Duct. *J. Fluid Mech.* **192**, 455-484.
- Tafti D.K. & Vanka S.P. 1991 A Numerical Study of Flow Separation and Reattachment on a Blunt Plate. *Phys. Fluids A* **3**(7), 1749-1759.
- Tan B.T., Morris P., Thompson M.C. & Hourigan K. 1988 Chaotic Mixing Simulations. *App. Math. Modelling* **22**, 1047-1057.
- Thompson J.F., Warsi Z.U.A. & Wayne Mastin C. 1995 Numerical Grid Generation, Foundations and Applications. New York; North-Holland.
- Thompson M.C., Hourigan K., Welsh M.C. & Soh W.K. 1987 Predictions of Vortex Shedding from Bluff Bodies in the Presence of a Sound Field. *IUTAM Symposium on Fundamental Aspects of Vortex Motion*, 31 Aug. - 4 Sept., Tokyo, Japan.
- Thompson M.C., Hourigan K. & Sheridan J. 1994 Three-dimensional Instabilities in the Wake of a Circular Cylinder. *International Colloquim on Jets, Wakes and Shear Layers* 18-20 Apr., Melbourne, Australia.
- Thompson M.C., Hourigan K. & Sheridan J. 1996 Three-dimensional Instabilities in the Wake of a Circular Cylinder. *Exp. Thermal Fluid Sci.* **12**, 190-196.
- Thompson M.C. 2000 : Private Communication.
- Welsh & Gibson 1979 Interaction of Induced Sound with Flow Past a Square Leading Edged Plate in a Duct. *J. Sound Vib.* **67**(4), 501-511.
- Tombazis N. & Bearman P.W. 1997 A Study of the Three-dimensional Aspect of Vortex Shedding from a Bluff Body with a Mild Geometric Disturbance. *J. Fluid Mech.* **330**, 85-112.

Welsh M.C., Stokes A.N. & Parker R. 1984 Flow-Resonant Sound Interaction in a Duct Containing a Plate, Part I: ‘Semi-circular Leading Edge. *J. Sound Vib.* **95**, (3), 305-323.

Welsh M.C., Hourigan K., Welch L.W., Downie R.J., Thompson M.C. & Stokes A.N. 1990 Acoustics and Experimental Methods: The Influence of Sound on Flow and Heat Transfer. *Exp. Thermal Fluid Sci.* **3**, 138-152.

Williamson C.H.K. 1988 The Existence of Two Stages in the Transition to Three-dimensionality of a Cylinder Wake. *Phys. Fluids* **31**, 3165-3168.

Williamson C.H.K. 1989 Oblique and Parallel Modes of Vortex Shedding in the Wake of a Circular Cylinder at Low Reynolds Numbers *J. Fluid Mech.* **206**, 579-627.

Williamson C.H.K. & Roshko A. 1990 Measurements of Base Pressure in the Wake of a Cylinder at low Reynolds Numbers. *Z. Flugwiss Weltraumforsch* **14**, 38-46.

Williamson C.H.K. 1996 Three-dimensional Wake Transition. *J. Fluid Mech.* **328**, 345-407.

Wu J., Sheridan J., Soria J., Welsh M. & Hourigan K. 1993 Experimental Investigation of Vortex Shedding from a Plate: Effect of External Velocity Perturbation. *J. Wind Eng. Ind. Aerodyn.* **49**, 401-410.

Wu J., Sheridan J., Soria J. & Welsh M.C. 1994 An Experimental Investigation of Stream-wise Vortices in the Wake of a Bluff Body. *J. Fluids Struct.* **8**, 621-625.

## 7.1 Publications resulting from this work

Thompson M.C., Tan B.T. & Hourigan K. 1997 Simulation of Perturbed Flows Past Long Blunt Plates *Proceedings of the ASME Fluids Engineering Division Summer Meeting* 22-26 June, Vancouver, British Columbia, Canada.

Tan B.T., Morris P., Thompson M.C., Hourigan K. 1997 Numerical Simulations of Chaotic Mixing. *Computational Fluid Dynamics in Mineral & Metal Processing and Power Generation*, 3 - 4 July, Melbourne, Australia, (Ed M.P. Schwarz, M.R. Davidson & A.K. Easton), pp 245-252.

Tan B.T., Morris P., Thompson M.C. & Hourigan K. 1988 Chaotic Mixing Simulations. *App. Math. Modelling* **22**, 1047-1057.

Tan B.T., Thompson M.C. & Hourigan K. 1998 Simulated Flow around Long Rectangular Plates under Cross Flow Perturbations. *Int. J. Fluid Dynamics* **2**, Article 1.

Tan B.T., Thompson M.C. & Hourigan K. 1998 Simulation of Perturbed Flow around a Rectangular Cylinder. *Proceedings of the ASME Fluids Engineering Division Summer Meeting* 21-25 June, Washington D.C., USA.

Tan B.T., Thompson M.C. & Hourigan K. 1998 Numerical Predictions of Forces on a Long Rectangular Plate Subjected to Cross-Flow Perturbation. *13th Australasian Fluid Mechanics Conference* 13-18 Dec., Melbourne, Australia, (Ed M.C. Thompson & Hourigan K.), pp. 789-794.

Tan B.T., Thompson M.C. & Hourigan K. 1998 Three Dimensional Vortical Structures in Flow around Plates. *13th Australasian Fluid Mechanics Conference* 13-18 Dec., Melbourne, Australia, (Ed M.C. Thompson & Hourigan K.), pp. 875-880.

# Contents